Mechanical Engineering Graduate Theses & Dissertations

Mechanical Engineering

Spring 1-1-2015

Room Temperature Ionic Liquid Electrolytes for Advanced Lithium-ion Batteries

Tyler Evans
University of Colorado Boulder, tyler.evans@colorado.edu

Recommended Citation

Room Temperature Ionic Liquid Electrolytes for Advanced
Lithium-Ion Batteries

by

Tyler Evans

B.S., University of Notre Dame, 2012

M.S., University of Colorado, Boulder, 2014

A thesis submitted to the

Faculty of the Graduate School of the

University of Colorado in partial fulfillment

of the requirements for the degree of

Doctor of Philosophy

Department of Mechanical Engineering

2015

This thesis entitled:
Room Temperature Ionic Liquid Electrolytes for Advanced Lithium-Ion Batteries
written by Tyler Evans
has been approved for the Department of Mechanical Engineering

_____

Prof. Se-Hee Lee

_____

Prof. Rich Noble

_____

Prof. Y.C. Lee

_____

Prof. Yifu Ding

_____

Prof. Ronggui Yang

Date _____

The final copy of this thesis has been examined by the signatories, and we find that both the
content and the form meet acceptable presentation standards of scholarly work in the above
mentioned discipline.

Evans, Tyler (Ph.D., Material Science)

Room Temperature Ionic Liquid Electrolytes for Advanced Lithium-Ion Batteries

Thesis directed by Prof. Se-Hee Lee

This dissertation presents a series of studies aimed towards the development of a compelling and commercially viable Li-ion battery containing a non-flammable room temperature ionic liquid (RTIL) electrolyte. Each study builds upon the previous, culminating in the demonstration of a high energy Li-ion system approaching the 700 Wh/L energy density benchmark. We begin by tackling several major issues associated with RTIL compatibility with the battery's passive, non-electroactive components, engineering solutions to each and enabling the utilization of certain RTIL materials in high voltage Li-ion systems. Since enabling the simple use of our RTIL electrolytes, we have been able to explore RTIL compatibility with a number of attractive, next-generation electrode chemistries including the high capacity silicon (Si) anode and high voltage, high capacity lithium-manganese-rich (LMR) cathode. Each of these studies contributes to a deeper understanding of the interfacial mechanisms occurring between the RTIL materials and various electrode surfaces, in several cases resulting in unprecedented half- and full-cell performance. The accomplishments presented herein represent important progress in working towards a safer, higher performance Li-ion system.

Dedication

Denver skyline (9News)
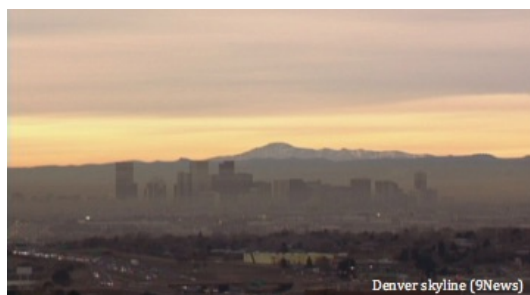
Growing up south east of Denver in Aurora, CO, I was accorded a similar view every day. The grandeur of the Front Range is stunning and undeniable. But the cloud looming over the city seems to never leave. It was images and views like this one that led me to work towards a degree in Environmental Science at the University of Notre Dame. What could I do to help preserve the world in which we live and the places that we love? Thinking more deeply about this question, I enrolled in a course in Notre Dame's Department of Chemical Engineering: Energy Storage and Conversion. I learned that we can use our world's greatest toolbox, the Periodic Table of Elements, to harness sustainable power needed for societal progress. Months later, Dr. Shelley Miller called my phone to congratulate me on my acceptance to the University of Colorado's Mechanical Engineering Ph.D. program. I was overjoyed with the prospect of returning home to CO to pursue that vision: contributing to a society that powers itself sustainably, one that works in harmony with the natural world.

I like to spend my free time exploring Colorado's mountains. Every time I get outside, I am reminded of my gratitude for the absolute beauty of our state. Colorado gets to me, every time. This is another, slightly different photograph of the Denver skyline, taken at sunrise from

the summit of Longs Peak on the morning of April 12, 2014. Along with two of my best friends, climbing partners, and graduate school peers, I completed a late winter climb of the Peak by an obscure route, through the night, for my birthday. It became one of my most personally meaningful experiences in the mountains. It is images and views like this one and the experiences associated with them that have motivated my graduate research, serving as reminders of my motivations and inspiration. While my contribution to the energy sciences, represented herein, is miniscule in the big picture, I feel that I have contributed to something positive. For this reason, I dedicate my Graduate Thesis to my home, Colorado.

Acknowledgements

I am very grateful to have had the support of incredible mentors, coworkers, family and friends during my doctoral program. I would first like to give a very special thank you to my advisor, Se-Hee Lee, for granting me the opportunity to join his group and earn my doctorate degree. He welcomed me from Day 1 and I truly feel lucky to have been a member of his group. Se-Hee's excitement for science is motivating, and his dedication to stay up to date with each of his student's projects along with his other responsibilities is admirable. Most importantly, Se-Hee taught me that there is no such thing as a bad idea; the best thing one can do in his/her research is to try something new and always think out of the box. Se-Hee's encouragement of creative research allowed me grow as a scientist, and his friendly attitude made me feel comfortable trying new things. I could not have succeeded without his guidance and help, and I am very grateful for the opportunities Se-Hee has afforded me. I look forward to continuing our relationship. More than an advisor and Professor, Se-Hee has been a source of personal guidance. This notion first came to me when Se-Hee and I were stuck in the airport in Tulsa after my first MAST Center conference; I was new to his lab group. Our flight was cancelled and a half dozen tornadoes had touched down in the area. Our flight was delayed and finally cancelled in the late hours, forcing us to stay in a hotel for a few short hours of sleep before a red eye flight. I got to know Se-Hee during this adventure; his tremendously positive outlook, his personable demeanor, and his calm style became a model for how I would like to approach my own career and professional relationships.

I am very thankful to have had Dr. Vinay Bhat from CoorsTek FluoroChemicals (previously Boulder Ionics) as a research mentor during the first several years of my graduate education. Vinay

has been an amazing resource. He taught me how to be thorough in my experimental design and how to always criticize my conclusions. He treats me as a colleague, and I will always be appreciative of his openness and our professional relationship.

I would like to thank a number of colleagues that I have had the privilege of collaborating with. I would like to thank my former and current labmates, Thomas A. Yersak, Seoung-Bum Son, Ji Woo Kim, Jae Ha Woo, Daniela Molina Piper, and Justin Whiteley for always offering their input and help with the numerous challenges I encountered throughout my doctoral career. I would especially like to thank Thomas A. Yersak and Daniela Molina Piper. In a sense, I was Tom's protégé. He taught me how to do battery research as I entered CU and Se-Hee's research group. He taught me patience, respect, and persistence. I had the opportunity to work very closely with Tom, Ji Woo, Justin, and Dani and I would like to thank them for not only involving me in their research, but for also contributing significantly to my own research. I would particularly like to thank Daniela Molina Piper for her close collaboration. Over the past couple of years, Dani and my research have crossed paths and allowed for many incredibly fruitful research opportunities. She is driven to make a difference and has always been an outstanding collaborator. She is easy to work with; I appreciate her can-do attitude and the energy and sincerity with which she approaches her work. We have been able to accomplish more together than I would have been able to do alone. This relationship has solidified my understanding that innovation is collaborative, and I am excited for what our professional partnership has in store. Justin and I started up in Se-Hee's lab around the same time, and his friendly demeanor, impressive work ethic, and adventurous research approach have helped keep me going. Justin and Dani have made my time in the office and lab most enjoyable, and of course Dani's puppy Mecha has been a constant stress reliever.

I would also like to thank Professor Oh's group at Seoul National University for their amazing characterization work. Seul Cham Kim, Chan Soon Kang, Sang Sub Han, and Yong-Seok Kim have been four amazing microscopists that have brought impactful meaning to our entire group's work, and particularly to my research work. Dr. Kevin Leung, Professor Buttry, Jarred Olson, and Tylan Watkins are colleagues I worked with during a major project for this dissertation, and I would like

to thank them for their amazing work and expertise. I would like to thank my defense committee for volunteering their time to be part of my doctoral defense. I would like to give a big thank you to Sharon Anderson and Kassie Ferraro. Both have gone above and beyond to always help me out. I owe them both enormously, as well as Vera Sebulsky, who was a massive help as I finished my graduate work.

Finally, thank you to my friends and family for their support and for reminding me of what is truly important. I am blessed to have great people in my life, and I look forward to sharing my next experiences with you.

Contents

Appendix

Figures

Figure

Chapter 1

Introduction

On April 18, 1977, U.S. President Jimmy Carter publicly declared the nation's energy crisis. Thermostats were turned down, sweaters were put on, research and development efforts increased, and carpooling was applauded. The energy crisis of the 1970's was a geopolitically driven battle dominated by soaring oil prices, which topped out at about $78 per barrel in today's dollars.

Almost 40 years after Carter's energy crisis, the world population has far exceeded 7 billion. It is time to evaluate our means. The modern energy landscape hosts a wider array of challenges, now including the political, environmental, health, and economic consequences of a long and heavy reliance on oil and gas, imploring a reconsideration of the industry's mechanisms and the means by which we obtain and use energy. How will the world sustain massive population growth and the swift pace of an increasingly globalized world economy?

The U.S. burns 900 million tons of coal per year [215]. China is now burning 3.8 billion tons of coal per year [215]. And yet this is only a fraction of the almost 8 billion tons of coal burned every year. In 2011, the number of fuel burning cars on the world's roads surpassed 1 billion, requiring the production of almost 90 million barrels of oil per day [209]. A particularly unsustainable consequence of our energy use is the environmental burden of burning fossil fuels. Since the industrial revolution, the atmospheric concentration of carbon dioxide has increased by more than 30% [20]. In 2012 the World Health Organization reported that 7 million people died as a result of air pollution exposure, calling pollution the world's largest single environmental health risk.

We are physically changing the environment in which we live, and the change is scientifically and statistically significant. These statistics are intended to bring to light the pace and quality of societal development and the means by which this growth is powered. Our species has enjoyed impressive progress, but it is necessary to re-evaluate our energy means such that society is capable of sustaining itself in the future.

The aforementioned numbers are simply stated as facts; the implications of these facts may be subjective. Despite differing arguments from the left, right, the 1%, the 99%, left field, and everywhere in between, it is apparent that the world is in transition. A dialogue is growing regarding world energy use and how the world should proceed in providing people with the energy needed to survive and participate in modern society. The changes discussed by all parties have environmental, economic, political, personal health, and even national security repercussions. I argue that the underlying question, regardless of one's belief in the severity of a looming energy crisis, should be:

Is this really the best way?

Are humans capable of more cost efficient, cleaner, healthier, more sustainable means of harnessing and using energy? Human society is innately progressive; we should be raising the bar. Can we find ways to capture electrons with out having to burn something, can we do this cheaply, and in such a way that provides everyone, regardless of location, the opportunity to use these electrons? Science says yes. There are ways. And many nations, across the world, are starting to adopt a higher standard.

Sweden, Norway, and Iceland generate over 80% of their energy free of carbon (note that these are not the sunniest places in the world) [155]. Germany generates over 40% of its energy renewably and exists as an economic leader in Europe [155]. Counting nuclear energy, the U.S. generates over 30% of its power from clean or renewable sources [155]. At least in the developed world, the revolution has begun. To some, the benefits of clean energy are obvious. One wind turbine can generate enough power for 300 homes, with the main costs incurred during initial capital investment and from miniscule operations and maintenance costs, resulting in the cheapest

levelized price per electron delivered in the energy industry.

Yet, growth in clean energy is far outpaced by the oil and gas industry. This is due largely to the maturity of the respective industries and their markets. Figure 1.1 illustrates a sort of return on investment (energy produced per dollar spent on equipment and research and development) for shale gas rigs, leading energy storage technology, and leading renewable energy technologies. Because the oil and gas industry is well-established and receives significantly more investment, it is able to improve at an unprecedented pace. With the current pace of technological development massively increasing the recoverable reserves of oil and gas in the world, British Petroleum estimates that there are over 53 years of oil left in the tank and the U.S. alone has enough natural gas to last well over 80 years [54]. In other words, this is not an acute resource problem. If one does not find clean energy in its present form affordable and finds that the resource problem is a misnomer, there is one fact left to consider: the environment is changing, and we will have to adapt. World carbon emissions doubled from 1960 to 1990, and are expected to double again, to at least 35 billion tonnes by the end of 2015 [162].

Regardless of the political climate or oil and gas economics, technological development offers an answer to the world's energy problem and the need for adaptation:

Energy storage.

Efficiently storing energy would pave the way for cost effective clean energy. As previously mentioned, wind power provides the cheapest way to bring electricity generation to the grid, and the cost of solar energy is dropping dramatically; but the intermittency and availability of such resources makes them unattractive to many. Energy storage brings the potential to eliminate the intermittency issues of solar and wind generation, make combustion engines a thing of the past, and could address global energy poverty in a rapidly growing population. Energy storage, because of its ability to enable renewables and revolutionize transportation, is the foundation of a better energy future.

This ideal future is already being manifest by numerous companies, new and old, which are
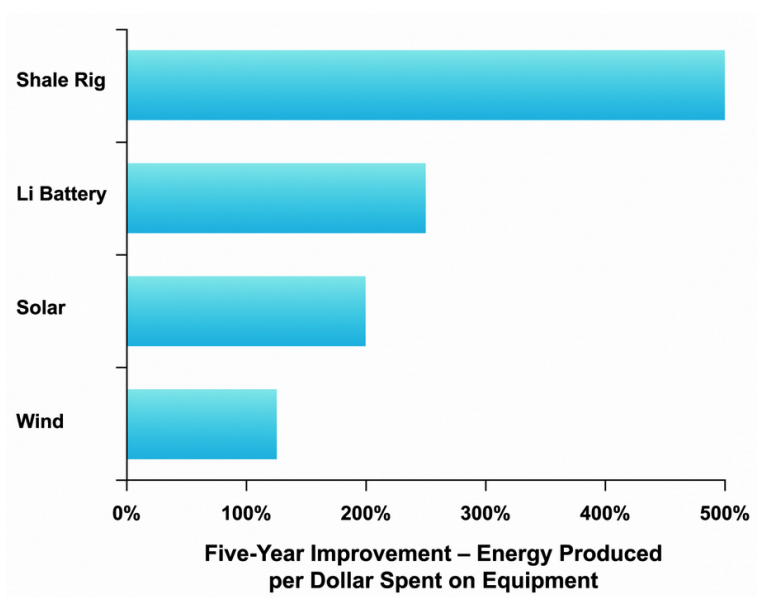
Figure 1.1: Improvements in energy produced per dollar spent on oil and gas recovery, Li-ion energy storage, and major renewable energy technologies.

developing large scale storage projects. From new, booming companies like Tesla, Ambri, AES, and OXIS Energy, to established behemoths the likes of Samsung, LG Chem, BYD, and GE, energy storage is catching on. Today, the most energy dense and cost effective means of storing electrons is the lithium-ion battery. With almost 95% of the batteries used in electronic devices based on the lithium chemistry, the global market for Li-ion batteries is expected to cross $30B by 2020. While rechargeable lithium-ion batteries have dominated the portable electronics market for nearly a decade, they have failed to gain widespread commercial success in high power and high capacity applications, including electric vehicles and grid-level storage. Those working on this problem have been unable to develop a battery capable of meeting the growing societal and environmental demand for safe, high-energy-density, long-lasting energy storage systems [12]. Such systems could serve to expedite a smooth transition to an electrified transportation market and enable intermittent renewable energy resources, both of which have been gaining attention in our increasingly carbon-constrained world. Figure 1.2 illustrates the projected growth in lithium demand over the next decade. The expected increase in demand creates a lucrative and highly meaningful opportunity for those capable of designing better batteries.

While battery technology continues to progress, its advance is slow and incremental. Slight improvements in materials processing and device manufacturing have allowed for an improvement in energy density of approximately 5-6% each year [214, 205]. Despite such a slow rate of improvement, demand for a battery providing 400 Wh/kg (almost double the specific energy of current state-of-the-art lithium-ion batteries) at $200/Wh (half the price of today's technology) is growing. This milestone, set by the U.S. Department of Energy's Vehicle Technology Office (DOE VTO) in collaboration with the U.S. Advanced Battery Consortium (USABC) is expected to enable the deep market penetration of Li-ion technology in the transportation and energy generation sectors. Reaching the DOE VTO's goal will require breakthroughs in next-generation electrode materials.

This graduate dissertation is an exercise in building higher energy battery technology at the cross-roads of materials science, electrochemistry, and device engineering. The research presented aims towards the development of next-generation Li-ion electrode chemistries through the utiliza-
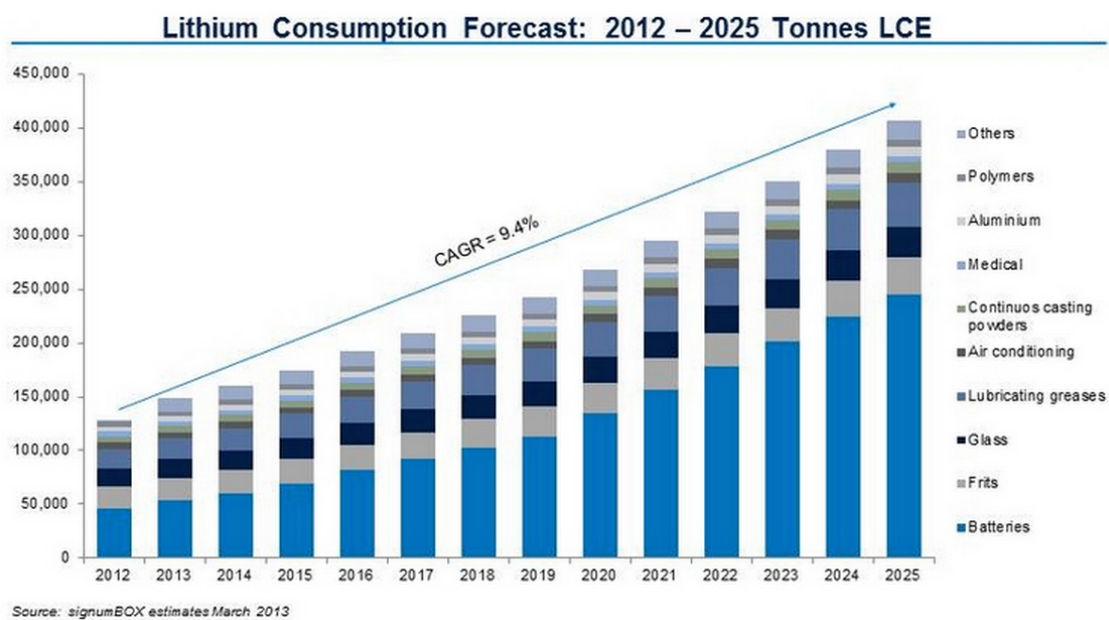
Figure 1.2: Lithium demand forecast 2011-2025.

tion of novel electrolyte compositions. All of the work presented in this project initiated under the premise that today's best battery materials are just that: today's materials. The world's next Li-ion battery will incorporate new, more energy dense materials, working together in a unique chemical balance. The following research highlights an up-and-coming class of electrolyte materials, room temperature ionic liquids, and their interactions with next-generation electrodes. Developing a complete scientific understanding of new Li-ion materials and their interactions is imperative to the successful development of the energy storage industry. I hope that this dissertation contributes to such an understanding, and that the scientific principals elucidated herein are a productive step in the battery community's efforts in working together to build a brighter, more sustainable energy future.

Chapter 2

Principals of Lithium-ion Batteries and State-of-the-Art

2.1   The Electrochemical Process

In general, a battery is a device that converts stored chemical energy into useful electrical energy through an electrochemical redox (reduction-oxidation) reaction. Reduction is defined as the addition of an electron while oxidation is the loss of an electron. In discussing electrochemical cells, the terminal undergoing galvanic reduction is referred to as the cathode (positive electrode), while the terminal undergoing oxidation is referred to as the anode (negative electrode). These electrodes are separated by an electrically insulating but ionically conducting layer referred to as the electrolyte separator. A state-of-the-art lithium-ion battery (LIB) is made up of a carbon-based anode (i.e. graphite) and a transition-metal oxide cathode (i.e. $LiCoO_2$) with a carbonate-based, organic electrolyte (i.e. $1M$ $LiPF_6$ in ethylene carbonate:diethyl carbonate, EC/DEC) as shown in Figure 2.1 [132].

The anode and cathode in conventional LIBs are composite structures engineered from a mixture of active material particles (i.e. graphite, Si, $LiCoO_2$, $LiNi_{1/3}Mn_{1/3}Co_{1/3}O_2$, etc.), polymeric binder (i.e. polyvinylidene difluoride), and a conductive additive (i.e. acetylene black). The porous nature of the composite structures allows for electrolyte permeation and ionic conduction throughout the electrodes, and the conductive additive allows for electronic contact within all the active material permitting good electronic conduction throughout the electrode network. A porous polymer separator is included to prevent physical contact between the two electrodes while wetting with electrolyte to be permeable only to Li^+.
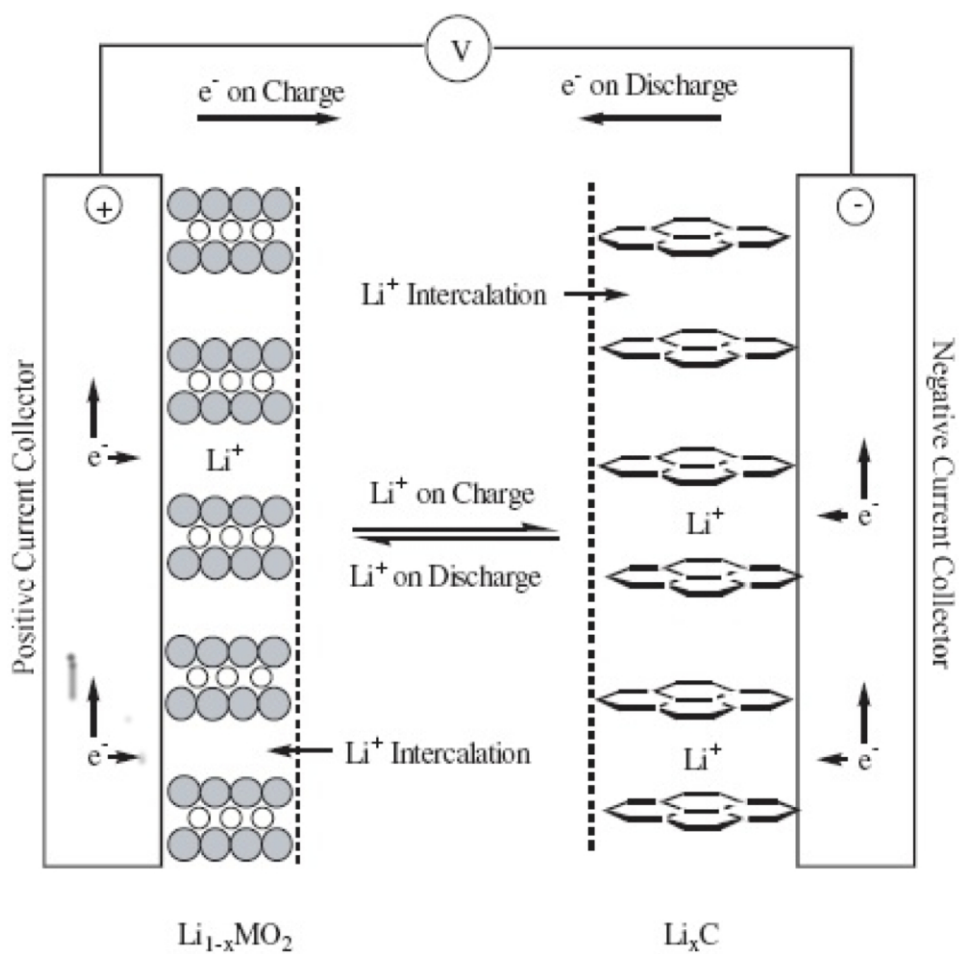
Figure 2.1: Schematic of the electrochemical process in a state-of-the-art lithium-ion cell [132].

Since the electrodes' chemical reactions (and release of energy) require the transfer of both lithium ions and electrons, the electronically insulating electrolyte allows effective storage of the chemical energy within the couples. However, when an external circuit is attached to each terminal, the couples become linked both ionically, through the electrolyte, and electronically, through the external circuit, and the redox reaction occurs. The driving force for these reactions is the difference in *chemical potential* of Li between the two electrodes, or the standard Gibbs free energy change per mole of reaction. In simple terms, the *chemical potential* measures the escaping tendency of a species. The greater the chemical potential of a species, the more likely that species is to move away from the system. When placed in a potential gradient, the species will spontaneously move from high to low chemical potential.

In the charged state, Li sits in the negative electrode, where its chemical potential is high. During discharge, the Li^+ flows from the negative (high chemical potential) to the positive electrode, where the chemical potential is lower. Throughout this discharge process, oxidation occurs at the negative electrode, while reduction occurs at the positive electrode. Concurrently, electrons released from the oxidation of the negative electrode travel through the external circuit, performing work before engaging in the reduction reaction at the positive electrode. The voltage of the battery is related to the difference in chemical potential of the two couples in the system,

$$E = \frac{-(\mu_{Li}^{pos} - \mu_{Li}^{neg})}{nF} = \frac{-\Delta G_{rxn}}{nF}, \tag{2.1}$$

where E is the voltage of the cell, μ^{pos} is the chemical potential of Li in the positive electrode, μ^{neg} is the chemical potential of Li in the negative electrode, n is the number of moles of electrons consumed in the electrochemical reaction, F is Faraday's constant (96,500 Coulombs per equivalent), and ΔG_{rxn} is the Gibbs free energy of the reaction. The chemical potential of Li in each electrode is given by [92, 149]

$$\mu_{Li} = \mu_{Li}^{\circ} + RT ln a_{Li}, \tag{2.2}$$
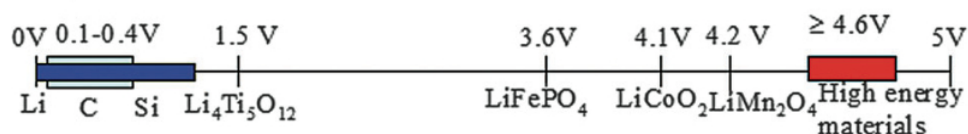
Figure 2.2: Schematic diagram showing the relative working potential of typical electrode materials for lithium-ion batteries [43].

where μ_{Li} is the chemical potential of Li in the electrode, $\mu^{\circ}{}_{Li}$ is the chemical potential of Li in its standard state, R is the ideal gas constant (8.315 J/mol K), T is absolute temperature, and a_{Li} is the activity of Li. Since activity is a measure of effective concentration, Equation 2.2 suggests that as Li is inserted or extracted from an electrode, the chemical potential of Li in the electrode changes, which also causes a change in the voltage of the cell (Equation 2.1). Generally, the voltage of the cell decreases during discharge (when you are acquiring energy from the cell) and increases during charge (when you are adding energy back to the cell), though the change in voltage can depend on the details of phase transformations at each couple, as discussed in the following section [92, 149].

2.2 Gibbs Phase Rule

As described in 2.1, the quantity that determines the voltage of a cell is the Gibbs free energy change associated with the cell's chemical reaction (chemical potentials of Li at the two coupled electrodes) [92] In practice, however, each electrode's voltage is also studied singly with respect to a common reference electrode (electrode with constant makeup or fixed potential) allowing to ascribe any potential changes to the working electrode. In LIBs, the reference electrode utilized is Li metal, which uses the reference value of the electrochemical potential of Li^+/Li redox reaction, -3.04 V *vs.* the standard hydrogen electrode (SHE). Common negative electrode materials for LIBs have potentials that are close to this value (0.01-0.4 V *vs.* Li^+/Li), while common positive electrode materials have higher potentials (3-5 V *vs.* Li^+/Li) as shown in Figure 2.2 [43].

The charge/discharge process of an electrochemical cell is always accompanied by the transport of matter (ions and electrons). When the amount of the transported matter exceeds a certain

threshold, a phase transition may happen either in the cathode or in the anode material. Such crystallographic changes can be observed by monitoring the voltage across an electrochemical cell, because variables in this thermodynamic system are governed by the Gibbs phase rule. Gibbs phase rule states that the relation among the number of degrees of freedom (the number of intensive thermodynamic parameters to define the system) F, the number of separate phases P, and the number of independent components C, in a closed system at equilibrium is given by Equation 2.3 [92].

$$F = C - P + 2 \tag{2.3}$$

In a LIB, the electrode can be treated as a binary system ($C = 2$) consisting of Li and the corresponding delithiated/lithiated phase, which reduces the degrees of freedom to Equation 2.4.

$$F = 4 - P \tag{2.4}$$

In the case of a single-phase solid solution system ($P=1$), the Gibbs phase rule yields 3 degrees of freedom. If temperature and pressure are constant (as they often are in electrochemical experiments), then there is still a residual degree of freedom that must be specified to fully define the system. In this case, the concentration of Li species varies during the reaction and therefore serves as the final thermodynamic parameter necessary to define the system. Thus, the potential of the electrode will vary with temperature, pressure, and concentration. In a voltage-composition plot, this would result in a decreasing potential as concentration of Li^+ increases in the working electrode. This behavior can also be justified by considering Equation 2.1 and 2.2. In the single-phase system, the activity of Li^+ in the working electrode varies with concentration, so the chemical potential of Li (μ_{Li}) in the working electrode and the electrode potential (E) also vary [149].

Now consider a two-phase system where phase separation occurs and the electrode contains two components ($P=2$). In this case, there are two components and two phases in coexistence. According to the Gibbs phase rule, this means that there are no residual degrees of freedom if the temperature and pressure are specified, which indicates that the potential of the electrode as this

electrochemical reaction initiates (and concentration begins to increase) will be constant. In other words, the activity of Li with both reacting phases in the working electrode is constant, so the chemical potential and the electrical potential are also constant according to Equations 2.1 and 2.2 [149].

Overall, Gibbs phase rule is a powerful tool that associates electrochemical measurements with physical material transformations during reactions. In an electrochemical test performed at near-equilibrium conditions, the contour of the measured voltage-capacity curve can be utilized to project the details of the phase diagram at a fixed temperature. This voltage-phase relation is illustrated in Figure 2.3 [149], where the potential of the electrode decreases in single-phase regions, whereas it is constant in two-phase regions. In LIBs, the implementation of both single- and two-phase reaction materials is commonly found.

2.3   Lithium-ion Batteries

Compared to other rechargeable battery systems such as lead-acid, nickel-cadmium and nickel-metal hydride batteries, LIBs provide higher volumetric and gravimetric energy density. The choice of Li^+ as the charge-carrying ion is advantageous for a number of reasons: 1) Li is the lightest of all metals, 2) Li has the greatest electrochemical potential (-3.04 *vs.* SHE), 3) Li is a relatively small atom easing the diffusion into electrode materials, and 4) Li provides the largest specific energy. The specific energy of a battery is calculated by multiplying the total charge capacity of the two electrodes (in mAh g^{-1}) by the voltage of the couple. Thus, the favorable properties of Li and Li-containing materials can result in high theoretical specific energies of Li battery systems.

Lithium's aforementioned advantages drove research to study Li-containing materials as battery electrodes. The first attempt to build a rechargeable Li battery was demonstrated by Whittingham in 1976 [224]. His work was groundbreaking because of the discovery of reversible insertion of Li in the TiS_2 crystal structure. For the first time Whittingham showed the electrochemical intercalation and de-intercalation of Li in the interstitial sites between the layers of the TiS_2 structure. The rechargeable cell demonstrated by Whittingham used TiS_2 as the cathode, metallic lithium as
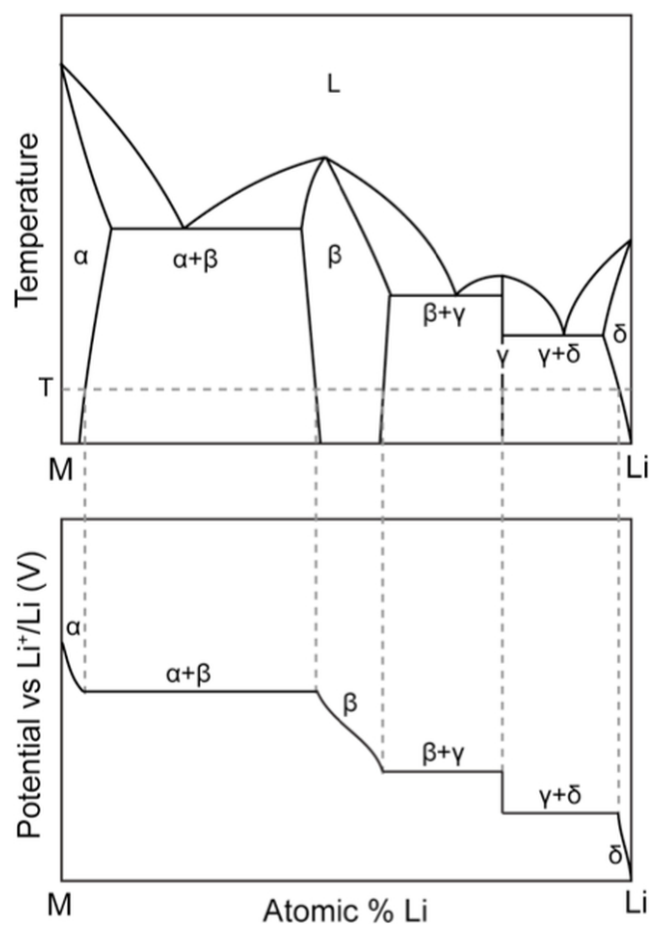
Figure 2.3: M is the species that Li reacts with to form Li$_x$M. In an electrochemical experiment in which Li is added under near-equilibrium conditions to an electrode material M, the phase diagram is traversed across the constant temperature dotted line in the phase diagram. The measured potential at each point in the phase diagram is schematically shown in the bottom panel. In single-phase regions, the potential decreases, while in two-phase regions, the potential is constant [149].

the anode and a non-aqueous electrolyte. And even though this initial work marked the beginning of a massive wave of research over the following decades to find other suitable intercalation materials for lithium-based batteries, soon after, it became apparent that there were critical issues with using Li metal as the negative electrode in the lithium-based battery systems.

The electrodeposition of Li at the Li metal negative electrode during charging is highly prone to the growth of dendrites and surface instabilities [92, 93] that lead to safety problems in the battery systems; short circuiting, thermal runaway and ignition of the flammable organic liquid electrolyte are some of the major safety concerns when dendrites grow and reach the positive terminal of the cell. Moreover, Li metal is highly reactive, especially at lower voltages, and since its potential lies below the thermodynamic stability of most organic electrolytes, reductive decomposition of the electrolyte occurs at the Li metal surface, forming a solid film referred to as the solid-electrolyte interphase (SEI). Although the formation of an SEI is not necessarily a problem without a solution, the dendritic deposition of high surface area Li increases the occurrence of this side reaction, which lowers the Coulombic efficiency of the battery and consumes not only Li but also electrolyte. Due to the aforementioned issues with Li metal, the search kicked in for safe and more efficient negative electrodes.

Not too long after, graphite was chosen as a commercially superior anode, replacing Li metal [234]. It was found that graphite's electrochemical reaction with Li was very similar to that of TiS$_2$ positive electrode. Li intercalates into the layered graphite structure at potentials very close to that of Li metal (0.01 - 0.3 V $vs.$ Li$^+$/Li) but above the equilibrium Li$^+$/Li potential so that the deposition and growth of Li dendrites is prevented, intuitively making graphite material a great candidate for the negative electrode. The discovery and development of graphite negative electrodes eventually led to the commercialization of the first Li-ion battery by Sony in 1991 [157]. The reaction that takes place during Li intercalation is

$$Li^+ + e^- + 6C \longrightarrow LiC_6, \tag{2.5}$$

providing a maximum theoretical specific capacity of 372 mAh g^{-1}; unfortunately having to sacrifice energy density (3860 mAh g^{-1} for Li metal) for safety. These layered materials are favored because intercalation/deintercalation of Li does not significantly alter the host lattice dimensions or structure and allows for a good cycle life. However, the specific capacity of these materials is limited due to the relatively low Li concentration possible in the host lattice. And even though most commercial LIBs today use graphite negative electrodes, a promising rout to higher specific energy LIBs is the development of electrode materials that react with Li via different mechanisms. The energy density limitation with commercially available LIBs and the rapidly growing demand for higher power and energy systems have led to widespread research on a low working potential and high theoretical specific capacity material such as silicon. Recently, silicon has been identified as one of the most attractive high-energy anode materials for LIBs and the development of a viable Si electrode composite is what this dissertation has been intended to realize. The following chapter will review the promises and challenges that come along with the utilization of Si as an active anode material.

2.4 Today's State-of-the-Art Lithium-Ion Battery and Future Research Directions

Li-ion batteries are comprised of three components: the anode, cathode, and electrolyte. Ultimately, the performance of the battery is determined by the individual electrochemical capability of each component and the electrochemical compatibility of the three components together. Early-generation Li-ion batteries were designed using metal and metal-oxide electrode materials and carbonate-based liquid-ion electrolyte solutions.

Graphite intercalation anodes and transition metal oxide intercalation cathodes are commonly used in commercially available Li-ion batteries. Graphite-based anodes are practical given graphite's relatively high theoretical capacity (372 mAh/g) and low potential versus lithium metal. Transition metal oxide cathodes pair well with the graphite anode given their high redox potential (about 4 V vs. Li$^+$/Li). Amongst the transition metal oxides, $LiCoO_2$, $Li(Ni_{1/3}Mn_{1/3}Co_{1/3})O_2$

(a.k.a. L333), and $LiNi_{0.8}Co_{0.15}Al_{0.05}O_2$ (a.k.a. NCA) are the most popular for commercial applications. Recently, incremental improvements in packaging efficiency and materials processing have allowed the lithium-ion battery to approach the 250 Wh/kg benchmark. A comparison of energy provided by today's best batteries, including comparisons to Li-ion battery packs currently utilized in leading EV products, is shown in Figure 2.4. While the progress made to-date has revolutionized the consumer electronics industry and led to the development of compelling EV technology, this plot highlights the major improvements that would be made possible by enabling the next-generation of anode and cathode materials (including the Si anode and LMR cathode).

As previously mentioned, today's state-of-the-art is not sufficient for applications such as EVs; batteries are still too expensive and do not provide adequate drive range for deep market penetration. Figure 2.5 presents a radar plot showing state-of-the-art Li-ion battery performance specifications (red line) compared to those goals set by the DOE VTO (plot edge). Enabling next-generation electrode materials with higher energy- and power-densities in a safe, cost-effective manner is the key to EV market success.

2.4.1   The Silicon Anode

Recently, silicon has been identified as one of the most attractive high-energy anode materials for LIBs. Silicon's low working voltage and high theoretical specific capacity of 3579 mAh g^-1, nearly ten times higher than that of state-of-the-art graphite anodes, have encouraged widespread research efforts aimed at developing a viable Si based electrode [243]. Despite the advantages of the Si electrode, a number of challenges, mainly associated with the material's severe volume expansion, impede its commercialization. While the commercialized graphite electrode expands roughly 10-13% during lithium intercalation [109], Si's expansion amounts to nearly 300%, generating structural degradation and instability of the all-important solid-electrolyte interphase (SEI) [109]. Such instabilities ultimately shorten the battery life to inadequate levels, as shown in Figure 2.6. Degradation of the active material can be mitigated by incorporating materials smaller than 150 nm or through the nanostructural design of electrode architectures capable of reducing expan-
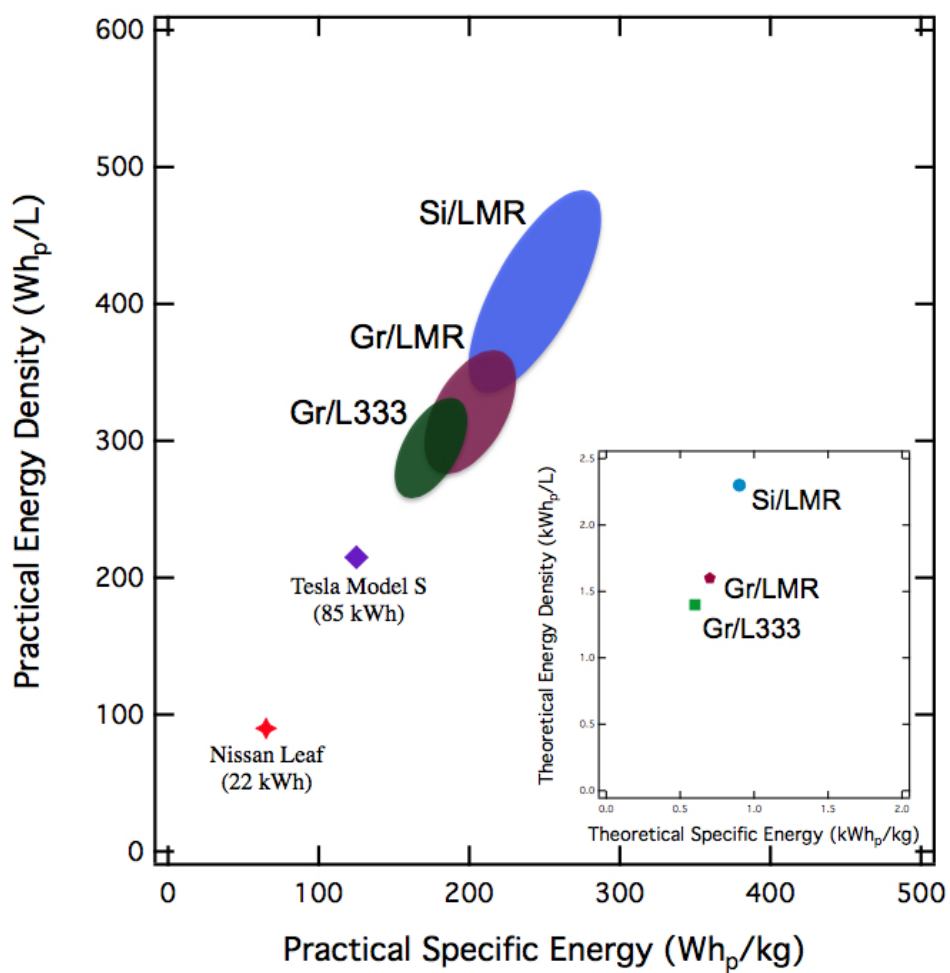
Figure 2.4: Energies of commercialized battery systems and future Li-ion technology.
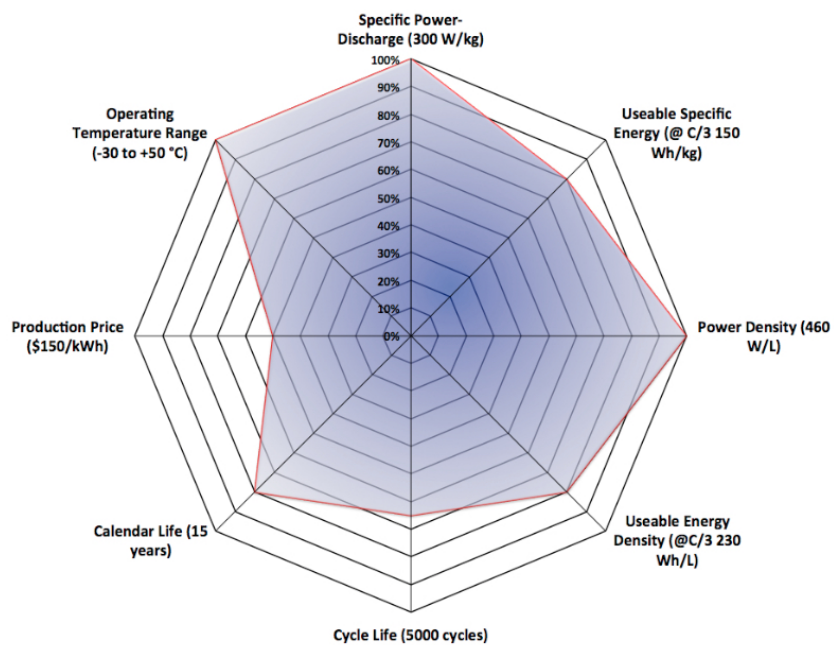
Figure 2.5: Radar plot showing state-of-the-art Li-ion battery performance specifications (red line) compared to those goals set by the DOE VTO (100% line).
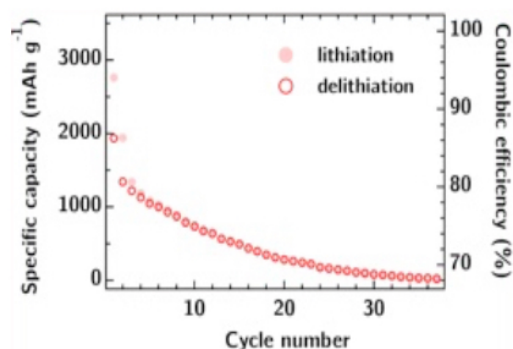
Figure 2.6: Failure of a conventional silicon anode system due to volume expansion and SEI instabilities.

sion [137]. Unfortunately, the electrode architectures presented in previous works [137, 227] lack sufficiently high coulombic efficiencies (CEs) largely because the volume change during Si alloying and de-alloying renders the SEI at the Si-electrolyte interface mechanically unstable. Chapter 8 of this dissertation will discuss the compatibility between new ionic liquid electrolyte materials and the silicon anode, highlighting the impressive ability of certain ionic liquid compositions to enable the previously elusive silicon materials long-term electrochemical stability.

2.4.2   Lithium-Manganese-Rich Oxide Cathodes

The cathode electroactive material currently accounts for greater than 30% of the total cost of a state-of-the-art Li-ion cell [230], over double that of the anode active material cost, yet it most significantly determines the overall working voltage and specific energy of the battery. Moreover, as research and development of new anode materials edges closer to a commercially viable product, the need for a more highly energy-dense cathode to match that of the anode is becoming more apparent.

Lithium-rich high capacity cathode materials have generated a great deal of interest within the battery research community. Chemistries containing high nickel- and manganese-content show the most promise for replacing the first generation of Li-ion cathodes. Because of their high capacities (greater than 250 mAh/g) and high operating voltages (4.5 V vs. Li^+/Li), composite materials

comprised of layered Li[Li$_{1/3}$Mn$_{2/3}$]O$_2$ (also designated as Li$_2$MnO$_3$) and LiMO$_2$ (M = Ni, Mn, Co) have come into the spotlight in recent years [211]. Such lithium-manganese-rich (LMR) oxides can be formulated as xLi$_2$MnO$_3$(1-x)LiMO$_2$ electrodes. These materials were first developed at Argonne National Laboratory, when a team of researchers aimed to stabilize and improve the properties of solid electrodes using structural units rather than cation or anion substituents. In addition to their high capacities and high working voltages, these materials reduce the need for the most expensive and toxic component of conventional cathode materials: cobalt. The electrochemical benefits of enabling such materials are illustrated in Figure 2.4, which compares the specific energies and energy densities of a number of Li-ion systems and two of the most popular commercialized EV battery systems.

While in theory, the LMR cathode is the best choice for a drop-in substitute to today's layered oxide materials, a number of serious problems hinder the chemistry from practical use. LMR materials suffer from voltage-fade, transition-metal dissolution, and structural changes during cycling that rapidly degrade the material's electrochemical performance [211]. These drawbacks have their roots in the change of the initially layered Li$_2$MnO$_3$ and LiMO$_2$ components to a spinel phase. This phase change lowers the average open-circuit potential, and hence the working voltage, of the cell, causing its energy to steadily decrease with cycling [88]. To date, none of the efforts designed to mitigate LMR phase change and capacity fade have resulted in a commercially viable solution. Chapter 9 of the present dissertation will discuss the ability of certain ionic liquid based electrolyte systems to mitigate voltage and capacity fade in the LMR material through favorable interfacial chemical interactions.

2.5   Note

Significant portions of this Chapter were copied from the graduate dissertation of Dr. Daniela Molina Piper.

Chapter 3

Room Temperature Ionic Liquids and Lithium-ion Batteries

Conventional organic electrolytes are composed of small, flammable, and toxic organic species. Typical electrolyte compositions include mixtures of ethylene carbonate (EC) and diethyl carbonate (DEC) or dimethyl carbonate (DMC), with EC providing solvation capabilities for charge carrying salts such as lithium hexafluorophosphate (LiPF$_6$) and DEC or DMC providing a low viscosity media for fast ion transport. Much of the concern regarding lithium-ion batteries focuses on safety issues associated with their organic electrolyte membranes. In 2012 alone, at the time of the commencement of the work presented herein, a number of highly publicized incidents of battery failure contributed to a rise in this sentiment. Examples of such events include the destruction of 16 Fisker Karmas when cars being stored at a New Jersey port caught fire due to battery shorts caused by sea water flooding and the grounding of Boeing's new Dreamliner fleet following malfunctioning batteries and battery management systems. Developing an electrolyte membrane based on a room temperature ionic liquid (RTIL) rather than conventional organic solvents would completely eliminate this major concern regarding lithium-ion battery safety.

Ionic liquids are an inherently unique and interesting class of materials. Simply put, ionic liquids are salts with melting points below 100 C. In addition to this distinctive property, these liquids have very high thermal stabilities and negligible vapor pressures [15]. Such properties make ionic liquids attractive when compared to more volatile organic solvents or catalysts. For this reason, ionic liquids have become a popular tool in the advent of green chemistry. Given the adequate specific conductivities of a number of ionic liquids, these materials have also become an attractive

alternative to organic electrolytes and solvents in electrochemical applications. While such developments are relatively recent, room temperature ionic liquids (RTILs) are under investigation as solvents for technological applications such as metal surface finishing, batteries, capacitors, fuel cells, electrosynthesis, and nuclear waste treatment [212].

Ionic liquids are attractive to battery research because they are non-flammable and have much lower vapor pressures and higher electrochemical stability windows than currently employed organic liquid electrolytes. As shown in Figure 3.1 [212], mixtures of RTIL and conventional organic electrolytes containing 40-60% volume RTIL are non-flammable. This holds true for the majority of RTIL materials. The ionic liquids considered for battery applications are composed of imidazolium- or sulfonium-based cations, as shown in Figure 3.2 [76], and complex halide anions. Their low melting points are related to lattice energy, the energy required to break the ionic bonds holding the species together. Given their large sizes and low electrical charges, ionic liquids comprised of quaternary ammonium cations have low melting points [92]. Quaternary ammonium ions are permanently charged, regardless of pH, and stable across a wide temperature range, allowing stability even as their environment changes chemically and physically [92, 76]. These materials conduct charge by the transport of one or both of their ions. Ionic conductivity of RTILs is typically on the order of mS cm^{-1}, highly dependent upon the size of the ions and the chain length of the alkyl cation component, and their lithium-ion conductivities are significantly lower than conventional carbonate electrolytes [92]. The goal of much early RTIL battery research focused on combining the favorable properties of organic electrolytes with those of ionic liquids [212].

The conductivity of RTILs used in electrochemical applications is significantly lower (typically about half) than electrolytes used in commercialized battery technology. The large size of the ions in RTILs causes them to be more viscous than organic electrolytes, and this hinders ion transport through the electrolyte membrane, as discussed later in Chapter 5. Recent work has shown that the addition of ionic liquids to conventional polymer electrolytes provides satisfactory ionic conductivity with out affecting their stability [191, 190, 192].

Given the number of RTILs capable of battery application, an extensive range of cation-anion
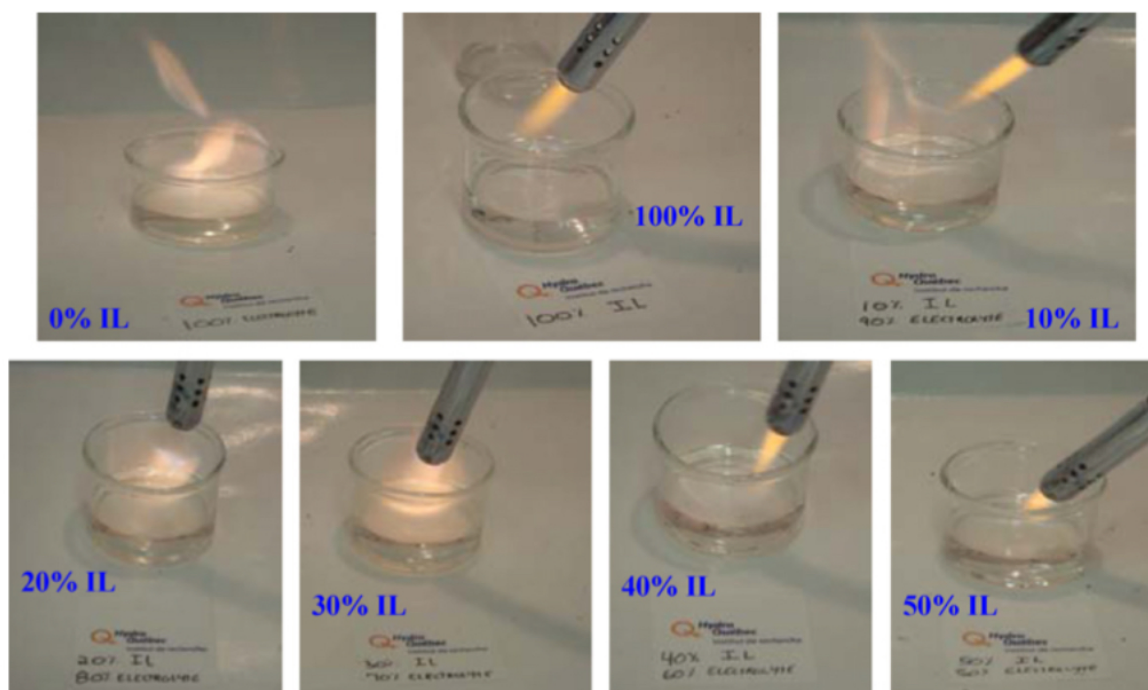
Figure 3.1: Utilization of RTIL solvents as a non-flammable additive to conventional Li-ion battery electrolytes [212].
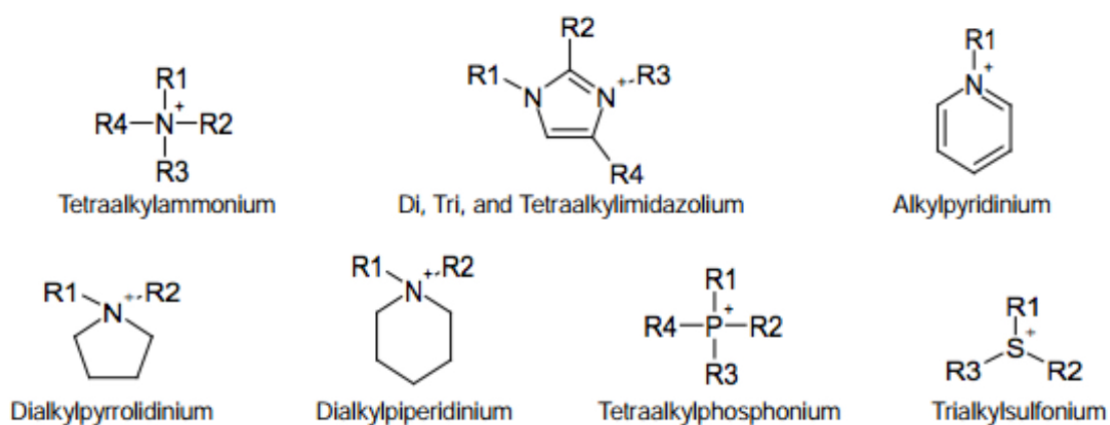
Figure 3.2: Common cation constituents of RTILs used in electrochemical applications [76].

pairs has been researched, with the most attractive cation-anion combinations shown in Figure 3.3 [76]. Each individual cation and ion, as well as each pair of ions, interacts differently with various battery components. Of primary interest is the compatibility between the electrolyte membrane, a graphite anode, various cathode materials, and the current collector substrates holding each electrode. Graphite is a commercially popular anode material, while popular cathode materials include layered intercalation materials such as $LiCoO_2$ and $Li(Ni_{1/3}Mn_{1/3}Co_{1/3})O_2$.

Graphite is not compatible with most RTILs due to the irreversible electrochemical reduction of imidazolium cations on graphite or the cointercalation of the cation species between graphene layers leading to an unstable SEI (solid-electrolyte-interphase) layer or the exfoliation of graphene layers, respectively [176, 247, 203, 145]. This effect is most pronounced at higher potentials. Use of the bis(fluorosulfonyl)imide (FSI^-) anion has been shown to mitigate this issue [8, 141]. This is attributed to the ability of the FSI^- anion, especially when paired with the PYR_{13}^+ cation, to form a protective, lithium-ion conducting SEI layer that avoids solvent molecules and stops the cations from penetrating the graphene lattice [8]. Addition of organic additives known to form stable SEI layers, such as vinylene carbonate (VC) and lithium bis(oxalato) borate (LiBOB), to the RTIL based electrolyte has also proven effective [203, 127].

As previously mentioned, the PYR_{13} cation aids in the formation of a stable SEI layer on a graphite anode. $PYR_{13}FSI$ also interacts relatively favorably with positive electrode materials, namely those with a layered structure. It has been shown that between a range of FSI^- based RTILs, $PYR_{13}FSI$ shows the lowest reactivity and best stability towards $LiCoO_2$, making it a good candidate for use in conjunction with layered cathode materials [222]. Furthermore, PYR_{13}^+ is smaller in size than other imidazolium cations suitable for use in battery electrolytes, and this leads to lower viscosity and higher conductivities.

Another component of the electrolyte, the lithium salt required for conduction of lithium ions through the membrane, must be addressed. $LiPF_6$ is conventionally utilized as the salt in organic electrolytes; however, $LiPF_6$ shows low solubility in RTILs. $LiPF_6$ also decomposes to form parasitic HF acid during battery charging and at high temperatures, which can attack electrode
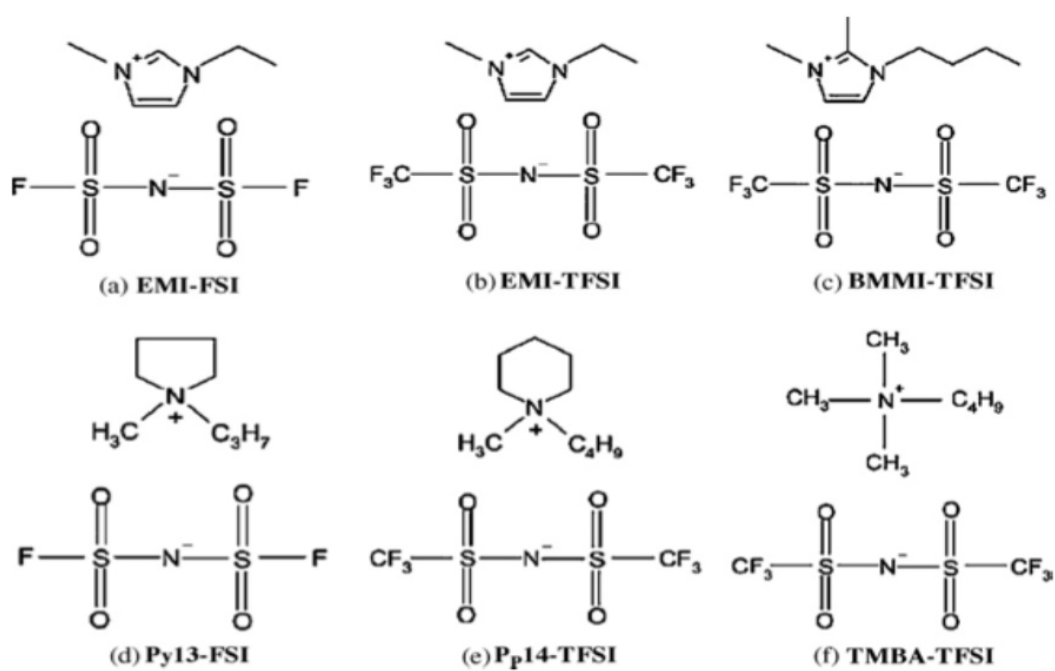
Figure 3.3: Most common cation-anion RTIL pairs used in electrochemical applications [76].

surfaces and lead to transition metal migration and leaching. LiTFSI and LiFSI are commonly used as lithium salts in RTIL solutions for battery electrolytes. FSI^- based RTILs have a slightly lower electrochemical stability window than the TFSI analogues [8], and they are more costly to produce. However, early trials of carbonaceous anode materials with imidazolium $TFSI^-$ ionic liquids show rapid loss of performance [87], and improved performance has been found when replacing $TFSI^-$ with FSI^- [8, 77]. Given the FSI^- anion's higher conductivity and compatibility with electrode materials, it is often utilized as the negative ion in lithium salts for RTIL electrolytes.

A number of companies are working to lower the cost and increase the performance of RTIL materials. For example, Boulder Ionics Corporation has developed a dependable, high-throughput synthesis method capable of producing a number RTILs. The development of ionic liquids for lithium-ion battery electrolyte membranes is a relatively new field. Much work remains to be done in order to enable RTILs as commercially attractive alternatives to organic electrolytes. The potential to completely eliminate flammability, arguably the most important concern holding back commercialization of lithium-ion battery technology in the large-scale energy storage market, represents a paradigm shift for the battery industry. However, if using non-flammable electrolyte is coupled with poor performance, RTILs will have a severely limited role. It is critical to develop RTIL electrolytes capable of performing just as well as their organic counterparts.

The research presented herein explores the utilization of today's best performing RTIL electrolytes in Li-ion batteries containing up-and-coming electrode materials. By replacing the conventional carbonate electrolyte with new sets of solvents and salts, new electrolyte-electrode chemical phenomena are induced which can lead to the increased performance of highly attractive electrodes. Chapters 4-6 will discuss tackling the major compatibility issues between RTIL materials and the passive components of Li-ion batteries (those not involved in the electrodes' faradaic redox chemistry), while Chapter 7-9 will discuss exciting opportunities to exploit these novel chemical interactions in enabling highly energy dense electrodes.

<div align="center">

Chapter 4

**Corrosion of Stainless Steel Battery Components by Bis(fluorosulfonyl)imide
Based Ionic Liquid Electrolytes**

</div>

<div align="center">

Summary

</div>

During our first trial experiments attempting to utilize RTILs in Li-ion cells with high voltage
cathode materials, we came across a number of issues. While the anodic behavior of aluminum
foil current collectors in imide-based room temperature ionic liquids (RTILs) is relatively well
understood, interactions between such RTILs and other passive battery components have been
largely disregarded. This study presents the solvent and potential dependent oxidation of SS316
coin-cell components in the N-methyl-N-propyl-pyrrolidinium bis(fluorosulfonyl)imide (PYR$_{13}$FSI)
RTIL. While this phenomenon prohibits high-voltage cycling of Li(Ni$_{1/3}$Mn$_{1/3}$Co$_{1/3}$)O$_2$ cathodes
in SS316 coin-type cells, Al-clad cell components or alternative cell configurations can be utilized
to avoid SS316 oxidation-induced cell failure.

4.1   Introduction

Room temperature ionic liquid (RTIL) based electrolyte solutions represent an attractive al-
ternative to conventional carbonate electrolytes for lithium-ion batteries (LIBs) due to their poten-
tial to mitigate safety concerns related to the volatility and flammability of commercialized organic
electrolytes. Much work has been dedicated to developing RTIL electrolytes that are compatible
with commercially attractive electrode materials and capable of high electrochemical performance
[127, 158]. Due to constraints associated with solution viscosity, which dictates ionic conductivity

in RTILs via the Walden Rule, and compatibility with low voltage negative electrode materials such as graphite, the most widely studied RTILs are those which contain pyrrolidinium cations and sulfonyl imide anions, namely bis(trifluoromethanesulfonyl)imide (TFSI) and bis(fluorosulfonyl)imide (FSI) [39]. In addition to understanding the electrochemical performance and interactions between RTIL-based electrolytes and electrode materials, it is imperative to develop an understanding of the compatibility of RTILs with a battery's structural components.

Unfortunately, the sulfonyl imide anion has been found to induce severe corrosion of the aluminum current collector used on the positive electrode of LIBs. This oxidation process is dependent on solvent content and electrolyte composition and has been documented in electrochemical cells containing the TFSI anion [112, 153, 117, 111] and the FSI anion [39, 56]. The oxidative dissolution of aluminum occurs through a mechanism initiated by sulfonyl imide anion attack of the native oxide layer on the surface of the aluminum current collector (Al_2O_3) at high potentials (greater than 4.2 V vs. Li/Li^+). The ions subsequently form Al-imide complexes, e.g. $Al(TFSI)_3$, which are solvated by the electrolyte solution, thereby leaving large pits in the aluminum sheet and introducing metal ions into the electrolyte [39, 117, 111]. While this mechanism is well understood, the possibility of an interaction between the RTIL and other battery components has largely been disregarded.

In this study, we demonstrate the voltage and solvent dependent oxidation of Grade 316 stainless steel (SS316) in electrochemical cells containing the N-methyl-N-propyl-pyrrolidinium bis(fluorosulfonyl)imide ($PYR_{13}FSI$) RTIL with $1.2M$ dissolved LiFSI salt. While steel corrosion and electropolishing by RTILs are not new phenomena [10, 213, 1, 2], this is, to our knowledge, the first study describing RTIL-induced steel oxidation in LIBs. SS316 coin-type cells are commonly used to test electrode and electrolyte materials for LIBs, thus it is essential to generate an awareness of the interactions between RTIL electrolytes and SS316 during electrochemical cycling. As a counter measure to eliminate such interactions, alternative testing apparatus such as Al-clad cathode casings can be utilized.

4.2   Discussion of SS Corrosion in High Voltage Conditions

Stainless steel casing oxidation was originally observed during a set of experiments designed to investigate the solvent dependent aluminum corrosion in $PYR_{13}FSI$ + LiFSI based electrolytes. High-grade aluminum foil discs were loaded into SS316 2032 coin-type cells with mixtures of $PYR_{13}FSI$ + $1.2M$ LiFSI and various volumetric amounts of organic solvent as electrolyte solutions. Figure 4.1 presents initial CV cycles and chronoamperometric data for all corrosion cells tested in this study. The solvent dependent oxidative current densities exhibited in aluminum corrosion cells increased with higher volumes of organic content in accordance with data from previous studies [112, 153, 117, 111]. However, the current densities observed in CV and extended charging at both 4.2 V vs. Li/Li$^+$ and 4.6 V vs. Li/Li$^+$ were higher than expected, with initial CV scans showing irreversible oxidative current densities approaching 1.5 mA cm^{-2} and current densities of approximately 1 mA cm^{-2} observed during chronoamperometry in cells containing 50% vol. organic solvent. Corrosion cells containing pure RTIL electrolyte showed irreversible oxidative current densities approaching 500 μA cm^{-2} during the initial CV scan and current densities of about 250 μA cm^{-2} during chronoamperometry. A study by Cho et al. demonstrates that pure FSI-based RTILs show initial scan current density amplitudes of 50 μA cm^{-2} during CV between 3.0 - 5.5 V vs. Li/Li$^+$ [39]. Because of the $PYR_{13}FSI$ RTIL's large electrochemical stability window (7.31 V), current densities were not attributed to electrolyte decomposition.

CV and chronoamperometry were performed on corrosion cells containing SS316 foil working electrodes in order to investigate the possible oxidation of the stainless steel cell components (Figure 1c,d). CV results were similar to those obtained during the same tests using pure aluminum foil working electrodes, while the oxidative currents observed during extended charging at both 4.2 V vs. Li/Li$^+$ and 4.6 V vs. Li/Li$^+$ were about twice as high as those in the aluminum corrosion cell experiments. Chronoamperometry of SS316 foil in the FSI-based electrolyte containing 50% vol. organic solvent showed an oxidative current density that continually increased over 12 hrs during exposure to 4.6 V vs. Li/Li$^+$. The data obtained from corrosion cells made in SS316 coin-type cells
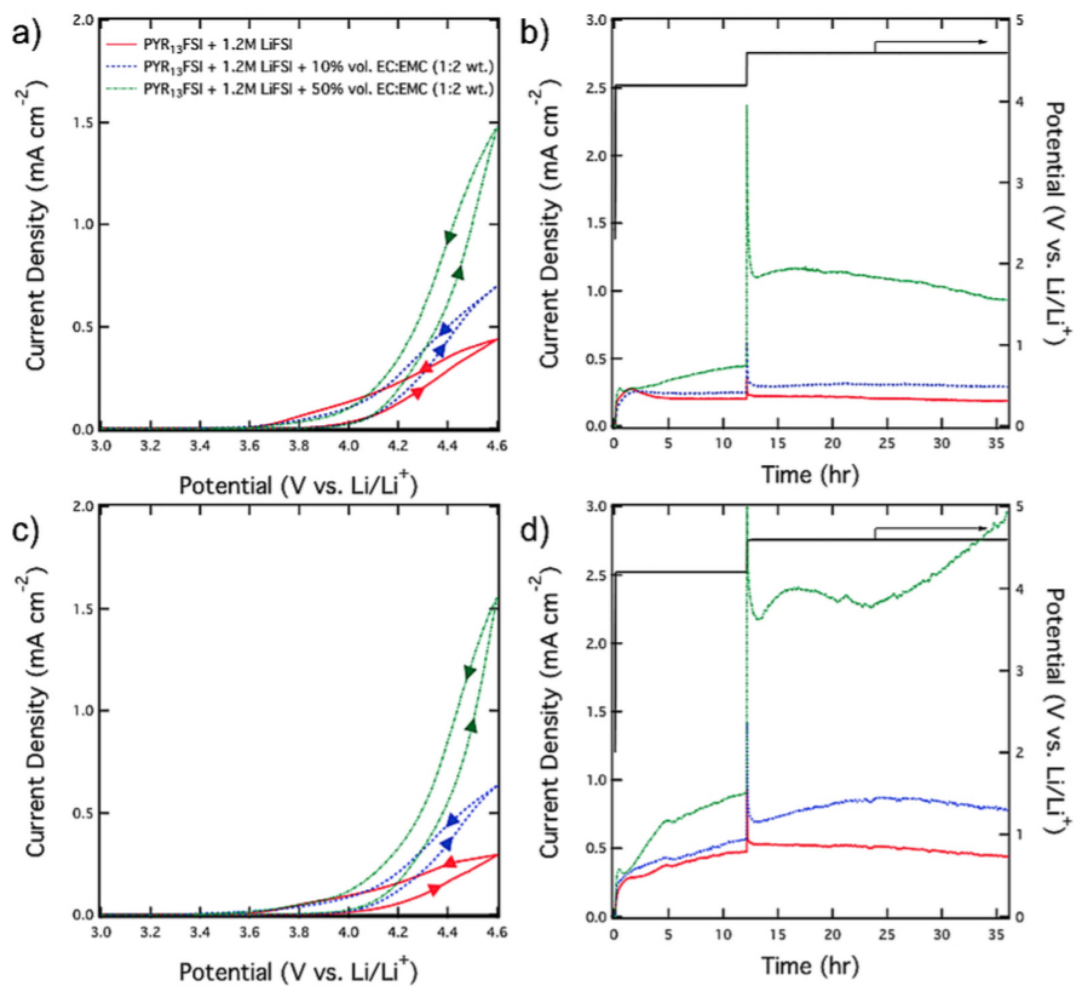
Figure 4.1: Cyclic voltammograms and chronoamperograms of pure aluminum foil (a, b) and SS316 foil (c, d) in SS316 2032 coin-type cells containing $PYR_{13}FSI + 1.2M$ LiFSI and various volumetric amounts of organic co-solvent.

show obvious contrast to data obtained under the same experimental conditions in Al-clad 2032 casings with pure aluminum foil working electrodes [56]. This result leads us to believe that the oxidative current densities observed in the aluminum corrosion cell experiments were significantly influenced by a parasitic interaction between the RTIL and SS316.

LVSEM imaging of SS316 working electrodes was performed subsequent to the chronoamperometry experiments to analyze morphological effects associated with the observed oxidative currents. High-resolution SEM micrographs, provided in Figure 4.2, reveal pitting corrosion on each sample, with the size and density of the pits increasing with organic co-solvent content in the corrosion cells. The corrosion cell with 50% vol. organic solvent shows a network of pits covering the entire surface of the SS316 foil.

The stainless steel corrosion phenomenon was substantiated by attempts to cycle L333 half-cells in SS316 2032 coin-type cells containing pure $PYR_{13}FSI$ + $1.2M$ LiFSI electrolyte. The $Li(Ni_{1/3}Mn_{1/3}Co_{1/3})O_2$ electrochemical cycling voltage profile is shown in Figure 4.3. During initial galvanostatic charge at a current density of 50 μA cm^{-2}, corresponding to a rate of C/10, cells were unable to charge to the target voltage of 4.2 V vs. Li/Li^+. The potential peaked at about 4.05 V vs. Li/Li^+, which corresponds to the onset of SS316 oxidation observed during CV. The cell potential remained below 4.05 V vs. Li/Li^+, suggesting that the 50 μA cm^{-2} current density was drawn from the oxidation of species present in the SS316 cell casing and possibly the aluminum current collector rather than delithiation of the $Li(Ni_{1/3}Mn_{1/3}Co_{1/3})O_2$ electrode.

IR spectroscopy was performed on the FSI-based electrolyte before and after extended charging of an SS316 sample in a cell containing $PYR_{13}FSI$ + $1.2M$ LiFSI solution, and results are presented in Figure 3b. The IR spectra reveal that the corrosion process does not affect the bonding chemistry of the $PYR_{13}FSI$ RTIL. While an -OH stretch at about 3500 cm^{-1} and a -C=O stretch at about 1600 cm^{-1} are attributed to moisture and CO_2 impurities introduced by the flow IR system in the post-corrosion sample, respectively, the electrolyte's IR fingerprint (500-1500 cm^{-1}) remains unchanged, suggesting that the RTIL maintains the same chemical structure and bonding environment while solvating cations pulled from the stainless steel.
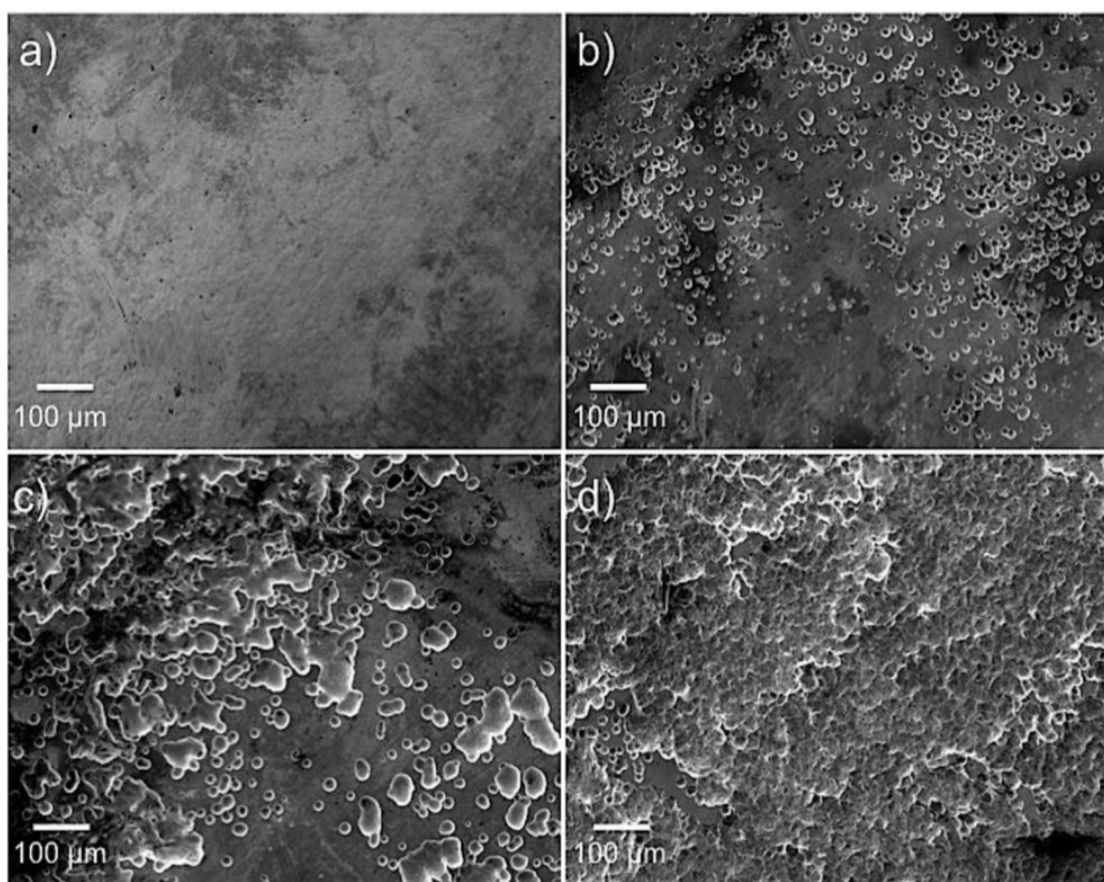
Figure 4.2: SEM micrographs of pristine SS316 foil (a) and SS316 foil after extended charging at 4.6 V vs. Li/Li$^+$ in PYR$_{13}$FSI + 1.2M LiFSI solutions containing 0% vol. organic solvent (b), 10% organic solvent (c), and 50% organic solvent (d).
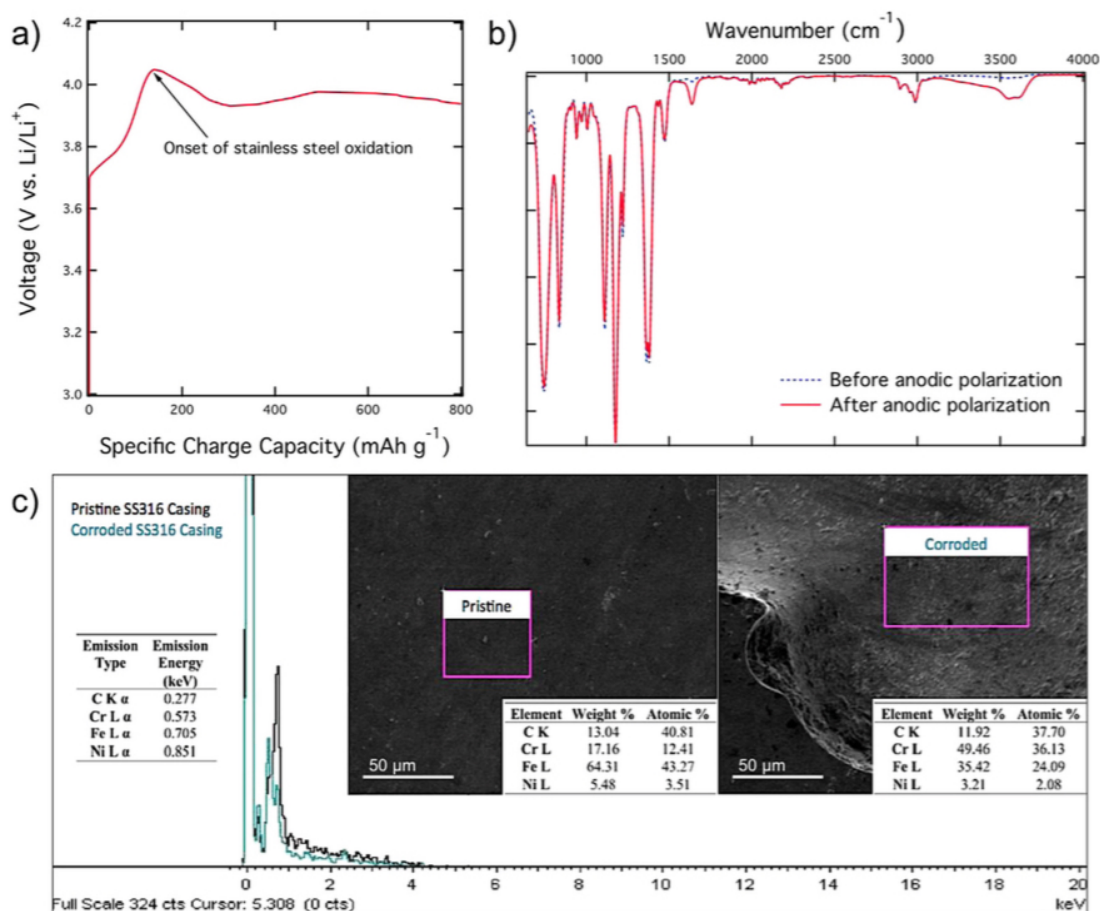
Figure 4.3: First charge voltage profile of a $Li(Ni_{1/3}Mn_{1/3}Co_{1/3})O_2$ half-cell in $PYR_{13}FSI + 1.2M$ LiFSI electrolyte in a SS316 2032 coin-type cell (a), IR spectra of the $PYR_{13}FSI + 1.2M$ LiFSI solution before and after extended charging at 4.6 V vs. Li/Li$^+$ (b), and EDX spectra of the surfaces of pristine SS316 and a pit formed by exposure of SS316 to extended charging at 4.6 V vs. Li/Li$^+$ in $PYR_{13}FSI + 1.2M$ LiFSI solution, including compositional analysis of both samples (c).

Using EDX analysis, the elemental composition of the SS316 surface was observed before oxidation and compared to the surface composition of a pit formed during extended charging in $PYR_{13}FSI$ + $1.2M$ LiFSI solution. Figure 3c provides EDX analysis of pristine and corroded SS316. The corroded sample shows significantly lower iron and nickel content, suggesting the selective oxidation and solvation of iron and nickel by the RTIL electrolyte during exposure to high potentials.

4.3   Mitigating SS Corrosion and Conclusions

The combination of CV, chronoamperometry, SEM, IR, and EDX data leads us to believe that the solvent and potential dependent corrosion of SS316 in electrochemical cells containing $PYR_{13}FSI$ + $1.2M$ LiFSI occurs by a mechanism similar to the aluminum oxidative dissolution previously observed in RTIL electrolytes [39, 117, 111, 56]. It is suggested that oxidized ions in the SS316 casing are solvated by the electrolyte solution, leaving pits in the metal surface and limiting battery performance. While SS316 corrosion prohibits electrochemical cycling under high voltage conditions, steel corrosion can be avoided by utilizing aluminum-clad cell components. $Li(Ni_{1/3}Mn_{1/3}Co_{1/3})O_2$ half-cells containing the $PYR_{13}FSI$ + $1.2M$ LiFSI electrolyte are capable of extended cycling between 3.0 - 4.2 V vs. Li/Li^+ in Al-clad 2032 coin-type cells [56]. It is imperative that future study of RTILs for application in lithium-ion batteries considers the stainless steel oxidation phenomenon.

This work demonstrates the voltage and solvent dependent oxidation of SS316 coin-cell components during electrochemical cycling of high-voltage electrode materials in $PYR_{13}FSI$ + $1.2M$ LiFSI electrolytes. SS316 oxidation likely occurs via a mechanism similar to the well-documented aluminum oxidative dissolution previously described in imide-based RTILs. While steel corrosion causes cell failure, the effect can be avoided by removing SS316 components from the cell by using materials such Al-clad cathode cups.

Chapter 5

Effect of Organic Solvent Addition to PYR$_{13}$FSI + LiFSI Electrolytes on Aluminum Oxidation and Rate Performance of Li(Ni$_{1/3}$Mn$_{1/3}$Co$_{1/3}$)O$_2$ Cathodes

Summary

Corrosion of the positive electrode's aluminum current collector in Li-ion cells at high voltages is regarded as one of the most serious problems facing the commercialization of RTIL electrolytes for electrochemical applications. The superior suppression of aluminum current collector oxidation by a 1.2M LiFSI in PYR$_{13}$FSI ionic liquid electrolyte is demonstrated. Addition of EC:EMC (1:2 wt.) is shown to significantly increase the severity of parasitic aluminum oxidation. Despite leading to increased aluminum oxidation at high voltages (greater than 4.2 V vs. Li/Li$^+$), adding organic solvent to PYR$_{13}$FSI based ionic liquids greatly enhances important electrochemical properties. The ionic conductivity and lithium ion transference number of the PYR$_{13}$FSI + 1.2M LiFSI electrolyte increase with increasing volumetric content of organic co-solvent (EC:EMC), resulting in significant improvements to high rate performance. The electrochemical benefits of organic co-solvent addition and the compatibility of the PYR$_{13}$FSI + 1.2M LiFSI electrolyte with Li(Ni$_{1/3}$Mn$_{1/3}$Co$_{1/3}$)O$_2$ demonstrated in this study substantiate the need to develop strategies to suppress aluminum oxidation during high voltage cycling of lithium-ion batteries in ionic liquid electrolytes.

5.1   Introduction

While lithium-ion batteries (LIBs) offer a potentially game-changing energy storage technology, safety concerns have hindered their widespread penetration into the electric vehicle market

and have discouraged their consideration in grid level applications. Many of these safety concerns stem from the utilization of volatile organic electrolytes. Currently commercialized LIB technology is based on electrolytes comprised of mixtures of organic carbonate solvents containing lithium hexafluorophosphate ($LiPF_6$) as a salt. These electrolytes are preferred due to their high ionic conductivities and compatibility with commercialized electrode materials, but their flammability and high volatility must be addressed [167, 231].

In order to mitigate electrolyte related safety risks without realizing a loss in performance, a new class of non-aqueous electrolyte should be developed. Due to their non-flammability, negligible vapor pressures, thermal stabilities, high voltage stability windows, and sufficient ionic conductivities, room temperature ionic liquids (RTILs or ILs) represent promising options as additives or drop-in replacements for organic electrolytes in LIBs [15, 152, 186, 63, 11, 187]. Extensive efforts are being made to develop high performance RTIL based electrolytes that are compatible with state of the art electrode materials [80, 128, 176, 182, 72, 86, 181, 148, 53, 188, 44], with a number of studies demonstrating the favorable electrochemical properties of pyrrolidinium-based ionic liquids [141, 156] and ionic liquids containing the bis(trifluoromethanesylfonyl)imide ($TFSI^-$) [8, 117, 61, 94, 116] or bis(fluorosulfonyl)imide (FSI^-) anion [187, 80, 128, 141, 8, 77, 202, 22, 238, 115, 24, 222, 164, 3]. Recent research has shown that pyrrolidinium and imidazolium FSI-based ionic liquids have higher conductivities compared to their corresponding TFSI-based analogs due to lower solution viscosities [80, 148, 22, 248] as well as adequate compatibility with electrode materials such as graphite, $LiCoO_2$, and $Li(Ni_{1/3}Mn_{1/3}Co_{1/3})O_2$ [80, 176]. Despite these efforts to develop high performance electrolytes based on the FSI chemistry, improvements in ionic conductivity must be made in order to compete with commercialized organic electrolytes.

Various strategies can be employed to enhance the electrochemical performance of IL based electrolytes. By lowering the viscosity of ionic liquids using organic solvents, significant increases in ionic conductivity and lithium ion mobility can be achieved [152, 76, 119, 72]. Addition of an organic solvent has also been shown to improve solid-electrolyte interphase (SEI) formation and stability on low voltage anode materials such as lithium metal or graphite [164, 87, 86, 183, 7,

37, 140]. Unfortunately, the addition of organic solvent to certain FSI and TFSI based ILs leads to a severe parasitic side reaction involving oxidation of the aluminum metal conventionally used as a current collector substrate on the cathode of LIBs [117, 39, 72]. While work has been done to characterize the solvent dependent oxidative dissolution mechanism for aluminum corrosion in TFSI-based electrolytes, relatively little work has been done to characterize similar effects in FSI-based electrolytes and the influence of such electrolyte solutions on electrochemical cycling performance.

This study examines the electrochemical properties of $PYR_{13}FSI$ ILs, developing a deeper understanding of the effect of increasing co-solvent content in $PYR_{13}FSI$-based electrolytes on aluminum oxidation behavior. Most notably, this research substantiates the electrochemical benefits of adding organic solvents to ILs by demonstrating increased ionic conductivities, increased Li^+ transference numbers, and the improved high rate performance of $Li(Ni_{1/3}Mn_{1/3}Co_{1/3})O_2$ in mixtures of $PYR_{13}FSI$ and carbonate solvent. Chronoamperometry, cyclic voltammetry (CV), and scanning electron microscopy (SEM) were used to identify parasitic aluminum corrosion via the oxidative dissolution mechanism, and potentio-galvanostatic cycling was utilized to characterize the effect of aluminum oxidative dissolution on battery cycling and rate performance of $Li(Ni_{1/3}Mn_{1/3}Co_{1/3})O_2$ half-cells with $PYR_{13}FSI + 1.2M$ LiFSI based electrolytes.

5.2   Oxidation Behavior of the Aluminum Current Collector

Preliminarily, an experimental matrix was designed to systematically characterize the compatibility of $PYR_{13}FSI + 1.2M$ LiFSI electrolytes with the aluminum current collector substrate during cycling of high voltage cathode materials. These results were compared with a similar study of $1.2M$ LiTFSI in $PYR_{13}FSI$ in order to gain further insight into the electrochemical performance of $PYR_{13}FSI$ when coupled with different lithium salts. Previous work suggests that electrolyte solutions comprised of LiFSI salt in organic solvent are capable of suppressing aluminum oxidation more effectively than combinations of the same solvent with LiTFSI salt [80]. Our results prove that the same is true in $PYR_{13}FSI$-based electrolytes.

Inspection of the initial CV cycle of corrosion cells containing $TFSI^-$ based salt reveal irreversible anodic currents indicative of aluminum oxidation on the surface of the metal. This effect increases in magnitude with the addition of organic solvent. Figure 5.1 presents initial CV cycles and chronoamperometric data for electrolytes containing $TFSI^-$. The most severe oxidative behavior occurs in the solution containing 50% vol. organic solvent (Figure 1a), with the initial CV shape representing that of typical aluminum corrosion CV curves [71, 30]. Chronoamperometric data supports this finding. During prolonged charging at 4.6 V vs. Li/Li^+, oxidative current densities exceeded 70 μA cm^{-2} in the solution containing 50% vol. organic solvent and remained under 5 μA cm^{-2} and 2 μA cm^{-2} in corrosion cells containing 10% vol. organic solvent and pure IL, respectively (Figure 1b). As currents are observed to increase during chronoamperometry of cells containing organic solvent, it is determined that $TFSI^-$ is unable to successfully passivate the aluminum current collector surface. The solvent dependent current amplitudes shown in CV and chronoamperometry are in agreement with a previous study conducted by Ref. [117] on $PYR_{14}TFSI$-solution induced aluminum corrosion, but the significantly lower current amplitudes found in our work lead us to believe that the FSI anion in the ionic liquid is itself capable of suppressing aluminum oxidation to some degree.

Inspection of the initial CV cycle of aluminum foil discs in $PYR_{13}FSI$ + $1.2M$ LiFSI solutions reveal much lower irreversible oxidative current densities than those seen with $PYR_{13}FSI$ + $1.2M$ LiTFSI solutions. Figure 5.2 presents initial CV cycles and chronoamperometric data for electrolytes containing FSI^-. Oxidative current densities observed during CV of corrosion cells with FSI-based ILs are also dependent on volumetric content of organic solvent, reaching 1.44 μA cm^{-2} in solutions containing 50% vol. organic solvent (Figure 2a). Chronoamperograms of aluminum corrosion cells in the same solutions reveal significant aluminum oxidation only in cells containing organic solvent (Figure 2b). During a 24 h constant voltage period at 4.6 V vs. Li/Li^+, oxidative currents reach about 8 μA cm^{-2} in cells containing 50% vol. organic solvent and remain below 4 μA cm^{-2} and 1 μA cm^{-2} for cells containing 10% vol. organic solvent and pure IL, respectively. As the oxidative current densities for cells containing pure ionic liquid and 10% vol. organic solvent
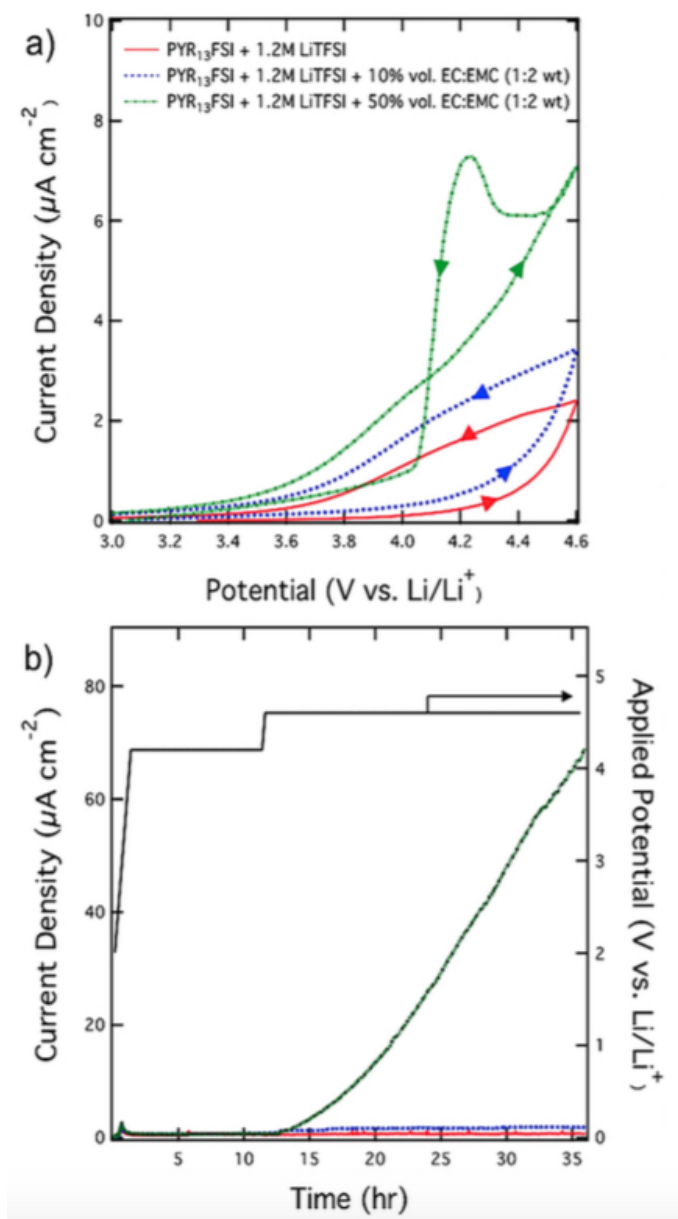
Figure 5.1: Cyclic voltammograms (a) showing the first voltage scans and chronoamperograms (b) of aluminum corrosion cells with electrolyte solutions comprised of mixtures of $PYR_{13}FSI + 1.2M$ LiTFSI and various volumetric amounts of EC:EMC (1:2 wt.).

do not continually increase over prolonged charging, it is determined that the FSI^- anion is able to passivate the aluminum surface to a higher degree than $TFSI^-$. This demonstrates that the LiFSI salt is strongly favored for protection against aluminum oxidation in $PYR_{13}FSI$ based electrolytes.

High-resolution SEM micrographs provided in Figure 5.3 show that the oxidative current densities observed in CV and chronoamperometry resulted in significant changes to the Al foil's surface morphology. Figure 3a-c indicates visible corrosion by solutions containing LiTFSI salt, with surface corrosion becoming most severe in the solution containing 50% vol. organic solvent. Large pits were formed on the Al sample charged in the solution containing 50% vol. organic solvent, with pit diameters approaching 300 μm. Non-uniform coloring in the SEM images is also indicative of corrosion, as gradients in shading represent changes in the sample's surface roughness. The Al samples charged in pure RTIL solution and solution containing 10% vol. organic solvent show non-uniform coloring, with the sample charged in solution containing 10% vol. organic solvent showing severe shading gradients indicative of the formation of surface pits. The SEM micrographs corroborate the CV and chronoamperometry results, showing more severe corrosion in cells containing LiTFSI salt.

While the observed aluminum oxidation was less severe in cells containing the LiFSI salt, SEM micrographs provided in Figure 3d-f prove that the oxidative current in $PYR_{13}FSI + 1.2M$ LiFSI solution containing 50% vol. organic solvent was sufficient to form large pits on the surface of the aluminum metal. Pits on this sample were observed with diameters exceeding 150 μm. The Al charged in pure IL shows uniform coloring while the image of the Al charged in a solution of 10% vol. organic solvent shows a non-uniform distribution of regions of lighter or darker coloring. This spotting is most apparent on the Al sample that was charged in a solution of 50% vol. organic solvent, with corrosion sites evolving into surface pitting. The combination of CV, chronoamperometry, and microscopy data suggests that pitting corrosion results from the oxidative dissolution mechanism characterized in $TFSI^-$ based electrolytes [117]. The suggested oxidative dissolution of aluminum occurs through a mechanism initiated by sulfonyl imide anion attack of the native oxide layer on the surface of the aluminum current collector (Al_2O_3) at high potentials (greater than 4.2
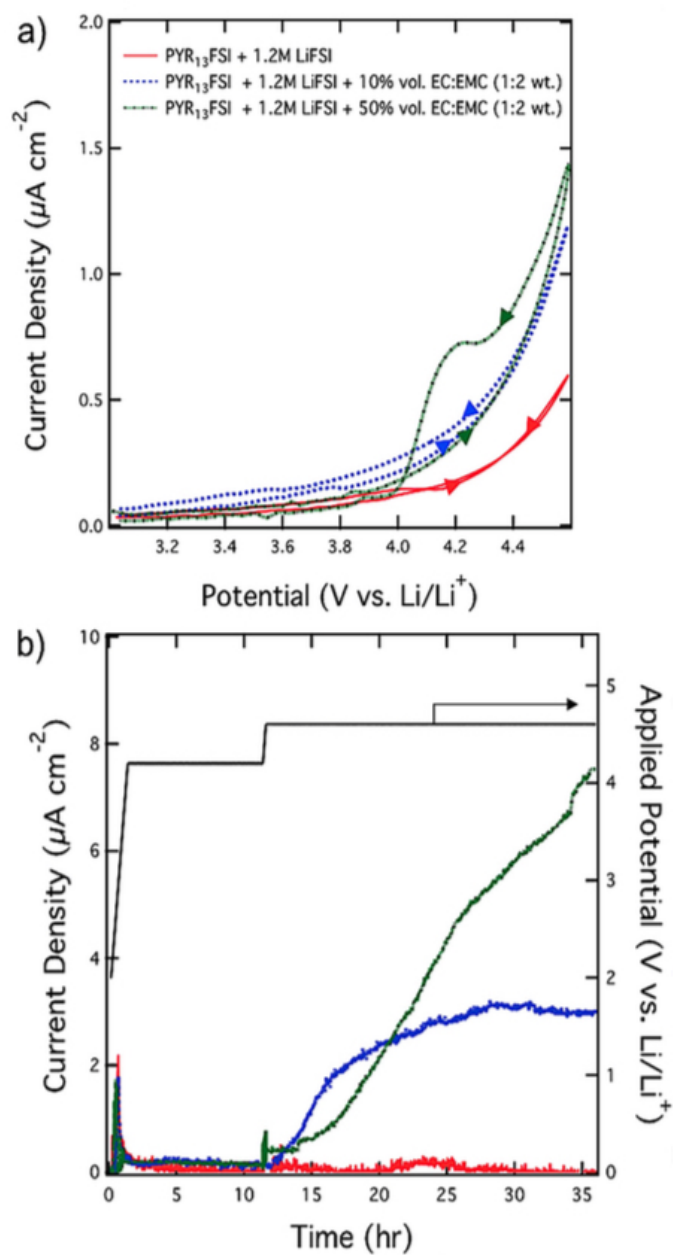
Figure 5.2: Cyclic voltammograms (a) showing the first voltage scans and chronoamperograms (b) of aluminum corrosion cells with electrolyte solutions comprised of mixtures of $PYR_{13}FSI + 1.2M$ LiFSI and various volumetric amounts of EC:EMC (1:2 wt.).
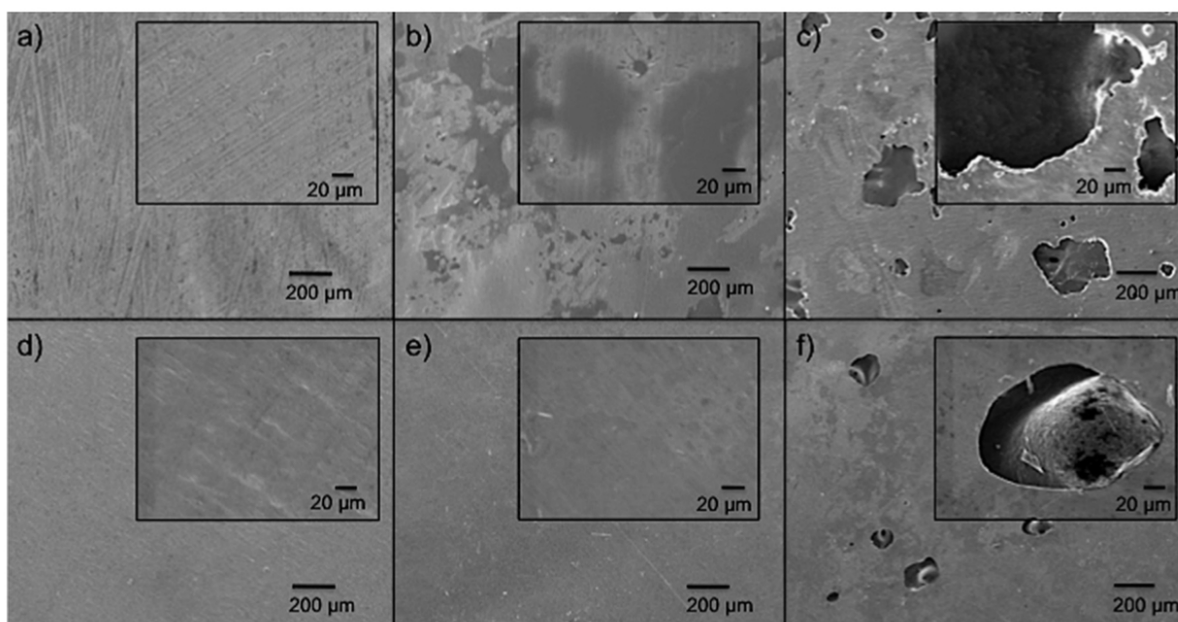
Figure 5.3: SEM micrographs taken subsequent to extended charging of Al corrosion cells at 4.6V vs. Li/Li$^+$ in electrolyte solutions comprised of pure PYR$_{13}$FSI + 1.2M LiTFSI (a), 1.2M LiTFSI in PYR$_{13}$FSI + 10% vol. EC:EMC (b), 1.2M LiTFSI in PYR$_{13}$FSI + 50% vol. EC:EMC (c), pure PYR$_{13}$FSI + 1.2M LiFSI (d), 1.2M LiFSI in PYR$_{13}$FSI + 10% vol. EC:EMC (e), and 1.2M LiFSI in PYR$_{13}$FSI + 50% vol. EC:EMC (f).

V vs. Li/Li$^+$). The ions subsequently form Al-imide complexes, e.g. Al(FSI)$_3$, which are solvated by organic carbonates in the electrolyte solution, thereby leaving large pits in the aluminum sheet and introducing metal ions into the electrolyte. Furthermore, this study shows that PYR$_{13}$FSI + 1.2M LiFSI based electrolytes containing 10% vol. or less of organic solvent suppress aluminum corrosion to a significant degree, especially when exposed to voltages higher than 4.2 V vs. Li/Li$^+$.

5.3   Organic Solvent Addition and Rate Performance of Li(Ni$_{1/3}$Mn$_{1/3}$Co$_{1/3}$)O$_2$

Despite finding significant aluminum corrosion in mixtures of PYR$_{13}$FSI + 1.2M LiFSI and organic solvent, we demonstrate the ability of organic solvent to greatly increase the electrochemical performance of such electrolytes. It is widely accepted that solution viscosity is the most important factor determining an IL's ionic conductivity. Therefore, ILs containing smaller ions, which lead to lower viscosities, are preferred. The relationship between viscosity and conductivity is defined by the Walden Rule, which states that the product of the limiting molar conductivity, A_{mo}, and the solvent's viscosity, η, is constant [185]. ILs have been found to obey this relationship [84, 185], and the addition of organic solvent to ILs is one strategy for lowering solution viscosity [152, 76].

This work supports the claim that adding organic solvent to ILs can increase lithium ion conductivity and mobility by showing that addition of a carbonate-based co-solvent to PYR$_{13}$FSI + 1.2M LiFSI leads to significantly increased ionic conductivities. Ionic conductivities for PYR$_{13}$FSI-based solutions are provided in Table 1. The benefits of organic solvent addition to ILs are substantiated by a rate study of Li(Ni$_{1/3}$Mn$_{1/3}$Co$_{1/3}$)O$_2$ half-cells in mixtures of PYR$_{13}$FSI + 1.2M LiFSI and EC:EMC (1:2 wt.). Rate study results are presented in Figure 5.4. Cells were cycled at rates from C/10 to 8C between 3 - 4.2V vs. Li/Li$^+$. Half-cells containing 50% vol. organic solvent show significantly increased capacities at all rates tested, maintaining specific discharge capacities above 90 mAh g^{-1} at the rate of 8C. This contrasts the rate performance of cells containing pure IL, which show capacities of approximately 56 mAh g^{-1} at the 8C rate.

Furthermore, Li(Ni$_{1/3}$Mn$_{1/3}$Co$_{1/3}$)O$_2$ half-cells show highly stable cycling behavior for at least 25 cycles at the rate of 1C subsequent to the rate test, with cells containing 50% vol. organic solvent
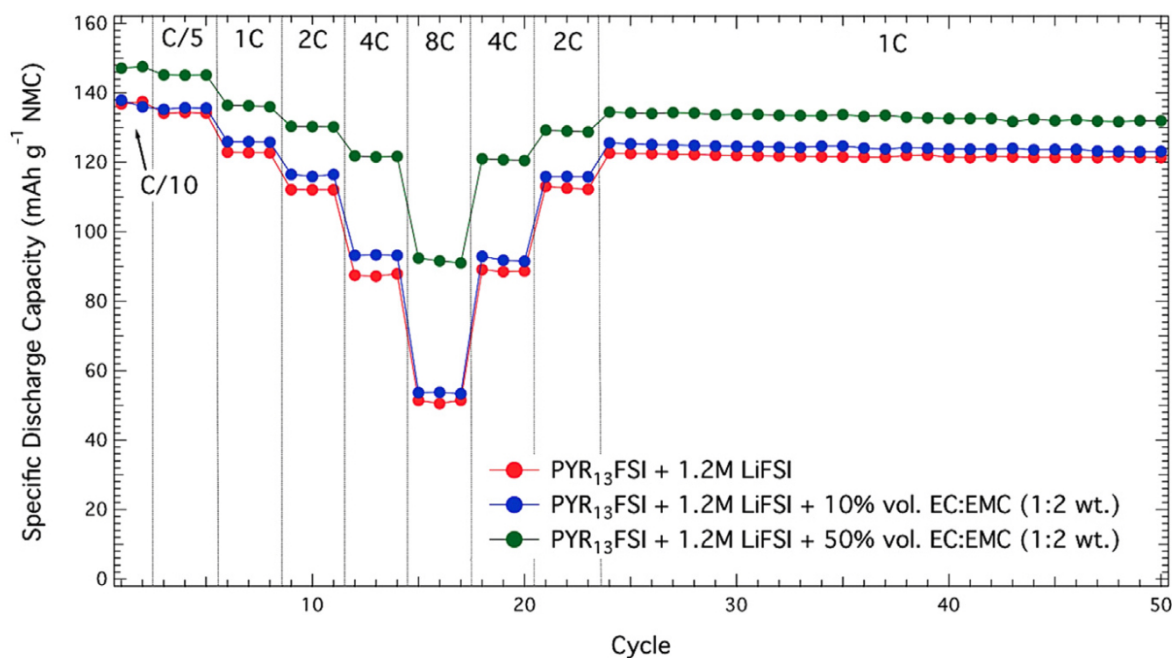
Figure 5.4: Rate study of $Li(Ni_{1/3}Mn_{1/3}Co_{1/3})O_2$ half-cells containing electrolyte solutions comprised of mixtures of $PYR_{13}FSI$ + $1.2M$ LiFSI and various volumetric amounts of EC:EMC (1:2 wt.). Electrochemical cycling was performed at room temperature between 3 - 4.2V vs. Li/Li^+.

and 10% vol. organic solvent maintaining greater than 98% discharge capacity and cells containing pure IL maintaining greater than 99% discharge capacity. Because the specific capacities during rate increase steps (increasing rates in steps from 1C to 8C) are equal to the corresponding specific capacities during decreasing rate steps, it is suggested that the IL based electrolytes do not induce degradation of the $Li(Ni_{1/3}Mn_{1/3}Co_{1/3})O_2$ structure under high current densities.

In order to further investigate the effect of organic solvent addition to ILs on electrochemical performance, lithium ion transference numbers ($t_{+,Li}$) were determined for each solution utilized in the rate study. $t_{+,Li}$, which is defined as the fraction of the total current passed through the cell by Li^+ ions, has implications for rate performance and cycling stability [236]. While *ionic conductivity* describes the electrolyte solution's contribution to ohmic overpotential losses during electrochemical cycling, $t_{+,Li}$ describes contributions to concentration overpotential losses. It follows that a low $t_{+,Li}$ limits power output and leads to poor performance at high rates, whereas a high $t_{+,Li}$ reduces the effects of concentration polarization while allowing for high power output.

$t_{+,Li}$ was determined through the PP method developed by Bruce and Vincent et al., in which the cation transference number is determined by dividing the steady-state cationic current by the initial current passing through the cell just after applying a small polarizing voltage [30, 29]. For small polarizations, $t_{+,Li}$ is found using equation 5.1, where I_{ss} is the steady-state current, I_O the initial current, ΔV the applied potential (10 mV), and R_{ss} and R_O the electrode-electrolyte interfacial resistances after and before polarization, respectively [249].

$$t_{+,Li} = \frac{I_{ss}(\Delta V - I_0 R_0)}{I_0(\Delta V - I_{ss}R_{ss})}, \tag{5.1}$$

In order to ensure accuracy of our experiments, the PP method was verified using $1.5 M$ $LiPF_6$ propylene carbonate (PC) solution and the results were found to agree with literature values [69]. The PP method data for the pure ionic liquid sample is shown in Figure 5.5 and is representative of PP method data for all samples. $t_{+,Li}$ values for the $PYR_{13}FSI$-based solutions are provided in Figure 5.6. The $t_{+,Li}$ value determined for the pure IL electrolyte was 0.14769 +/− 0.0328, which

correlates with literature $t_{+,Li}$ values for $PYR_{13}FSI$ based electrolytes [236]. It was found that $t_{+,Li}$ of $PYR_{13}FSI + 1.2M$ LiFSI electrolytes increases significantly with the addition of organic solvent. As organic solvent is added to the IL solutions, the relative concentrations of PYR_{13}^+ and FSI^- decrease while Li^+ concentration remains fixed at $1.2M$. It is suggested that the effects of two-cation competition decrease as the relative concentration of PYR_{13}^+ decreases, allowing Li^+ to carry a larger portion of faradic current during cycling. Consequently, it is expected that the concentration gradients which develop during charge and discharge of electrochemical cells containing $1.2M$ LiFSI in $PYR_{13}FSI + 50\%$ vol. EC:EMC are significantly less severe than those which develop in the pure IL electrolyte. The higher values of $t_{+,Li}$ in IL based electrolytes containing organic solvent contribute to their higher rate performance in our $Li(Ni_{1/3}Mn_{1/3}Co_{1/3})O_2$ half-cells. In addition to providing high-rate cycling stability, the significantly higher $t_{+,Li}$ value for the $PYR_{13}FSI$ electrolyte containing 50% vol. organic solvent allows for remarkably less overpotential loss during charge-discharge cycling. Overpotential effects are illustrated by comparing cycling voltage profiles provided in Figure 5.7. This phenomenon is particularly evident as the rates are increased, demonstrating the value of high $t_{+,Li}$ and its relationship to electrochemical cycling behavior.

In order to fully realize the advantages in energy and power density of high-voltage cathode materials such as $Li(Ni_{1/3}Mn_{1/3}Co_{1/3})O_2$, electrochemical cells containing such materials should be cycled to voltages higher than 4.2 V vs. Li/Li^+. Figure 5.8 provides specific discharge capacities for $Li(Ni_{1/3}Mn_{1/3}Co_{1/3})O_2$ half-cells containing each electrolyte solution under high voltage cycling conditions. $Li(Ni_{1/3}Mn_{1/3}Co_{1/3})O_2$ cells show very poor cycling stability when cycled between 3 - 4.5 V vs. Li/Li^+. While half-cells containing pure IL maintain greater than 95% capacity after 20 cycles at a rate of C/10 during cycling between 3 - 4.5 V vs. Li/Li^+, cells containing 10% vol. organic solvent and 50% vol. organic solvent maintain only greater than 85% capacity and greater than 75% capacity, respectively, under the same cycling conditions (Figure 7a). The poor cycling stability is exacerbated at higher rates and is shown to be irreversible, as the capacity lost during high voltage cycling is not recovered when the cycling voltage range is lowered to 3 - 4.2 V vs. Li/Li^+ (Figure 5.88). The poor cycling stability is attributed to the introduction of aluminum
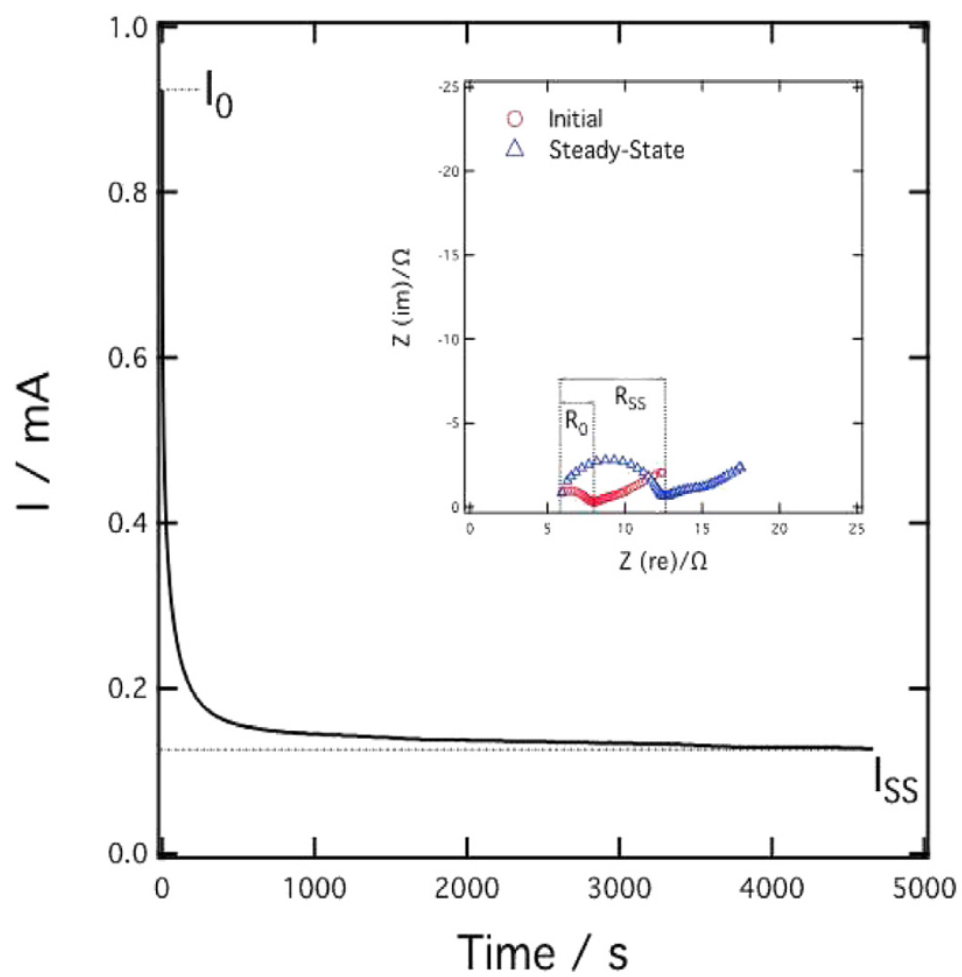
Figure 5.5: PP method data for extraction of $t_{+,Li}$ for PYR$_{13}$FSI + $1.2M$ LiFSI.

Electrolyte Composition	$t_{+, Li}$	σ_{ionic} (mS cm^{-1})
PC (1.5M LiPF$_6$)	0.37125 ± 0.0493	---
PYR$_{13}$FSI (1.2M LiFSI)	0.14769 ± 0.0328	3.9735 ± 0.3413
PYR$_{13}$FSI + 10% vol. EC:EMC (1.2M LiFSI)	0.19785 ± 0.0405	5.0322 ± 0.1501
PYR$_{13}$FSI + 50% vol. EC:EMC (1.2M LiFSI)	0.40968 ± 0.0584	7.8639 ± 1.254

Figure 5.6: Lithium transference numbers and specific ionic conductivities for electrolyte solutions comprised of mixtures of PYR$_{13}$FSI + 1.2M LiFSI and various volumetric amounts of EC:EMC (1:2 wt.). All measurements were conducted at room temperature.
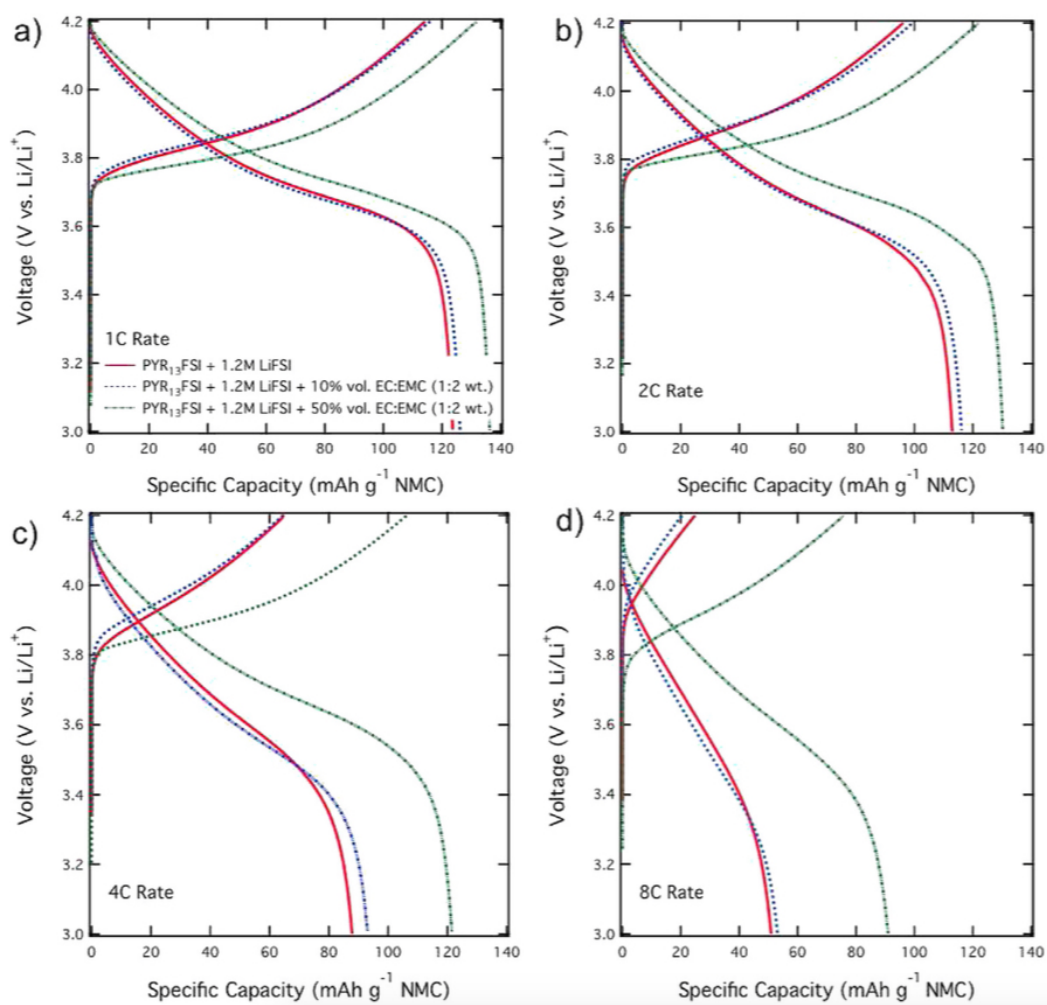
Figure 5.7: Charge-discharge voltage profiles of $Li(Ni_{1/3}Mn_{1/3}Co_{1/3})O_2$ half-cells containing electrolyte solutions comprised of mixtures of $PYR_{13}FSI + 1.2M$ LiFSI and various volumetric amounts of EC:EMC (1:2 wt.) at rates of 1C (a), 2C (b), 4C (c), and 8C (d).

into the electrolyte following the oxidative dissolution process, most likely leading to increased resistance through the bulk of the cell and possibly leading to performance-limiting interactions with the layered cathode material.

5.4   Conclusions Regarding RTIL-induced Al Corrosion

While the addition of organic solvent to $PYR_{13}FSI$ + $1.2M$ LiFSI is shown to lead to a parasitic oxidation reaction with the aluminum current collector conventionally used in lithium-ion batteries, the enhancements in conductivity, lithium transference number, and rate performance are significant. It is therefore of great interest to suppress the aluminum oxidation process in order to enable high performance ionic liquid based electrolytes for application in lithium-ion batteries.

In this study we demonstrated that $PYR_{13}FSI$ + $1.2M$ LiFSI shows higher compatibility with aluminum current collectors than $PYR_{13}FSI$ + $1.2M$ LiTFSI electrolytes. The oxidation of aluminum in such IL solutions increases with addition of organic solvent, and the oxidative dissolution mechanism was characterized in corrosion cells containing LiFSI salt in $PYR_{13}FSI$. Furthermore, we demonstrated that the addition of organic solvent to the $PYR_{13}FSI$ + $1.2M$ LiFSI electrolyte leads to higher ionic conductivities and higher lithium transference numbers, and these enhanced electrochemical properties allow for significantly increased rate performance in $Li(Ni_{1/3}Mn_{1/3}Co_{1/3})O_2$ half-cells when cycled at room temperature between 3 - 4.2V vs. Li/Li^+. The use of organic solvents in combination with ILs was substantiated as a convenient and effective strategy for the realization of high performance, non-flammable electrolyte solutions for lithium-ion batteries.
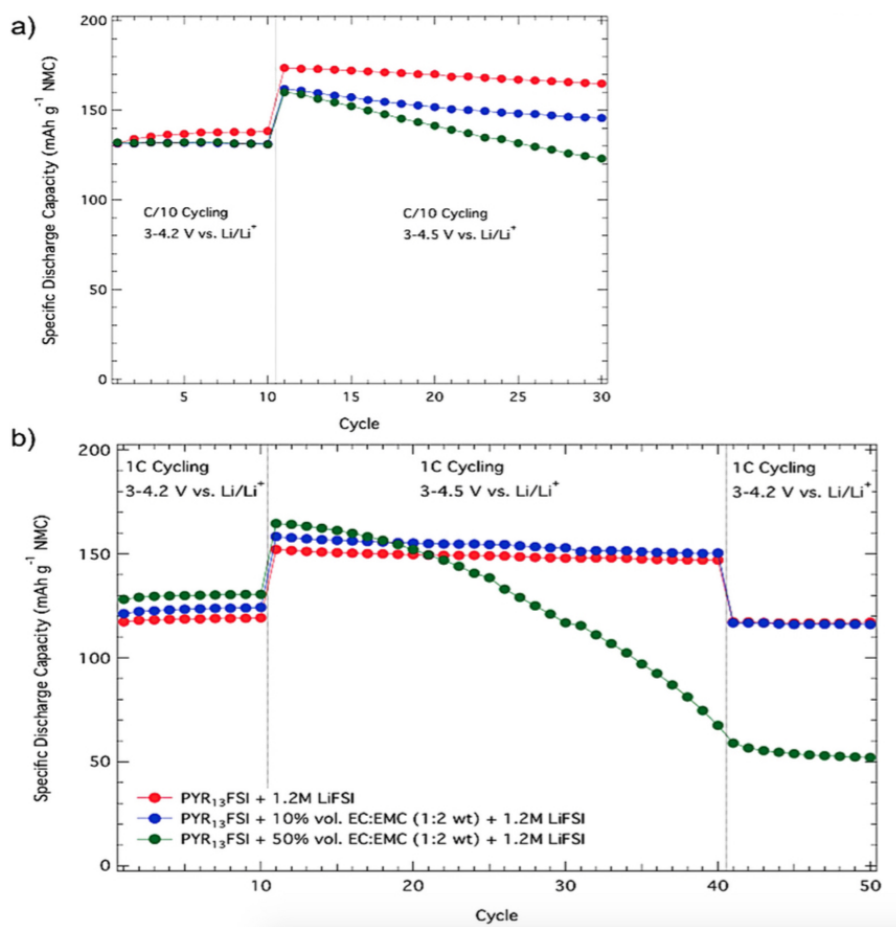
Figure 5.8: High voltage potentio-galvanostatic cycling of $Li(Ni_{1/3}Mn_{1/3}Co_{1/3})O_2$ half-cells containing electrolyte solutions comprised of mixtures of $PYR_{13}FSI + 1.2M$ LiFSI and various volumetric amounts of EC:EMC (1:2 wt.). Charge/discharge rates were held constant at C/10 (a) and 1C (b).

Chapter 6

Electrospun Polyacrylonitrile Microfiber Separators for Ionic Liquid Electrolytes in Li-ion Batteries

Summary

After characterizing and developing a cycling protocol to avoid high-potential aluminum corrosion, we turned to another issue hindering widespread utilization of RTIL electrolytes. Most RTIL research for Li-ion battery applications uses glass fiber separator materials. These materials are not compatible with commercial battery manufacturing processes, and a new separator must be developed if RTILs are to be commercialized for Li-ion technology.

Despite much recent progress in the development of room temperature ionic liquid (RTIL) electrolytes for lithium-ion batteries (LIBs), relatively little work has been done in terms of investigating commercially applicable separator materials capable of accommodating RTILs. In this work, we demonstrate an electrospun polyacrylonitrile (PAN) microfiber separator. The PAN microfiber separators show high degrees of porosity (83%), wettability, and mechanical strength ($\sigma_{UTS} = 16.98$ MPa and $E = 5.95$ MPa). The physical properties of our electrospun separators lead to impressive electrochemical performance, showing an apparent MacMullin number (NM) of less than 5 when combined with the $PYR_{13}FSI$ (1.2M LiFSI) electrolyte. These results are validated by superior rate performance and the exhibition of a high capacity full-cell utilizing a PAN microfiber separator in combination with the $PYR_{13}FSI$ (1.2M LiFSI) RTIL electrolyte. Such work represents significant progress in the advancement of RTIL electrolytes for LIBs, indicating that nonwoven separators are a commercially viable solution to the previous lack of separator materials for RTIL electrolytes.

6.1   Introduction

While commercialized lithium-ion batteries (LIBs) are capable of achieving energy-densities of up to 800 Wh L^{-1} in the 18650-type cell configuration, the advent of electrified transportation and renewable energy technologies demands safer and higher performance energy storage. In the search for the next generation LIB, researchers are developing new materials, modifying existing materials, and investigating unique combinations of materials. One such approach towards a safer, higher energy-density battery involves replacing the conventional carbonate-based electrolyte with a room temperature ionic liquid (RTIL) electrolyte system. RTIL materials have attracted attention in electrochemical applications because of their non-flammability, negligible vapor pressures, high thermal and electrochemical stabilities, and adequate ionic conductivities [15, 186]. Utilizing a RTIL electrolyte induces new surface and reaction chemistries, recently showing success in demonstrating high performance Li-ion cells.

RTIL electrolytes based on the bis(fluorosulfonyl)imide (FSI^-) or bis(trifluoromethanesulfonyl)imide ($TFSI^-$) anion show particularly advantageous properties in Li-ion cells [187, 80, 128, 141, 8]. For example, $TFSI^-$ has been shown to mitigate sulfur dissolution and polysulfide redox shuttle in sulfur-based electrodes [58, 165], FSI^- shows strong compatibility with $Li(Ni_{1/3}Mn_{1/3}Co_{1/3})O_2$ cathodes [57] and graphite anodes [80, 176], and both anions allow good reversibility of the Li metal electrode [164, 89]. While much progress has been made in regards to developing high energy-density electrode-RTIL systems, research has overlooked one major hurdle for the commercialization of RTILs as LIB electrolytes: the separator material. Most reports on RTIL electrolytes for LIBs use thick (ca. 300 μm) glass fiber separators that are too brittle for incorporation in the conventional jelly-roll configuration.

In short, commercial separator materials are incompatible with RTIL electrolytes. Commercially produced batteries utilize thin polyolefin separators, such as Celgard's polypropylene (PP) membranes. Such separators have small pore sizes (less than 1 μm pore diameter); due to their high viscosities, RTIL electrolytes are unable to sufficiently wet these separators. In order to develop an

RTIL electrolyte membrane that is compatible with both commercially attractive electrode materials and the winding processes in the existing LIB manufacturing infrastructure, a new separator material should be developed. One recent study by M. Kirchhofer et al. studied different RTIL electrolytes in combination with various separator materials and their compatibilities with the Li metal electrode [107]. While this study provides insight into alternative separator materials specifically for RTIL electrolytes, a separator must be developed that can accommodate the electrochemistry of RTILs while maintaining adequate mechanical properties for employment in the jelly-roll cell configuration (ie; 18650-type cells).

To this end, we turn to electrospun polyacrylonitrile (PAN) microfiber mats. PAN based separators have been studied as alternatives to conventional microporous polymer materials [242, 13, 42, 41, 233, 175, 32, 45], but all previous work related to PAN nonwoven separators was tailored to the utilization of conventional organic electrolyte. A separator material must be electronically insulating, allow for minimal ionic resistance, possess high mechanical and dimensional stability, have sufficient physical strength to allow for easy handling, possess chemical resistance to degradation by electrolyte impurities, allow for easy wetting by the electrolyte, and be inert against the electrode materials [13]. Based on previous demonstration of nonwoven separators' superior ionic transport properties and the ability to tune the separators' physical properties via the electrospinning fabrication process, we identified PAN fiber mats as a candidate separator material for RTIL electrolytes.

In this study, we have developed an electrospun PAN microfiber separator that is highly compatible with RTIL electrolytes and well-suited to the winding processes in commercial battery manufacturing. We report the major physical, mechanical, and electrochemical properties of the separator and ultimately demonstrate the separator in a high capacity Li-ion full-cell.

6.2   PAN Microfiber Separator Morphology, Electrolyte Compatibility, and Mechanical Properties

Building on the previous studies of PAN nonwoven separators for utilization in electrochemical cells with conventional organic electrolytes, this work proves that PAN separators are a strong candidate for RTIL based membranes. While the literature suggests a fiber diameter of approximately 500 nm or less, as controlled by electrospinning solution flow rate and electric field strength [49], allows for optimal performance with conventional organic electrolyte materials, it is proposed that a different microstructure is necessary to accommodate an RTIL electrolyte. For this reason, we aimed to develop a separator with a larger average pore size in order to allow for high wettability with a more viscous electrolyte solution.

Figure 6.1 shows a high-resolution scanning electron microscope (SEM) image of our PAN fiber mat as made, showing a relatively uniform fiber diameter of approximately 1 μm. The morphology of this mat is significantly different than those previously demonstrated, with much thicker fiber diameters. It was proposed that the larger fiber diameter, which leads to higher porosity, should allow for adequate wettability by a RTIL electrolyte.

The porosity of the nonwoven PAN separator designed in this work was determined both experimentally and theoretically. The porosity of a wide variety of materials is determined by the Archimedes Technique, also known as the Immersion Technique, using Equation 6.1:

$$P_{exp} = \frac{m_{sat} - m_{dry}}{m_{sat} - m_{dry}},\tag{6.1}$$

where m_{dry} is the mass of the dry material, m_{sat} is the mass of the material after becoming saturated with the liquid, and m_{sus} is the mass of the material when suspended in the liquid. De-ionized water was chosen as a suitable immersion medium for the PAN separators. Using this method, the porosity of the nonwoven PAN separator mat was determined to be 83%. The porosity of the PAN separator was also calculated using the known density of electrospun PAN (1.12 g cm^{-3}) and the mass and volume of a punched and dried PAN separator sheet ($P_{theoretical} =$
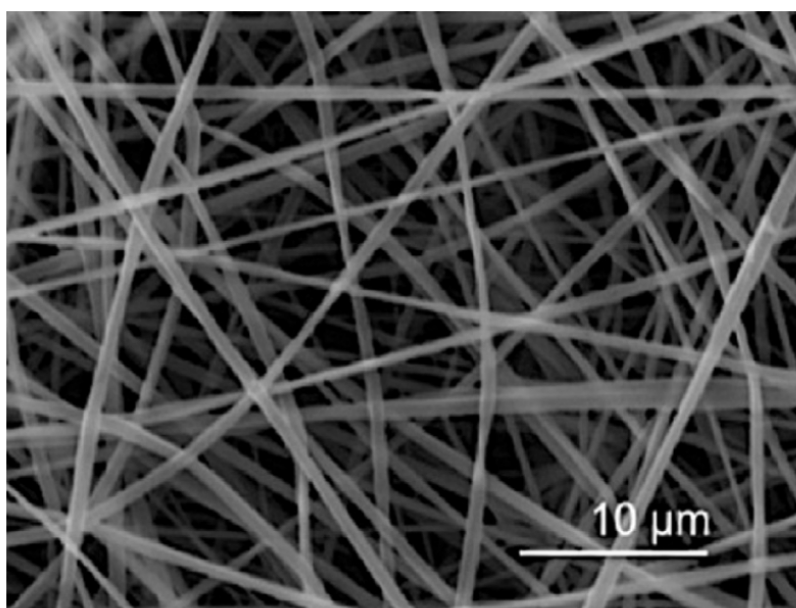
Figure 6.1: SEM micrograph of the as-made electrospun PAN microfiber mat.

$V_{PAN}/V_{separator}$). Using this method, the porosity of the nonwoven PAN separator was determined to be 84.66%, thereby substantiating the experimentally determined value. This is much higher than the Celgard PP separator porosity of 39% and meets the known requirement for battery separator porosity of at least 35%. This data also conforms to the trend found in previously studied nonwoven separators in which larger fiber diameters result in a higher degree of porosity [41]. PAN separators with fiber diameters of <500 nm have been shown to possess porosities of up to 76% [41]. This data suggests that the PAN separators fabricated in this work may be better suited to wetting with an RTIL electrolyte.

The wettability of our PAN separator was estimated using high-speed photography and compared to the wettability of a PP separator and glass fiber separator by two RTIL electrolytes and a conventional organic electrolyte. Electrolytes used include $PYR_{13}FSI$ (1.2M LiFSI), the more viscous RTIL $PYR_{13}TFSI$ (0.6M LiTFSI), and the conventional organic electrolyte EC/DEC (1M $LiPF_6$). The results of our wettability study are shown in Figure 6.2. A lower contact angle is indicative of a higher degree of wettability, and a faster change in contact angle suggests a higher rate of wetting. In all cases, the nonwoven PAN separators showed the highest wettability, with the Celgard PP membrane proving to be the least wettable. Good wettability proves the separator's ability to effectively wick electrolyte, thereby facilitating smooth diffusion of the electrolyte during assembly of an electrochemical cell. Thus, these results further suggest that the PAN nonwoven separators are a strong candidate for utilization with an RTIL electrolyte.

In addition to the physical properties of the electrospun PAN nonwoven separators, it is important to study their mechanical properties. The separators used in spiral wound cells (conventional design) require high tensile strength because the separator is wound together with the electrodes under tension; the separator must not elongate significantly under tension in order to avoid contraction in the direction perpendicular to winding [13]. Commercial separators require a tensile strength corresponding to 2% stretch (strain) at 1000 psi, or 6.89 MPa [13]. To this end, the tensile strength of our PAN separator mats was determined and compared to that of Celgard PP and Whatman GF/F separators. The results of the tensile tests are reported in Figure 6.3. The
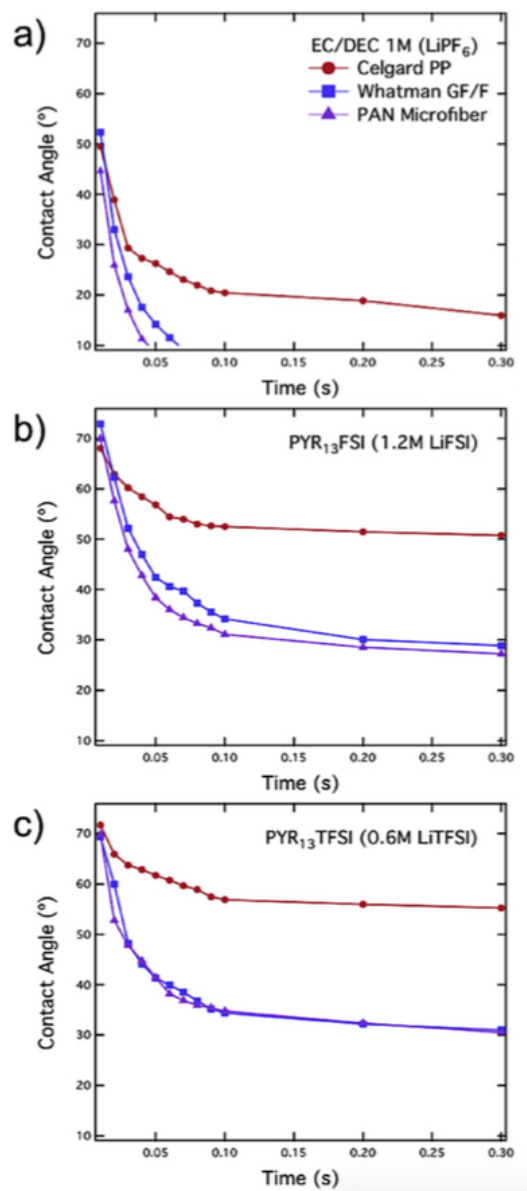
Figure 6.2: Wettabilities of PP, glass fiber, and electrospun PAN microfiber separators by EC/DEC $(1M$ LiPF$_6$) (a), PYR$_{13}$FSI $(1.2M$ LiFSI) (b), and PYR$_{13}$TFSI $(0.6M$ LiTFSI) (c), as estimated by measuring change in electrolyte droplet-separator plane contact angle over time.

tensile strength of the PP separator coincides well with previous academic reports of the tensile strength of similar materials [41]. While the PAN separator's ultimate tensile strength (σ_{UTS}) and yield strength (σ_{yield}) are lower than that of the PP separator, they are much higher than the σ_{UTS} and σ_{yield} of the glass fiber separator and meet the aforementioned requirements for a commercial separator. Our PAN microfiber separators show a σ_{UTS} of approximately 16.39 MPa. Moreover, the PAN separators showed the highest elastic modulus (E), with $E = 5.95$ MPa, of the separator materials tested, suggesting a lower degree of stretch in the elastic region for a given stress. This compares to $E = 4.01$ MPa for the PP separator, and $E = 0.319$ for the glass fiber separator. The combination of physical and mechanical characterization demonstrated in this study substantiates our claim that electrospun PAN fiber separators are a feasible choice for employment in Li-ion cells containing RTIL electrolyte.

6.3 Electrochemical Performance of Li-ion Cells Using PAN Microfiber Separators

Nonwoven separators have exhibited excellent battery performance with carbonate-based electrolytes in terms of cycling life and high rate capability. Because of their high degrees of porosity and wettabilities, nonwoven separators provide a less tortuous path for Li$^+$ transport and therefore show lower ionic resistances than polyolefin separator materials [41]. In order to demonstrate the adequate ionic conductivity of the RTIL-PAN separator system developed in this work, the system's apparent MacMullin number (NM) was calculated and compared to that of a conventional system. The NM is defined as the ratio of the conductivity of the pure electrolyte (σ_0) to that of the immersed separator (σ_{eff}).

A lower apparent NM infers higher rate and power capability. Commercial separator systems possess apparent NM values of <12 [13, 41]. The PAN microfiber separator immersed in RTIL electrolyte shows a relatively low NM of 4.96, well with in the bounds of the commercial standard. It is therefore expected that our electrospun PAN separators should allow for high rate performance in Li-ion cells.
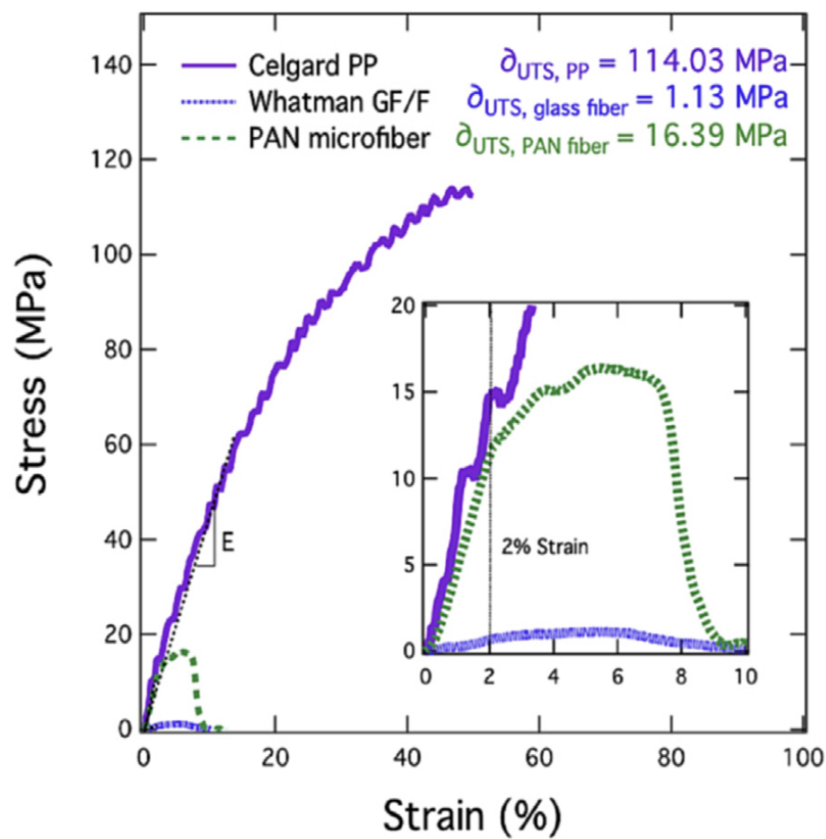
Figure 6.3: Tensile tests of PP, glass fiber, and electrospun PAN microfiber separators. Inset shows detail for the glass fiber and PAN microfiber separator tests.

A rate study of a $Li(Ni_{1/3}Mn_{1/3}Co_{1/3})O_2$ half-cell was carried out in order to examine the rate performance using a PAN separator with RTIL electrolyte, and the results of this experiment were compared to the same rate study using a Whatman GF/F separator. The rate study and cycling stability results are presented in Figure 6.4. The nonwoven PAN separator allows for high capacities at all rates tested as well as high cycling stability. These results corroborate similar studies of nonwoven separators used in combination with organic electrolytes in which the better cycling performances shown when using nonwoven separators are attributed to their higher porosities and the subsequent enhancements in ionic conductivity and uptake of liquid electrolyte [42, 41]; as shown in Figure 6.1, the PAN microfiber mat possesses a very open microstructure that facilitates better uptake of electrolyte. The high cycling stability suggests that the PAN microfiber mat is electrochemically stable against the electrode materials utilized and the electrolyte, as side reactions that might occur with in the cycling voltage range would induce capacity instabilities. A post-cycling morphological analysis was conducted on a separate but identical half-cell allowed to cycle 100 times at a rate of 1C. SEM imaging of the PAN separator after cycling, presented in Figure 6.5, reveals physical change in the separator after cycling. It is proposed that the tighter packing of the fibers, as compared to the as-made PAN microfiber mat, is due to compaction during fabrication and cycling of the cell in a coin-type configuration. Swelling due to absorption of electrolyte may have also occurred. It is noted that such changes have no detrimental effects on performance as proven in the cycling experiments.

Finally, Figure 6.6 demonstrates our electrospun PAN microfiber separator in a high-capacity nSi-cPAN/$Li(Ni_{1/3}Mn_{1/3}Co_{1/3})O_2$ full-cell developed in a recent report [58]. The cycling stability observed in this experiment validates our claim that a nonwoven separator is an adequate replacement for conventional polyolefin materials in RTIL-based LIBs. Demonstration of the PAN microfiber separator in a full-cell is the ultimate test of its electrochemical and physical stability, proving the chemical stability of the separator and its compatibility with commercially attractive electrode materials. While a full safety and thermal stability analysis should be completed for the RTIL-PAN separator system, this combination of data provides strong evidence for the compatibil-
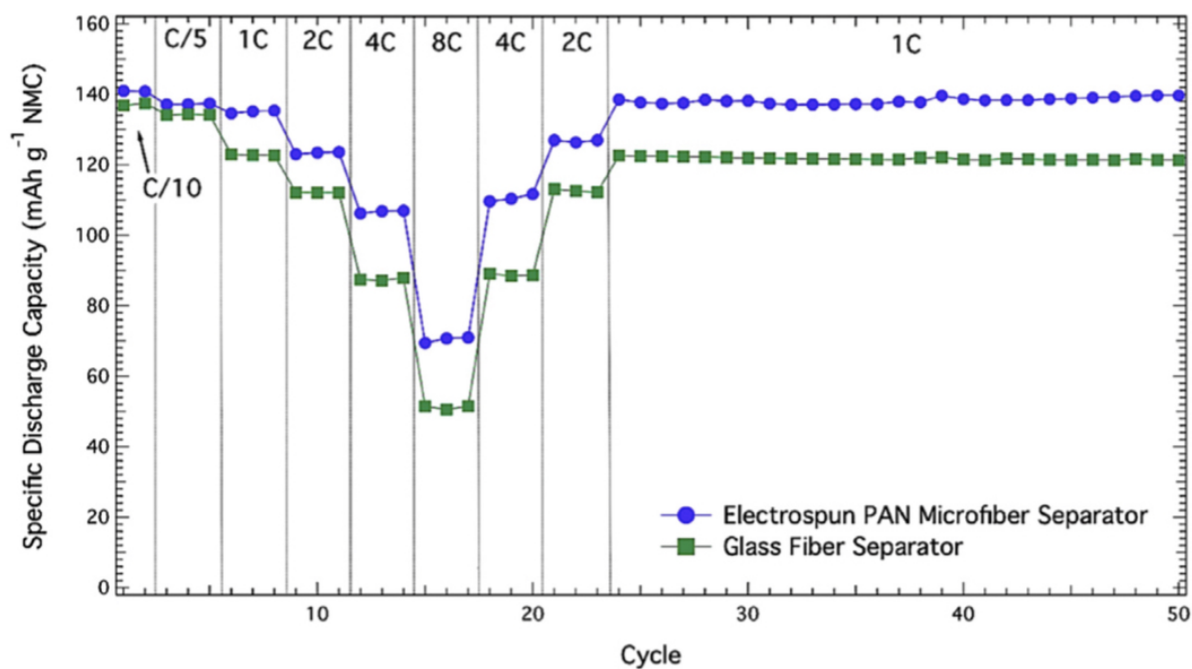
Figure 6.4: Rate study of $Li(Ni_{1/3}Mn_{1/3}Co_{1/3})O_2$ half-cells containing $PYR_{13}FSI$ ($1.2M$ LiFSI) comparing performance of a glass fiber separator and the electrospun PAN microfiber separator. Electrochemical cycling was performed at room temperature between 3 - 4.2V vs. Li/Li^+.
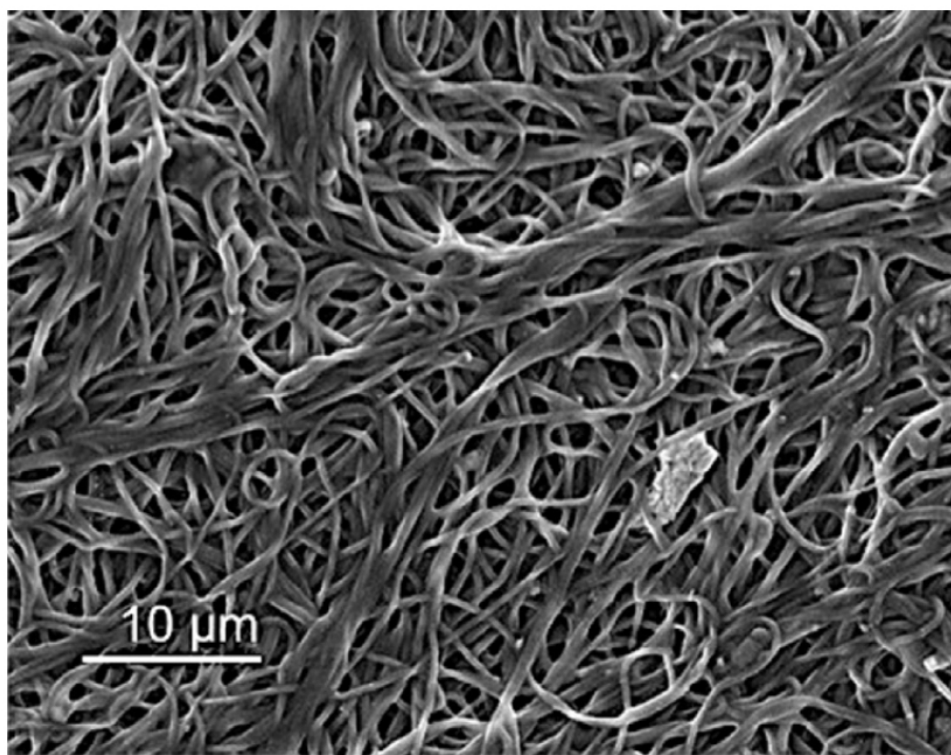
Figure 6.5: SEM micrograph of the electrospun PAN microfiber separator after 100 cycles in a Li(Ni$_{1/3}$Mn$_{1/3}$Co$_{1/3}$)O$_2$ half-cell.

ity of PAN microfiber separators with a RTIL-based battery. Thus, this work represents important progress in the field of RTIL electrolytes and demonstrates their potential for commercialization.

6.4   Conclusions Regarding PAN Microfiber Separators

In this project, we have developed a separator material compatible with both RTIL electrolytes and the commercial LIB manufacturing infrastructure for 18650 cells. Based on the established commercial electrospinning process, PAN microfiber separators present a viable alternative to polyolefin materials. Most importantly, electrospun PAN microfiber separators show superior physical, mechanical, and electrochemical properties when used in combination with RTIL electrolytes.
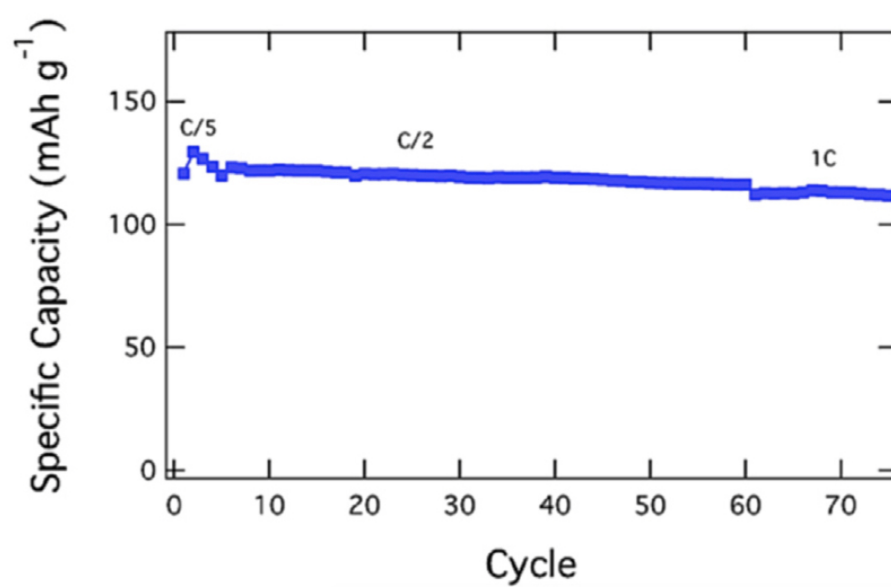
Figure 6.6: High-capacity nSi-cPAN/Li(Ni$_{1/3}$Mn$_{1/3}$Co$_{1/3}$)O$_2$ full-cell containing an electrospun PAN microfiber separator. Capacities normalized to total active material mass (L333 + Si).

Chapter 7

Ionic Liquid Enabled FeS$_2$ for High Energy-Density Lithium-Ion Batteries

Summary

With the energy density of conventional Li-ion batteries (LIBs) approaching a practical upper limit, next generation electrode materials must be developed in order to satisfy the demand for an inexpensive, highly energy dense battery for future energy storage applications. Significant progress has been made on high-capacity tin and silicon-based anodes, but new cathode chemistries must be developed in order to accommodate such materials [36, 103]. While the stable cycling of a Si anode has been demonstrated with capacities above 1500 mAh g^{-1} [173], work in this field has been unable to demonstrate the long-term cycling of a cathode material with capacities higher than 250 mAh g^{-1} [36]. Because of their ability to accommodate more than one Li atom per transition-metal cation, materials that undergo a conversion reaction with lithium have gained attention as promising candidates for high-capacity cathodes [217]. Among such conversion chemistries, FeS$_2$ represents a promising alternative to replace the conventional LiMO$_2$ (M = transition metal) intercalation mechanism because FeS$_2$ is inexpensive, highly energy dense, naturally abundant, and environmentally benign [198, 135, 235, 201, 60, 70, 216, 5]. The four electron reduction of cubic-FeS$_2$ (pyrite) exhibits a theoretical specific capacity of 894 mAh g^{-1}, as compared to the best LiMO$_2$ intercalation electrodes which only provide approximately 200 mAh g^{-1} [225, 74, 66, 47].

7.1   Introduction

Despite the FeS_2/Li system's advantages and recent commercialization by Energizer as a primary battery, its conversion chemistry suffers from a series of obstacles that has hindered its further advancement. In addition to the safety issues associated with lithium metal anodes [14], unfavorable interactions between the electroactive species of the FeS_2 electrode and conventional organic electrolyte solvents leads to rapid capacity fade. While the mechanism for the reduction of cubic-FeS_2 remains the subject of debate, it was recently proposed that the charge products of the FeS_2 system include a multiphase mixture of orthorhombic FeS_2 (marcasite), FeS_y, and S [198, 235]. Given that sulfur is one of the charge products of the FeS_2 conversion reaction, the most important factor determining the FeS_2 electrode's efficiency and reversibility lies in the dissolution of highly mobile polysulfide species $(S_n{}^{2-})$ produced during the reduction of sulfur. The dissolution of such polysulfides into organic liquid electrolytes results in a parasitic redox shuttle, introducing unfavorable side reactions with a lithium metal negative electrode, reducing charging efficiency and quickly degrading cell performance [198, 165, 168, 150, 96, 189, 55].

Recently, research has focused on fabrication of novel FeS_2/carbon matrices capable of confining electroactive species and preventing active material loss [198, 135, 239]. Unfortunately, such electrode architectures require complex fabrication methods and utilize high weight percentages of non-electrochemically active auxiliary materials that significantly limit the energy density of the cathode composite. In this study, we take advantage of the limited polysulfide solubility in an ionic liquid electrolyte, for the first time demonstrating the reversible cycling of a highly energy dense, conventionally prepared FeS_2 electrode.

The design of a liquid electrolyte with a lower solubilizing power for $S_n{}^{2-}$ species is the simplest approach for suppressing polysulfide dissolution and the subsequent redox shuttle mechanism. Such an electrolyte system should show low solvation of the redox-active species of the cathode while maintaining the ability to conduct Li^+. While much work has been done to tailor the polysulfide solubility properties of ILs for sulfur-based electrodes [106, 204, 218, 143], a recent study by J.-W.

Park et al. suggests the electron donor ability of the anion constituent of an IL solvent to be the most crucial factor in designing an electrolyte for utilization with a sulfur-based electrode [165]. Because of the weak Lewis basicity of the charge-delocalized bis(trifluoromethanesulfonyl)imide (TFSI$^-$) anion, room temperature ionic liquids (RTILs or ILs) containing TFSI$^-$ show a low degree of polysulfide solvation. In this work, we exploit the suppression of polysulfide dissolution by TFSI$^-$ and the favorable electrochemical properties of the relatively small N-methyl-N-propylpyrrolidinium (PYR$_{13}$+) cation in order to enable a FeS$_2$ cathode with minimal use of auxiliary electrode components. We demonstrate the highly reversible cycling of a FeS$_2$/Li cell using a PYR$_{13}$TFSI (0.6M LiTFSI) electrolyte and confirm the TFSI$^-$ anion's ability to suppress active material loss, along the way elucidating sulfur's role in the FeS$_2$/Li system's complex conversion mechanism.

7.2   Preliminary Electrochemical Study

The IL anion donor effect was initially substantiated through a cycling stability test utilizing FeS$_2$ electrodes combined with various IL cation-anion pairs. Figure 7.1 depicts the results of this study, proving the impressive stability and reversibility of the FeS$_2$ cell in a TFSI$^-$-based IL as compared to conventional organic electrolytes and ILs comprised of the bis(fluorosulfonyl)imide (FSI$^-$) anion. In the PYR$_{13}$TFSI (0.6M LiTFSI) solution, the FeS$_2$ electrode maintains greater than 80% of its initial capacity after 50 cycles (Figure 1a). This compares to the cycling of FeS$_2$ in a EC/DEC (1/1 vol.) (1M LiPF$_6$) electrolyte, which maintains only about 20% of its initial capacity after 50 cycles, and the rapid capacity fade exhibited by FeS$_2$ electrodes cycled in ILs composed of the FSI$^-$ anion (Figure 1b). As proposed by J.-W. Park et al. [165], our data suggests that the TFSI$^-$ anion (Figure 1c) significantly mitigates cell degradation induced by polysulfide dissolution. Several possible side reactions offer explanations for the poor performance of the FSI$^-$-based ILs (Figure 1d), and the mechanisms of such interactions are detailed in the Supplementary Information.

Based on the cycling data provided in Figure 1, the PYR$_{13}$TFSI (0.6M LiTFSI) electrolyte enables a conventionally prepared FeS$_2$ electrode with an energy density of 542 Wh kg^{-1}, based
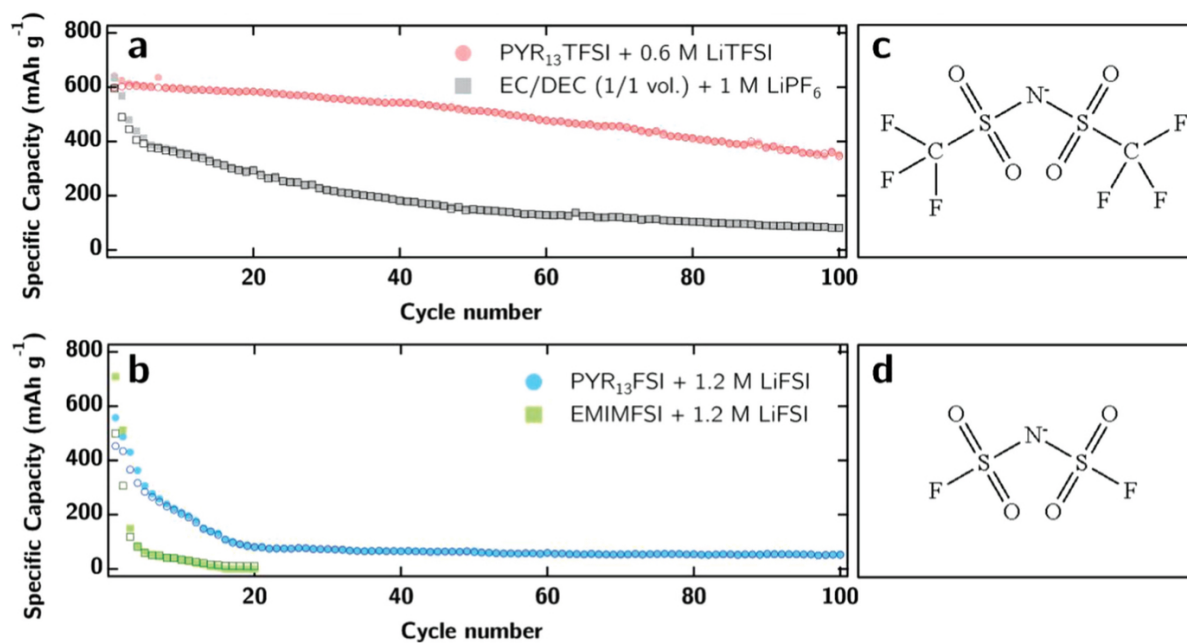
Figure 7.1: Cyclic stability of the FeS_2 electrodes in a) $TFSI^-$-based IL and conventional organic electrolyte and b) FSI^--based ILs, proving the impressive stability and reversibility of the FeS_2 cell in a $TFSI^-$-based IL as compared to conventional organic electrolytes and ILs comprised of the FSI^- anion. Molecular structures of the c) $TFSI^-$ and d) FSI^- anions utilized.

on the total composite electrode mass. This system allows for a much higher energy density than previously reported FeS_2/carbon electrode matrices, with a FeS_2/polyacrylonitrile (PAN) composite showing the highest previously reported energy density of 428 Wh kg^{-1} [198]. While our cycling stability data upholds the proposed mechanism for the suppression of polysulfide dissolution by ILs containing $TFSI^-$, a closer look at the electrochemical data is required to fully understand the advantages of our $PYR_{13}TFSI$ (0.6M LiTFSI) electrolyte.

Reductive dQ/dV analysis and the evolution of the voltage plateaus in the FeS_2 electrode's electrochemical cycling profile highlight the sulfur dissolution's effect on capacity fade. As sulfur is a product formed on reduction of the FeS_2 electrode, this analysis will focus primarily on the discharge processes observed during cycling. As previously mentioned, the redox mechanism of FeS_2 is highly convoluted, and is therefore subject to debate. The literature provides a general mechanism for the initial discharge of cubic-FeS_2 at ambient temperatures, provided below in Equation (1) and Equation (2) [235, 66, 28].

FeS_2 Initial Discharge Mechanism

$$FeS_2 + 2Li^+ + 2e^- \rightarrow Li_2FeS_2 \qquad (1)$$

$$Li_2FeS_2 + 2Li^+ + 2e^- \rightarrow Fe^0 + 2Li_2S \qquad (2)$$
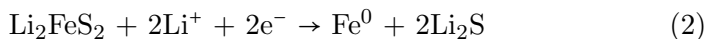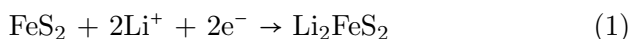
Figure 7.2 provides voltage profiles (Figure 2a and 2b) and dQ/dV profiles (Figure 2c and 2d) for the FeS_2 electrodes cycled in the $PYR_{13}TFSI$ (0.6M LiTFSI) and EC/DEC (1/1 vol.) (1M $LiPF_6$) electrolytes. In agreement with literature, we observe the FeS_2 electrodes' initial discharge profile to have one plateau and subsequent discharges to have two voltage plateaus, labeled 1 and 2 in Figure 2a and 2b, occurring at approximately 2.1 V and 1.5 V vs. Li/Li^+. Due to the low diffusivity of Li^+ into cubic-FeS_2, Equations (1) and (2) proceed simultaneously and share one voltage plateau at 1.5 V during initial discharge.

Subsequent discharges are expected to follow a slightly different mechanism, as ortho-FeS_2 and FeS_y are proposed as charge products in FeS_2 electrodes [198, 235]. This study will provide further evidence of the formation of such charge products, and this mechanism will be discussed later. Literature provides a likely charging mechanism for the FeS_2 electrode, which is shown below
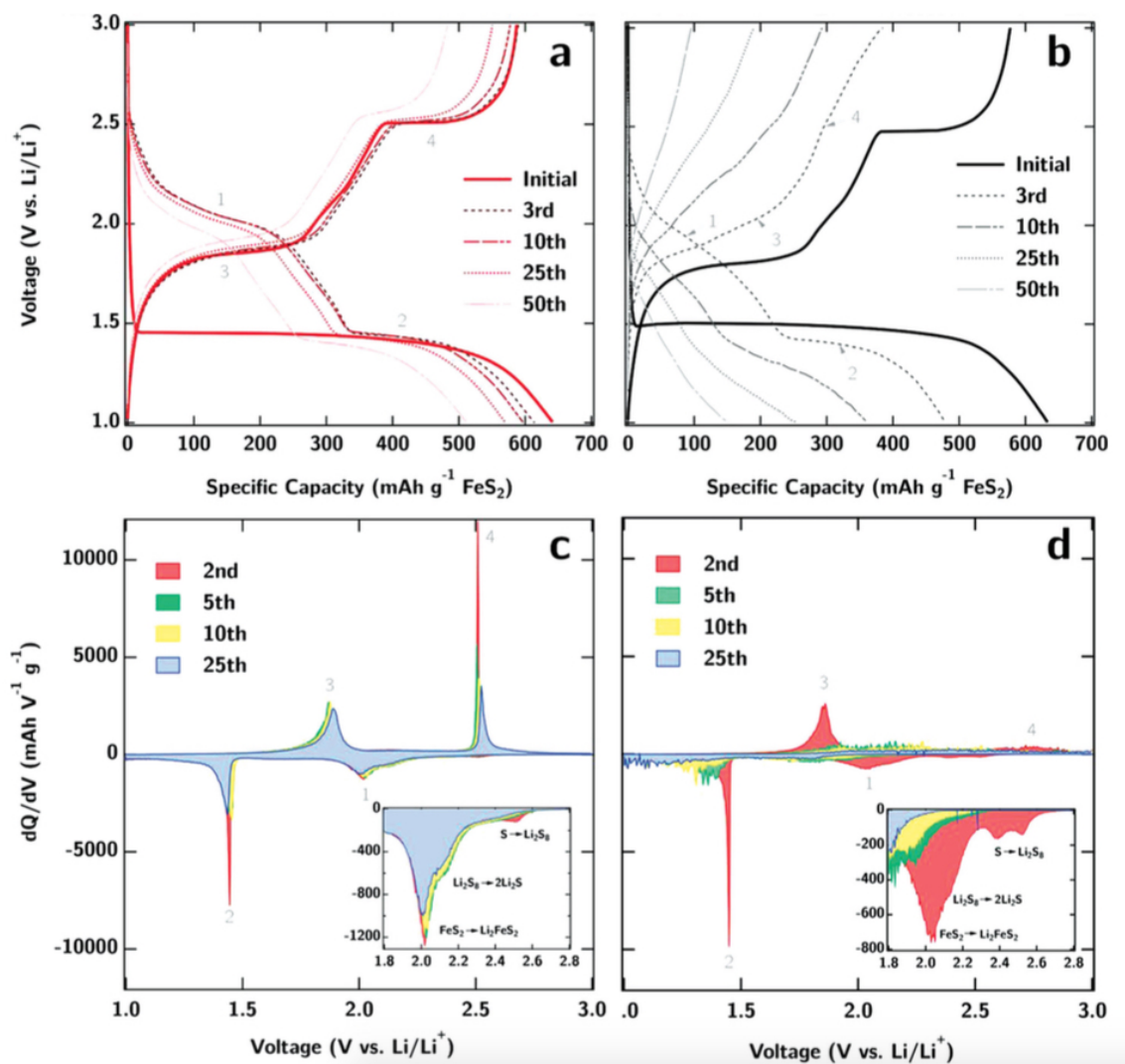
Figure 7.2: Voltage profiles of the FeS$_2$ electrode in a) TFSI$^-$-based IL and b) conventional organic electrolyte. dQ/dV profiles for the FeS$_2$ electrode in c) TFSI$^-$-based IL and d) conventional organic electrolyte with respective reductive deconvolution of peak 1 (sulfur reduction) insets for each electrolyte system.

in order to provide a basis for discussion of sulfur loss during discharge [198, 235].

FeS$_2$ Charge Mechanism

$$Fe^0 + 2Li_2S \rightarrow Li_2FeS_2 + 2Li^+ + 2e^- \hspace{2cm} (3)$$

$$Li_2FeS_2 \rightarrow Li_2\text{-}xFeS_2 + xLi^+ + xe^- \ (x= 0.5 \ to \ 0.8) \hspace{1cm} (4)$$

$$Li_2\text{-}xFeS_2 \rightarrow 0.8ortho\text{-}FeS_2 + 0.2FeS_{8/7} + 0.175S + (2\text{-}x)Li^+ + (2\text{-}x)e^- \hspace{1cm} (5)$$
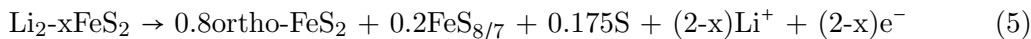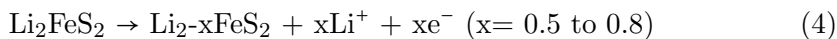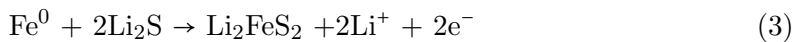
According to this reaction cascade, charge products available for reduction during subsequent discharges include ortho-FeS$_2$, FeS$_y$, and S. This charging mechanism is substantiated by the evolution of three distinct discharging steps illustrated in the dQ/dV profiles provided in Figure 2c and 2d. Peak 1, corresponding to the discharge plateau at 2.1 V vs. Li/Li$^+$, represents the reduction steps associated with the charge products proposed in Equation (5). Peak 1 is de-convoluted by taking a closer look at the reductive dQ/dV profiles between 1.8 - 2.8 V vs. Li/Li$^+$ (insets in Figure 2c and 2d), showing three defined reduction peaks coinciding with the reduction of S and ortho-FeS$_2$, consistent with previous work [198]. As shown in Figure 2d, the capacities obtained by reduction of S in an organic electrolyte fade rapidly between the 2nd cycle and subsequent discharges. This is attributed to the loss of electroactive sulfur during dissolution of S$_n{}^{2-}$ into the organic solvent. Figure 2c shows that the reductive dQ/dV profiles of FeS$_2$ in TFSI$^-$-based IL remain largely unchanged over cycling, owed to the retention of S in the composite. This provides strong evidence for the inhibition of S$_n{}^{2-}$ dissolution in TFSI$^-$-based electrolytes.

As sulfur is lost from the electrode matrix over cycling in the organic electrolyte, the voltage profiles change drastically (Figure 2b), developing large overpotentials and showing diminishing charge and discharge plateaus associated with the sulfur redox chemistry. Such changes in voltage profile behavior are much less severe over cycling in the TFSI$^-$-based electrolyte. Because the effects of polysulfide dissolution in the TFSI$^-$-based IL are minimal, variations in the voltage profiles of FeS$_2$ over cycling in this electrolyte are attributed to other degradation processes and are described later. Voltage traces for the FeS$_2$ electrodes cycled in the PYR$_{13}$FSI (1.2M LiFSI) electrolyte and 1-ethyl-3-methylimidazolium (EMIM) FSI (1.2M LiFSI) electrolyte are provided in Figure 7.3, showing clear evidence of severe overpotential growth during the first five cycles leading to rapid

cell failure.

To further probe the proposed polysulfide dissolution's effect on the FeS_2 electrodes' degradation, electrochemical impedance spectroscopy (EIS) was performed on FeS_2 half-cells at various stages of cycle life. The EIS spectra for FeS_2 electrodes cycling in conventional organic electrolyte and TFSI$^-$-based IL are provided in Figure 7.4, respectively. Both impedance spectra consist of an intercept on the real Z' axis and a semicircle in the high frequency region, a semicircle in the medium frequency region, and a 45° slash in the low frequency region. The spectra can be analyzed using the equivalent circuit model provided in Figure 3b, which was fit to each curve in order to quantify the impedance contributions of each circuit element. These modeling fit quantifications are provided in Figure 7.5, showing the evolution of the impedances caused by each element.

The major difference between the EIS spectra of the cells containing IL and organic electrolyte lies in the growth of the large semicircle in the medium frequency range. This semicircle is attributed to the charge transfer resistances (R_{ct}) [108]. While R_{ct} in the cell containing TFSI$^-$-based IL experiences growth during the first five cycles and then stabilizes, R_{ct} in the cell containing conventional organic electrolyte grows throughout cycling. The evolution of the R_{ct} impedance component is attributed to the presence of soluble S_n^{2-} species in the cell. Interactions between polysulfide species and the electrode interfaces, especially that of the lithium metal counter electrode, greatly increase charge transfer impedance due to the insulating nature of elemental sulfur and poor electrical contacts leading to poor electrochemical accessibility [229]. The TFSI$^-$ anion has also been shown to form a stable passivation layer on the surface of lithium electrodes during electrochemical cycling [229], protecting the surface from interaction with any polysulfides that may be present and allowing for a more stable R_{ct} circuit element. The relatively slow capacity fade observed during cycling in the TFSI$^-$-based IL electrolyte is therefore attributed mainly to the innate material degradation associated with continuous formation and deformation of charge-discharge products. Contrastingly, the effects of polysulfide dissolution continue to increase throughout cycling in conventional organic electrolyte, leading to continuous and rapid capacity fade.
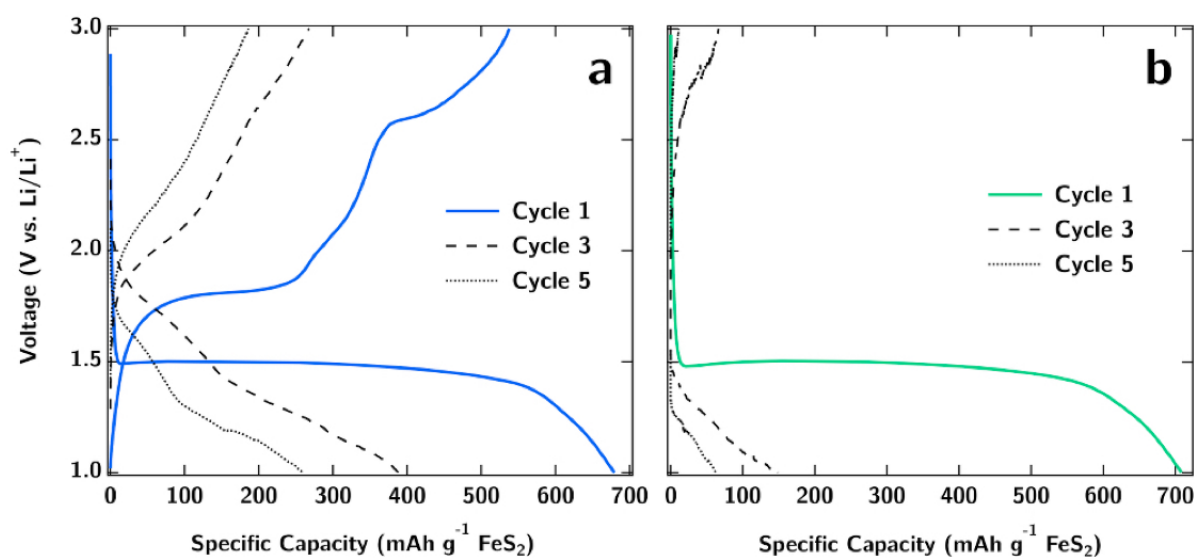
Figure 7.3: Voltage profiles of the FeS$_2$ electrode in a) (1.2M LiFSI) PYR$_{13}$FSI electrolyte and b) (1.2M LiFSI) EMIMFSI electrolyte showing clear evidence of severe overpotential growth and loss of sulfur redox plateaus during the first five cycles of both FSI-based ILs leading to rapid cell failure.
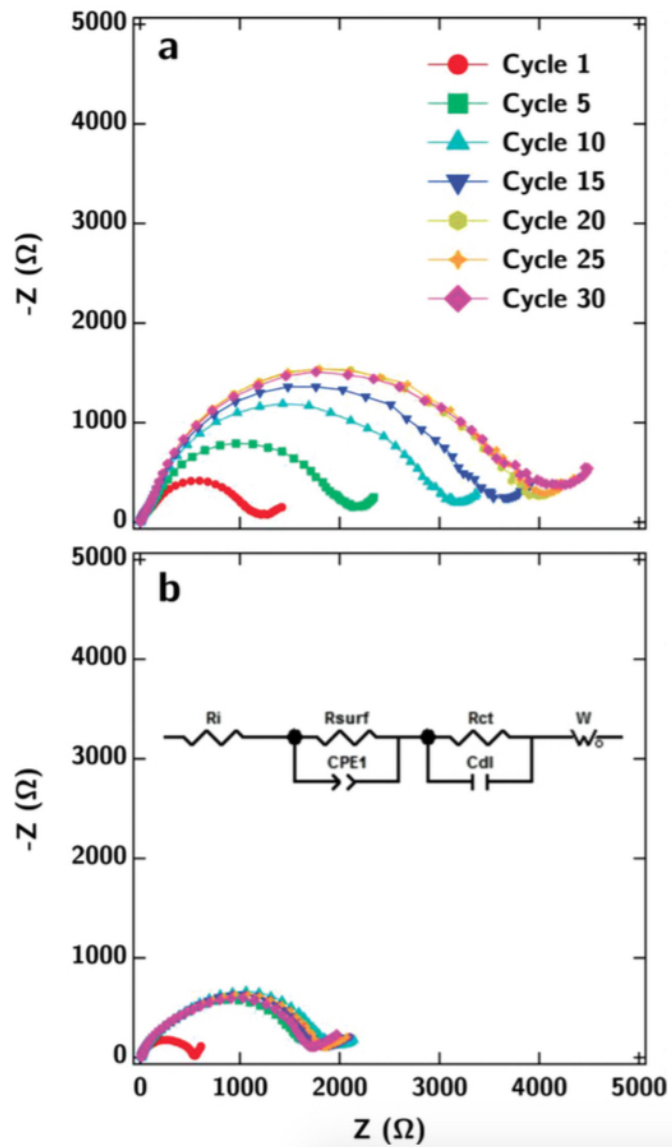
Figure 7.4: EIS spectra taken every 5th charging cycle for the FeS$_2$ electrode cycled in a) conventional organic electrolyte and b) TFSI$^-$-based IL. The equivalent circuit model for the cells is included in the inset.
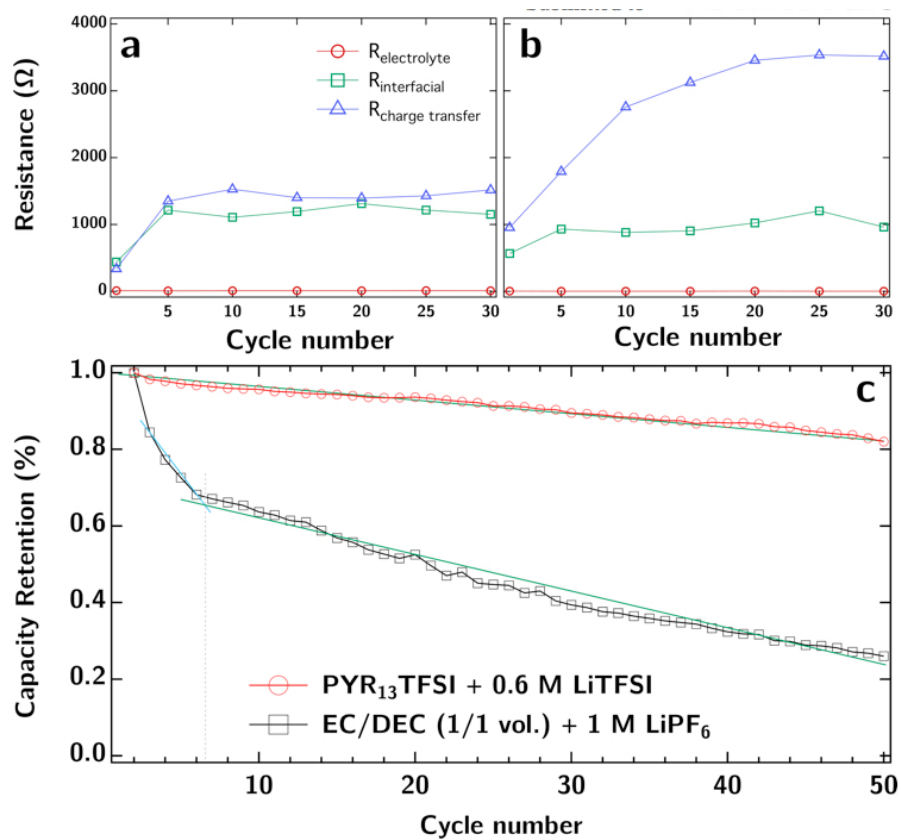
Figure 7.5: EIS resistance component quantification, as modeled by the Solartron ZPlot-Lab software, as a function of cycle number for FeS$_2$ cells cycled in a) TFSI$^-$-based IL and b) conventional organic electrolyte. c) Capacity retention, calculated as (discharge capacity n/ 2nd discharge capacity) for FeS$_2$ electrodes cycled in TFSI$^-$-based IL and conventional organic electrolyte. Lines of fit in c) correspond to linear trends in degradation, highlighting the impedance contributions of the R_{ct} circuit element during the first five cycles.

7.3   Morphological and Crystallographic Analysis

Up to this point in the study, we have worked under the assumption that the success of the TFSI$^-$-based IL in enabling the FeS$_2$ chemistry lies in its ability to mitigate polysulfide dissolution. This assumption is based upon recent literature and the well-known polysulfide redox shuttle mechanism which occurs in traditional organic electrolytes. To this end, we use high-resolution transmission electron microscopy (HRTEM) and energy-dispersive X-ray spectroscopy (EDS) to provide concrete evidence of the sulfur retention in the FeS$_2$ electrodes during cycling in the TFSI$^-$-based IL. We use the same analysis to show the disappearance of sulfur from the electrode matrix when cycled in organic electrolyte. TEM and EDS were performed on an uncycled FeS$_2$ cathode composite as well as on electrodes after 20 cycles in both TFSI$^-$-based IL and conventional organic electrolyte. Figure 7.6 presents TEM images and locations of representative EDS point locations (red markings) for each sample. The compositional integrity of the FeS$_2$ composite can be analyzed in terms of the ratio of atomic percentages of S to Fe (at.% S/ at.% Fe). If the active material exists in a FeS$_2$ phase, this ratio should be equal to about 2 based on stoichiometry. EDS at a point on the pristine, uncycled electrode yields a ratio of 1.99 (Figure 4a). EDS at a point on the sample cycled 20 times in PYR$_{13}$TFSI (0.6M LiTFSI) electrolyte yields a ratio of 1.90 (Figure 4b). This provides concrete evidence that the TFSI$^-$-based IL prevents polysulfide dissolution, allowing the active material particles and composite to retain their sulfur composition. EDS linescans were also performed on particles in the uncycled electrode and particles cycled in TFSI$^-$- based IL, showing constant S and Fe content through out the entire cross-section of the active material particles (Figure 7.7. The retention of S in the sample cycled in TFSI$^-$-based IL allows for excellent preservation of the composite microstructure and particle morphology, as observed in the TEM images.

In contrast, the FeS$_2$ electrode cycled in EC/DEC (1/1 vol.) (1M LiPF$_6$) shows very poor retention of S content. Taking EDS at various points on the sample cycled 20 times in organic electrolyte yields a ratio of at.% S to at.% Fe well below 1. Point 2 in Figure 4c, representative of the entire sample, shows a ratio of at,% S to at.% Fe of 0.37. Atomic percentages for all points are
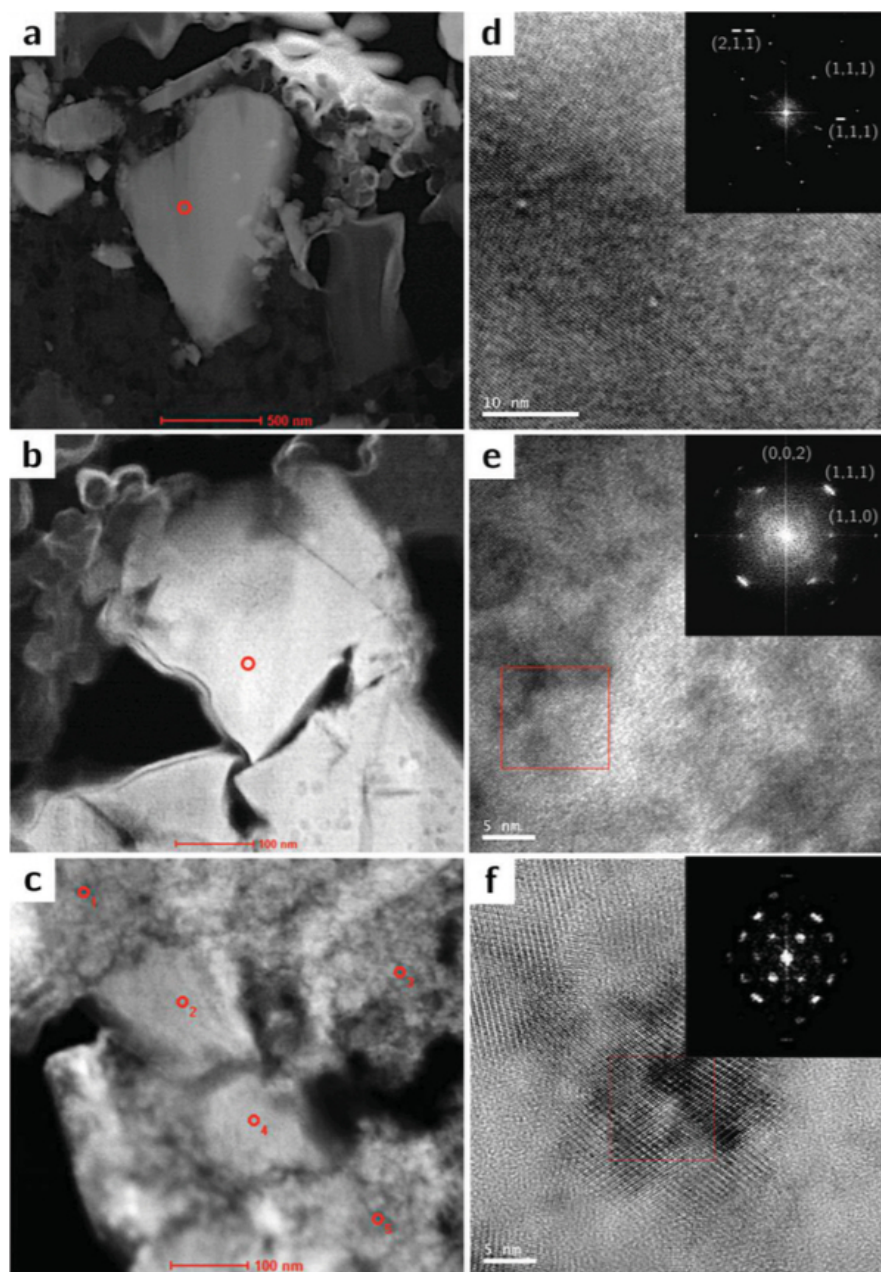
Figure 7.6: TEM micrographs of a particle in an (a) uncycled FeS$_2$ electrode, (b) a 20th cycled particle in TFSI-based IL, and (c) 20th cycled particles in conventional organic electrolyte. Red markings depicted represent EDS point-and-shoot analysis at each electrode particle. (d-f) HRTEM micrographs along with FFT analysis were performed for each particle observed.
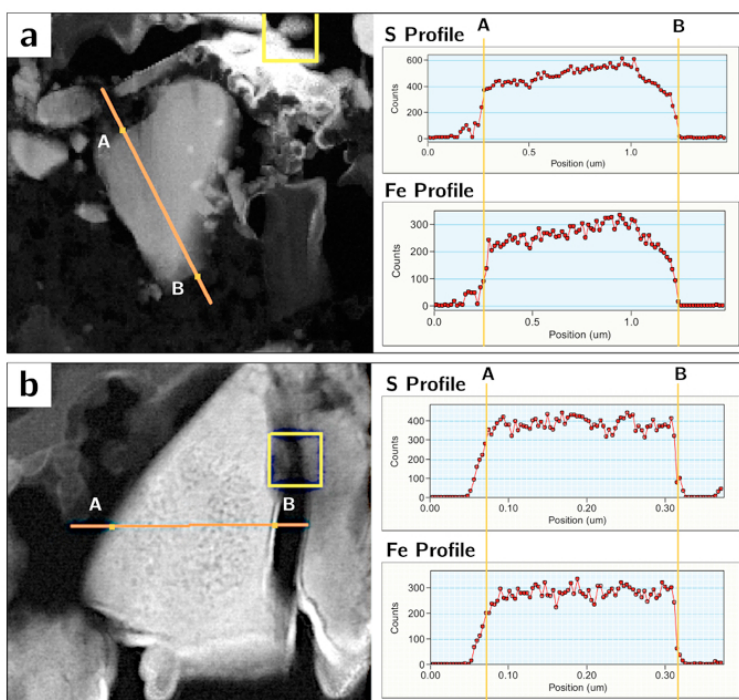
Figure 7.7: EDS linescans were also performed on particles in the a) uncycled electrode and particles cycled in b) TFSI$^-$- based IL, showing constant S and Fe content through out the entire cross-section of the active material particle. The retention of sulfur in the sample cycled in TFSI$^-$- based IL allows for excellent preservation of the composite microstructure and particle morphology, as observed in the TEM images.

provided in Figure 7.8, showing sulfur deficiencies throughout the composite. The absence of S in this sample is clear evidence of sulfur dissolution into the electrolyte during cycling. This deficiency leads to severe degradation of the composite microstructure and particle morphology, as observed in the TEM image.

HRTEM images and fast Fourier transform (FFT) analysis of the same particles shown in Figure 4a-c are provided in Figure 7.6. As expected, the active material in the uncycled electrode (Figure 4d) was found to be phase pure cubic-FeS_2 (pyrite). FFT analysis of the HRTEM image of the sample cycled in $TFSI^-$-based IL (Figure 4e) matches with ortho-FeS_2 (marcasite). This provides further evidence that ortho-FeS_2 is produced electrochemically on charge, validating the charge-discharge mechanism discussed earlier and coinciding with previous findings [198, 235]. Analysis of the FFT pattern obtained from HRTEM image of the sample cycled in organic electrolyte (Figure 4f) shows no evidence of FeS_2, suggesting that the polysulfide dissolution-induced sulfur deficiency hinders the electrochemical stability of the cathode. However, evidence of the hexaganol FeS phase was found in the sample cycled in organic electrolyte. Details on the indexing of the FFT pattern in Figure 4f are provided in Figure 7.9. Existence of the FeS phase provides reason for the capacities delivered by the electrode cycled in organic electrolyte. Our EDS and HRTEM analysis contribute greatly to the understanding of the complex FeS_2 conversion mechanism. The loss of sulfur in the electrode cycled in organic electrolyte can now be more accurately correlated to the loss of reduction peaks in the electrode's dQ/dV profiles (Figure 2d). Furthermore, the finding of a FeS_y phase in the same sample demonstrates the plausibility of the charging mechanism described by Equation 3-5. Such correlations provide clarity for a previously convoluted conversion mechanism.

7.4　　Conclusions Regarding RTIL Enabled FeS_2

In summary, this work demonstrates the ability of a $TFSI^-$-based IL electrolyte to enable a conventionally prepared FeS_2 cathode. The $TFSI^-$-based IL significantly inhibits polysulfide dissolution, and therefore the parasitic redox shuttle mechanism that plagues sulfur based electrode
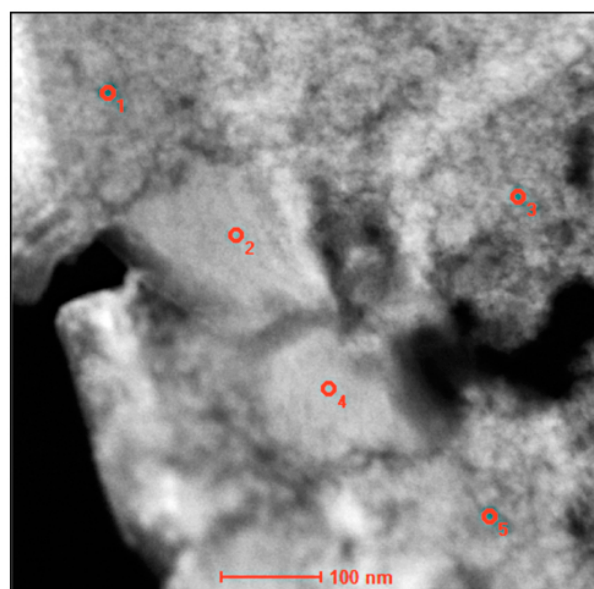
Point	C (at%)	S (at%)	Fe (at%)
1	25.47	18.21	56.32
2	21.57	21.29	57.14
3	44.66	13.89	41.45
4	0	17.86	82.14
5	26.92	12.65	60.43

Figure 7.8: Atomic percentages for all the point-and-shoot (red markings) executed on the TEM micrograph of the composite electrode cycled in conventional organic electrolyte, showing sulfur deficiencies throughout. The absence of S in this sample is clear evidence of sulfur dissolution into the electrolyte during cycling. This deficiency leads to severe degradation of the composite microstructure and particle morphology, as observed in the TEM image.
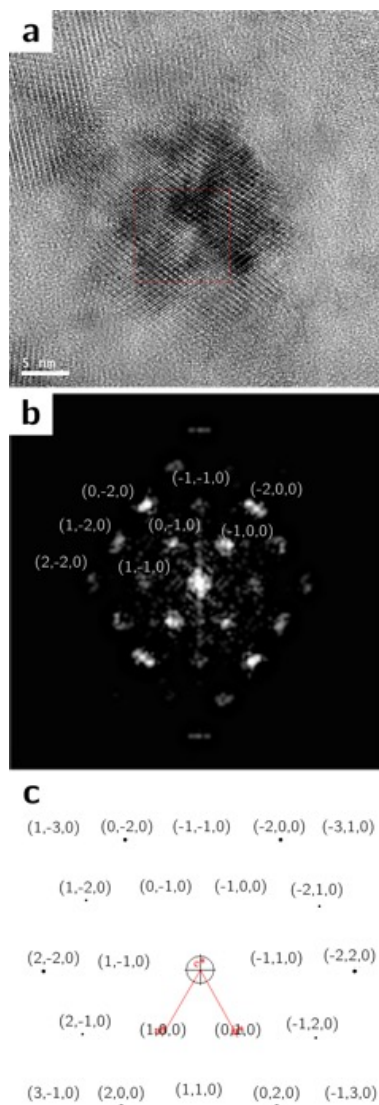
Figure 7.9: a) HRTEM image of the sample cycled in organic electrolyte along with b) FFT pattern analysis showing no evidence of FeS_2, suggesting that the polysulfide dissolution-induced sulfur deficiency hinders the electrochemical stability of the cathode. Evidence of the hexaganol FeS phase was found though. c) Details on the indexing of the FFT pattern show existence of the FeS phase providing reasons for the capacities delivered by the electrode cycled in organic electrolyte.

chemistries. Most importantly, by eliminating the need for complex auxiliary electrode components previously necessary for confinement of electroactive species, we provide highly stable cycling and an exceptional energy density of 542 Wh kg^{-1} of electrode composite. Such research substantiates the ability of RTIL electrolytes to enable high capacity electrode materials. While the sulfur-RTIL system described by J.-W. Park et al. [165] reports an average cycling capacity of about 435 mAh g^{-1} (normalized to total electrode mass) over 50 cycles, as compared to our system's 330 mAh g^{-1}, the Li-S is yet to be commercialized do to a number of serious drawbacks, mainly the need for complex composite architectures and high quantities of conductive additives. Our study demonstrates a significant improvement to a commercially available Li-ion system. When viewed in the context of the search for high energy density cathode materials and recent developments in advanced anode systems, this work represents important progress towards a safer, higher performance secondary Li-ion battery.

7.5 Supplementary Characterization of RTIL Enabled FeS$_2$

7.5.1 Mechanism of Cell Failure for FSI$^-$-based RTILs

While the anion donor effect can explain the high performance of FeS$_2$ in the TFSI$^-$-based IL, a different mechanism must explain why the FSI$^-$-based ILs perform so poorly compared to the organic electrolyte solvent. It has been suggested that the FSI$^-$ anion decomposes in the presence of nucleophilic polysulfide species due to the instability of its -SO$_2$F group in the presence of Li$_2$S$_n$, leading to an irreversible side reaction during discharge likely forming Li$_2$S and Li$_2$SO$_4$ on the cathode surface [184, 79]. Such a mechanism is possible given that sulfonylfluorides containing the -SO$_2$F group have been utilized as precursors in a reaction with nucleophilic species in the preparation of fluorinated sulfonylamide compounds [184, 241].

The 1-ethyl-3-methylimidazolium (EMIM$^+$) FSI electrolyte shows very poor performance with the FeS$_2$ chemistry. Because previous research has demonstrated low polysulfide dissolution in EMIMTFSI electrolytes, our results using the EMIMFSI composition confirm that the anion donor effect dominates an IL electrolyte's compatibility with sulfur-based electrodes. Based on the

proposed mechanism, anions with stronger Lewis basicity are susceptible to interactions with the Li_2Sn species present in the fully discharged state of sulfur-based electrodes, leaving behind highly soluble and mobile $S_n{}^{2-}$ species. Given the relatively high Lewis acidity of imidazolium cations, especially $EMIM^+$, we suggest the possibility of an irreversible side reaction between $EMIM^+$ and $S_n{}^{2-}$. Such reactions seem plausible since EMIM-based ILs have recently attracted great attention as fuel purifiers because of their ability to selectively remove sulfur and sulfur-containing compounds from organic liquids at room temperature [241, 26]. This interaction would explain the severe capacity degradation of the FeS_2 electrode observed in the EMIMFSI electrolyte solvent. It is proposed that $EMIM^+$-based ILs are incompatible with sulfur chemistries when paired with an anion that shows a weak ability to suppress $S_n{}^{2-}$ solvation.

Chapter 8

Stable Silicon-Ionic Liquid Interface for Next Generation Lithium-ion Batteries

8.1   Introduction

While rechargeable lithium-ion batteries (LIBs) have dominated the portable electronic market for nearly a decade, they have failed to gain widespread commercial success in high power and high capacity applications. Industry and academia alike have been unable to develop a battery capable of meeting the growing societal and environmental demand for safe, high-energy-density, long-lasting energy storage systems [75, 101, 226, 12]. Such systems could serve to expedite a smooth transition to an electrified transportation market and enable intermittent renewable energy resources, both of which have been gaining attention in our increasingly carbon-constrained world. The search is on for the next generation of electrode materials that will meet such guidelines in a cost effective and efficient manner [121, 207].

Recently, silicon has been identified as one of the most attractive high-energy anode materials for LIBs. Silicon's low working voltage and high theoretical specific capacity of 3579 mAh g^{-1}, nearly ten times higher than that of state-of-the-art graphite anodes, have encouraged widespread research efforts aimed at developing a viable Si based electrode [21, 243]. The substantial gains in specific and volumetric capacity simply through the implementation of an active material such as Si offer a glimpse into the future of lighter and smaller batteries.

Despite the advantages of the Si electrode, a number of challenges impede its commercialization. Many of these challenges are associated with the Si material's severe volume expansion during lithiation. While the commercialized graphite electrode expands roughly 10-13% during lithium

intercalation [109, 120], Si's expansion amounts to nearly 300%, generating structural degradation and instability of the all-important solid-electrolyte interphase (SEI) [243, 227]. Such instabilities ultimately shorten the battery life to inadequate levels. Degradation of the active material can be mitigated by incorporating materials smaller than 150 nm [139]; however, research is yet to develop a practical solution to the expansion-induced breaking of conduction channels, active material isolation, and continuous SEI reformation [91, 240].

Pioneering works have found some success in addressing material instability through the nanostructural design of electrode architectures capable of reducing expansion and its consequences [227, 174, 134, 172, 34, 166, 171, 142, 138]. The ultimate goal of such research is to incorporate a Si-based negative electrode into a lithium-ion full-cell, requiring the Si electrode to maintain a half-cell coulombic efficiency (CE) of >99.994% for 5,000 cycles [227]. These values, although somewhat unrealistic for current applications needs, truly emphasize the importance of half-cell CEs in order to achieve a long-lasting LIB. Unfortunately, the electrode architectures presented in previous works [227, 174, 134, 172, 34, 166, 171, 142, 138], despite providing significant improvements to Si electrode performance, lack the needed CEs largely because the volume change during Si alloying and de-alloying renders the SEI at the Si-electrolyte interface mechanically unstable.

The SEI layer forms on the anode surface through reductive decomposition of the electrolyte during charging of the battery. Si anodes suffer extensively from a dynamic SEI that must reform each cycle as expansion during lithiation causes the layer to break [21]. Formation of the SEI consumes Li^+ and depletes electrolyte during every cycle [35]. In contrast to half-cells, which utilize a Li metal counter electrode with an effectively unlimited supply of Li^+, full-cells have a limited supply of Li^+ provided by the cathode. It follows that the continuous breaking and reforming of the SEI layer quickly destroys the cell's cycling performance.

Alternative electrolyte compositions [161, 199, 160, 17] and active material surface treatments [136] have been studied in the effort to enhance SEI formation on high-capacity anode materials and improve half-cell CEs. In spite of these efforts, the CEs achieved throughout cycling are still insufficient for a long-lasting Si-based full-cell [17, 122, 25, 95] or the methods employed to manufacture

the full-cells introduce large excesses of Li^+ (>200%) into the system that affects its true performance [81, 82, 33]. In the effort to design next generation electrolyte materials, room temperature ionic liquids (RTILs or ILs) are of particular interest due to their low volatilities, negligible vapor pressures, thermal stabilities, high voltage stability windows, and sufficient ionic conductivities [15]. Previous work has reported that RTILs, particularly those consisting of the pyrrolidinium ($PYR_{1n}{}^+$) or 1-ethyl-3-methyl-imidazolium ($EMIM^+$) cation and the bis(trifluoromethanesulfonyl)imide ($TFSI^-$) or bis(fluorosulfonyl)imide (FSI^-) anion, are cathodically stable with popular negative electrode materials [81, 61, 146, 123] including Si [199, 160, 17]. While the compatibility of ILs with such materials has been proven, a clear understanding of their electrochemical properties and interfacial chemistries has not yet been developed. Moreover, relatively little work has been dedicated to the study of the compatibility between RTIL electrolytes and Si-based nanocomposite electrodes, with all published work in this field, to date, investigating Si-RTIL systems in thin film type electrodes [199, 160, 17].

A combinatorial approach, one involving a mechanically resilient electrode architecture merged with an electrolyte capable of forming a favorable SEI, is the most promising option to integrate structural integrity with stable interfacial chemistry in a bulk type Si anode. To this end, we have designed a Si-RTIL system that exhibits a highly stable and resilient SEI, providing a solution to the drawbacks of the Si-anode and enabling the long-term operation of a lithium-ion full-cell with a bulk type Si-based anode. Through a systematic and comprehensive experimental matrix, we have studied the composition and structure of the SEI formed by an FSI^--based IL on our previously reported cyclized-polyacrylonitrile (cPAN)-based Si nanocomposite architecture (nSi-cPAN) [174]. Using experimental and theoretical data, we propose a mechanism for the formation of the SEI at the Si-RTIL interface and discuss the importance of CE in half-cell configurations. Most notably, this study is highlighted by the groundbreaking demonstration of the highly reversible cycling of a nSi-cPAN/Li($Ni_{1/3}Mn_{1/3}Co_{1/3}$)O_2-(L333) full-cell using a $PYR_{13}FSI$ (1.2M LiFSI) electrolyte.

8.2　Electrochemical Characterization of Half-cells in Various Electrolyte Systems

The simple fabrication, scalability, low volume expansion, and structural robustness of our previously reported nSi-cPAN architecture [174] make it an ideal candidate to merge with a suitable electrolyte system. In pursuit of a stable Si-electrolyte interface, the nSi-cPAN composite was cycled under galvanostatic conditions in RTILs comprised of cation-anion combinations known for their cathodic stabilities against various negative electrode materials [199, 160, 17, 81, 61, 146, 123]. The cycling performances of the Si-based electrode in RTIL solutions, including $PYR_{13}FSI$ ($1.2M$ LiFSI), $PYR_{13}TFSI$ ($0.6M$ LiTFSI), and EMIMFSI ($1.2M$ LiFSI), were directly compared to the electrode's performance in the commercial EC/DEC ($1M$ $LiPF_6$) electrolyte. The results of the preliminary cycling study are presented in Figure 8.1, demonstrating the exceptional cycling stability of the nSi-cPAN anodes in FSI^--based ILs and their unprecedented CE in the $PYR_{13}FSI$ system. The high CE manifested in the $PYR_{13}FSI$ ($1.2M$ LiFSI) electrolyte stabilizes after 8 cycles, with an average stable CE of 99.945% and a charge capacity retention of 76.7% after 100 cycles (blue profiles, Figure 8.1a). While exhibiting stable half-cell cycling, the lower average CE (98.451%) observed using EMIMFSI ($1.2M$ LiFSI) electrolyte (orange profiles, Figure 8.1b) is ascribed to the instability of the $EMIM^+$ cation below 1.5 V (*vs.* Li^+/Li) [146]. Such impressive data contrasts that of the cycling behavior of our nSi-cPAN electrode in a conventional organic electrolyte, which maintains only 45.2% of its initial charge capacity after 100 cycles with an average stable CE of 97.824% (red profiles, Figure 8.1a), and the rapid capacity fade and low active material utilization in a $TFSI^-$-based IL (green profiles, Figure 8.1b). The results obtained with organic electrolyte differ from our previous work [174] due to the absence of a voltage hold step during cycling, typically required to add stability and increase CE, and a higher active material mass loading in this study (over double that of our previous work). The charge-discharge profiles generated by cycling the nSi-cPAN in each electrolyte solution are depicted in Figure 8.2.

The unparalleled CEs of the $Si-PYR_{13}FSI$ system are attributed to the formation of a highly
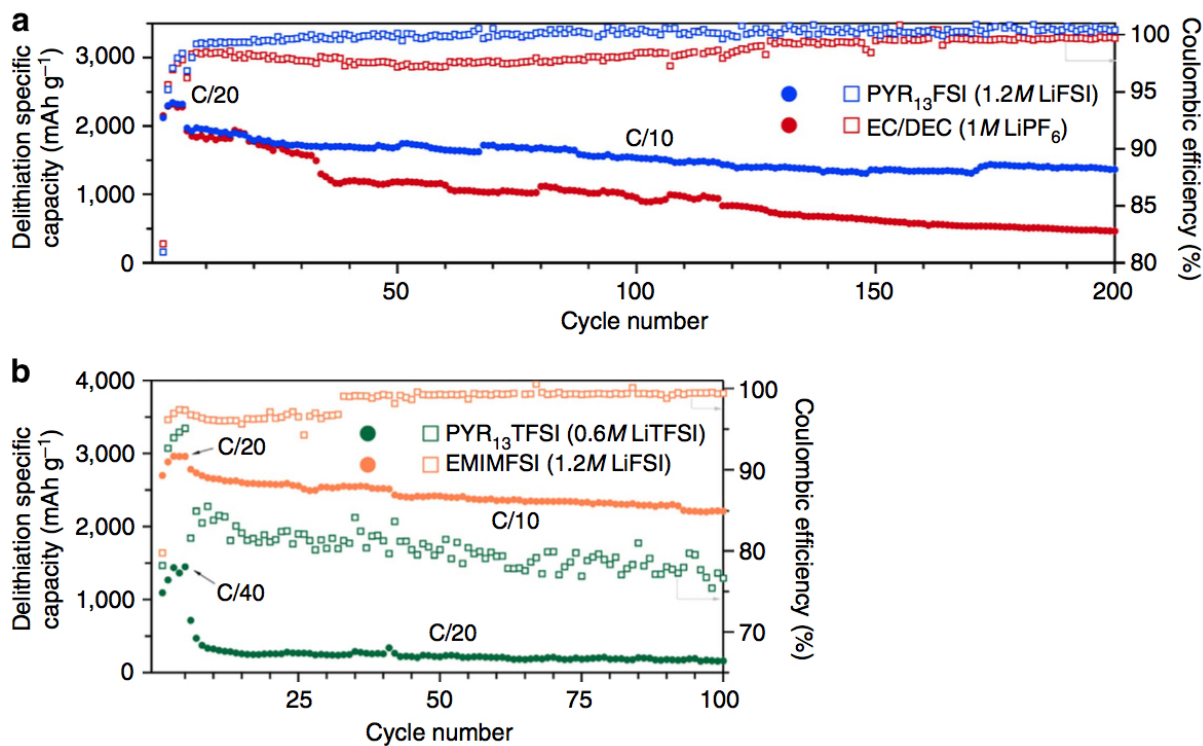
Figure 8.1: (a) Specific capacities and coulombic efficiencies of nSi-cPAN electrode in $PYR_{13}FSI$ ($1.2M$ LiFSI) and EC/DEC ($1M$ $LiPF_6$). (b) Specific capacities and coulombic efficiencies of nSi-cPAN electrode in $PYR_{13}TFSI$ ($0.6M$ LiTFSI) and EMIMFSI ($1.2M$ LiFSI) electrolyte systems. Cycling was carried out at room temperature in 2032 coin-type half-cells operated between 0.05-1 V ($vs.$ Li^+/Li).
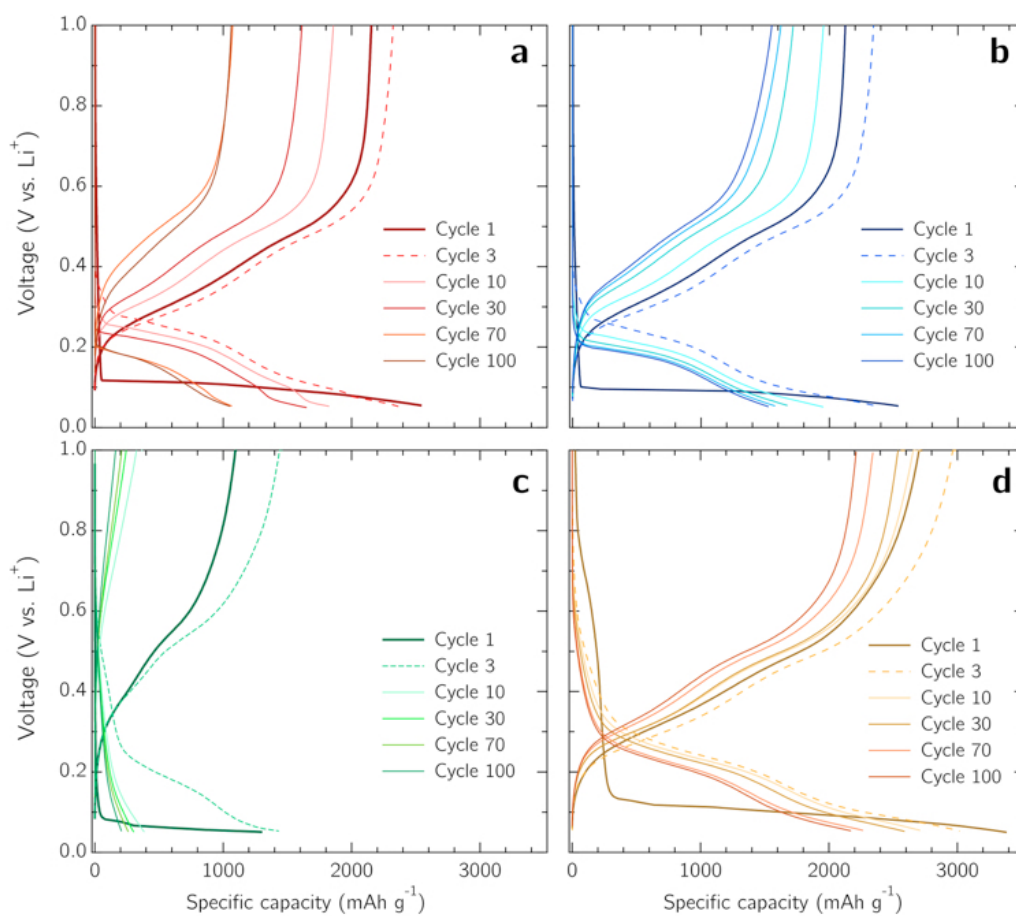
Figure 8.2: Voltage profiles of various electrolyte systems with nSi-cPAN: (a) EC/DEC ($1M$ LiPF$_6$; (b) PYR$_{13}$FSI ($1.2M$ LiFSI); (c) PYR$_{13}$TFSI ($0.6M$ LiTFSI); (d) EMIMFSI ($1.2M$ LiFSI).

stable SEI. We suggest that the breakdown of the ions present in the electrolyte solutions leads to varying SEI compositions dependent on the ionic make-up of the RTILs. We postulate that the interface formed by the decomposition products of the FSI$^-$-based IL mitigates the continuous SEI formation experienced in organic electrolyte, and this proposal is substantiated by the longer cycling life of the Si-PYR$_{13}$FSI half-cell (Figure 8.1a, blue profile), achieving an average CE of 99.97% in 200 cycles. Given the distinct incongruity of the nSi-cPAN electrode with the TFSI$^-$-based electrolyte, the decomposition mechanisms and SEI compositions resulting from ILs comprised of TFSI$^-$ and FSI$^-$ were explored using density functional theory (DFT) electronic structure methods.

8.3   Density Functional Theory Electronic Structure Analysis

Mechanisms for the reductive decomposition of the FSI$^-$ and TFSI$^-$ anions on Li metal surfaces and in bulk solution have been examined in the literature [146, 31]. Through a parallel modeling treatment in two different environments, we are able to compare potential SEI formation pathways in ILs containing both anions. The first type of theoretical study consists of cluster-based, localized basis calculations on isolated FSI$^-$ (Figure 8.3a) and TFSI$^-$ (Figure 8.3c) anions, mimicking one-electron reduction pathways in environments that do not react rapidly with the reduced species, including those inside the bulk liquid electrolyte or at cPAN interfaces. The second study consists of periodic boundary condition simulations of PYR$_{13}$$^+$/FSI$^-$ and PYR$_{13}$$^+$/TFSI$^-$ ion pairs on a Li$_{13}$Si$_4$ slab (010) surface and mimics RTIL components that may have diffused into the more reactive electrode environments. Similar initial bond-breaking pathways are obtained by both modeling treatments, thus we will focus the following analysis on the study of ion pairs on a lithiated silicon surface. A detailed description of the localized basis calculations (first modeling study) is provided in the Supplementary Information section 8.9 and depicted in Figure 8.13. In order to model our electrolyte molecules in direct contact with a pristine anode surface [31, 124], we first optimize PYR$_{13}$$^+$/FSI$^-$ and PYR$_{13}$$^+$/TFSI$^-$ ion pairs on the Li$_{13}$Si$_4$ surface (Figures 8.3e and 8.3g, respectively). The same model surface was previously studied in the context of fluoroethylene carbonate (FEC) decomposition [125] and represents a low-potential anode surface with Si directly

exposed to the liquid electrolyte, serving as an electron source that can readily reduce electrolyte molecules in its vicinity.

After the geometric optimizations, which do not lead to chemical reaction, *ab initio* molecular dynamics (AIMD) simulations were initiated at 350 K. The FSI^- anion rapidly decomposes within 1.2 ps (Figure 8.3f). The S-F bond breaks first, releasing F^- as shown in Figure 8.3b, followed by detachment of the SO_2 group which is expected to undergo further reaction with the anode surface and absorb a second electron. This rapid reaction cascade is reminiscent of the FSI^- reactions predicted on Li metal surfaces [31].

$TFSI^-$ proves to be much less reactive than FSI^-, staying intact on the $Li_{13}Si_4$ surface for 21 ps at which point it decomposes (Figure 8.3d). Neither of the two resulting fragments have a net magnetic moment, indicating that a two-electron reduction has occurred and formed $SO_2CF_3^-$ and $NSO_2CF_3^{2-}$ on the electrode surface (Figure 8.3h). This prediction correlates with the initial majority product proposed by Markevich *et al.* [146]. PYR_{13}^+ remains inert throughout all of the aforementioned simulations.

To summarize our modeling study, we find that FSI^- and $TFSI^-$ undergo quite different decomposition mechanisms upon electrochemical reduction. FSI^- rapidly releases F^-, most likely forming LiF in the SEI, in combination with the release of SO_2, suggesting the formation of an SEI composed of relatively small inorganic compounds. Contrastingly, $TFSI^-$ forms different products, including $-SO_2CF_3$ groups, at much slower timescales. While some of the latter reduced fragments may eventually yield F^- according to mechanisms proposed by Markevich *et al.* [146], slower F^- release, similar to the slow PF_6^- decomposition by organic electrolyte [124], is expected by $TFSI^-$. We speculate that the fast release of F^- and SO_2 may be correlated to the high cycling performance exhibited by the $Si-PYR_{13}FSI$ system. This argument dovetails with earlier modeling studies of FEC decomposition, which show that FEC also rapidly releases F^- to form LiF, as well as empirical data showing favorable Si half-cell cycling behavior when using FEC as an electrolyte additive in organic carbonate-based electrolyte [125].

It should be noted that FEC decomposition also releases large organic fragments [125] not
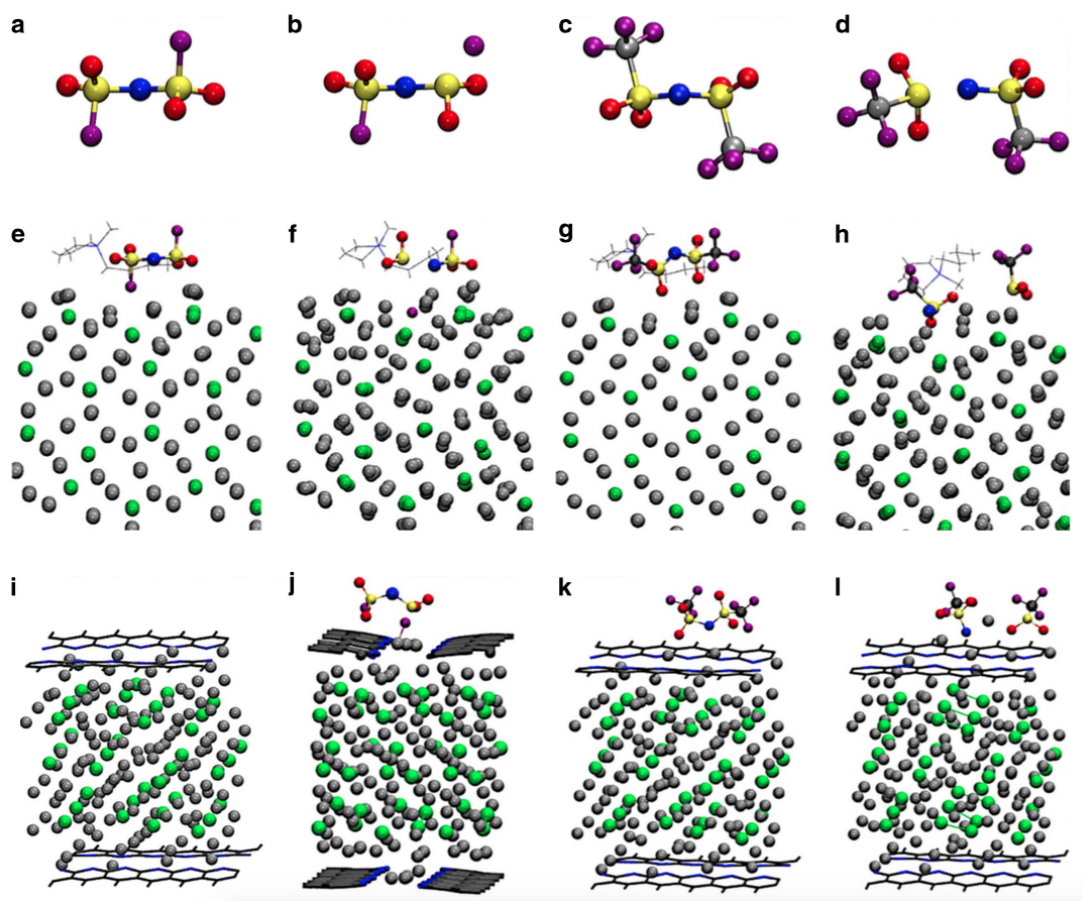
Figure 8.3: Ball and stick models of the (a) FSI$^-$ anion (b) decomposed FSI$^-$ radical di-anion, (c) TFSI$^-$ anion, and (d) decomposed TFSI$^-$ di-anion. DFT simulations of the (e) intact PYR$_{13}^+$/FSI$^-$ pair on Li$_{13}$Si$_4$, (f) decomposed PYR$_{13}^+$/FSI$^-$ pair on Li$_{13}$Si$_4$, (g) intact PYR$_{13}^+$/TFSI$^-$ pair on Li$_{13}$Si$_4$, and (h) decomposed PYR$_{13}^+$/TFSI$^-$ pair on Li$_{13}$Si$_4$. In (e-h) excess electrons on FSI$^-$ or TFSI$^-$ are not added explicitly but come from Li$_{13}$Si$_4$. Li, Si, C, O, N, S, and F atoms are depicted as silver, green, grey, red, blue, yellow, and purple spheres, respectively. The PYR$_{13}^+$ cation is shown as a grey line diagram in the background. All panels are optimized geometries except (f) and (h) which are AIMD snapshots at T=350 K.
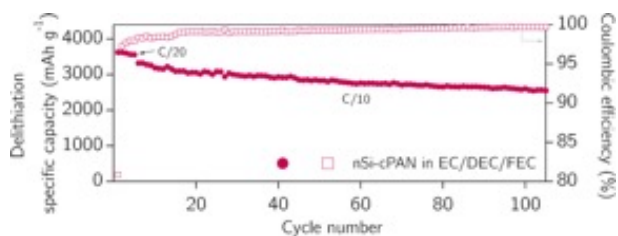
Figure 8.4: Specific capacities and coulombic efficiencies of a nSi-cPAN electrode in EC/DEC/FEC (5:70:25 vol.) (1.5M LiPF$_6$) electrolyte showing average stable coulombic efficiencies of 99.216% in 100 cycles. Although the FEC additive in a carbonate-base electrolyte does allow for further stability and higher coulombic efficiency values, these do not compare with those values obtained with the PYR$_{13}$FSI electrolyte system. Cycling was carried out at room temperature in 2032 coin-type half-cells operated between 0.005 - 1 V (vs. Li$^+$/Li).

found in the RTIL reduction pathway. Therefore, FEC and FSI$^-$ are not expected to yield identical SEI chemical compositions. To fully understand the unique role of the PYR$_{13}$FSI as an electrolyte system and SEI former, we have investigated an EC/DEC/FEC (1.5M LiPF$_6$) electrolyte system with our nSi-cPAN electrode architecture (Figure 8.4). Despite the significant improvement in half-cell CEs (average stable CE of 99.216% in the first 100 cycles) compared to the EC/DEC (1M LiPF$_6$) electrolyte, the CEs are still much lower than the PYR$_{13}$FSI electrolyte system. These results illustrate the importance of the fast release of F$^-$ for the formation of LiF in combination with the formation of oxygen and sulfur-based compounds in the proposed SEI. PYR$_{13}$FSI (1.2M LiFSI) becomes, to the best of our knowledge, the first electrolyte system to enable such high half-cell CE values with a high capacity anode material such as Si.

8.4   Characterization of Solid-electrolyte Interphase via Electron Energy Loss Spectroscopy and X-ray Photoelectron Spectroscopy

By using electron energy loss spectroscopy (EELS) to study the elemental composition of the surface of nSi-cPAN particles during cycling (16th delithiation), we further confirm our DFT predictions and gain insight into the potential elemental constitution of the proposed SEI. Figure 8.5 displays high-resolution transmission electron microscopy (HRTEM) images of the cycled/delithiated nSi-cPAN cross-section (Figure 8.5a) with EELS mapping of silicon (Figure 8.5b), carbon (Figure

8.5c), sulfur (Figure 8.5d), fluorine (Figure 8.5e), lithium (Figure 8.5f), and oxygen (Figure 8.5g). The well-defined silhouette of F coating the surface of the Si particles, in combination with the presence of Li, provides further evidence on an SEI composition containing LiF [25, 125] as proposed in literature [31] and found in our DFT simulations. Moreover, the clear mapping of O over the cPAN surface coating and evidence of S correlates with the proposed reaction of previously determined FSI^- breakdown-products, such as SO_2 and LiO [31]. Similar analysis of a conventional Si-based electrode cycled in conventional, organic electrolyte shows no specific adherence of electrolyte decomposition products around the cycled Si particles (Figure 8.6). To elucidate the precise chemical composition of the proposed SEI, X-ray photoelectron spectroscopy (XPS) is utilized to verify the chemical bonding environments of the species observed physically with EELS and simulated through DFT. Alongside our EELS characterization, Fig. 8.5 displays the deconvolution of the C 1s, S 2p, F 1s, Li 1s, and O 1s XPS spectra. Deconvolution of the C 1s spectrum shows a chemical environment consistent with that of the cyclized-PAN coating, showing the formation of ladder-like structures of thermally stable pyridine rings and conjugation of the backbone. Deconvolution of the F 1s and Li 1s spectra provide direct chemical evidence of the formation of an SEI composition containing LiF and lithium-oxygen containing species (that is, LiO, LiOH), consistent with previous studies of SEIs formed by (fluorosulfonyl)imide-based RTILs. Moreover, the deconvolution of the S 2p and O 1s spectra reveals evidence of the detachment and reaction of the SO_2 group from FSI breakdown, confirming our DFT simulation and our EELS elemental mapping, in which the presence of sulfur- and oxygen-containing species was observed. The S 2p spectrum clearly shows the presence of SO_2 and its reaction on the surface of the particles to form sulfates, sulfites and sulfides, consistent with other works. In addition to revealing the formation of sulfates, such as Li_2SO_4, and lithium-oxygen species, the deconvolution of the O 1s spectra affirms the formation of carbon-oxygen components assigned to the reaction of O with the cPAN coating, suggesting the interaction of the SEI components with the coated electrode surface.
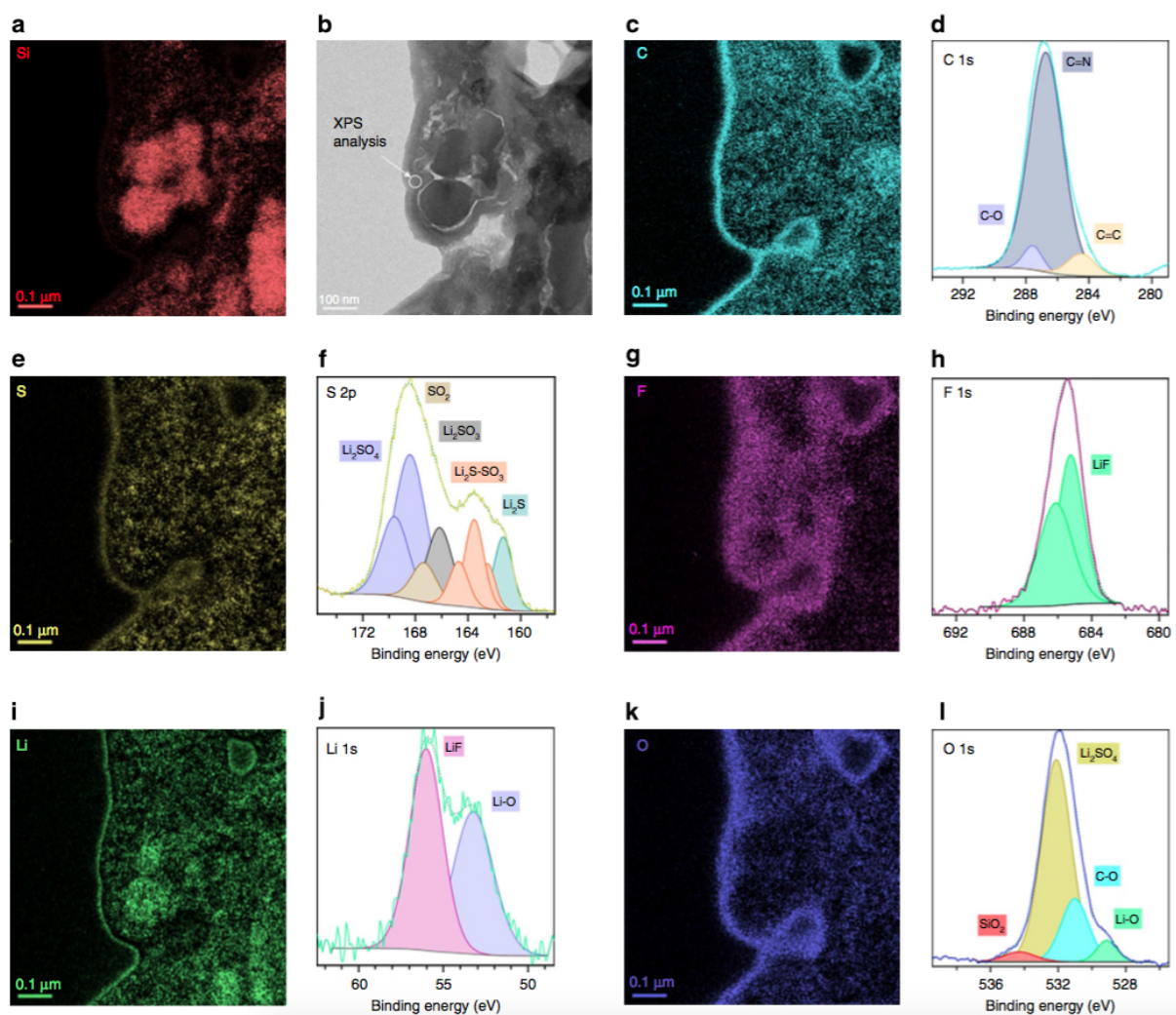
Figure 8.5: (a) TEM micrograph of cycled nSi-cPAN electrode at the 16th delithiation along with EELS elemental mapping and XPS spectra of (b) silicon, (c) carbon, (d) sulfur, (e) fluorine, (f) lithium, and (g) oxygen, defining the elemental constitution and favored nucleation sites of the SEI formed.
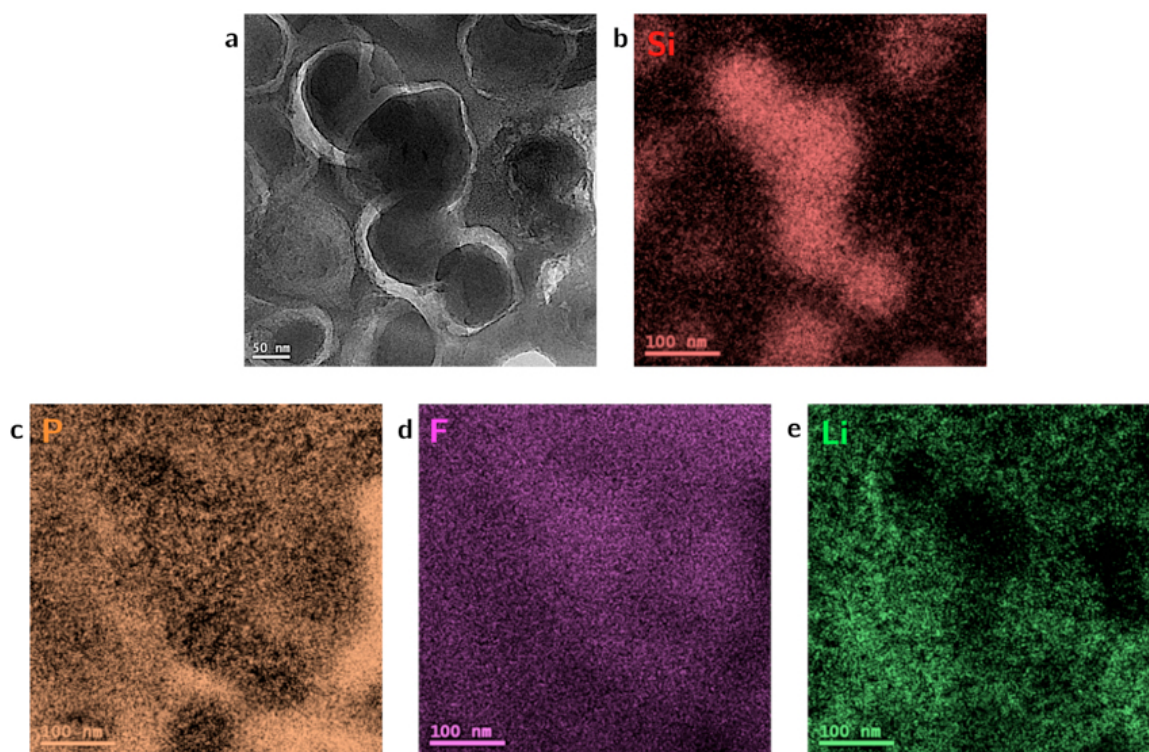
Figure 8.6: Cross-section of an electrode composed of active material (Si, 50 nm Alfa Aesar), conductive additive (acetylene black, AB), and binder (polyvinylidene difluoride, PVDF) in 60:20:20 ratio, respectively, and cycled from 0.05-1 V (*vs.* Li$^+$/Li) with EC/DEC (1M LiPF$_6$) electrolytes. (a) TEM micrograph of 20th delithiated cycled conventional Si-based electrode section along with EELS elemental mapping of (b) silicon, (c) phosphorous, (d) fluorine, and (e) lithium, defining the probable elemental constitution of the SEI formed and showing no preferential adherence onto the Si particles.

8.5 Characterization of Solid-electrolyte Interphase via Electrochemical Quartz Crystal Microbalance

In order to investigate the formation mechanism of the proposed SEI on the nSi-cPAN electrode, we turn to an examination of the mass changes on this interface during the first charge-discharge cycle using *in situ* electrochemical quartz crystal microbalance (EQCM). By monitoring mass increases and decreases on the electrode in real time during the first cycle, at which time the SEI forms its foundational structure, we gain an appreciation for the fragility of this interface in the conventional, organic electrolyte based system while further proving the mechanical resilience of the Si-RTIL interface.

Figure 8.7 conveys EQCM massograms for the nSi-cPAN initial formation cycle in both organic electrolyte (Figure 8.7a) and FSI$^-$-based IL (Figure 8.7b). Both systems reveal two very distinct behaviors during lithiation, as alluded to in our modeling study. The gradual rise in mass of about 43 μg cm^{-2} during the initial 20% of lithiation in both systems corresponds to the uptake of lithium by cPAN [172], other non-faradaic processes, and initial alloying of Li with Si.

Subsequently, the electrodes undergo rapid mass changes, attributed mainly to the decomposition of electrolyte and deposition of decomposition products on the electrode-electrolyte interface. The onset of these rapid mass changes are visible in the voltage trace of each system through the "potential overshoot" phenomenon, a known artifact of electrolyte decomposition in EQCM experiments (further explained in the Supplementary Information section 8.9) [180]. The onset of this rapid mass change occurs earlier (20.5% lithiation) and at a significantly higher rate (reaching *73 g mol^{-1} of e$^-$* at 57.8% lithiation) in conventional organic electrolyte. Mass change per mol of electrons (m.p.e., *g mol^{-1} of e$^-$*) values were extracted from data in Figure 8.8 and a more detailed analysis is provided in the Supplementary Information. This is owed to the lower electrochemical stability of the conventional organic electrolyte as compared to the PYR$_{13}$FSI system, which has a voltage stability window of 7.31 V (*vs.* Li$^+$/Li) [57]. The higher average m.p.e. in the conventional electrolyte system, along with the very slow F$^-$ release during EC/DEC (1M LiPF$_6$) decomposition
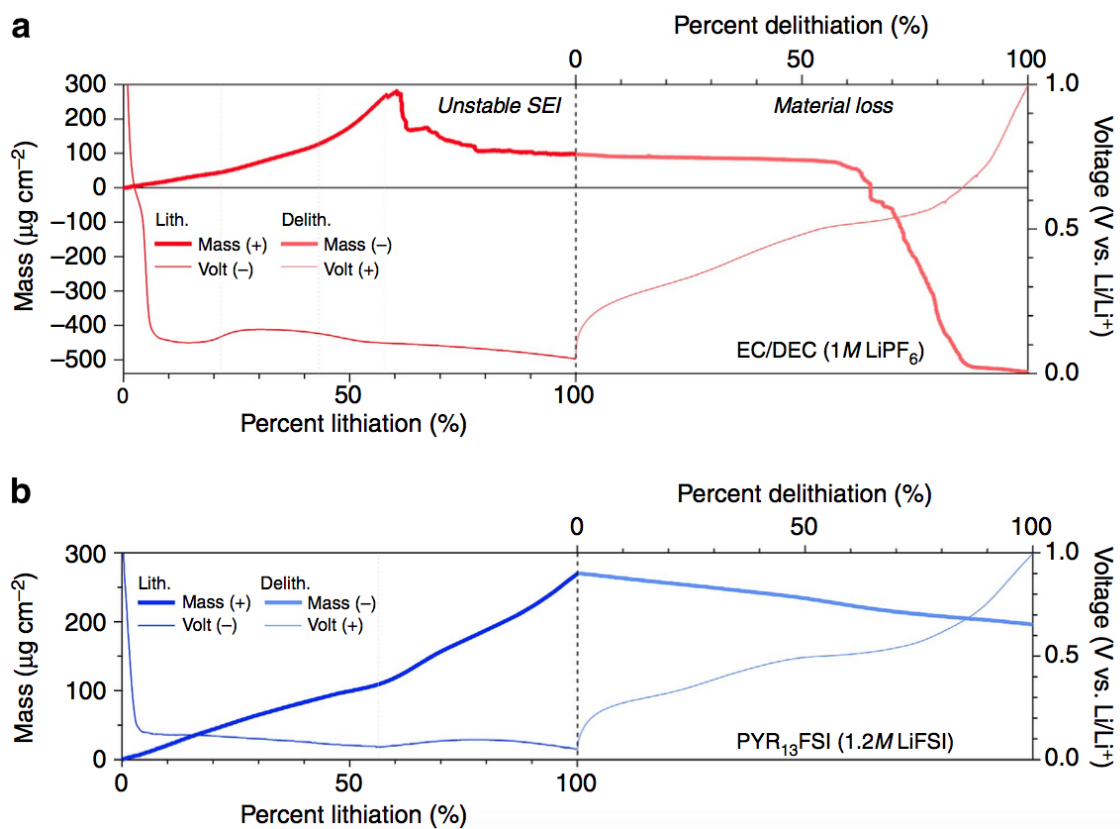
Figure 8.7: EQCM massograms obtained during the initial SEI formation cycle for the nSi-cPAN electrodes cycled in (a) conventional organic electrolyte and (b) $PYR_{13}FSI$ ($1.2M$ LiFSI) electrolyte, along with the voltage traces corresponding to each system.

as proposed in literature [124], suggests the formation of an SEI composed primarily of broken-down organic molecules. Conversely, the controlled mass gains, lower average m.p.e. (reaching *25 g mol^{-1}of e$^-$* after 56% lithiation and raising to *33 g mol^{-1}of e$^-$* toward the end of lithiation), and fast release of F$^-$ and SO$_2$, as demonstrated earlier in this work, of the PYR$_{13}$FSI (1.2M LiFSI) electrolyte throughout lithiation substantiates our prediction of the formation of an SEI comprised of relatively small inorganic compounds such as LiF and other sulfur and oxygen-containing species.

After reaching a critical mass of 282 μg cm^{-2}, the mass of the Si-conventional organic electrolyte system crashes. The crash in mass could be caused by a number of factors, including the severe volume expansion known to occur in this system causing breakage of the electrode matrix, and the build-up and rupturing of an unstable interfacial layer. During delithiation, contraction of the nSi-cPAN composite leads to further breakage of the electrode matrix and material loss. The inability of this system to exhibit stable mass changes corresponds to the incompatibility of Si with conventional electrolyte. Contrastingly, the Si-RTIL system massogram exhibits more gradual mass growth and loss, with approximately 73% of the mass gained during initial lithiation remaining after delithiation. We attribute this behavior to the irreversible formation of a stable interfacial layer on the Si electrode, manifesting stable cycling and high CEs throughout an impressive cycling life.

8.6 Material Microstructure and Electrode Morphology Characterization

While the theoretical and experimental data described provide insight into the formation mechanism and composition of the proposed SEI, we turn to a more comprehensive imaging examination to develop a direct understanding of the morphological effects of the PYR$_{13}$FSI electrolyte on our Si-based electrode. Consistent with our previous work [174], EELS and TEM reveal a thin, conformal coating of PAN on the nano-Si particles throughout the uncycled composite (Figure 8.9a and 8.9b). Our previous work verified the mechanical advantages of the cPAN coating by analyzing electrode cross-sections at different stages of cycle life, finding an overall electrode volumetric expansion of only 40% after full initial lithiation with an EC/DEC (1M LiPF$_6$) electrolyte [174]. Through the same treatment of electrode cross-section samples taken before (Figure 8.9c) and after
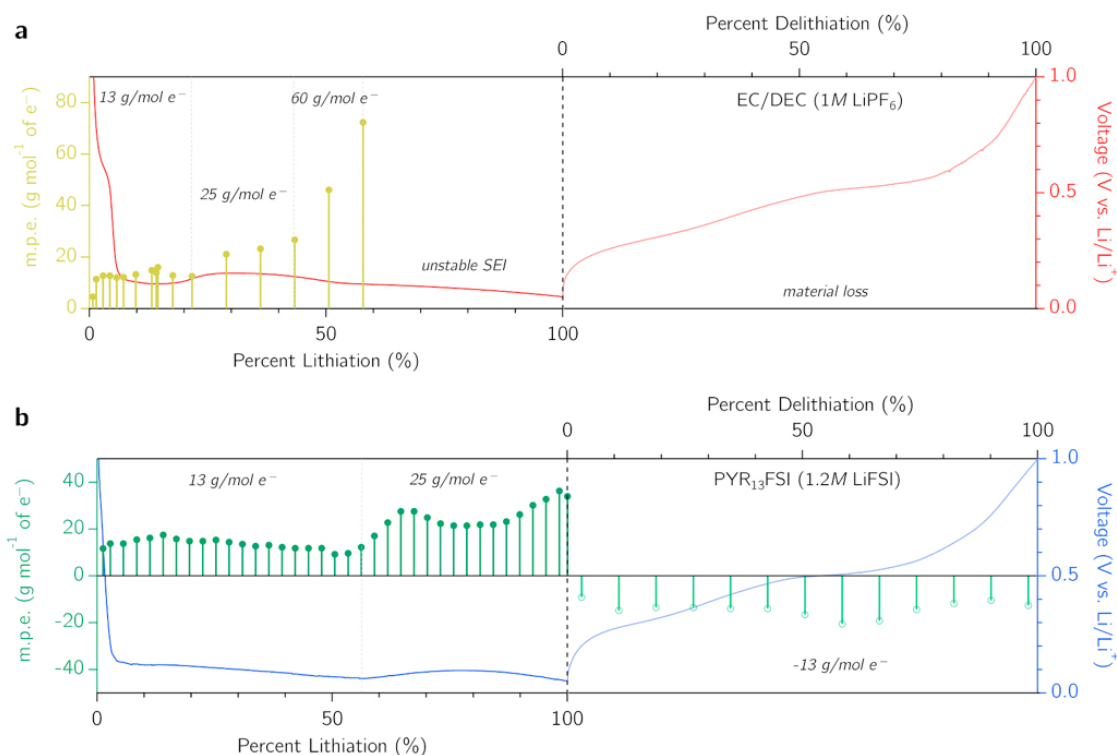
Figure 8.8: EQCM m.p.e. data obtained during the initial SEI formation cycle for the nSi-cPAN electrodes cycled in (a) conventional organic electrolyte and (b) $PYR_{13}FSI$ ($1.2M$ LiFSI) electrolyte, along with the voltage traces corresponding to each system. The m.p.e. data has been segmented (grey dotted lines) between points of onset of different rates of mass change and these average values are depicted within each system's plot. Initial average m.p.e. values observed for both conventional electrolyte and FSI-based IL, *13 g mol^{-1} of e$^-$*, is attributed to Li$^+$ uptake by cPAN, other non-faradaic processes, and initial alloying of Li and Si. After this initial state the difference in m.p.e. values between both systems are true to each system's ability to lithiate-delithiate the nSi-cPAN electrodes and form a stable interfacial layer. Of note is the average *25 g mol^{-1} of e$^-$* m.p.e. found in the lower voltage region of the discharge trace in RTIL electrolyte, corresponding well with the formation of LiF compounds, and the raise to *33 g mol^{-1} of e$^-$* m.p.e. toward the end of lithiation, corresponding well with the incorporation of S-containing decomposition fragments.

(Figure 8.9d) initial lithiation in a $PYR_{13}FSI$ ($1.2M$ LiFSI) electrolyte, we find the volumetric expansion of the nSi-cPAN composite to be just 17%. To further investigate this remarkable volume control, TEM micrographs were taken upon initial lithiation (Figure 8.9e and 8.9f) and after the 16th delithiation (Figure 8.9g and 8.9h). The TEM images of both the fully lithiated and cycled electrodes show no mechanical deficiencies or morphological changes within the Si particles or the composite structure. Most notably, after the 16th delithiation the Si-$PYR_{13}FSI$ system exhibits no severance of connection between the Si particles and cPAN network with striking preservation of the nano-Si's spherical shape, contrasting the relatively poor nano-structural preservation of the same electrode in conventional electrolyte [174]. The impressive structural integrity of the Si-$PYR_{13}FSI$ system is undoubtedly linked to the system's cycling stability, suggesting that the Si-RTIL interface concurrently promotes favorable electrochemistry and structural resilience.

8.7   Electrochemical Characterization of Full-cells

As previously mentioned, the ultimate goal of much electrochemical materials research is to incorporate high capacity electrodes into a lithium-ion full-cell. Up to this point in our study, we have provided in-depth characterization of the Si-$PYR_{13}FSI$ system and proposed a mechanism for the system's stability through a remarkably robust SEI. The most dependable means of substantiating our claim of a stable SEI is to demonstrate the long-term cycling of a full-cell incorporating the Si-$PYR_{13}FSI$ system. Combining this work and our previous study of the compatibility between $PYR_{13}FSI$ electrolytes and the L333 cathode chemistry [57], we have built nSi-cPAN/$PYR_{13}FSI$ ($1.2M$ LiFSI)/L333 LIBs capable of maintaining high energy-densities for an exceptionally long cycling life (see Appendix for details on full-cell fabrication).

Figure 8.10a compares the performance of nSi-cPAN/L333 full-cells assembled with conventional EC/DEC ($1M$ $LiPF_6$) and $PYR_{13}FSI$ ($1.2M$ LiFSI) electrolytes. Both cells presented in Figure 8.10a contain the same electrode mass loading on both cathode and anode (within 10%) and were operated and controlled under the same parameters for fair comparison. All of the full-cells presented in this work were preconditioned to accurately control the amounts of Li in the cell
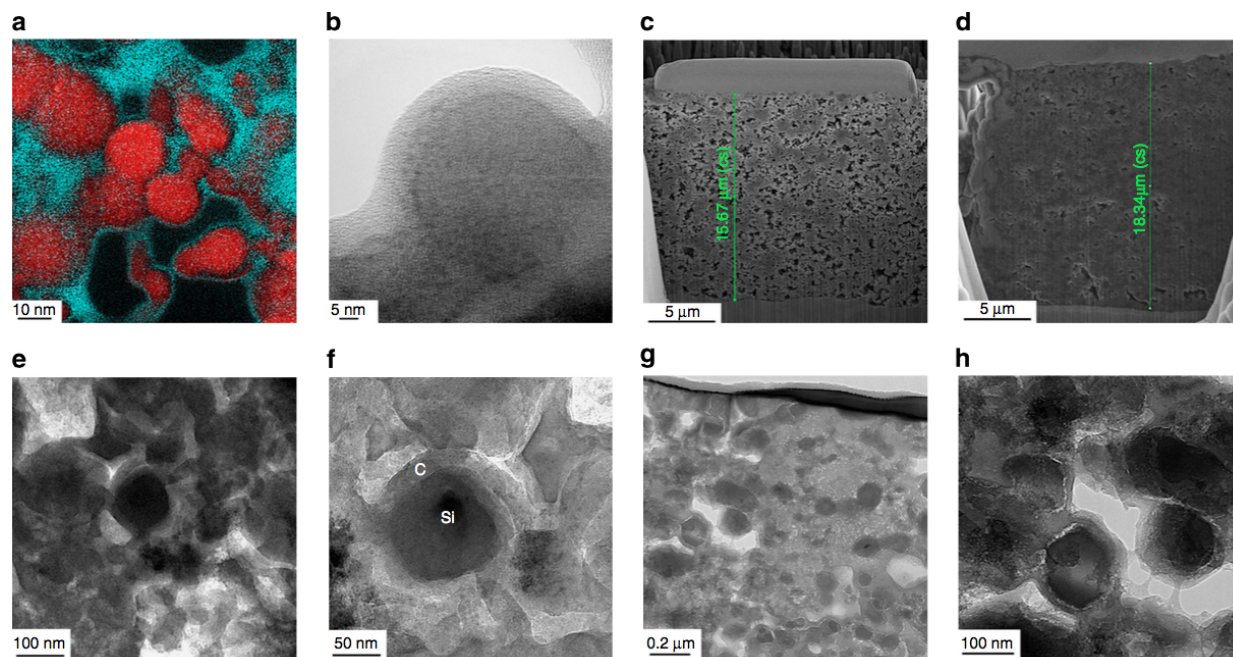
Figure 8.9: (a) EELS elemental mapping of carbon (cyan) and silicon (red) and (b) TEM micrograph of the pristine nSi-cPAN electrode reveal a thin, conformal coating of PAN on the nano-Si particles throughout the uncycled composite. (c, d) FESEM images of electrode cross-sections before (c) and after (d) initial lithiation showing an electrode volume expansion of only 17%. (e-h) TEM micrographs of fully lithiated (e, f) and 16th delithiated (g, h) nSi-cPAN electrodes showing no mechanical deficiencies or significant morphological changes.
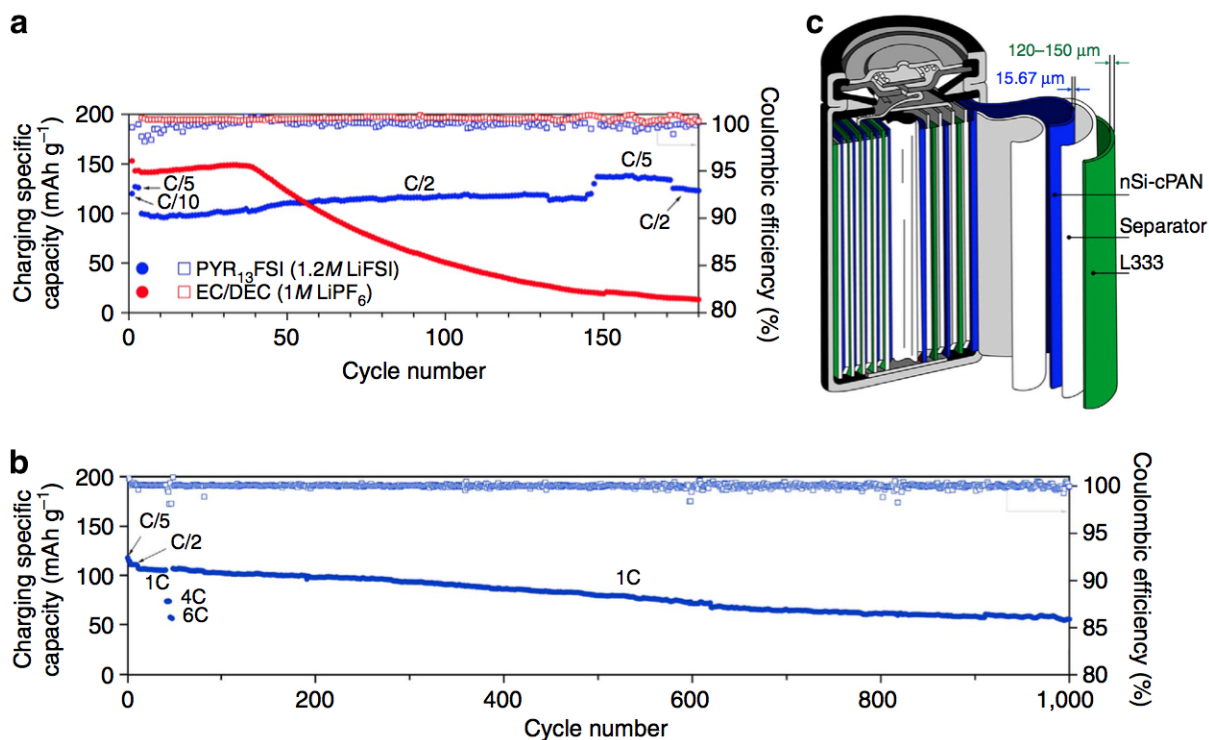
Figure 8.10: (a) Specific charge capacities and coulombic efficiencies of nSi-PAN/L333 full-cells assembled with PYR$_{13}$FSI (1.2M LiFSI) and conventional EC/DEC (1M LiPF$_6$) electrolytes. (b) nSi-cPAN/PYR$_{13}$FSI/L333 full-cell rate study and long term cycling. (c) Mock-up of a commercial 18650 cell showing the possibility of incorporating more electro-active material due to the relatively thin nSi-cPAN electrode. Cycling was carried out at room temperature in 2032 coin-type half-cells operated between 2.0-4.15 V (*vs.* Li$^+$/Li).

and state of charge of the electrodes (see *Appendix A* for details on full-cell fabrication), allowing for accurate comparison between cells. Initial charge capacities of 143.21 mAh g^{-1} and 127.10 mAh g^{-1} (all full-cell specific capacities are normalized with respect to total active material mass) were observed at the $C/5$ rate for the EC/DEC ($1M$ LiPF$_6$) and PYR$_{13}$FSI ($1.2M$ LiFSI) LIBs, respectively. The difference in initial capacity is attributed to the higher resistance of the RTIL electrolyte, though this limitation is countered by unparalleled cycling stability. After 35 cycles, the cell cycled in carbon-based electrolyte degrades rapidly. The degradation, ascribed to low half-cell CEs with an average irreversible charge loss of 2.31% per cycle (Figure 8.1a, red profile), occurs as the system exhausts its supply of Li through continuous SEI breaking and reformation. Contrastingly, the cell cycled in PYR$_{13}$FSI ($1.2M$ LiFSI) electrolyte shows remarkable stability, attributed to the high half-cell CEs, with an average irreversible charge loss of just 0.076% for the first 100 cycles (Figure 8.1a, blue profile) followed by negligible Li consumption, providing an average charge capacity of 110.98 mAh g^{-1} at a rate of $C/2$ (Figure 8.10a, blue profile). To further investigate the SEI stability of the Si-PYR$_{13}$FSI system, a full-cell was cycled for longevity with a brief rate study. Figure 8.10b depicts the nSi-cPAN/PYR$_{13}$FSI ($1.2M$ LiFSI)/L333 cell run for 1000 cycles delivering 107.33, 74.70, and 58.26 mAh g^{-1} at rates of $1C$, $4C$, and $6C$, respectively (1C rate capacity value pertains to the average of the first 40 cycles at this rate).

8.8 Summary and Conclusions Regarding RTIL Enabled Si

It is noted that the PYR$_{13}$FSI RTIL strengthens the performance of a range of previously developed Si-based anode architectures, not just those containing PAN (Figure 8.11). Moreover, preliminary study of the high-temperature performance of the Si-RTIL system has also yielded promising results (Figure 8.12), suggesting that the SEI formed by PYR$_{13}$FSI is stable even at elevated temperature. It is understood that the overall energy-density of LIBs is limited by the capacity of the positive electrode. While this study demonstrates a significant advancement in the study of LIB anode materials, a high-capacity cathode compatible with the Si-PYR$_{13}$FSI pair should be developed to truly realize the benefits of the system. In spite of limitations introduced

by the battery's cathode capacity, we propose that introducing the Si-PYR$_{13}$FSI system into a commercial 18650 cell configuration, as shown in Figure 8.10c, would allow for incorporation of more electro-active material due to the relatively thin nSi-cPAN electrode. Based on a commercial battery with a 2 mAh cm^{-2} areal capacity and nominal voltage of 3.6 V, utilizing the nSi-cPAN electrode, which is less than 1/4 the thickness of a conventional graphite electrode and needs less than 1/5 electro-active material to achieve similar battery capacities, would allow for at least a 35% increase in battery capacity and thus the production of a higher energy-density LIB. Validated by impressive cycling data and a combination of theoretical and experimental results, our approach to developing a stable high energy-density anode-electrolyte system represents important progress towards a safer, higher-performance secondary LIB.

8.9   Supplementary Characterization of the Si-RTIL Interface

Modeling Study 1: Single-Electron Reductions of FSI$^-$ and TFSI$^-$ in Bulk Liquid Electrolyte

The first type of theoretical study consists of cluster-based, localized basis calculations on isolated FSI$^-$ (Figure 8.13a) and TSFI$^-$ (Figure 8.13b) anions coordinated to Li$^+$ and "solvated" in a dielectric continuum which approximates the effect of the ionic liquid around them. These mimic one-electron reduction pathway(s) in bulk liquid electrolyte, which should occur when the electron transfer rate is slowed by the initial SEI formation.

Adding an excess electron to the dielectrically solvated Li$^+$(FSI$^-$)$_2$ cluster spontaneously leads to the loss of F$^-$ from the resulting FSI^{2-} radical di-anion in geometry optimization calculations (Figure 8.13c), in agreement with the first reaction step in Ref. [31]. Injecting an e^- into Li$^+$(TFSI$^-$)$_2$ and performing geometry optimization decomposes the resulting TFSI^{2-}, yielding the two fragments shown in Figure 8.13d: SO$_2$CF$_3$$^-$ and NSO$_2$CF$_3$$^-$. The latter is a radical anion. Our predictions for TFSI$^-$ agree with the first reaction step proposed in Ref. [146], where the calculations were performed on an isolated TFSI$^-$ without Li$^+$. The predictions are similar when the hybrid PBE0 functional is used. Two FSI$^-$ or TFSI$^-$ are used in these calculations to give 4-coordinated Li$^+$. Adding one excess electron to Li$^+$FSI$^-$ or Li$^+$TFSI$^-$ clusters leads to the
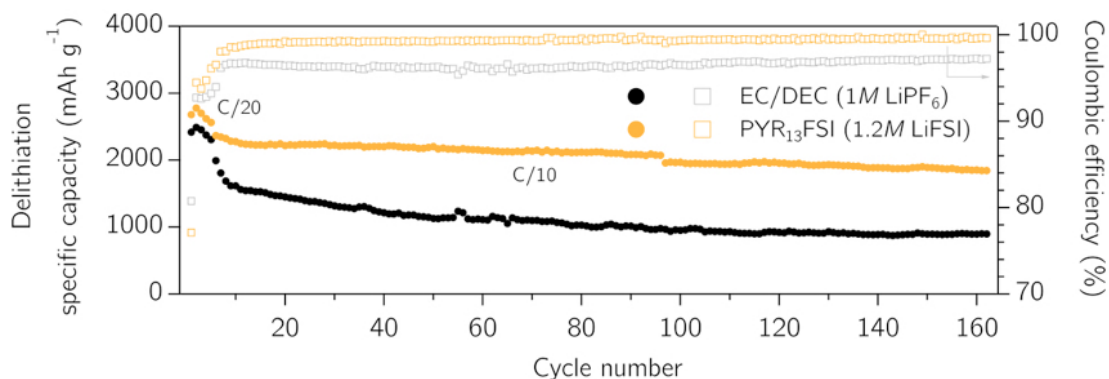
Figure 8.11: An electrode composed of active material (Si, 50 nm Alfa Aesar), conductive additive (acetylene black, AB), and binder (polyvinylidene difluoride, PVDF) in 60:20:20 ratio, respectively, is heat treated at 300°C (for improved performance of PVDF binder) [129] and cycled from 0.05-1 V (vs. Li$^+$/Li) with EC/DEC (1M LiPF$_6$), black profile, and PYR$_{13}$FSI (1.2M LiFSI), orange profile electrolytes. Consistent with the results found with the nSi-cPAN/PYR$_{13}$FSI system, a faster capacity stability is observed, with an average stable charge capacity of 2065.77 mAh g^{-1} for 160 cycles along with an average CE of 99.377% for the conventional Si-based electrodes ran with PYR$_{13}$FSI electrolyte. This compares with an average stable specific capacity of 1092.19 mAh g^{-1} along with an average CE of 96.553% for the conventional Si anodes ran with EC/DEC electrolyte. The performance improvement and high CE achieved with PYR$_{13}$FSI IL system is attributed to the highly stable SEI formed, which again shows to maintain high capacities suggesting electrode mechanical conservation throughout cycling.
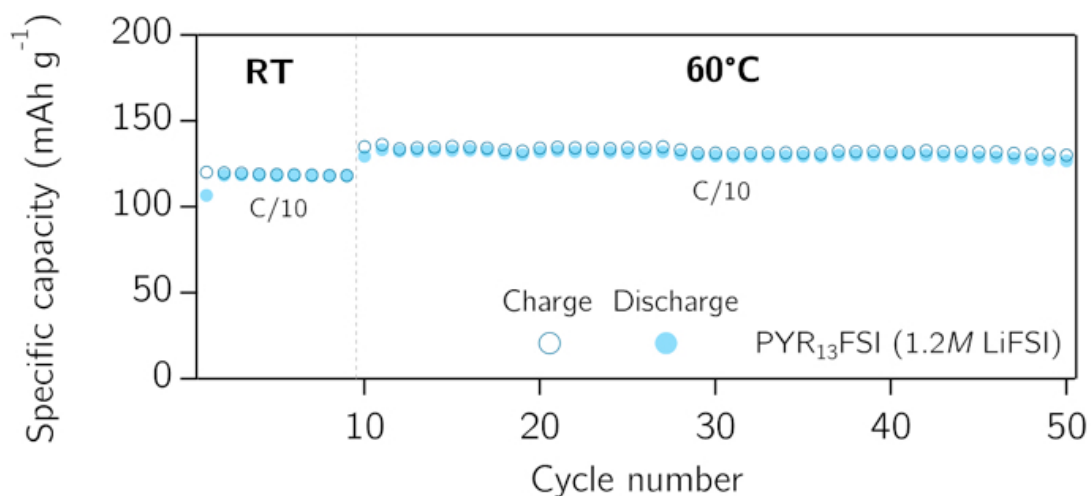
Figure 8.12: Specific charge capacities of a nSi-PAN/L333 full-cell assembled with PYR$_{13}$FSI (1.2M LiFSI) and cycled at 60°C. The cell was cycled preconditioned for 9 cycles at room temperature (RT) and then taken up to 60°C for subsequent cycles. This preliminary cycling data suggests SEI formed by PYR$_{13}$FSI is stable even at elevated temperature.

unphysical reduction of the under-coordinated Li^+ to Li^0.

Note: The above are single-excess-electron based, static calculations that are agnostic about reaction kinetics or electron transfer rates.

Electrochemical Quartz Crystal Microbalance (EQCM): Potential Overshoot and Mass per Mole of Electron (m.p.e.) Analysis

The mentioned "potential overshoot" phenomenon has been observed in previous studies using both organic and IL based electrolytes in coin-cell and EQCM flooded cell set-ups. It has been seen on vapor deposited SiO_x films as well as on amorphous SiO slurries imbedded within a polymer matrix [199, 180, 159]. The overshoot is generally attributed to nucleation of Li_2O and other decomposition products as the native oxide on the silicon film is reduced as in Equation 8.1 [180].

$$SiO_x + 2xLi^+ + 2xe^- \longrightarrow xLi_2O + Si \tag{8.1}$$
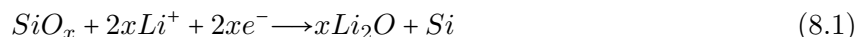
As alluded to in the main text, m.p.e. values can be used to infer reaction products being adsorbed on the electrode. While the following analysis offers a tentative explanation of the mechanistic aspects of our EQCM experiments and the m.p.e. data, future work will focus on an in depth and thorough study of the reactions and molecular interactions on the Si-RTIL interface, as observed in this paper. The m.p.e. values are calculated by dividing the mass increase by the passed charge and multiplying by Faraday's constant. The m.p.e. values plotted in Figure 8.8 are averages taken periodically over the course of the SEI formation steps. In the case of an already oxidized Si surface, reduction by Li would give a m.p.e. of *6.9 g mol^{-1} of e$^-$* (that of pure Li deposition or insertion). If the oxygen is pulled from the solvent, the overall m.p.e. would be *14.9 g mol^{-1} of e$^-$* (molecular weight of Li_2O divided by 2 moles of electrons). For the organic electrolyte the overshoot at 20% lithiation, observed as a significant increase in potential in the voltage trace, gives rise to an even more rapid spike in m.p.e. until certain stresses in the system cause a sudden drop in mass around 58% lithiation. The m.p.e. values for the organic run suggest that as the
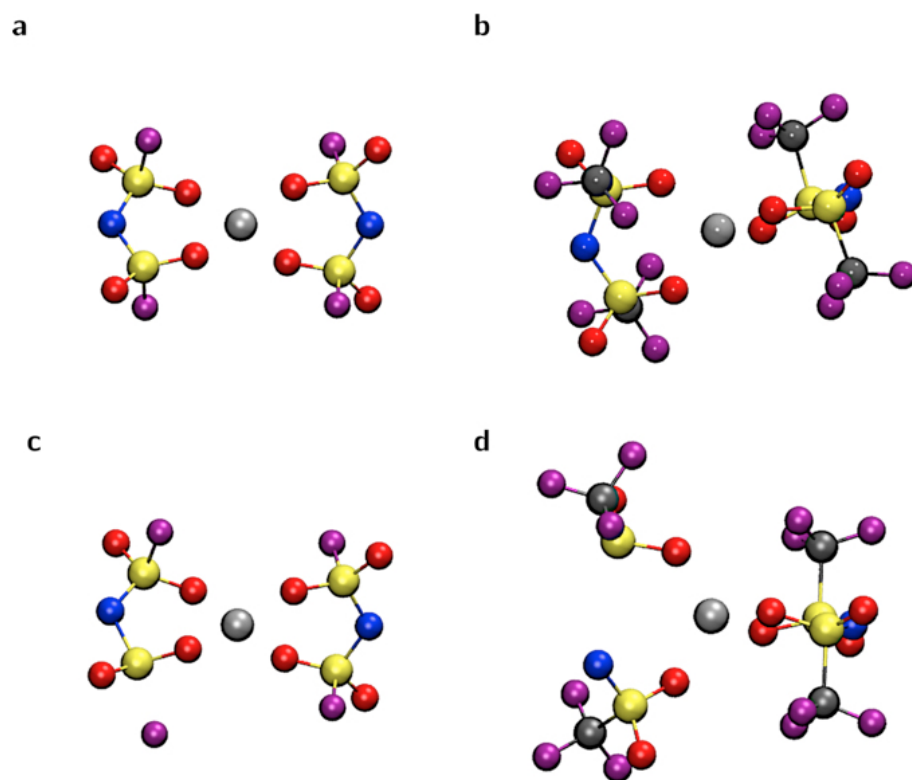
Figure 8.13: (a) Li$^+$(TFSI$^-$)$_2$; (b) adding an excess electron to (a) spontaneously decomposes a resulting FSI$^-$ radical di-anion; (c) Li$^+$(TFSI$^-$)$_2$; (d) adding an electron to c decomposes the resulting TFSI$^-$ di-anion.

potential is driven more negative the decomposition pathways move from Li_2O formation to ethylene carbonate adsorption and decomposition (perhaps as described by Martinez *et al.*) [147], and finally to decomposition of phosphorous and fluoride species from $LiPF_6$ (as described by Ryu *et al.*) [180]. Further work would be required to validate these claims, but the initial data is promising in terms of understanding what components are producing the organic derived SEI layer and why it is inherently unstable with the Si based electrode.

The potential overshoot that correlated with Li_2O formation for the RTIL electrolyte was a much smaller overshoot, if indeed an overshoot is present at around 0.12 V, than that observed when the potential reached 0.06 V. At this point, a significant rise in the potential also saw a rise in the mass gain slope (i.e., m.p.e. values). Just prior to the rise, m.p.e. values hovered around or below *9 g mol^{-1} of e$^-$*. Subsequently, the m.p.e. values rose toward, and leveled off around, *25 g mol^{-1} of e$^-$* suggesting, nucleation of LiF. This supports the EELS measurements as well as the computational simulations which suggest the S-F bond is the first to be cleaved as FSI^- undergoes decomposition. It also supports our modeling study and previous findings by Budi *et al.*, with regards to the reactivity of FSI^- in the presence of Li metal [31]. A small dip down to about *20 g mol^{-1} of e$^-$* likely indicates a weighted average of LiF as well as lighter products like LiO, and perhaps more Li_2O. Finally, toward the end of the SEI formation step, m.p.e. values climbed no higher than *33 g mol^{-1} of e$^-$* possibly indicating the incorporation of S containing decomposition fragments. This would make sense, considering these fragments are thought to be the final decomposition products remaining when FSI^- reacts with Li [31].

8.10   Notes

Daniela Molina Piper and Tyler Evans contributed equally to the work presented in this chapter.

Chapter 9

Optimized Silicon Electrode-architecture, -interface, and -micro-geometry for Next-generation Lithium-ion Batteries

Summary

Our previous work demonstrated the success in simultaneously addressing the two afore-mentioned issues by pairing a robust, yet simple, electrode-architecture with a room temperature ionic liquid electrolyte (RTIL or IL) to create a highly favorable Si-electrolyte interface [170]. The study highlighted the groundbreaking demonstration of the cycling of a full-cell incorporating a Si anode by using a $PYR_{13}FSI$ ($1.2M$ LiFSI) electrolyte with an unprecedented cycling life. A combinatorial approach involving a mechanically resilient electrode-architecture [173] merged with an electrolyte capable of forming a favorable SEI was the solution to incorporate structural integrity with stable interfacial chemistry in a bulk-type Si anode [170]. While this study validated an unconventional approach to enabling the Si anode, one issue remains to be solved: optimization of the Si electrode-micro-geometry.

9.1   Introduction

In this study, we aim to optimize the performance of the Si-RTIL system through the implementation of a new electrode-micro-geometry. The incorporation of 1D silicon nanowires (SiNW) into the cyclized-polyacrylonitrile (cPAN) based electrode-architecture allows for greatly improved active material utilization, higher rate capabilities, and reduced interfacial reactions. Both nanoparticles and nanowires allow for better accommodation of large volumetric changes [139] while also

shortening lithium-ion diffusion pathways. However, only the utilization of the micro-geometry created through incorporation of Si nanowires allows for the unique properties such as high aspect ratios, direct 1D electronic and ionic pathways along the materials axial direction, and improved inter-particle (wire) contact area [104, 221, 220].

9.2   Morphological Characterization

The SiNW micro-geometry suits the necessary physical parameters required to improve active material utilization, rate capability, and enhance secondary surface reactions at initial cycling. Focused ion beam (FIB) cross-sectioning and transmission electron microscopy (TEM) were utilized to characterize the morphology of SiNW-cPAN electrode-architecture and -micro-geometry. Figure 9.1 shows a comprehensive imaging examination of the uncycled SiNW-cPAN electrodes. Field emission scanning electron microscopy (FESEM) images of FIB cross-sections (Figure 1a-c) and TEM analysis (Figure 1e and 1f) reveal the characteristic properties of a Si-cPAN electrode-architecture. The active SiNW material, is randomly dispersed and well coated by a thin, robust and conductive cPAN film [173]. However, the electrode-micro-geometry here differs drastically from our previous works utilizing nano-spherical Si (nSi) [170, 173]. FIB cross-sections show honeycomb-like clusters (Figure 1c and 1d) of SiNW-cPAN. There are clear contacts between the SiNWs along their axial direction, which is not possible with the Si nanoparticle micro-geometry, as spherical materials are limited to inter-particle point contacts. The highly enhanced levels of material interconnectivity, bound and protected with a robust and conductive cPAN coating, create an intimately linked framework that not only connects all of the SiNWs throughout the electrode, but also allows for deep and fast penetration of the relatively viscous $PYR_{13}FSI$ ($1.2M$ LiFSI) electrolyte through the highly porous electrode framework. The micron- and nano-sized pores allow effective electrolyte access to all of the SiNWs in the electrode, and the enhanced interconnectivity provided by the SiNW geometry allows for the full electrochemical utilization of the Si material.
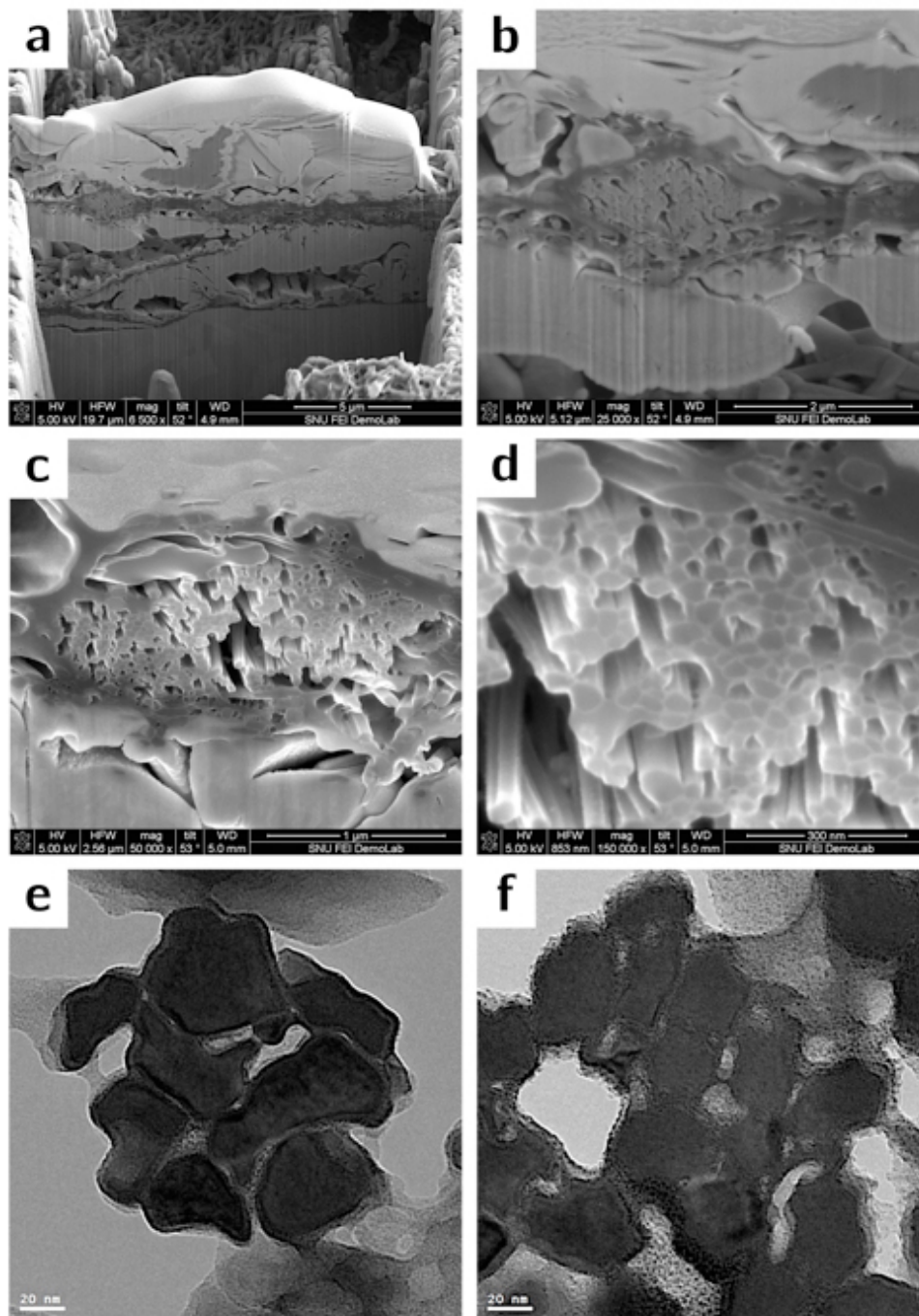
Figure 9.1: a-d) FESEM images of electrode cross-sections showing the unique electrode-micro-geometry and honeycomb-like clusters of SiNW-cPAN. (e), (f) TEM micrographs of an uncycled SiNW-cPAN electrode revealing the characteristic properties of a Si-cPAN electrode-architecture.

9.3   Electrochemical Characterization

Electrochemical characterization was utilized to study the ability of the SiNW-cPAN electrode-micro-geometry to improve the cycling performance of the high capacity Si material. Figure 9.2 presents the half-cell cycling stability and CEs of the SiNW-cPAN electrodes cycled under galvanostatic conditions in both $PYR_{13}FSI$ ($1.2M$ LiFSI) and commercial EC/DEC ($1M$ $LiPF_6$) electrolytes. The results demonstrate the exceptional cycling stability, retaining capacities over 1700 mAh g^{-1} over 700 cycles, and high CEs of the SiNW-cPAN anode (green profiles) cycled in $PYR_{13}FSI$ ($1.2M$ LiFSI). The high CEs manifested in the $PYR_{13}FSI$ ($1.2M$ LiFSI) electrolyte stabilize after only 2 cycles, with a first cycle CE of 85.03%. Such outstanding cycling data contrast that of the cycling behavior of the SiNW-cPAN in conventional EC/DEC ($1M$ $LiPF_6$) electrolyte, which reveals fast initial degradation between cycle 1 and cycle 100, low CEs that dont stabilize until nearly 200 cycles, and capacities of only 837.4 mAh g^{-1} after 500 cycles (brown profiles).

The unparalleled cycling performance and high CEs of the SiNW-cPAN/$PYR_{13}FSI$ system are attributed to the pairing of a superior electrode-micro-geometry and the formation of a highly stable SEI, further validating our previous work [170]. However, with this works improved electrode-micro-geometry we achieve incredibly fast CE stabilization and higher capacities. The SiNW-cPAN micro-geometry allows for reduced surface reactions around SiNW clusters, resulting in the creation of a favorable SEI within just 2 cycles, while the interconnectivity within the clusters leads to a high degree of active material utilization. The porous architectural framework observed in the SiNW-cPAN electrodes (Figure 1) permits maximum electrolyte penetration, reaching all active material sites of the electrode for average capacities of over 2800 mAh g^{-1} in 200 cycles compared to only 2048 mAh g^{-1} in our previous work [170].

Moreover, the SiNW-cPAN micro-geometry shows to be robust enough to allow for reversible expansion and contraction without mechanical deficiencies. This is impressive given the full penetration of the electrolyte and high levels of active material utilization. Figure 2b and 2c show an FESEM image of FIB cross-section and TEM micrograph after the 16th delithiation, respec-
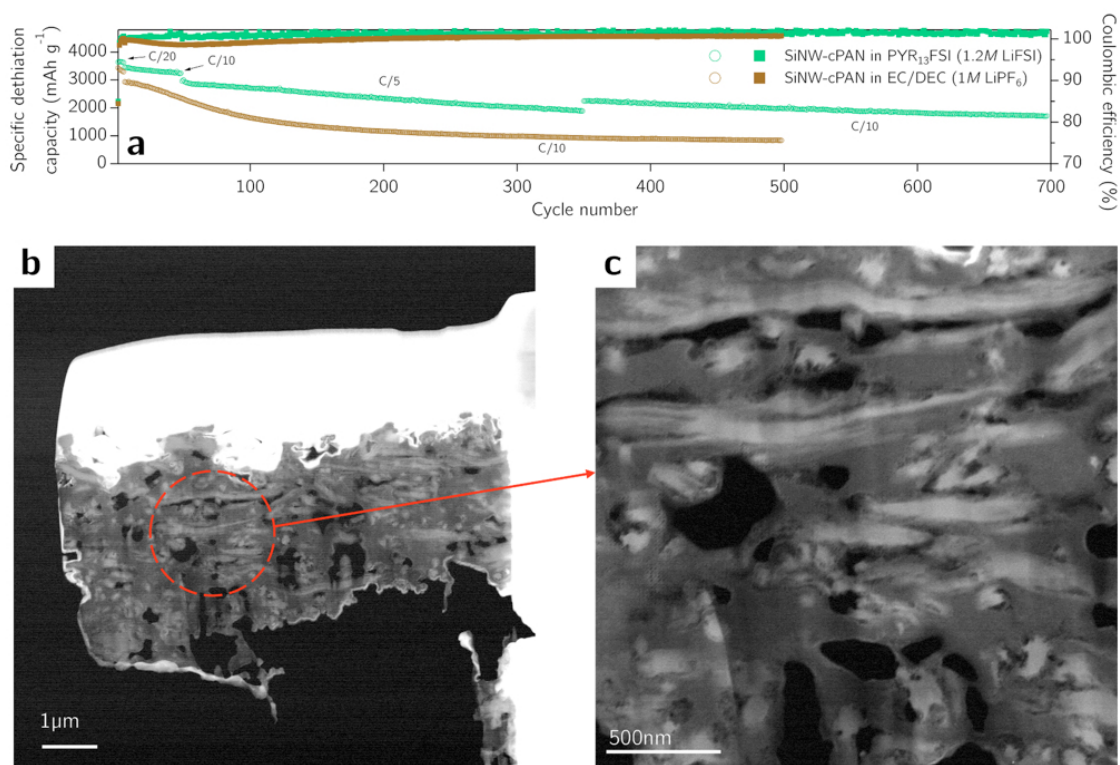
Figure 9.2: (a) Half-cell cycling stability and coulombic efficiencies of the SiNW-cPAN electrodes cycled under galvanostatic conditions in both PYR$_{13}$FSI (1.2M LiFSI) and commercial EC/DEC (1M LiPF$_6$) electrolytes. (b) and (c) TEM micrograph of 16th delithiated SiNW-cPAN electrode showing mechanical reversibility and maintenance of the electrode-micro-geometry.

tively, demonstrating electrochemical and mechanical reversibility of the electrode-micro-geometry as it maintains its porous structure upon delithiation and still shows its original scaffolding-like micro-geometry (Figure 9.3). This Si electrode-architecture, -interface, and -micro-geometry is the optimal combination to achieve stability, reversibility, and high capacities.

Another predictable advantage of the SiNW micro-geometry is enhanced electrochemical rate performance given the ability of 1D nanowires to efficiently conduct charge and the axial interconnectivity within the SiNW-cPAN clusters. In order to explore the rate performance of the SiNW-cPAN micro-geometry, an asymmetric rate study was conducted to focus on the high lithiation rate capability of the electrode at room temperature. This study is particularly relevant considering the commercial demand for supercharging batteries or achieving full charge of a battery in very short times. Figure 9.4 shows the rate testing results of our SiNW-cPAN electrode (green circles) as compared to our previous nSi-cPAN electrode (blue squares) cycled in the PYR$_{13}$FSI (1.2M LiFSI) electrolyte. The charging (delithiation) rates of both electrode micro-geometries begin at C/20 for 3 cycles and continue at C/10 for subsequent cycles. The discharging (lithiation) rates, simulating charging in a full-cell, run in sets of 3 cycles from rates of C/20 to 1C. The data exhibits higher capacities for the SiNW-cPAN electrode at every rate set except for 1C, which will be discussed later. The SiNW-cPAN framework permits higher degrees of material utilization and faster charge and mass transport, which are manifested in the higher capacities at each rate. The ability of the SiNW-cPAN framework to allow high material utilization and full electrode reversibility is remarkable.

At the 1C rate, both the SiNW-cPAN and nSi-cPAN structures show the same capacities. This behavior is due to the inherent viscosity limitation of the electrolyte to conduct lithium-ions at such high rates (beyond 750 μA cm^{-2}). Due to the higher viscosity of the PYR$_{13}$FSI (1.2M LiFSI) electrolyte, there is a current threshold at which the lithium-ion concentration gradient becomes a limiting factor. To push beyond this barrier and to test the ability of the SiNW micro-geometry to allow for faster electrode lithiation, we have conducted a supercharging rate study at elevated temperatures of 60 degrees C to enhance electrolyte conductivity, electrode kinetics, and
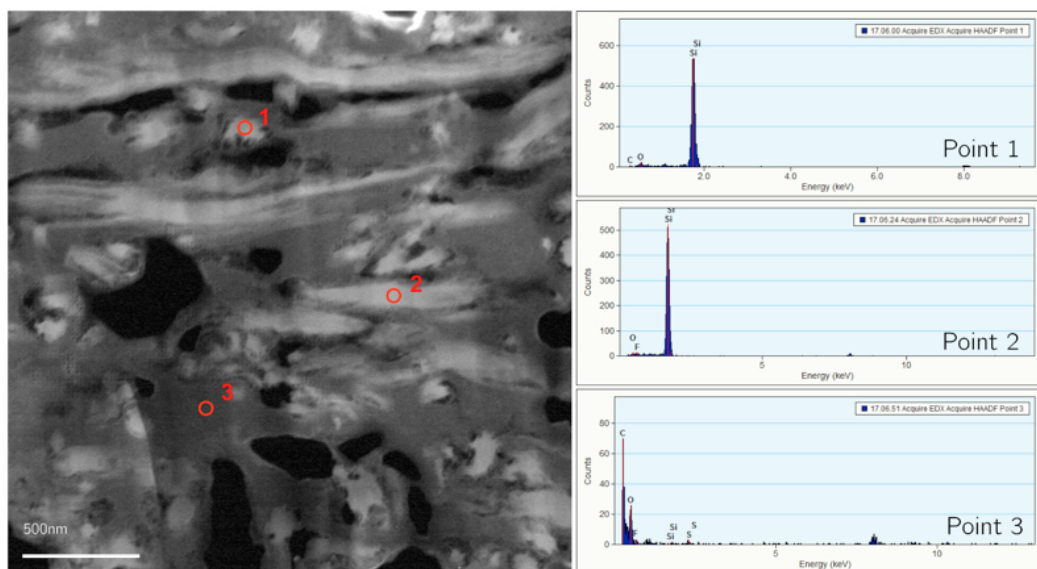
Figure 9.3: TEM micrograph of 16th delithiated SiNW-cPAN electrode with respective EDS point analysis clearly showing the presence of cPAN (point 3) intimately adhered to the SiNWs (point 1 and point 2), preserving the original electrode-architecture, and -micro-geometry even after 16 full charging and discharging cycles.
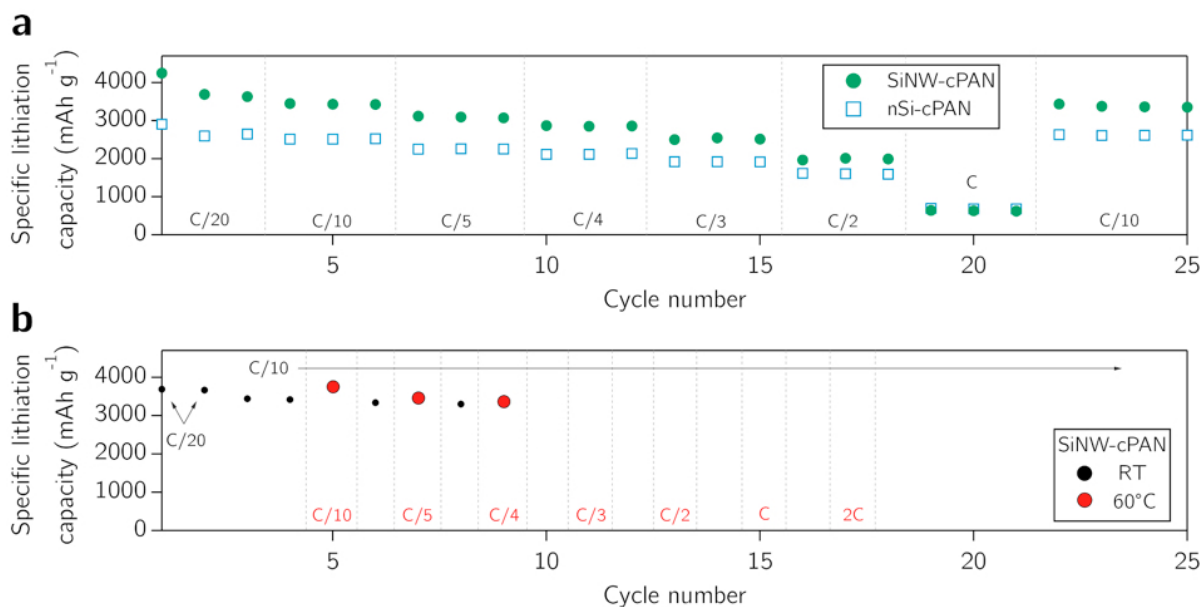
Figure 9.4: (a) Asymmetric rate study conducted to focus on the high lithiation rate capability of SiNW-cPAN and nSi-cPAN electrodes at room temperature. (b) Supercharging rate study of the SiNW-cPAN electrodes at elevated temperatures of 60C showing enhanced ion conduction and alloying kinetics.

the battery system as a whole. With commercialized organic solvent-based electrolytes, elevated temperatures instigate drastic electrolyte and SEI decomposition, leading to thermal runaway [64, 179]. Leveraging the thermal stability of the RTIL material, this study demonstrates the impressive performance of the $PYR_{13}FSI$ (1.2M LiFSI) electrolyte at high temperatures and the stability of the Si-$PYR_{13}FSI$ (1.2M LiFSI) interface. Figure 3 shows the improved performance of the $PYR_{13}FSI$ (1.2M LiFSI) solution at elevated temperatures, demonstrating improved ion conduction and rate performance while maintaining interfacial stability. Impressively, this experiment indicates the ability of the new electrode-micro-geometry to enable a 95% battery charge in just 30 minutes (equivalent to a 2C charging rate). The SiNW-cPAN/$PYR_{13}FSI$ (1.2M LiFSI) system is robust enough to facilitate rapid lithiation kinetics which result in high capacities in very short periods of time. The SiNW-cPAN electrodes can deliver a charge capacity of 3749.8 mAh g^{-1} in 8 hours (equivalent to C/8 charging rates), which is higher than the charge capacity achieved in 20 hours (equivalent to C/20 charging rates) at room temperature, 3666.5 mAh g^{-1}. Moreover, the SiNW-cPAN system can achieve a 60% state-of-charge, which translates to over 1800 mAh g^{-1} of capacity, in just 12 minutes (equivalent to 5C charging rates). This study truly validates the remarkable combinatorial benefits of an optimized electrode-architecture, -interface, and -micro-geometry.

The high percentage of active material utilization observed is directly translated to the unprecedented full-cell performance shown in Figure 9.5. The plot compares the performance of SiNW-cPAN/L333 full-cells assembled with $PYR_{13}FSI$ (1.2M LiFSI) and conventional EC/DEC (1M LiPF$_6$) electrolytes. Both cells contain the same electrode mass loadings on both the cathode and anode (within 10%) and were operated and controlled under the same parameters for fair comparison (see Appendix A for details on full-cell fabrication). Initial charge capacities of 127.24 and 140.23 mAh g^{-1} (all full-cell specific capacities are normalized with respect to total active material mass) were observed at the C/5 rate for the $PYR_{13}FSI$ (1.2M LiFSI) and EC/DEC (1M LiPF$_6$) LIBs, respectively. The difference in initial capacity is attributed to the higher ohmic resistance of the RTIL electrolyte, though this limitation is countered by unparalleled cycling stability. After 25 cycles, the cell cycled in carbonate-based (EC/DEC) electrolyte degrades rapidly. The degrada-
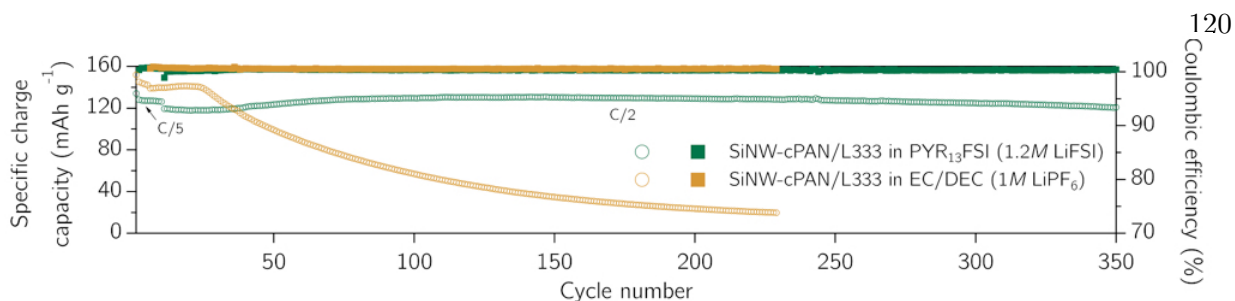
Figure 9.5: Specific charge capacities and coulombic efficiencies of SiNW-cPAN/L33 full-cells assembled with $PYR_{13}FSI$ (1.2M LiFSI) and conventional EC/DEC (1M $LiPF_6$) electrolytes.

tion, ascribed to low half-cell CEs with an average irreversible charge loss of 1.02% per cycle for the first 100 cycles (Figure 2a, brown squares), occurs as the system exhausts its supply of Li through continuous SEI breaking and reformation. In contrast, the cell cycled in $PYR_{13}FSI$ (1.2M LiFSI) electrolyte shows remarkable stability, attributed to the high half-cell CEs, stabilizing immediately after cycle 2 and followed by negligible Li consumption (Figure 2a, green squares), providing an average full-cell charge capacity of 126.73 mAh g^{-1} and a capacity retention of 99.62% at a rate of C/2 (Figure 4, green circles).

9.4 Summary and Conclusions Regarding SiNW-cPAN Micro-geometry

In summary, this work demonstrates the importance of simultaneously addressing the concerns of volumetric change, interfacial stability, and the need for an electrode-micro-geometry designed to optimize the performance of the active material-electrolyte combination. When working with high capacity materials with complex mechanical and electrochemical challenges such as Si, it is imperative to engineer the entire system rather than focusing only on either material or interfacial solutions. Taking on these issues in tandem allows for more effective solutions to each individual problem; for example, building a porous network of SiNW-cPAN clusters allows for better electrolyte penetration and interfacial stabilization while also maintaining high electrochemical reversibility. By optimizing the Si-cPAN-RTIL system utilizing a SiNW micro-geometry, we enable the high reversibility of a Si anode capable of stabilizing after just 2 cycles and providing

over 2800 mAh g^{-1} of Si. This multifaceted approach, and the resulting performance benefits, are substantiated by the SiNW-cPAN electrodes implementation in a Si/L333 full-cell which retains 99.62% of its original capacity after 350 cycles at a rate of C/2. In addition, this system opens the door for rapid silicon anode lithiation through the implementation of elevated temperatures, achieving nearly full charge capacities, 95% battery charge, in only 30 minutes. When viewed in the context of the race to develop commercially viable high energy density anode materials and recent advances in next-generation cathode systems, this work embodies important progress and a successful developmental approach towards safer, higher performance Li-ion technology.

Chapter 10

In Situ Engineering of the Electrode-Electrolyte Interface for Stabilized High-Energy Cathodes

10.1   Introduction

At the turn of the 21st century, a team of scientists at Argonne National Laboratory (ANL) was working hard to develop a lithium-ion (Li-ion) cathode technology that would change the way people viewed energy storage. In fact, their new cathode had the potential to revolutionize the transportation industry. The material was proposed to truly enable the electric vehicle (EV), driving down battery costs to less than \$200/kWh while supplying double the drive range of state-of-the-art Li-ion technology. This material, formulated as $x\text{Li}_2\text{MnO}_3.(1\text{-}x)\text{LiMO}_2$ (M = Ni, Mn, Co), is known as the lithium-manganese-rich (LMR) oxide.

While the true theoretical capacities of layered intercalation cathode materials lie at about 270 mAh g^{-1}, surface reactivity and instabilities at low states of charge limit the practical capacities of traditional layered cathode materials such as LiCoO_2 (about 140 mAh g^{-1}) and $\text{LiNi}_{1/3}\text{Mn}_{1/3}\text{Co}_{1/3}\text{O}_2$ (about 180 mAh g^{-1}). The beauty of the LMR material lies in the stabilization of the LiMO_2 crystal lattice using a structural constituent. Leading up to the development of this strategy, the primary tactic for lattice stabilization comprised cation or anion substitution. For example, Al3$^+$ ions were used to provide greater binding energy to oxygen sheets in layered insertion materials upon delithiation, and fluorine ion substitution for oxygen in layered electrodes provided enhanced cycling stability [6, 46, 102]. Guided by early work in stabilizing MnO_2 compounds using Li_2O structural units, Thackeray et al. [210] set out to integrate a structurally compatible component into

the $LiMO_2$ layered electrode. The compatibility of close-packed layers in Li_2MnO_3 allowed for its smooth atomic scale integration with $LiMO_2$, thereby creating the layered-layered $xLi_2MnO_3.(1-x)LiMO_2$ material [178]. While previously thought to be electrochemically inert, Kalyani et al. made the discovery that monoclinic Li_2MnO_3 could be activated by charging to high voltages (greater than 4.4 V vs. Li/Li^+) [100]. Thus, the Li_2MnO_3 component of the LMR material is both structurally advantageous and functional, as significant amounts of Li from these structural units can be reversibly extracted and re-intercalated following its electrochemical activation upon first charge [50]. With an unprecedentedly high operating voltage and capacities of about 260 mAh g^{-1}, the $xLi_2MnO_3.(1-x)LiMO_2$ cathode material gained the world's attention with the potential to double the energy density of the world's best Li-ion systems.

Despite these advantages and the potential for massive technological impact, worldwide research has struggled to enable the LMR material. The scientists at ANL impressively laid the foundation for widespread efforts targeting this material and its signature drawback: the gradual lowering of the cell operating voltage over cycling life as the originally layered crystal structure transforms to a spinel phase, accompanied by oxygen evolution during activation of the Li_2MnO_3 component and transition metal dissolution. The practical issue arising from this voltage fade is the continuous alteration of cell capacity associated with a given state of charge over the cycle life of the LMR material, leading to a failure to satisfy the performance requirements of any application requiring constant power and energy throughout operation.

The pristine $xLi_2MnO_3.(1-x)LiMO_2$ oxide structure has previously been described as a composite of O3 oxygen stacked layered rhombohedral or trigonal $LiMO_2$ (R-$3m$ space group) and monoclinic Li_2MnO_3 (C2/m space group) phases [151]. As both structures contain a transition metal (TM) layer consisting of periodic sequences of Li and two TM atoms, they can be considered α-$NaFeO_2$-type rock-salt structures, with all octahedral sites occupied [237]. During initial cycling of the LMR material, the Li_2MnO_3 component, initially holding Li^+ and Mn^{4+} ions in the octahedral sites of its cubic close-packed oxygen lattice, undergoes transformation (activation) by which Li_2O is de-intercalated from the layered lattice, accompanied by the generation of oxygen

vacancies and the migration of Mn ions into the newly formed vacancies. Throughout cycling, the LMR material further exhibits a transformation from a layered structure to a defect spinel, initially forming a surface reconstruction layer (SRL) which progressively grows inwards from particle edge to bulk during cycling [27, 232]. The severe structural changes of the LMR material can generally be understood as 1) an initial activation of the Li_2MnO_3 component with concurrent oxygen loss from the initially layered lattice followed by the parallel effects of 2) TM cations filling Li sites upon discharge with simultaneous dissolution of TM ions (most significantly Mn^{2+}) and 3) reduction of TM cations to lower valence states. The result of these structural changes is the loss of Li intercalation sites and the formation of a spinel phase (Fd-$3m$ space group) with a significantly lower operating voltage compared to that of the initial layered material, with the changes becoming more severe with cycling. In an attempt to alleviate oxygen evolution and mitigate phase transformation in the LMR material, myriad efforts have focused on surface modification, ion substitution or doping, and morphological control of particles and grains, all with limited success in enhancing long term cell energy retention.

10.2   Preliminary Findings

With the pressure mounting for the development of the next-generation Li-ion cathode system, the LMR material remains the subject of intensified research efforts. As the Li-ion industry is already commercializing Si materials in various anode composite structures while making major strides to enable pure Si nano-structures, the heat is on to perfect a high energy cathode capable of matching these new high capacity anode systems. In this work, we focus our efforts on the electrode-electrolyte interactions known to affect phase change in the LMR system. Leveraging the understandings of LMR interfacial behavior built by decades of research, we employ a unique electrolyte composition to form a cathode-electrolyte interface (CEI) that allows for the long-term voltage stability of the LMR cathode. Our novel CEI is formed in situ through the oxidative decomposition of a room temperature ionic liquid (RTIL) electrolyte doped with a sacrificial salt additive. For the first time, we demonstrate an LMR system capable of 1000 high capacity cycles

with minimal voltage decay, shedding light on the importance of the LMR CEI and elucidating the complex interplay between the electrolyte and the atomic scale transformations of a previously unstable crystal lattice.

Unfortunately, given timing conflicts with the date of this dissertation, intellectual property concerns, and publication of the results and mechanisms behind the LMR-RTIL system, the remainder of the LMR work completed during the course of this graduate project cannot be disclosed in this thesis. Figure 10.1 shows the half-cell cycling performance of an LMR cathode resulting from this project. This is, to our knowledge, the best LMR cycling data demonstrated academically, to-date. Please keep an eye out for the publication listed below, which will be submitted to the journal, Nature Materials, in early 2016.

In Situ Engineering of the Electrode-Electrolyte Interface for Stabilized Over-lithiated Cathodes

Tyler Evans, Daniela Molina Piper, Huaxing Sun, Timothy Porcelli, Seul Cham Kim, Sang Sub Han, Yong Suk Kim, Chunmei Ban, Feng Lin, Sung-Jin Cho, Kevin Leung, Kyu Hwan Oh, and Se-Hee Lee*

10.3 Applying Modified-RTILs to Nickel-Rich Cathode Compositions

The high cost and toxicity of cobalt pose major obstacles that limit cathode applications in large-format battery applications such as EVs. Thus, the nickel-rich transition metal oxide chemistries ($LiNi_xM_{1-x}O_2$; M = Mn, Co, and Al; x greater than 0.5) are considered as promising candidates to meet the performance and cost requirements of EVs; also of note are the specific capacities of such materials (>160 mAh g^{-1}) [105, 9, 131]. Unfortunately, the nickel-rich chemistries exhibit structural degradation and thermal instabilities; these problems worsen with higher nickel content, higher temperature, and higher cutoff voltages (greater than 4.4 V vs. Li/Li$^+$) [98]. In general, Ni-rich cathode materials with a layered structure undergo structural degradation from the layered R-3m phase to the spinel-like Fd-3m phase and the rock-salt Fm-3m phase) [105, 9].
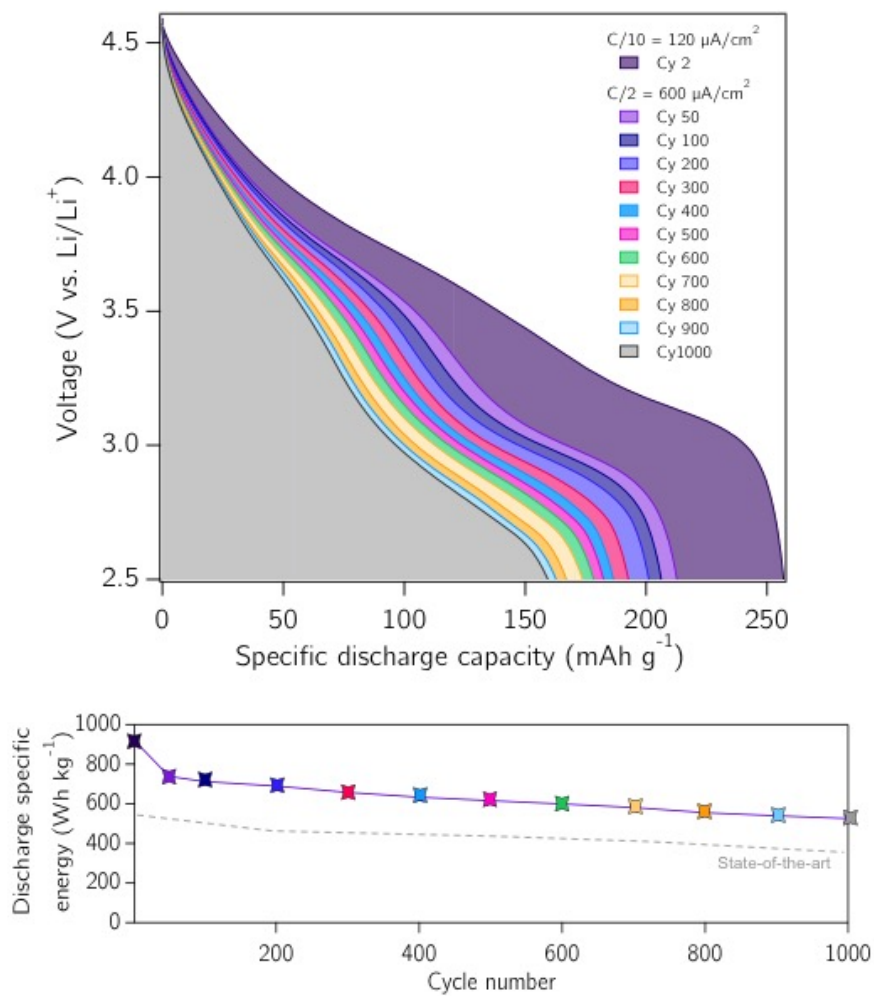
Figure 10.1: Half-cell performance of LMR active material in a modified-RTIL electrolyte, showing high levels of energy retention and the best maintenance of voltage trace shape demonstrated to-date (two-step voltage profile maintained for 1000 cycles).

This structural change is caused by the migration of the transition metal ions into the lithium layer during charge/discharge cycling. The metal ion migration leads to the layered-to-spinel phase transformation, and this transformation is exacerbated by cycling conditions such as high voltage and high temperature due to the increasing number of vacant Li sites during full delithiation and the diffusion of transition metal ions. This structural change leads to capacity fade (decreasing number of Li vacancies for intercalation and active material loss due to metal dissolution). Moreover, the decomposition of organic electrolytes at high voltages leads to higher interfacial resistances and increased rates of structural degradation.

Most efforts aimed at solving the aforementioned problems with the $LiNi_xM_{1-x}O_2$ material attempt to passivate the electrode-electrolyte interface using complex surface modifications, often with a conductive polymer) [9, 97, 40, 38]. Despite resulting in significant improvements in cycling stability, such advances are not sufficient for commercial application, which requires high stability for over 1000 cycles.

The hypothesis behind the work presented in herein was formulated by observing the origins of the phase change and metal dissolution which plague the nickel-rich material. This phase change is intimately linked to the dissolution of Mn^{2+} and Ni^{2+} ions, which are formed during the disproportionation of Mn^{3+} and Ni^{3+} also known to lead to the Mn and Ni migration associated with layered-to-spinel phase change. These mechanisms are closely related to the decomposition of organic electrolytes most typically used to study high-voltage materials. Carbonate electrolytes, including those containing $LiPF_6$, undergo oxidative decomposition during battery charging above 4.4 V vs. Li/Li$^+$, forming acidic H$^+$ and HF species [38]. Subsequently, these protons promote disproportionation of Mn^{3+} and Ni^{3+}, accelerating the dissolution/ migration of Mn and Ni and leading to the capacity fade that stigmatizes the nickel-rich chemistry [38]. Also of note is the fact that the spinel phase of oxide materials is more thermodynamically stable in acidic environments. Moreover, the accumulation of a thick solid electrolyte interphase layer on the cathode and attack by acidic species readily damage the electrode/electrolyte interface, inducing large charge transfer resistances (R_{ct}) that reduce capacity and rate performance.

In this work, we piggy-back on our LMR-RTIL work by hypothesizing that the phase change and capacity degradation of the nickel-rich material can be mitigated by utilizing an unconventional electrolyte, one with a high electrochemical stability window which does not decompose to form acidic species. Impressively, cycling between 2.5 - 4.5 V vs. Li/Li^+ in certain RTIL electrolytes allows for 100% capacity retention at the rate of 1C over 100 cycles. This is the first time that 100% capacity retention of the nickel-rich oxide material has been demonstrated over long-term cycling. Again, given timing conflicts with the date of this dissertation, intellectual property concerns, and publication of the results and mechanisms behind various cathode-RTIL systems, the remainder of the Ni-rich cathode work completed during the course of this graduate project cannot be disclosed in this thesis. Figure 10.2 shows the half-cell cycling performance of a $Li(Ni_{0.6}Mn_{0.2}Co_{0.2})O_2$ cathode resulting from this project. This is, to our knowledge, the best Ni-rich cathode cycling data demonstrated academically, to-date.
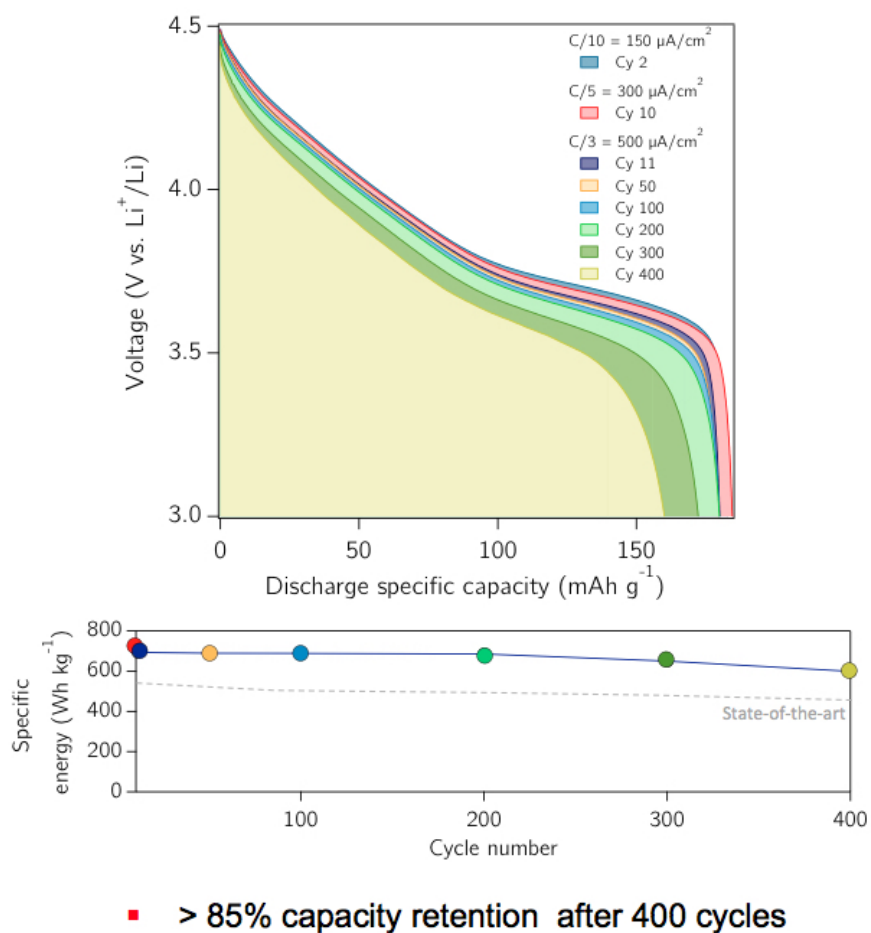
Figure 10.2: Ni-Rich NMC (622 composition) half-cell cycled in a chemistry specific, modified RTIL electrolyte with voltage profiles (a), specific capacities (b), and specific energies (c) shown over 100 cycles..

Chapter 11

Thesis Summary and a CU Spin-Out

11.1   Introduction

This graduate dissertation aimed to contribute to the science and body of knowledge relating to building higher energy battery technology at the cross-roads of materials science, electrochemistry, and device engineering. Specifically, the research presented works towards the development of next-generation Li-ion electrode chemistries through the utilization of novel electrolyte compositions. The world's next Li-ion battery will incorporate new, more energy dense materials, working together in a unique chemical balance. This dissertation highlighted an up-and-coming class of electrolyte materials, room temperature ionic liquids, and their interactions with next-generation electrodes. The research presented herein explores the utilization of today's best performing RTIL electrolytes in Li-ion batteries containing next-generation electrode materials. By replacing the conventional carbonate electrolyte with new sets of solvents and salts, new electrolyte-electrode chemical phenomena are induced which can lead to the increased performance of highly attractive electrodes. Chapters 4-6 discussed strategies related to tackling the major compatibility issues between RTIL materials and the passive components of Li-ion batteries (those not involved in the electrodes' faradaic redox chemistry), while Chapter 7-9 discussed exciting opportunities to exploit these novel chemical interactions in enabling highly energy dense electrodes.

11.2 Corrosion of Stainless Steel Battery Components by Bis(fluorosulfonyl)imide Based Ionic Liquid Electrolytes

During our first trial experiments attempting to utilize RTILs in Li-ion cells with high voltage cathode materials, we came across a number of issues. While the anodic behavior of aluminum foil current collectors in imide-based room temperature ionic liquids (RTILs) is relatively well understood, interactions between such RTILs and other passive battery components have been largely disregarded. This study presents the solvent and potential dependent oxidation of SS316 coin-cell components in the N-methyl-N-propyl-pyrrolidinium bis(fluorosulfonyl)imide (PYR$_{13}$FSI) RTIL. While this phenomenon prohibits high-voltage cycling of Li(Ni$_{1/3}$Mn$_{1/3}$Co$_{1/3}$)O$_2$ cathodes in SS316 coin-type cells, Al-clad cell components or alternative cell configurations can be utilized to avoid SS316 oxidation-induced cell failure.

11.3 Effect of Organic Solvent Addition to PYR$_{13}$FSI + LiFSI Electrolytes on Aluminum Oxidation and Rate Performance of Li(Ni$_{1/3}$Mn$_{1/3}$Co$_{1/3}$)O$_2$ Cathodes

Corrosion of the positive electrode's aluminum current collector in Li-ion cells at high voltages is regarded as the most serious problems facing the commercialization of RTIL electrolytes for electrochemical applications. The superior suppression of aluminum current collector oxidation by a 1.2M LiFSI in PYR$_{13}$FSI ionic liquid electrolyte is demonstrated. Addition of EC:EMC (1:2 wt.) is shown to significantly increase the severity of parasitic aluminum oxidation. Despite leading to increased aluminum oxidation at high voltages (>4.2V vs. Li/Li$^+$), adding organic solvent to PYR$_{13}$FSI based ionic liquids greatly enhances important electrochemical properties. The ionic conductivity and lithium ion transference number of the PYR$_{13}$FSI + 1.2M LiFSI electrolyte increase with increasing volumetric content of organic co-solvent (EC:EMC), resulting in significant improvements to high rate performance. The electrochemical benefits of organic co-solvent addition and the compatibility of the PYR$_{13}$FSI + 1.2M LiFSI electrolyte with Li(Ni$_{1/3}$Mn$_{1/3}$Co$_{1/3}$)O$_2$ demonstrated in this study substantiate the need to develop strategies to suppress aluminum oxi-

dation during high voltage cycling of lithium-ion batteries in ionic liquid electrolytes.

11.4 Electrospun Polyacrylonitrile Microfiber Separators for Ionic Liquid Electrolytes in Li-ion Batteries

After characterizing and developing a cycling protocol to avoid high-potential aluminum corrosion, we turned to another issue hindering widespread utilization of RTIL electrolytes. Most RTIL research for Li-ion battery applications uses glass fiber separator materials. These materials are not compatible with commercial battery manufacturing processes, and a new separator must be developed if RTILs are to be commercialized for Li-ion technology.

Despite much recent progress in the development of room temperature ionic liquid (RTIL) electrolytes for lithium-ion batteries (LIBs), relatively little work has been done in terms of investigating commercially applicable separator materials capable of accommodating RTILs. In this work, we demonstrate an electrospun polyacrylonitrile (PAN) microfiber separator. The PAN microfiber separators show high degrees of porosity (about 83%), wettability, and mechanical strength (UTS = 16.98 MPa and E = 5.95 MPa). The physical properties of our electrospun separators lead to impressive electrochemical performance, showing an apparent MacMullin number (NM) of less than 5 when combined with the $PYR_{13}FSI$ ($1.2M$ LiFSI) electrolyte. These results are validated by superior rate performance and the exhibition of a high capacity full-cell utilizing a PAN microfiber separator in combination with the $PYR_{13}FSI$ ($1.2M$ LiFSI) RTIL electrolyte. Such work represents significant progress in the advancement of RTIL electrolytes for LIBs, indicating that nonwoven separators are a commercially viable solution to the previous lack of separator materials for RTIL electrolytes.

11.5 Ionic Liquid Enabled FeS_2 for High Energy-Density Lithium-Ion Batteries

With the energy density of conventional Li-ion batteries (LIBs) approaching a practical upper limit, next generation electrode materials must be developed in order to satisfy the demand for an

inexpensive, highly energy dense battery for future energy storage applications. Significant progress has been made on high-capacity tin and silicon-based anodes, but new cathode chemistries must be developed in order to accommodate such materials. While the stable cycling of a Si anode has been demonstrated with capacities above 1500 mAh g^{-1}, work in this field has been unable to demonstrate the long-term cycling of a cathode material with capacities higher than 250 mAh g^{-1}. Because of their ability to accommodate more than one Li atom per transition-metal cation, materials that undergo a conversion reaction with lithium have gained attention as promising candidates for high-capacity cathodes. Among such conversion chemistries, FeS_2 represents a promising alternative to replace the conventional $LiMO_2$ (M = transition metal) intercalation mechanism because FeS_2 is inexpensive, highly energy dense, naturally abundant, and environmentally benign. The four electron reduction of cubic-FeS_2 (pyrite) exhibits a theoretical specific capacity of 894 mAh g^{-1}, as compared to the best $LiMO_2$ intercalation electrodes which only provide approximately 200 mAh g^{-1}.

11.6 Stable Silicon-Ionic Liquid Interface for Next Generation Lithium-ion Batteries

Recently, silicon has been identified as one of the most attractive high-energy anode materials for LIBs. Silicon's low working voltage and high theoretical specific capacity of 3579 mAh g^{-1}, nearly ten times higher than that of state-of-the-art graphite anodes, have encouraged widespread research efforts aimed at developing a viable Si based electrode. The substantial gains in specific and volumetric capacity simply through the implementation of an active material such as Si offer a glimpse into the future of lighter and smaller batteries. Despite the advantages of the Si electrode, a number of challenges impede its commercialization. Many of these challenges are associated with the Si material's severe volume expansion during lithiation. While the commercialized graphite electrode expands roughly 10-13% during lithium intercalation, Si's expansion amounts to nearly 300%, generating structural degradation and instability of the all-important solid-electrolyte interphase (SEI).

By combining a high performance Si electrode architecture with a room temperature ionic liquid electrolyte, here we demonstrate a highly energy-dense lithium-ion cell with an impressively long cycling life, maintaining over 75% capacity after 500 cycles. Such high performance is enabled by a stable half-cell coulombic efficiency of 99.97%, averaged over the first 200 cycles. Equally as significant, our detailed characterization elucidates the previously convoluted mechanisms of the solid-electrolyte interphase on Si electrodes. We provide a theoretical simulation to model the interface and microstructural-compositional analyses that confirm our theoretical predictions and allow us to visualize the precise location and constitution of various interfacial components. This work provides new science related to the interfacial stability of Si-based materials while granting positive exposure to ionic liquid electrochemistry.

11.7   Optimized Silicon Electrode-architecture, -interface, and -micro-geometry for Next-generation Lithium-ion Batteries

Our previous work demonstrated the success in simultaneously addressing the two aforementioned issues by pairing a robust, yet simple, electrode-architecture with a room temperature ionic liquid electrolyte (RTIL or IL) to create a highly favorable Si-electrolyte interface. The study highlighted the groundbreaking demonstration of the cycling of a full-cell incorporating a Si anode by using a $PYR_{13}FSI$ (1.2M LiFSI) electrolyte with an unprecedented cycling life. A combinatorial approach involving a mechanically resilient electrode-architecture merged with an electrolyte capable of forming a favorable SEI was the solution to incorporate structural integrity with stable interfacial chemistry in a bulk-type Si anode. While this study validated an unconventional approach to enabling the Si anode, one issue remains to be solved: optimization of the Si electrode-micro-geometry.

11.8   *In Situ* Engineering of the Electrode-Electrolyte Interface for Stabilized High-Energy Cathodes

At the turn of the 21st century, a team of scientists at Argonne National Laboratory (ANL) was working hard to develop a lithium-ion (Li-ion) cathode technology that would change the way people viewed energy storage. In fact, their new cathode had the potential to revolutionize the transportation industry. The material was proposed to truly enable the electric vehicle (EV), driving down battery costs to less than \$200/kWh while supplying double the drive range of state-of-the-art Li-ion technology. This material, formulated as $xLi_2MnO_3.(1-x)LiMO_2$ (M = Ni, Mn, Co), is known as the lithium-manganese-rich (LMR) oxide. With an unprecedentedly high operating voltage and capacities of about 260 mAh g^{-1}, the $xLi_2MnO_3.(1-x)LiMO_2$ cathode material gained the world's attention with the potential to double the energy density of the world's best Li-ion systems. Despite these advantages and the potential for massive technological impact, worldwide research has struggled to enable the LMR material. The scientists at ANL impressively laid the foundation for widespread efforts targeting this material and its signature drawback: the gradual lowering of the cell operating voltage over cycling life as the originally layered crystal structure transforms to a spinel phase, accompanied by oxygen evolution during activation of the Li_2MnO_3 component and transition metal dissolution. The practical issue arising from this voltage fade is the continuous alteration of cell capacity associated with a given state of charge over the cycle life of the LMR material, leading to a failure to satisfy the performance requirements of any application requiring constant power and energy throughout operation.

In this work, we focus our efforts on the electrode-electrolyte interactions known to affect phase change in the LMR system. Leveraging the understandings of LMR interfacial behavior built by decades of research, we employ a unique electrolyte composition to form a cathode-electrolyte interface (CEI) that allows for the long-term voltage stability of the LMR cathode. Our novel CEI is formed in situ through the oxidative decomposition of a room temperature ionic liquid (RTIL) electrolyte doped with a sacrificial additive. For the first time, we demonstrate an LMR system

capable of 1000 high capacity cycles with minimal voltage decay, shedding light on the importance of the LMR CEI and elucidating the complex interplay between the electrolyte and the atomic scale transformations of a previously unstable crystal lattice.

We then applied our understanding of the LMR-RTIL system to other high energy intercalation cathode materials with similar problems. Such materials include the nickel-rich layered oxides ($LiNi_xM_{1-x}O_2$). We hypothesized that the phase change and capacity degradation of the nickel-rich material can be mitigated by utilizing an unconventional electrolyte, one with a high electrochemical stability window which does not decompose to form acidic species. Impressively, cycling between 2.5 - 4.5 V vs. Li/Li^+ in certain RTIL electrolytes allows for 100% capacity retention at the rate of 1C over 100 cycles. This is the first time that 100% capacity retention of the nickel-rich oxide material has been demonstrated over long-term cycling.

11.9   SiILion, Inc.

The work highlighted in this dissertation presents an interesting commercial opportunity. Given the high energy and the potential cost savings and safety of the LMR/RTIL/Si battery, Dr. Se-Hee Lee, Dr. Daniela Molina Piper, and Tyler Evans have joined together to commercialize the technology, spearheading SiILion, Inc. in an effort to bring safer, more affordable, higher energy battery technology to the EV market. See below for a brief description of the company:

Rechargeable lithium-ion batteries (LIBs) have dominated the portable electronics market for nearly a decade, but better batteries are needed as consumer electronics get smaller and emerging markets such as electric vehicles demand more power and range at a lower cost. The growing electric vehicle market in particular offers a compelling opportunity for advanced battery companies, as evidenced by the Tesla battery gigafactory currently under construction that will single-handedly double worldwide battery cell production once complete. Tesla and other automotive companies still use conventional Li-ion electrode materials that have changed little in the last 25 years. Improvements in materials processing and device manufacturing have allowed for a modest improvement

in battery energy density and cost of approximately 5-6% each year, and electric vehicle costs have remained high compared to conventional vehicles.

In order for electric vehicles to gain true market traction with middle class consumers, batteries with lower cost and energy density as high as 400 Wh/kg (nearly 2X improvement) are in high demand. The Li-ion battery chemistry that currently holds the world record for energy density and appears most likely to reach these targets is one based on a silicon anode (negative electrode) and a lithium and manganese-rich (LMR) cathode (positive electrode). This combination delivers unprecedented energy per mass and volume as well as low cost, but it also has a notorious problem of rapid energy loss during cycling. Hundreds of millions of dollars have been invested in silicon anodes and LMR cathodes to date, and the company that successfully addresses the challenges of this system will have a strong foothold in the advanced battery market.

SiILion, Inc. is uniquely positioned to be a leader in the battery space because it has already demonstrated better performance with a silicon anode and LMR cathode than any other company or academic institution at the laboratory scale. While its competitors attempt to achieve long cycle life using complex nanostructured electrodes and material treatments, SiILion achieves its transformative results using materials that are drop-in replacements for conventional Li-ion materials without the need for expensive and impractical nanomaterials.

SiILion's technology platform leverages breakthroughs at the University of Colorado at Boulder (CU-Boulder) for which SiILion is working to obtain exclusive rights to the resulting patent applications (currently holds an 'Exclusive Option,' negotiations under way for Exclusive License). SiILion and CU-Boulder have demonstrated long cycle life for a nanostructured silicon anode as published recently in Nature Communications, and they are to their knowledge the only entity to also achieve long full-cell cycle life with inexpensive micron-sized silicon. Several battery startups have been founded around the less promising nano-silicon anode alone, but SiILion combines its best-in-class silicon performance with LMR cathodes that show marked improvement in energy retention during cycling compared with any other published result. All of the materials needed for the cells are available in quantities appropriate for mass production, and SiILion's cells can be produced on

conventional Li-ion manufacturing lines to leverage the industry's decades of experience in driving down costs while maintaining high quality.

To ensure its technical and commercial success, SiILion has established a premier team of researchers and advisors to assist in developing and positioning the technology for market insertion. To-date, the SiILion team has filed provisional patents through CU-Boulder on its key anode technology (U.S. 62/110,286) and its key cathode technologies (U.S. 62/110,286 and U.S. 62/151,918) and has engaged the highly regarded firm, Perkins Coie, for conversion of its provisional applications to utility patents in late 2015 and early 2016. SiILion has secured angel investment to help enable these conversions with plans to file both domestic and foreign patents for its inventions once reduced to practice and once an Exclusive License agreement is reached with the CU TTO. SiILion has extensively reviewed the existing patent literature and is confident that its approach, enabling next-generation electrode materials through interfacial chemistry with RTIL materials, is both novel and transformative.

SiILion has been awarded an SBIR Phase I grant from the Department of Energy and has successfully committed angel investors for a seed investment round; SiILion's angel investors have allowed the company to earmark funds for patent filings and conversion of the company's provisional patent applications to utility patents following the procurement of an Exclusive License to all SiILion/CU-Boulder inventions, and SiILion's DOE SBIR Phase I project will help advance and refine the company's key technologies.

If successful, it is anticipated that the proposed technology will result in a full-cell having a specific energy approaching 400 Wh/kg with the added benefit of a non-flammable RTIL electrolyte.

To-date, SiILion has demonstrated high performance long-term cycling of LMR and NMC622/uSi full-cells in coin-type configurations and has demonstrated high performance short-term cycling of a 200 mAh pouch-type cell (currently cycling). The SiILion team is now working to scale its technology to a commercially attractive prototype.

Bibliography

[1] Andrew P Abbott, Glen Capper, Katy J McKenzie, Andrew Glidle, and Karl S Ryder. Electropolishing of stainless steels in a choline chloride based ionic liquid: an electrochemical study with surface characterisation using SEM and atomic force microscopy. Physical Chemistry Chemical Physics, 8(36):4214–4221, 2006.

[2] Andrew P Abbott, Glen Capper, Katy J McKenzie, and Karl S Ryder. Voltammetric and impedance studies of the electropolishing of type 316 stainless steel in a choline chloride based ionic liquid. Electrochimica Acta, 51(21):4420–4425, 2006.

[3] A Abouimrane, Jianfu Ding, and IJ Davidson. Liquid electrolyte based on lithium bisfluorosulfonyl imide salt: Aluminum corrosion studies and lithium ion battery investigations. Journal of Power Sources, 189(1):693–696, 2009.

[4] Carlo Adamo and Vincenzo Barone. Toward reliable density functional methods without adjustable parameters: The PBE0 model. The Journal of Chemical Physics, 110(13):6158–6170, 1999.

[5] In-Shup Ahn, Dong Woong Kim, Deuk Kyun Kang, and Dong-Kyu Park. The effects of the particle size and active materials on the discharge properties of the Li/Fe_xS_2 electrode. Metals and Materials International, 14(1):65–70, 2008.

[6] GG Amatucci, N Pereira, T Zheng, I Plitz, and JM Tarascon. Enhancement of the electrochemical properties of $li_1mn_2o_4$ through chemical substitution. Journal of power sources, 81:39–43, 1999.

[7] Yongxin An, Pengjian Zuo, Chunyu Du, Yulin Ma, Xinqun Cheng, Jianyi Lin, and Geping Yin. Effects of VC-LiBOB binary additives on SEI formation in ionic liquid–organic composite electrolyte. RSC Adv., 2(10):4097–4102, 2012.

[8] Giovanni B Appetecchi, Maria Montanino, Andrea Balducci, Simon F Lux, Martin Winterb, and Stefano Passerini. Lithium insertion in graphite from ternary ionic liquid-lithium salt electrolytes: Electrochemical characterization of the electrolytes. Journal of Power Sources, 192(2):599–605, 2009.

[9] Hajime Arai, Shigeto Okada, Yoji Sakurai, and Jun-ichi Yamaki. Thermal behavior of $li_{1-y}nio_2$ and the decomposition mechanism. Solid State Ionics, 109(3):295–302, 1998.

[10] MF Arenas and RG Reddy. Corrosion of steel in ionic liquids. Journal of Mining and Metallurgy, Section B: Metallurgy, 39(1-2):81–91, 2003.

[11] Michel Armand, Frank Endres, Douglas R MacFarlane, Hiroyuki Ohno, and Bruno Scrosati. Ionic-liquid materials for the electrochemical challenges of the future. Nature materials, 8(8):621–629, 2009.

[12] Michel Armand and J-M Tarascon. Building better batteries. Nature, 451(7179):652–657, 2008.

[13] Pankaj Arora and Zhengming Zhang. Battery separators. Chemical reviews, 104(10):4419–4462, 2004.

[14] Doron Aurbach, Ella Zinigrad, Yaron Cohen, and Hanan Teller. A short review of failure mechanisms of lithium metal and lithiated graphite anodes in liquid electrolyte solutions. Solid state ionics, 148(3):405–416, 2002.

[15] A Balducci, SS Jeong, GT Kim, S Passerini, M Winter, M Schmuck, GB Appetecchi, R Marcilla, D Mecerreyes, V Barsukov, et al. Development of safe, green and high performance ionic liquids-based batteries (ILLIBATT project). Journal of Power Sources, 196(22):9719–9730, 2011.

[16] A Balducci, SS Jeong, GT Kim, S Passerini, M Winter, M Schmuck, GB Appetecchi, R Marcilla, D Mecerreyes, V Barsukov, et al. Development of safe, green and high performance ionic liquids-based batteries (ILLIBATT project). Journal of Power Sources, 196(22):9719–9730, 2011.

[17] V Baranchugov, E Markevich, E Pollak, G Salitra, and D Aurbach. Amorphous silicon thin films as a high capacity anodes for Li-ion batteries in ionic liquid electrolytes. Electrochemistry Communications, 9(4):796–800, 2007.

[18] Allen J Bard and Larry R Faulkner. Electrochemical methods: fundamentals and applications, 2nd. Hoboken: Wiley & Sons, 2001.

[19] Evgenij Barsoukov and J Ross Macdonald. Impedance spectroscopy: theory, experiment, and applications. John Wiley & Sons, 2005.

[20] Georges Bartoli. 10 facts on climate change and health. World Health Organization, July 2015.

[21] LY Beaulieu, TD Hatchard, A Bonakdarpour, MD Fleischauer, and JR Dahn. Reaction of Li with alloy thin films studied by in situ AFM. Journal of The Electrochemical Society, 150(11):A1457–A1464, 2003.

[22] AS Best, AI Bhatt, and AF Hollenkamp. Ionic liquids with the bis (fluorosulfonyl) imide anion: electrochemical properties and applications in battery technology. Journal of The Electrochemical Society, 157(8):A903–A911, 2010.

[23] Nandana Bhardwaj and Subhas C Kundu. Electrospinning: a fascinating fiber fabrication technique. Biotechnology Advances, 28(3):325–347, 2010.

[24] Anand I Bhatt, Adam S Best, Junhua Huang, and Anthony F Hollenkamp. Application of the n-propyl-n-methyl-pyrrolidinium bis (fluorosulfonyl) imide RTIL containing lithium bis (fluorosulfonyl) imide in ionic liquid based lithium batteries. Journal of The Electrochemical Society, 157(1):A66–A74, 2010.

[25] Arnaud Bordes, KwangSup Eom, and Thomas F Fuller. The effect of fluoroethylene carbonate additive content on the formation of the solid-electrolyte interphase and capacity fade of Li-ion full-cell employing nano Si–graphene composite anodes. Journal of Power Sources, 257:163–169, 2014.

[26] A Bösmann, L Datsevich, A Jess, A Lauter, C Schmitz, and P Wasserscheid. Deep desulfurization of diesel fuel by extraction with ionic liquids. Chemical Communications, pages 2494–2495, 2001.

[27] Adrien Boulineau, Loïc Simonin, Jean-François Colin, Carole Bourbon, and Sébastien Patoux. First evidence of manganese–nickel segregation and densification upon cycling in li-rich layered oxides for lithium batteries. Nano letters, 13(8):3857–3863, 2013.

[28] R Brec, A Dugast, and A Le Mehauté. Chemical and electrochemical study of the li_xfes_2 cathodic system. Materials Research Bulletin, 15(5):619–625, 1980.

[29] Peter G Bruce, James Evans, and Colin A Vincent. Conductivity and transference number measurements on polymer electrolytes. Solid State Ionics, 28:918–922, 1988.

[30] Peter G Bruce and Colin A Vincent. Steady state current flow in solid binary electrolyte cells. Journal of electroanalytical chemistry and interfacial electrochemistry, 225(1):1–17, 1987.

[31] Akin Budi, Andrew Basile, George Opletal, Anthony F Hollenkamp, Adam S Best, Robert J Rees, Anand I Bhatt, Anthony P O'Mullane, and Salvy P Russo. Study of the initial stage of solid electrolyte interphase formation upon chemical reaction of lithium metal and N-methyl-N-propyl-pyrrolidinium-bis (fluorosulfonyl) imide. The Journal of Physical Chemistry C, 116(37):19789–19797, 2012.

[32] Priya Carol, Prakash Ramakrishnan, Bibin John, and Gouri Cheruvally. Preparation and characterization of electrospun poly (acrylonitrile) fibrous membrane based gel polymer electrolytes for lithium-ion batteries. Journal of Power Sources, 196(23):10156–10162, 2011.

[33] Changju Chae, Hyung-Joo Noh, Jung Kyoo Lee, Bruno Scrosati, and Yang-Kook Sun. A high-energy Li-ion battery using a silicon-based anode and a nano-structured layered composite cathode. Advanced Functional Materials, 24(20):3036–3042, 2014.

[34] Candace K Chan, Hailin Peng, Gao Liu, Kevin McIlwrath, Xiao Feng Zhang, Robert A Huggins, and Yi Cui. High-performance lithium battery anodes using silicon nanowires. Nature Nanotechnology, 3(1):31–35, 2007.

[35] Candace K Chan, Riccardo Ruffo, Seung Sae Hong, and Yi Cui. Surface chemistry and morphology of the solid electrolyte interphase on silicon nanowire lithium-ion battery anodes. Journal of Power Sources, 189(2):1132–1140, 2009.

[36] Jiajun Chen. Recent progress in advanced materials for lithium ion batteries. Materials, 6(1):156–183, 2013.

[37] Zonghai Chen, WQ Lu, Jun Liu, and K Amine. LiPF$_6$/LiBOB blend salt electrolyte for high-power lithium-ion batteries. Electrochimica acta, 51(16):3322–3326, 2006.

[38] Zonghai Chen, Yan Qin, Khalil Amine, and Y-K Sun. Role of surface coating on cathode materials for lithium-ion batteries. J. Mater. Chem., 20(36):7606–7612, 2010.

[39] Erang Cho, Junyoung Mun, Oh B Chae, Oh Min Kwon, Hyung-Tae Kim, Ji Heon Ryu, Young Gyu Kim, and Seung M Oh. Corrosion/passivation of aluminum current collector in bis (fluorosulfonyl) imide-based ionic liquid for lithium-ion batteries. Electrochemistry Communications, 22:1–3, 2012.

[40] Jaephil Cho, Young-Woon Kim, Byoungsoo Kim, Joon-Gon Lee, and Byungwoo Park. A breakthrough in the safety of lithium secondary batteries by coating the cathode material with alpo$_4$ nanoparticles. Angewandte Chemie International Edition, 42(14):1618–1621, 2003.

[41] Tae-Hyung Cho, Masanao Tanaka, Hiroshi Onishi, Yuka Kondo, Tatsuo Nakamura, Hiroaki Yamazaki, Shigeo Tanase, and Tetsuo Sakai. Battery performances and thermal stability of polyacrylonitrile nano-fiber-based nonwoven separators for li-ion battery. Journal of Power Sources, 181(1):155–160, 2008.

[42] TH Cho, T Sakai, S Tanase, K Kimura, Y Kondo, T Tarao, and M Tanaka. Electrochemical performances of polyacrylonitrile nanofiber-based nonwoven separator for lithium-ion battery. Electrochemical and solid-state letters, 10(7):A159–A162, 2007.

[43] Nam-Soon Choi, Zonghai Chen, Stefan A Freunberger, Xiulei Ji, Yang-Kook Sun, Khalil Amine, Gleb Yushin, Linda F Nazar, Jaephil Cho, and Peter G Bruce. Challenges facing lithium batteries and electrical double-layer capacitors. Angewandte Chemie International Edition, 51(40):9994–10024, 2012.

[44] Nam-Soon Choi, Yongbeom Lee, Sung-Soo Kim, Soon-Cheol Shin, and Yong-Mook Kang. Improving the electrochemical properties of graphite/LiCoO$_2$ cells in ionic liquid-containing electrolytes. Journal of Power sources, 195(8):2368–2371, 2010.

[45] SW Choi, JR Kim, SM Jo, WS Lee, and Y-R Kim. Electrochemical and spectroscopic properties of electrospun PAN-based fibrous polymer electrolytes. Journal of the Electrochemical Society, 152(5):A989–A995, 2005.

[46] W Choi and A Manthiram. Superior capacity retention spinel oxyfluoride cathodes for lithium-ion batteries. Electrochemical and solid-state letters, 9(5):A245–A248, 2006.

[47] YJ Choi, NW Kim, KW Kim, KK Cho, GB Cho, HJ Ahn, JH Ahn, KS Ryu, and HB Gu. Electrochemical properties of nickel-precipitated pyrite as cathode active material for lithium/pyrite cell. Journal of Alloys and Compounds, 485(1):462–466, 2009.

[48] EJ Chong, TT Phan, IJ Lim, YZ Zhang, BH Bay, S Ramakrishna, and CT Lim. Evaluation of electrospun PCL/gelatin nanofibrous scaffold for wound healing and layered dermal reconstitution. Acta Biomaterialia, 3(3):321–330, 2007.

[49] Bogdan Cramariuc, Radu Cramariuc, Roxana Scarlet, Liliana Rozemarie Manea, Iuliana G Lupu, and Oana Cramariuc. Fiber diameter in electrospinning process. Journal of Electrostatics, 71(3):189–198, 2013.

[50] Jason R Croy, Joong Sun Park, Fulya Dogan, Christopher S Johnson, Baris Key, and Mahalingam Balasubramanian. First-cycle evolution of local structure in electrochemically activated li$_2$mno$_3$. Chemistry of Materials, 26(24):7091–7098, 2014.

[51] JM Deitzel, JD Kleinmeyer, JK Hirvonen, and NC Beck Tan. Controlled deposition of electrospun poly(ethylene oxide) fibers. Polymer, 42(19):8163–8170, 2001.

[52] Jayesh Doshi and Darrell H Reneker. Electrospinning process and applications of electrospun fibers. In Industry Applications Society Annual Meeting, 1993., Conference Record of the 1993 IEEE, pages 1698–1703. IEEE, 1993.

[53] Minato Egashira, Maika Tanaka-Nakagawa, Izumi Watanabe, Shigeto Okada, and Jun-ichi Yamaki. Charge–discharge and high temperature reaction of LiCoO$_2$ in ionic liquid electrolytes based on cyano-substituted quaternary ammonium cation. Journal of power sources, 160(2):1387–1390, 2006.

[54] United States E.I.A. How much natural gas does the United States have and how long will it last? EIA - Independent Statistics and Analysis, December 2014.

[55] Brian L Ellis, Kyu Tae Lee, and Linda F Nazar. Positive electrode materials for Li-ion and li-batteries. Chemistry of Materials, 22(3):691–714, 2010.

[56] Tyler Evans, Jarred Olson, Vinay Bhat, and Se-Hee Lee. Effect of organic solvent addition to PYR$_1$3FSI + LiFSI electrolytes on aluminum oxidation and rate performance of Li(Ni$_{1/3}$Mn$_{1/3}$Co$_{1/3}$)O$_2$ cathodes. Journal of Power Sources, 265:132–139, 2014.

[57] Tyler Evans, Jarred Olson, Vinay Bhat, and Se-Hee Lee. Effect of organic solvent addition to PYR$_1$3FSI + LiFSI electrolytes on aluminum oxidation and rate performance of Li(Ni$_{1/3}$Mn$_{1/3}$Co$_{1/3}$)O$_2$ cathodes. Journal of Power Sources, 265:132–139, 2014.

[58] Tyler Evans, Daniela Molina Piper, Seul Cham Kim, Sang Sub Han, Vinay Bhat, Kyu Hwan Oh, and Se-Hee Lee. Ionic liquid enabled FeS$_2$ for high-energy-density lithium-ion batteries. Advanced Materials, 26(43):7386–7392, 2014.

[59] XDHR Fang and DH Reneker. Dna fibers by electrospinning. Journal of Macromolecular Science, Part B: Physics, 36(2):169–173, 1997.

[60] Xu Feng, Xiangming He, Weihua Pu, Changyin Jiang, and Chunrong Wan. Hydrothermal synthesis of FeS$_2$ for lithium batteries. Ionics, 13(5):375–377, 2007.

[61] A Fernicola, F Croce, B Scrosati, T Watanabe, and H Ohno. LiTFSI-BEPyTFSI as an improved ionic liquid electrolyte for rechargeable lithium batteries. Journal of Power Sources, 174(1):342–348, 2007.

[62] A Fernicola, F Croce, B Scrosati, T Watanabe, and H Ohno. LiTFSI-BEPyTFSI as an improved ionic liquid electrolyte for rechargeable lithium batteries. Journal of Power Sources, 174(1):342–348, 2007.

[63] A Fernicola, B Scrosati, and H Ohno. Potentialities of ionic liquids as new electrolyte media in advanced electrochemical devices. Ionics, 12(2):95–102, 2006.

[64] Donal P Finegan, Mario Scheel, James B Robinson, Bernhard Tjaden, Ian Hunt, Thomas J Mason, Jason Millichamp, Marco Di Michiel, Gregory J Offer, Gareth Hinds, et al. In-operando high-speed tomography of lithium-ion batteries during thermal runaway. Nature communications, 6, 2015.

[65] Hao Fong and Darrell H Reneker. Electrospinning and the formation of nanofibers, volume 6. chapter, 2001.

[66] Rosamaría Fong, JR Dahn, and CHW Jones. Electrochemistry of pyrite-based cathodes for ambient temperature lithium batteries. Journal of The Electrochemical Society, 136(11):3206–3210, 1989.

[67] Mark Fox and George F Bertsch. Optical properties of solids. American Journal of Physics, 70(12):1269–1270, 2002.

[68] MJEA Frisch, GW Trucks, Hs B Schlegel, GE Scuseria, MA Robb, JR Cheeseman, G Scalmani, V Barone, B Mennucci, GA Petersson, et al. Gaussian 09, revision A. 02, gaussian. Inc., Wallingford, CT, 200, 2009.

[69] T Fromling, M Kunze, M Schonhoff, J Sundermeyer, and B Roling. Enhanced lithium transference numbers in ionic liquid electrolytes. The Journal of Physical Chemistry B, 112(41):12985–12990, 2008.

[70] Peng Gao, Yi Xie, Lina Ye, Ying Chen, and Qixun Guo. From 2D nanoflats to 2D nanowire networks: A novel hyposulfite self-decomposition route to semiconductor FeS_2 nanowebs. Crystal growth and design, 6(2):583–587, 2006.

[71] Béatrice Garcia and Michel Armand. Aluminium corrosion in room temperature molten salt. Journal of power sources, 132(1):206–208, 2004.

[72] Béatrice Garcia, Serge Lavallée, Gérald Perron, Christophe Michot, and Michel Armand. Room temperature molten salts as lithium battery electrolyte. Electrochimica Acta, 49(26):4583–4588, 2004.

[73] David R Gaskell. Introduction to the Thermodynamics of Materials, volume 2. CRC Press, 2008.

[74] John B Goodenough. Cathode materials: A personal perspective. Journal of Power Sources, 174(2):996–1000, 2007.

[75] John B Goodenough and Youngsik Kim. Challenges for rechargeable li batteries. Chemistry of Materials, 22(3):587–603, 2009.

[76] A Guerfi, M Dontigny, P Charest, M Petitclerc, M Lagacé, A Vijh, and K Zaghib. Improved electrolytes for li-ion batteries: Mixtures of ionic liquid and organic electrolyte with enhanced safety and electrochemical performance. Journal of Power Sources, 195(3):845–852, 2010.

[77] A Guerfi, S Duchesne, Y Kobayashi, A Vijh, and K Zaghib. $LiFePO_4$ and graphite electrodes with ionic liquids based on bis (fluorosulfonyl) imide $(FSI)^-$ for li-ion batteries. Journal of Power Sources, 175(2):866–873, 2008.

[78] A Guerfi, S Duchesne, Y Kobayashi, A Vijh, and K Zaghib. LiFePO$_4$ and graphite electrodes with ionic liquids based on bis (fluorosulfonyl) imide (FSI)- for Li-ion batteries. Journal of Power Sources, 175(2):866–873, 2008.

[79] BB Hallac, OE Geiculescu, RV Rajagopal, SE Creager, and DD DesMarteau. Lithium-conducting ionic melt electrolytes from polyether-functionalized fluorosulfonimide anions. Electrochimica Acta, 53(20):5985–5991, 2008.

[80] Hong-Bo Han, Si-Si Zhou, Dai-Jun Zhang, Shao-Wei Feng, Li-Fei Li, Kai Liu, Wen-Fang Feng, Jin Nie, Hong Li, Xue-Jie Huang, et al. Lithium bis (fluorosulfonyl) imide (LiFSI) as conducting salt for nonaqueous liquid electrolytes for lithium-ion batteries: Physicochemical and electrochemical properties. Journal of Power Sources, 196(7):3623–3632, 2011.

[81] J Hassoun, A Fernicola, MA Navarra, S Panero, and B Scrosati. An advanced lithium-ion battery based on a nanostructured Sn–C anode and an electrochemically stable LiTFSi-Py$_{24}$TFSI ionic liquid electrolyte. Journal of Power Sources, 195(2):574–579, 2010.

[82] Jusef Hassoun, Ki-Soo Lee, Yang-Kook Sun, and Bruno Scrosati. An advanced lithium ion battery based on high performance electrode materials. Journal of the American Chemical Society, 133(9):3139–3143, 2011.

[83] TD Hatchard and JR Dahn. In situ XRD and electrochemical study of the reaction of lithium with amorphous silicon. Journal of The Electrochemical Society, 151(6):A838–A842, 2004.

[84] Kikuko Hayamizu, Yuichi Aihara, Hiroe Nakagawa, Toshiyuki Nukuda, and William S Price. Ionic conduction and ion diffusion in binary room-temperature ionic liquids composed of [emim][BF$_4$] and LiBF$_4$. The Journal of Physical Chemistry B, 108(50):19527–19532, 2004.

[85] Günther Höhne, Wolfgang Hemminger, and H-J Flammersheim. Differential scanning calorimetry. Springer, 2003.

[86] M Holzapfel, C Jost, A Prodi-Schwab, F Krumeich, A Würsig, H Buqa, and P Novak. Stabilisation of lithiated graphite in an electrolyte based on ionic liquids: an electrochemical and scanning electron microscopy study. Carbon, 43(7):1488–1498, 2005.

[87] Michael Holzapfel, Carsten Jost, and Petr Novák. Stable cycling of graphite in an ionic liquid based electrolyte. Chemical communications, pages 2098–2099, 2004.

[88] Jihyun Hong, Dong-Hwa Seo, Sung-Wook Kim, Hyeokjo Gwon, Song-Taek Oh, and Kisuk Kang. Structural evolution of layered Li$_1$.2Ni$_0$.2Mn$_0$.6O$_2$ upon electrochemical cycling in a li rechargeable battery. Journal of Materials Chemistry, 20(45):10179–10186, 2010.

[89] Patrick C Howlett, Douglas R MacFarlane, and Anthony F Hollenkamp. High lithium metal cycling efficiency in a room-temperature ionic liquid. Electrochemical and Solid-State Letters, 7(5):A97–A101, 2004.

[90] Zheng-Ming Huang, Y-Z Zhang, M Kotaki, and S Ramakrishna. A review on polymer nanofibers by electrospinning and their applications in nanocomposites. Composites Science and Technology, 63(15):2223–2253, 2003.

[91] Robert A Huggins. Lithium alloy negative electrodes. Journal of Power Sources, 81:13–19, 1999.

[92] Robert A. Huggins. Advanced batteries: materials science aspects. Springer, 2008.

[93] Robert A. Huggins and D Elwell. Morphological stability of a plane interface during electroncrystallization from molten salts. Journal of Crystal Growth, 37(2):159–162, 1977.

[94] Masashi Ishikawa, Toshinori Sugimoto, Manabu Kikuta, Eriko Ishiko, and Michiyuki Kono. Pure ionic liquid electrolytes compatible with a graphitized carbon negative electrode in rechargeable lithium-ion batteries. Journal of power sources, 162(1):658–662, 2006.

[95] Liwen Ji, Honghe Zheng, Ariel Ismach, Zhongkui Tan, Shidi Xun, Eric Lin, Vincent Battaglia, Venkat Srinivasan, and Yuegang Zhang. Graphene/Si multilayer structure anodes for advanced half and full lithium-ion cells. Nano Energy, 1(1):164–171, 2012.

[96] Xiulei Ji, Kyu Tae Lee, and Linda F Nazar. A highly ordered nanostructured carbon–sulphur cathode for lithium-sulphur batteries. Nature materials, 8(6):500–506, 2009.

[97] Seo Hee Ju, Ik-Su Kang, Yoon-Sung Lee, Won-Kyung Shin, Saheum Kim, Kyomin Shin, and Dong-Won Kim. Improvement of the cycling performance of $lini_{0.6}co_{0.2}mn_{0.2}o_2$ cathode active materials by a dual-conductive polymer coating. ACS applied materials & interfaces, 6(4):2546–2552, 2014.

[98] Sung-Kyun Jung, Hyeokjo Gwon, Jihyun Hong, Kyu-Young Park, Dong-Hwa Seo, Haegyeom Kim, Jangsuk Hyun, Wooyoung Yang, and Kisuk Kang. Understanding the degradation mechanisms of $lini_{0.5}co_{0.2}mn_{0.3}o_2$ cathode material in lithium ion batteries. Advanced Energy Materials, 4(1), 2014.

[99] Yoon Seok Jung, Andrew S Cavanagh, Anne C Dillon, Markus D Groner, Steven M George, and Se-Hee Lee. Enhanced stability of $LiCoO_2$ cathodes in lithium-ion batteries using surface modification by atomic layer deposition. Journal of The Electrochemical Society, 157(1):A75–A81, 2010.

[100] P Kalyani, S Chitra, T Mohan, and S Gopukumar. Lithium metal rechargeable cells using li_2mno_3 as the positive electrode. Journal of power sources, 80(1):103–106, 1999.

[101] Byoungwoo Kang and Gerbrand Ceder. Battery materials for ultrafast charging and discharging. Nature, 458(7235):190–193, 2009.

[102] S-H Kang and K Amine. Layered li $(li_{0.2}ni_{0.15+0.5z}co_{0.10}mn_{0.55-0.5z})o_{2-z}f_z$ cathode materials for li-ion secondary batteries. Journal of power sources, 146(1):654–657, 2005.

[103] Uday Kasavajjula, Chunsheng Wang, and A John Appleby. Nano-and bulk-silicon-based insertion anodes for lithium-ion secondary cells. Journal of Power Sources, 163(2):1003–1039, 2007.

[104] Hansu Kim, Eung-Ju Lee, and Yang-Kook Sun. Recent advances in the si-based nanocomposite materials as high capacity anode materials for lithium ion batteries. Materials Today, 17(6):285–297, 2014.

[105] Hyejung Kim, Min Gyu Kim, Hu Young Jeong, Haisol Nam, and Jaephil Cho. A new coating method for alleviating surface degradation of $lini_{0.6}co_{0.2}mn_{0.2}o_2$ cathode material: Nanoscale surface treatment of primary particles. Nano letters, 15(3):2111–2119, 2015.

[106] Seok Kim, Yongju Jung, and Soo-Jin Park. Effects of imidazolium salts on discharge performance of rechargeable lithium–sulfur cells containing organic solvent electrolytes. Journal of power sources, 152:272–277, 2005.

[107] Marija Kirchhöfer, Jan von Zamory, Elie Paillard, and Stefano Passerini. Separators for li-ion and li-metal battery including ionic liquid based electrolytes based on the TFSI and FSI anions. International journal of molecular sciences, 15(8):14868–14890, 2014.

[108] VS Kolosnitsyn, EV Kuz'mina, EV Karaseva, and SE Mochalov. Impedance spectroscopy studies of changes in the properties of lithium-sulfur cells in the course of cycling. Russian Journal of Electrochemistry, 47(7):793–798, 2011.

[109] Yukinori Koyama, Timothy E Chin, Urs Rhyner, Richard K Holman, Steven R Hall, and Y-M Chiang. Harnessing the actuation potential of solid-state intercalation compounds. Advanced Functional Materials, 16(4):492–498, 2006.

[110] Yukinori Koyama, Timothy E Chin, Urs Rhyner, Richard K Holman, Steven R Hall, and Y-M Chiang. Harnessing the actuation potential of solid-state intercalation compounds. Advanced Functional Materials, 16(4):492–498, 2006.

[111] Elisabeth Krämer, Stefano Passerini, and Martin Winter. Dependency of aluminum collector corrosion in lithium ion batteries on the electrolyte solvent. ECS Electrochemistry Letters, 1(5):C9–C11, 2012.

[112] Larry J Krause, William Lamanna, John Summerfield, Mark Engle, Gary Korba, Robert Loch, and Radoslav Atanasoski. Corrosion of aluminum at high voltages in non-aqueous electrolytes containing perfluoroalkylsulfonyl imides; new lithium salts for lithium-ion cells. Journal of power sources, 68(2):320–325, 1997.

[113] Georg Kresse and Jürgen Furthmüller. Efficient iterative schemes for ab initio total-energy calculations using a plane-wave basis set. Physical Review B, 54(16):11169, 1996.

[114] Georg Kresse and D Joubert. From ultrasoft pseudopotentials to the projector augmented-wave method. Physical Review B, 59(3):1758, 1999.

[115] Keigo Kubota, Toshiyuki Nohira, Takuya Goto, and Rika Hagiwara. Novel inorganic ionic liquids possessing low melting temperatures and wide electrochemical windows: Binary mixtures of alkali bis (fluorosulfonyl) amides. Electrochemistry Communications, 10(12):1886–1888, 2008.

[116] R-S Kühnel, N Böckenfeld, S Passerini, M Winter, and A Balducci. Mixtures of ionic liquid and organic carbonate as electrolyte with improved safety and performance for rechargeable lithium batteries. Electrochimica Acta, 56(11):4092–4099, 2011.

[117] Ruben-Simon Kühnel, Mechthild Lübke, Martin Winter, Stefano Passerini, and Andrea Balducci. Suppression of aluminum current collector corrosion in ionic liquid containing electrolytes. Journal of Power Sources, 214:178–184, 2012.

[118] Byoung H Lee, Byunghoon Yoon, Aziz I Abdulagatov, Robert A Hall, and Steven M George. Growth and properties of hybrid organic-inorganic metalcone films using molecular layer deposition techniques. Advanced Functional Materials, 23(5):532–546, 2013.

[119] HS Lee, XQ Yang, X Sun, and J McBreen. Synthesis of a new family of fluorinated boronate compounds as anion receptors and studies of their use as additives in lithium battery electrolytes. Journal of power sources, 97:566–569, 2001.

[120] Jae Hyun Lee, Hyang Mok Lee, and Soonho Ahn. Battery dimensional changes occurring during charge/discharge cycles—thin rectangular lithium ion and polymer cells. Journal of Power Sources, 119:833–837, 2003.

[121] Jang-Soo Lee, Sun Tai Kim, Ruiguo Cao, Nam-Soon Choi, Meilin Liu, Kyu Tae Lee, and Jaephil Cho. Metal–air batteries with high energy density: Li–air versus Zn–air. Advanced Energy Materials, 1(1):34–50, 2011.

[122] Jung-In Lee, Eun-Ho Lee, Jang-Hoon Park, Soojin Park, and Sang-Young Lee. Ultrahigh-energy-density lithium-ion batteries based on a high-capacity anode and a high-voltage cathode with an electroconductive nanoparticle shell. Advanced Energy Materials, 2014.

[123] Kyung-Ho Lee and Seung-Wan Song. One-step hydrothermal synthesis of mesoporous anatase TiO_2 microsphere and interfacial control for enhanced lithium storage performance. ACS Applied Materials and Interfaces, 3(9):3697–3703, 2011.

[124] Kevin Leung. Electronic structure modeling of electrochemical reactions at electrode/electrolyte interfaces in lithium ion batteries. The Journal of Physical Chemistry C, 117(4):1539–1547, 2012.

[125] Kevin Leung, Susan B Rempe, Michael E Foster, Yuguang Ma, Julibeth M Martinez del la Hoz, Na Sai, and Perla B Balbuena. Modeling electrochemical decomposition of fluoroethylene carbonate on silicon anode surfaces in lithium ion batteries. Journal of The Electrochemical Society, 161(3):A213–A221, 2014.

[126] Kevin Leung and Craig M Tenney. Toward first principles prediction of voltage dependences of electrolyte/electrolyte interfacial processes in lithium ion batteries. The Journal of Physical Chemistry C, 117(46):24224–24235, 2013.

[127] Andrzej Lewandowski and Agnieszka Świderska-Mocek. Properties of the lithium and graphite–lithium anodes in n-methyl-n-propylpyrrolidinium bis (trifluoromethanesulfonyl) imide. Journal of Power Sources, 194(1):502–507, 2009.

[128] AP Lewandowski, AF Hollenkamp, SW Donne, and AS Best. Cycling and rate performance of Li–$LiFePO_4$ cells in mixed FSI-TFSI room temperature ionic liquids. Journal of Power Sources, 195(7):2029–2035, 2010.

[129] Jing Li, L Christensen, MN Obrovac, KC Hewitt, and JR Dahn. Effect of heat treatment on Si electrodes using polyvinylidene fluoride binder. Journal of the Electrochemical Society, 155(3):A234–A238, 2008.

[130] Pimpa Limthongkul, Young-Il Jang, Nancy J Dudney, and Yet-Ming Chiang. Electrochemically-driven solid-state amorphization in lithium-silicon alloys and implications for lithium storage. Acta Materialia, 51(4):1103–1113, 2003.

[131] Feng Lin, Isaac M Markus, Dennis Nordlund, Tsu-Chien Weng, Mark D Asta, Huolin L Xin, and Marca M Doeff. Surface reconstruction and chemical evolution of stoichiometric layered cathode materials for lithium-ion batteries. Nature communications, 5, 2014.

[132] David Linden and TB Reddy. Handbook of batteries, 2002.

[133] David Linden and TB Reddy. Handbook of batteries, 2002.

[134] Gao Liu, Shidi Xun, Nenad Vukmirovic, Xiangyun Song, Paul Olalde-Velasco, Honghe Zheng, Vince S Battaglia, Linwang Wang, and Wanli Yang. Polymers with tailored electronic structure for high capacity lithium battery electrodes. Advanced Materials, 23(40):4679–4683, 2011.

[135] Ling Liu, Zhongzhi Yuan, Caixia Qiu, and Jincheng Liu. A novel FeS_2/CNT micro-spherical cathode material with enhanced electrochemical characteristics for lithium-ion batteries. Solid State Ionics, 241:25–29, 2013.

[136] Nian Liu, Liangbing Hu, Matthew T McDowell, Ariel Jackson, and Yi Cui. Prelithiated silicon nanowires as an anode for lithium ion batteries. ACS Nano, 5(8):6487–6493, 2011.

[137] Nian Liu, Zhenda Lu, Jie Zhao, Matthew T McDowell, Hyun-Wook Lee, Wenting Zhao, and Yi Cui. A pomegranate-inspired nanoscale design for large-volume-change lithium battery anodes. Nature nanotechnology, 9(3):187–192, 2014.

[138] Nian Liu, Zhenda Lu, Jie Zhao, Matthew T McDowell, Hyun-Wook Lee, Wenting Zhao, and Yi Cui. A pomegranate-inspired nanoscale design for large-volume-change lithium battery anodes. Nature Nanotechnology, 9(3):187–192, 2014.

[139] Xiao Hua Liu, Li Zhong, Shan Huang, Scott X Mao, Ting Zhu, and Jian Yu Huang. Size-dependent fracture of silicon nanoparticles during lithiation. ACS Nano, 6(2):1522–1531, 2012.

[140] Wenquan Lu, Zonghai Chen, H Joachin, J Prakash, J Liu, and K Amine. Thermal and electrochemical characterization of MCMB/$LiNi_{1/3}Co_{1/3}Mn_{1/3}O_2$ using LiBoB as an electrolyte additive. Journal of power sources, 163(2):1074–1079, 2007.

[141] Simon F Lux, Martin Schmuck, Giovanni B Appetecchi, Stefano Passerini, Martin Winter, and Andrea Balducci. Lithium insertion in graphite from ternary ionic liquid–lithium salt electrolytes: Ii. evaluation of specific capacity and cycling efficiency and stability at room temperature. Journal of Power Sources, 192(2):606–611, 2009.

[142] A Magasinski, P Dixon, B Hertzberg, A Kvit, J Ayala, and G Yushin. High-performance lithium-ion anodes using a hierarchical bottom-up approach. Nature Materials, 9(4):353–358, 2010.

[143] Ninie SA Manan, Leigh Aldous, Yatimah Alias, Paul Murray, Lesley J Yellowlees, M Cristina Lagunas, and Christopher Hardacre. Electrochemistry of sulfur and polysulfides in ionic liquids. The Journal of Physical Chemistry B, 115(47):13873–13879, 2011.

[144] Aleksandr V Marenich, Christopher J Cramer, and Donald G Truhlar. Universal solvation model based on solute electron density and on a continuum model of the solvent defined by the bulk dielectric constant and atomic surface tensions. The Journal of Physical Chemistry B, 113(18):6378–6396, 2009.

[145] E Markevich, V Baranchugov, G Salitra, D Aurbach, and Michael A Schmidt. Behavior of graphite electrodes in solutions based on ionic liquids in in situ raman studies. Journal of The Electrochemical Society, 155(2):A132–A137, 2008.

[146] E Markevich, R Sharabi, V Borgel, H Gottlieb, G Salitra, D Aurbach, Guenter Semrau, and Michael A Schmidt. In situ FTIR study of the decomposition of N-butyl-N-methylpyrrolidinium bis (trifluoromethanesulfonyl) amide ionic liquid during cathodic polarization of lithium and graphite electrodes. Electrochimica Acta, 55(8):2687–2696, 2010.

[147] Julibeth M Martinez de la Hoz, Kevin Leung, and Perla B Balbuena. Reduction mechanisms of ethylene carbonate on Si anodes of lithium-ion batteries: Effects of degree of lithiation and nature of exposed surface. ACS Applied Materials & Interfaces, 5(24):13457–13465, 2013.

[148] Hajime Matsumoto, Hikari Sakaebe, Kuniaki Tatsumi, Manabu Kikuta, Eriko Ishiko, and Michiyuki Kono. Fast cycling of Li/LiCoO$_2$ cell with low-viscosity ionic liquids based on bis (fluorosulfonyl) imide [FSI]-. Journal of Power Sources, 160(2):1308–1313, 2006.

[149] Matthew Todd Mcdowell. Understanding the electrochemical reaction of lithium with single silicon nanostructures. PhD thesis, Stanford University, 2013.

[150] Yuriy V Mikhaylik and James R Akridge. Polysulfide shuttle study in the Li/S battery system. Journal of the Electrochemical Society, 151(11):A1969–A1976, 2004.

[151] Debasish Mohanty, Jianlin Li, Daniel P Abraham, Ashfia Huq, E Andrew Payzant, David L Wood III, and Claus Daniel. Unraveling the voltage-fade mechanism in high-energy-density lithium-ion batteries: Origin of the tetrahedral cations for spinel conversion. Chemistry of Materials, 26(21):6272–6280, 2014.

[152] Dominik Moosbauer, Sandra Zugmann, Marius Amereller, and Heiner J Gores. Effect of ionic liquids as additives on lithium electrolytes: Conductivity, electrochemical stability, and aluminum corrosion. Journal of Chemical and Engineering Data, 55(5):1794–1798, 2010.

[153] Masayuki Morita, Takuo Shibata, Nobuko Yoshimoto, and Masashi Ishikawa. Anodic behavior of aluminum in organic solutions with different electrolytic salts for lithium ion batteries. Electrochimica Acta, 47(17):2787–2793, 2002.

[154] John F Moulder, William F Stickle, Peter E Sobol, and Kenneth D Bomben. Handbook of X-ray photoelectron spectroscopy, volume 40. Perkin Elmer Eden Prairie, MN, 1992.

[155] B. Murphy and A. Abramowitz. European nations are increasing electricity generation using no-carbon sources. U.S. Energy Information Administration, September 2014.

[156] Martina Nádherná, Jakub Reiter, Jože Moškon, and Robert Dominko. Lithium bis (fluorosulfonyl) imide–PYR$_1$4TFSI ionic liquid electrolyte compatible with graphite. Journal of power sources, 196(18):7700–7706, 2011.

[157] T Nagaura and K Tozawa. Progress in batteries and solar cells. Progress in Batteries and Solar Cells, 9, 1990.

[158] Maria Assunta Navarra. Ionic liquids as safe electrolyte components for Li-metal and Li-ion batteries. MRS bulletin, 38(07):548–553, 2013.

[159] Andreas Netz, Robert A Huggins, and Werner Weppner. The formation and properties of amorphous silicon as negative electrode reactant in lithium systems. Journal of Power Sources, 119:95–100, 2003.

[160] Cao Cuong Nguyen and Seung-Wan Song. Characterization of SEI layer formed on high performance Si–Cu anode in ionic liquid battery electrolyte. Electrochemistry Communications, 12(11):1593–1595, 2010.

[161] Mengyun Nie, Daniel P Abraham, Yanjing Chen, Arijit Bose, and Brett L Lucht. Silicon solid electrolyte interphase (SEI) of lithium ion battery characterized by microscopy and spectroscopy. The Journal of Physical Chemistry C, 117(26):13403–13412, 2013.

[162] United States N.O.A.A. Carbon dioxide at NOAA's Mauna Loa observatory reaches new milestone. National Oceanic and Atmospheric Administration - ESRL News, May 2013.

[163] M Ali Omar. Elementary solid state physics: principles and applications, volume 157. Addison-Wesley Reading, MA, USA:, 1975.

[164] Elie Paillard, Qian Zhou, Wesley A Henderson, Giovanni B Appetecchi, Maria Montanino, and Stefano Passerini. Electrochemical and physicochemical properties of PY_14FSI-based electrolytes with LiFSI. Journal of The Electrochemical Society, 156(11):A891–A895, 2009.

[165] Jun-Woo Park, Kazuhide Ueno, Naoki Tachikawa, Kaoru Dokko, and Masayoshi Watanabe. Ionic liquid electrolytes for lithium–sulfur batteries. The Journal of Physical Chemistry C, 117(40):20531–20541, 2013.

[166] Mi-Hee Park, Min Gyu Kim, Jaebum Joo, Kitae Kim, Jeyoung Kim, Soonho Ahn, Yi Cui, and Jaephil Cho. Silicon nanotube battery anodes. Nano Letters, 9(11):3844–3847, 2009.

[167] Myounggu Park, Xiangchun Zhang, Myoungdo Chung, Gregory B Less, and Ann Marie Sastry. A review of conduction phenomena in li-ion batteries. Journal of Power Sources, 195(24):7904–7929, 2010.

[168] E Peled, Y Sternberg, A Gorenshtein, and Y Lavi. Lithium-sulfur battery: evaluation of dioxolane-based electrolytes. Journal of the Electrochemical Society, 136(6):1621–1625, 1989.

[169] John P Perdew, Kieron Burke, and Matthias Ernzerhof. Generalized gradient approximation made simple. Physical Review Letters, 77(18):3865, 1996.

[170] Daniela Molina Piper, Tyler Evans, Kevin Leung, Tylan Watkins, Jarred Olson, Seul Cham Kim, Sang Sub Han, Vinay Bhat, Kyu Hwan Oh, Daniel A Buttry, et al. Stable silicon-ionic liquid interface for next-generation lithium-ion batteries. Nature communications, 6, 2015.

[171] Daniela Molina Piper, Jonathan J Travis, Matthias Young, Seoung-Bum Son, Seul Cham Kim, Kyu Hwan Oh, Steven M George, Chunmei Ban, and Se-Hee Lee. Reversible high-capacity Si nanocomposite anodes for lithium-ion batteries enabled by molecular layer deposition. Advanced Materials, 26(10):1596–1601, 2014.

[172] Daniela Molina Piper, Jae Ha Woo, Seoung-Bum Son, Seul Cham Kim, Kyu Hwan Oh, and Se-Hee Lee. Hierarchical porous framework of Si-based electrodes for minimal volumetric expansion. Advanced Materials, 26(21):3520–3525, 2014.

[173] Daniela Molina Piper, Thomas A Yersak, Seoung-Bum Son, Seul Cham Kim, Chan Soon Kang, Kyu Hwan Oh, Chunmei Ban, Anne C Dillon, and Se-Hee Lee. Conformal coatings of cyclized-PAN for mechanically resilient Si nano-composite anodes. Advanced Energy Materials, 3(6):697–702, 2013.

[174] Daniela Molina Piper, Thomas A. Yersak, Seoung-Bum Son, Seul Cham Kim, Chan Soon Kang, Kyu Hwan Oh, Chunmei Ban, Anne C. Dillon, and Se-Hee Lee. Conformal coatings of cyclized-PAN for mechanically resilient Si nano-composite anodes. Advanced Energy Materials, 3(6):697–702, 2013.

[175] Prasanth Raghavan, James Manuel, Xiaohui Zhao, Dul-Sun Kim, Jou-Hyeon Ahn, and Changwoon Nah. Preparation and electrochemical characterization of gel polymer electrolyte based on electrospun polyacrylonitrile nonwoven membranes for lithium batteries. Journal of Power Sources, 196(16):6742–6749, 2011.

[176] Jakub Reiter, Martina Nádherná, and Robert Dominko. Graphite and $LiCo_1/3Mn_1/3Ni_1/3O_2$ electrodes with piperidinium ionic liquid and lithium bis (fluorosulfonyl) imide for li-ion batteries. Journal of Power Sources, 205:402–407, 2012.

[177] Leah Autumn Riley. Atomic layer deposition for improved electrochemical stability for lithium ion batteries. PhD thesis, University of Colorado at Boulder, 2011.

[178] MH Rossouw and MM Thackeray. Lithium manganese oxides from li 2 mno 3 for rechargeable lithium battery applications. Materials research bulletin, 26(6):463–473, 1991.

[179] E Peter Roth and Christopher J Orendorff. How electrolytes influence battery safety. Electrochemical Society Interface, 21(2):45–49, 2012.

[180] Young-Gyoon Ryu, SeokSoo Lee, SangKook Mah, Dong Joon Lee, Kyungjung Kwon, SeungSik Hwang, and SeokGwang Doo. Electrochemical behaviors of silicon electrode in lithium salt solution containing alkoxy silane additives. Journal of the Electrochemical Society, 155(8):A583–A589, 2008.

[181] Hikari Sakaebe, Hajime Matsumoto, and Kuniaki Tatsumi. Discharge–charge properties of $Li/LiCoO_2$ cell using room temperature ionic liquids (RTILs) based on quaternary ammonium cation–effect of the structure. Journal of power sources, 146(1):693–697, 2005.

[182] Hikari Sakaebe, Hajime Matsumoto, and Kuniaki Tatsumi. Application of room temperature ionic liquids to li batteries. Electrochimica Acta, 53(3):1048–1054, 2007.

[183] Takaya Sato, Tatsuya Maruo, Shoko Marukane, and Kentaro Takagi. Ionic liquids containing carbonate solvent as electrolytes for lithium ion cells. Journal of Power Sources, 138(1):253–261, 2004.

[184] Johan Scheers, Sébastien Fantini, and Patrik Johansson. A review of electrolytes for lithium–sulphur batteries. Journal of Power Sources, 255:204–218, 2014.

[185] Christian Schreiner, Sandra Zugmann, Robert Hartl, and Heiner J Gores. Fractional walden rule for ionic liquids: examples from recent measurements and a critique of the so-called ideal kcl line for the walden plot. Journal of Chemical Engineering Data, 55(5):1784–1788, 2009.

[186] Bruno Scrosati and Jürgen Garche. Lithium batteries: Status, prospects and future. Journal of Power Sources, 195(9):2419–2430, 2010.

[187] Shiro Seki, Yo Kobayashi, Hajime Miyashiro, Yasutaka Ohno, Akira Usami, Yuichi Mita, Nobuo Kihira, Masayoshi Watanabe, and Nobuyuki Terada. Lithium secondary batteries using modified-imidazolium room-temperature ionic liquid. The Journal of Physical Chemistry B, 110(21):10228–10230, 2006.

[188] Shiro Seki, Yasutaka Ohno, Yo Kobayashi, Hajime Miyashiro, Akira Usami, Yuichi Mita, Hiroyuki Tokuda, Masayoshi Watanabe, Kikuko Hayamizu, Seiji Tsuzuki, et al. Imidazolium-based room-temperature ionic liquid for lithium secondary batteries effects of lithium salt concentration. Journal of The Electrochemical Society, 154(3):A173–A177, 2007.

[189] Joongpyo Shim, Kathryn A Striebel, and Elton J Cairns. The lithium/sulfur rechargeable cell effects of electrode composition and solvent on cell performance. Journal of the Electrochemical Society, 149(10):A1321–A1325, 2002.

[190] J-H Shin, WA Henderson, GB Appetecchi, F Alessandrini, and S Passerini. Recent developments in the ENEA lithium metal battery project. Electrochimica acta, 50(19):3859–3865, 2005.

[191] Joon-Ho Shin, Wesley A Henderson, and Stefano Passerini. Ionic liquids to the rescue? overcoming the ionic conductivity limitations of polymer electrolytes. Electrochemistry Communications, 5(12):1016–1020, 2003.

[192] Joon-Ho Shin, Wesley A Henderson, and Stefano Passerini. An elegant fix for polymer electrolytes. Electrochemical and solid-state letters, 8(2):A125–A127, 2005.

[193] Ewen Smith and Geoffrey Dent. Modern Raman spectroscopy: a practical approach. John Wiley & Sons, 2005.

[194] Seoung-Bum Son, Seul Cham Kim, Chan Soon Kang, Thomas A Yersak, Yoon-Chang Kim, Chun-Gyoo Lee, Sung-Hwan Moon, Jong Soo Cho, Jeong-Tak Moon, Kyu Hwan Oh, et al. A highly reversible nano-si anode enabled by mechanical confinement in an electrochemically activated $Li_xTi_4Ni_4Si_7$ matrix. Advanced Energy Materials, 2(10):1226–1231, 2012.

[195] Seoung-Bum Son, Seul Cham Kim, Chan Soon Kang, Thomas A Yersak, Yoon-Chang Kim, Chun-Gyoo Lee, Sung-Hwan Moon, Jong Soo Cho, Jeong-Tak Moon, Kyu Hwan Oh, et al. A highly reversible nano-Si anode enabled by mechanical confinement in an electrochemically activated $Li_xTi_4Ni_4Si_7$ matrix. Advanced Energy Materials, 2(10):1226–1231, 2012.

[196] Seoung-Bum Son, James E Trevey, Hyunchul Roh, Sung-Hwan Kim, Kee-Bum Kim, Jong Soo Cho, Jeong-Tak Moon, Christopher M DeLuca, Kurt K Maute, Martin L Dunn, et al. Microstructure study of electrochemically driven Li_xSi. Advanced Energy Materials, 1(6):1199–1204, 2011.

[197] Seoung-Bum Son, James E Trevey, Hyunchul Roh, Sung-Hwan Kim, Kee-Bum Kim, Jong Soo Cho, Jeong-Tak Moon, Christopher M DeLuca, Kurt K Maute, Martin L Dunn, et al. Microstructure study of electrochemically driven lixsi. Advanced Energy Materials, 1(6):1199–1204, 2011.

[198] Seoung-Bum Son, Thomas A Yersak, Daniela Molina Piper, Seul Cham Kim, Chan Soon Kang, Jong Soo Cho, Soon-Sung Suh, Young-Ugk Kim, Kyu Hwan Oh, and Se-Hee Lee. A stabilized PAN-FeS$_2$ cathode with an EC/DEC liquid electrolyte. Advanced Energy Materials, 4(3), 2014.

[199] Jin-Woo Song, Cao Cuong Nguyen, and Seung-Wan Song. Stabilized cycling performance of silicon oxide anode in ionic liquid electrolyte for rechargeable lithium batteries. RSC Adv., 2:2003–2009, 2012.

[200] Taeseup Song, Jianliang Xia, Jin-Hyon Lee, Dong Hyun Lee, Moon-Seok Kwon, Jae-Man Choi, Jian Wu, Seok Kwang Doo, Hyuk Chang, Won Il Park, et al. Arrays of sealed silicon nanotubes as anodes for lithium ion batteries. Nano Letters, 10(5):1710–1716, 2010.

[201] E Strauss, G Ardel, V Livshits, L Burstein, D Golodnitsky, and E Peled. Lithium polymer electrolyte pyrite rechargeable battery: comparative characterization of natural pyrite from different sources as cathode material. Journal of power sources, 88(2):206–218, 2000.

[202] Toshinori Sugimoto, Yosuke Atsumi, Manabu Kikuta, Eriko Ishiko, Michiyuki Kono, and Masashi Ishikawa. Ionic liquid electrolyte systems based on bis (fluorosulfonyl) imide for lithium-ion batteries. Journal of Power Sources, 189(1):802–805, 2009.

[203] Xiao-Guang Sun and Sheng Dai. Electrochemical investigations of ionic liquids with vinylene carbonate for applications in rechargeable lithium ion batteries. Electrochimica Acta, 55(15):4618–4626, 2010.

[204] Naoki Tachikawa, Kento Yamauchi, Eriko Takashima, Jun-Woo Park, Kaoru Dokko, and Masayoshi Watanabe. Reversibility of electrochemical reactions of sulfur supported on inverse opal carbon in glyme-Li salt molten complex electrolytes. Chemical Communications, 47(28):8157–8159, 2011.

[205] J-M Tarascon. Key challenges in future Li-battery research. Philosophical Transactions of the Royal Society of London A: Mathematical, Physical and Engineering Sciences, 368(1923):3227–3241, 2010.

[206] J-M Tarascon. Key challenges in future Li-battery research. Philosophical Transactions of the Royal Society A: Mathematical, Physical and Engineering Sciences, 368(1923):3227–3241, 2010.

[207] J-M Tarascon and Michel Armand. Issues and challenges facing rechargeable lithium batteries. Nature, 414(6861):359–367, 2001.

[208] Geoffrey Taylor. Electrically driven jets. Proceedings of the Royal Society of London. A. Mathematical and Physical Sciences, 313(1515):453–475, 1969.

[209] Daniel Tencer. World's car population hits 1 billion. The Huffington Post, February 19 2013.

[210] Michael M Thackeray, Sun-Ho Kang, Christopher S Johnson, John T Vaughey, Roy Benedek, and SA Hackney. Li$_2$mno$_3$-stabilized limo 2 (m= mn, ni, co) electrodes for lithium-ion batteries. Journal of Materials Chemistry, 17(30):3112–3125, 2007.

[211] Michael M Thackeray, Sun-Ho Kang, Christopher S Johnson, John T Vaughey, Roy Benedek, and SA Hackney. Li_2MnO_3-stabilized $LiMO_2$ (M= Mn, Ni, Co) electrodes for lithium-ion batteries. Journal of Materials Chemistry, 17(30):3112–3125, 2007.

[212] Tetsuya Tsuda and Charles L Hussey. Electrochemical applications of room-temperature ionic liquids. Interface-Electrochemical Society, 16(1):42–49, 2007.

[213] Marc Uerdingen, Claudia Treber, Martina Balser, Günter Schmitt, and Christoph Werner. Corrosion behaviour of ionic liquids. Green Chemistry, 7(5):321–325, 2005.

[214] Berkeley Lab Venkat Srinivasan. The future of batteries. Interview by Sabin Russel, June 2011.

[215] Bryan Walsh. The scariest environmental fact in the world. Time Magazine, January 2013.

[216] De-Wei Wang, Qi-Hua Wang, and Ting-Mei Wang. Controlled growth of pyrite FeS_2 crystallites by a facile surfactant-assisted solvothermal method. CrystEngComm, 12(3):755–761, 2010.

[217] Feng Wang, Rosa Robert, Natasha A Chernova, Nathalie Pereira, Fredrick Omenya, Fadwa Badway, Xiao Hua, Michael Ruotolo, Ruigang Zhang, Lijun Wu, et al. Conversion reaction mechanisms in lithium ion batteries: study of the binary metal fluoride electrodes. Journal of the American Chemical Society, 133(46):18828–18836, 2011.

[218] Lina Wang and Hye Ryung Byon. N-methyl-n-propylpiperidinium bis (trifluoromethanesulfonyl) imide-based organic electrolyte for high performance lithium–sulfur batteries. Journal of Power Sources, 236:207–214, 2013.

[219] Wei Wang, Dan Li, Miao Tian, Yung-Cheng Lee, and Ronggui Yang. Wafer-scale fabrication of silicon nanowire arrays with controllable dimensions. Applied Surface Science, 258(22):8649–8655, 2012.

[220] Wei Wang, Miao Tian, Aziz Abdulagatov, Steven M George, Yung-Cheng Lee, and Ronggui Yang. Three-dimensional Ni/TiO_2 nanowire network for high areal capacity lithium ion microbattery applications. Nano letters, 12(2):655–660, 2012.

[221] Wei Wang, Miao Tian, Yujie Wei, Se-Hee Lee, Yung-Cheng Lee, and Ronggui Yang. Binder-free three-dimensional silicon/carbon nanowire networks for high performance lithium-ion battery anodes. Nano Energy, 2(5):943–950, 2013.

[222] Yadong Wang, K Zaghib, A Guerfi, Fernanda FC Bazito, Roberto M Torresi, and JR Dahn. Accelerating rate calorimetry studies of the reactions between ionic liquids and charged lithium ion battery electrode materials. Electrochimica acta, 52(22):6346–6352, 2007.

[223] Anthony R West. Basic solid state chemistry. Wiley New York, 1988.

[224] M Stanley Whittingham. Electrical energy storage and intercalation chemistry. Science, 192(4244):1126–1127, 1976.

[225] M Stanley Whittingham. Lithium batteries and cathode materials. Chemical reviews, 104(10):4271–4302, 2004.

[226] M Stanley Whittingham. Lithium batteries and cathode materials. Chemical Reviews, 104(10):4271–4302, 2004.

[227] Hui Wu, Gerentt Chan, Jang Wook Choi, Yan Yao, Matthew T McDowell, Seok Woo Lee, Ariel Jackson, Yuan Yang, Liangbing Hu, and Yi Cui. Stable cycling of double-walled silicon nanotube battery anodes through solid-electrolyte interphase control. Nature Nanotechnology, 7(5):310–315, 2012.

[228] Hui Wu, Gerentt Chan, Jang Wook Choi, Yan Yao, Matthew T McDowell, Seok Woo Lee, Ariel Jackson, Yuan Yang, Liangbing Hu, and Yi Cui. Stable cycling of double-walled silicon nanotube battery anodes through solid-electrolyte interphase control. Nature nanotechnology, 7(5):310–315, 2012.

[229] Shizhao Xiong, Kai Xie, Erik Blomberg, Per Jacobsson, and Aleksandar Matic. Analysis of the solid electrolyte interphase formed with an ionic liquid electrolyte for lithium-sulfur batteries. Journal of Power Sources, 252:150–155, 2014.

[230] Jiantie Xu, Shixue Dou, Huakun Liu, and Liming Dai. Cathode materials for next generation lithium ion batteries. Nano Energy, 2(4):439–442, 2013.

[231] Kang Xu. Nonaqueous liquid electrolytes for lithium-based rechargeable batteries. Chemical reviews, 104(10):4303–4418, 2004.

[232] Pengfei Yan, Anmin Nie, Jianming Zheng, Yungang Zhou, Dongping Lu, Xiaofeng Zhang, Rui Xu, Ilias Belharouak, Xiaotao Zu, Jie Xiao, et al. Evolution of lattice structure and chemical composition of the surface reconstruction layer in $li_{1.2}ni_{0.2}mn_{0.6}o_2$ cathode material for lithium ion batteries. Nano letters, 15(1):514–522, 2014.

[233] Min Yang and Junbo Hou. Membranes in lithium ion batteries. Membranes, 2(3):367–383, 2012.

[234] R Yazami and Ph Touzain. A reversible graphite-lithium negative electrode for electrochemical generators. Journal of Power Sources, 9(3):365–371, 1983.

[235] Thomas A Yersak, H Alex Macpherson, Seul Cham Kim, Viet-Duc Le, Chan Soon Kang, Seoung-Bum Son, Yong-Hyun Kim, James E Trevey, Kyu Hwan Oh, Conrad Stoldt, et al. Solid state enabled reversible four electron storage. Advanced Energy Materials, 3(1):120–127, 2013.

[236] Hyun Yoon, GH Lane, Youssof Shekibi, PC Howlett, Maria Forsyth, AS Best, and DR MacFarlane. Lithium electrochemistry and cycling behaviour of ionic liquids using cyano based anions. Energy and Environmental Science, 6(3):979–986, 2013.

[237] Haijun Yu and Haoshen Zhou. High-energy cathode materials (li_2mno_3-$limo_2$) for lithium-ion batteries. The Journal of Physical Chemistry Letters, 4(8):1268–1280, 2013.

[238] K Zaghib, P Charest, A Guerfi, J Shim, M Perrier, and K Striebel. Safe Li-ion polymer batteries for HEV applications. Journal of Power Sources, 134(1):124–129, 2004.

[239] D Zhang, XL Wang, YJ Mai, XH Xia, CD Gu, and JP Tu. Enhanced electrochemical performance of Fes_2 synthesized by hydrothermal method for lithium ion batteries. Journal of Applied Electrochemistry, 42(4):263–269, 2012.

[240] Huigang Zhang and Paul V Braun. Three-dimensional metal scaffold supported bicontinuous silicon battery anodes. Nano Letters, 12(6):2778–2783, 2012.

[241] Shuguang Zhang and Z Conrad. Novel properties of ionic liquids in selective sulfur removal from fuels at room temperature. Green Chemistry, 4(4):376–379, 2002.

[242] Wei-Jun Zhang. Lithium insertion/extraction mechanism in alloy anodes for lithium-ion batteries. Journal of Power Sources, 196(3):877–885, 2011.

[243] Wei-Jun Zhang. A review of the electrochemical performance of alloy anodes for lithium-ion batteries. Journal of Power Sources, 196(1):13–24, 2011.

[244] Wei-Jun Zhang. A review of the electrochemical performance of alloy anodes for lithium-ion batteries. Journal of Power Sources, 196(1):13–24, 2011.

[245] Xiang-Wu Zhang, Prashanth K Patil, Chunsheng Wang, A John Appleby, Frank E Little, and David L Cocke. Electrochemical performance of lithium ion battery, nano-silicon-based, disordered carbon composite anodes with different microstructures. Journal of Power Sources, 125(2):206–213, 2004.

[246] Xueyuan Zhang, Bryon Winget, Marca Doeff, James W Evans, and Thomas M Devine. Corrosion of aluminum current collectors in lithium-ion batteries with electrolytes containing $LiPF_6$. Journal of The Electrochemical Society, 152(11):B448–B454, 2005.

[247] Honghe Zheng, Kai Jiang, Takeshi Abe, and Zempachi Ogumi. Electrochemical intercalation of lithium into a natural graphite anode in quaternary ammonium-based ionic liquid electrolytes. Carbon, 44(2):203–210, 2006.

[248] Qian Zhou, Wesley A Henderson, Giovanni B Appetecchi, Maria Montanino, and Stefano Passerini. Physical and electrochemical properties of n-alkyl-n-methylpyrrolidinium bis (fluorosulfonyl) imide ionic liquids: PY_13FSI and PY_14FSI. The Journal of Physical Chemistry B, 112(43):13577–13580, 2008.

[249] S Zugmann, M Fleischmann, M Amereller, Ruth M Gschwind, HD Wiemhöfer, and HJ Gores. Measurement of transference numbers for lithium ion electrolytes via four different methods, a comparative study. Electrochimica Acta, 56(11):3926–3933, 2011.

[250] Steven Zumdahl and Donald J DeCoste. Chemical principles. Cengage Learning, 2012.

Appendix A

Materials and Methods

A.1   Test cell (coin-type) fabrication

A.1.0.1   Conventional electrode fabrication

Conventional composite electrodes are made from the following mixture of ingredients: 1) an active material which acts as the storage site for Li, 2) a conductive agent, typically acetylene black (AB), which is added to promote the electronic conductivity throughout the composite network, and 3) a non-reactive binder, typically polyvinylidene difluoride (PVDF), which adheres all of the electrode components together. First, the active material and the AB are uniformly mixed in a mortar and pestle. After the PVDF is fully dissolved in n-methylpyrrolidone (NMP) solvent the active material/AB powder mixture is added along with some excess NMP until a desired viscosity is achieved. This solvent-solute mixture is all placed in a glass vial and on a magnetic stirrer overnight (12-15 hours) to produce a homogeneously mixed slurry. The slurry is then bladed with a notch bar onto a thin Cu (anode) or aluminum (cathode) foil current collector. Before the slurry is bladed onto the foil, both sides of the foil are cleaned with acetone and free from any noticeable bends, wrinkles, or blemishes. Once the slurry is spread, the electrodes are dried for 3 hours at 60-80°C in air. The dried electrode is then roll pressed to about 75% of its initial thickness and cut with a 0.5" punch. Before assembling the cells, the punched electrodes are dried overnight at 120°C in a vacuum oven.

A.1.0.2 Polyacrylonitrile-based electrode fabrication

The polyacrylonitrile (PAN)-based composite electrode architecture was developed following the same concept behind conventional electrode fabrication, except this architecture utilizes PAN (Mw = 150,000 g mol$_{-1}$) as both binder and conductive additive. The preparation of this architecture requires the mixing of PAN and nano-Si particles in a mortar and pestle and then mixing of the powders into N,N-dimethylformamide (DMF) solvent via magnetic stirring, producing a viscous slurry. Again, the slurry is directly bladed onto a Cu foil and dried for 3 hours at 60-80°C in air. The dried electrode is then calendared and cut with a 0.5" punch. Before assembling the cells, each punch went through a heat treatment under argon in a tube furnace at 300°C for 12 hours to cyclize PAN, turning it into a conductive and resilient conjugated polymer binder.

A.1.1 Electrospinning

Electrospinning was utilized to synthesize the PAN microfiber separators in Chapter 6. Electrospinning has been recognized as an efficient technique for the fabrication of polymer nanofibers. Since the 1980s and especially in recent years, the electrospinning process has gained more interest and attention due to its versatility and potential for applications in diverse fields, especially that of nanotechnology (since ultrafine fibers or fibrous structures of various polymers with diameters down to submicrons or nanometers can be easily fabricated with this process).

A schematic diagram to interpret electrospinning of polymer nanofibers is shown in Figure A.1. There are basically three components involved in the process: a high voltage supply, a syringe with a needle of small diameter, and a metal collecting target. In the electrospinning process a high voltage is used to create an electrically charged jet of polymer solution out of the needle. The voltage supply is directly connected to the needle where the solution/melt is ejected and the collector is grounded as indicated in Figure A.1. An electric field is induced at the needle tip where the solution fluid is held by its surface tension. This creates a charge on the surface of the liquid. Mutual charge repulsion and the attraction of the surface charges to the grounded target cause a
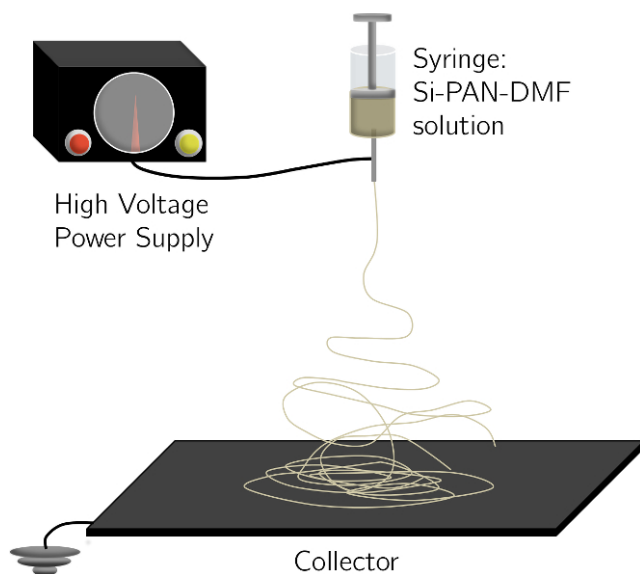
Figure A.1: Simple schematic of electrospinning set-up.

force directly opposed to the surface tension [59]. As the intensity of the electric field is increased, the hemispherical surface of the fluid at the tip of the capillary tube elongates to form a conical shape known as the Taylor cone [208]. By further increasing the electric field, a critical value is attained with which the repulsive electrostatic force overcomes the surface tension and the charged jet of the fluid is ejected from the tip of the Taylor cone. The discharged polymer (or nano-Si/PAN) solution jet undergoes an instability and elongation process, which allows the jet to become long and thin. Before reaching the collecting screen, the solution jet evaporates or solidifies, and is collected as an interconnected web of small fibers [51, 65].

Many parameters can influence the transformation of polymer solutions into nanofibers through electrospinning. These parameters include 1) the solution properties such as viscosity, elasticity, conductivity, molecular weight, and surface tension, 2) process variables such as applied electric field, tip to collector distance and feeding or flow rate, and 3) ambient parameters such as solution temperature, humidity, and air velocity in the electrospinning chamber [52]. Each of these parameters significantly affect the fibers morphology obtained as a result of electrospinning, and by proper manipulation of these parameters one can get nanofibers of desired morphology and diameters [48]. For further information on the effect each of these parameters has on the morphology of

the grown fibers and for more details on the electrospinning technique we refer the reader to Refs. [23, 90, 65].

A.1.2   Coin cell fabrication

All the electrodes in this dissertation were tested in a CR2032 stainless steel coin cell architecture, unless otherwise stated. Electrodes are punched to 0.5" diameter and then vacuum dried at 120°C before entering an argon filled glove box. Lithium metal foil, 0.5625" diameter punch, is used as a counter electrode for half-cell tests. Both electrodes are physically isolated by a glass microfiber disk separator and a liquid organic electrolyte of 1 M LiPF$_6$ in 1:1 EC:DEC (volume ratio) is used for the fast ion transport through the separator, unless stated otherwise. A schematic illustrating the coin cell architecture can be found in Figure A.2.

A.2   Material characterization methods

Characterization techniques used in this dissertation include X-ray photoelectron spectroscopy (XPS), Raman spectroscopy, field emission scanning electron microscopy (FESEM), low vacuum SEM (LVSEM), electrochemical quartz crystal microscopy (EQCM), transmission electron microscopy (TEM), fast Fourier transform of high resolution TEM micrographs, electron energy loss spectroscopy (EELS), energy-dispersive x-ray spectrometry (EDX or EDS), infrared spectroscopy (IR), and high-angle annular dark-field scanning transmission electron microscopy (HAADF-STEM). The purpose of this dissertation was not to advance the state-of-the-art of microscopy or spectroscopic techniques. For this reason, the reader is referred to introductory texts by Anthony West [223] and others [67, 193, 163, 85, 154] for descriptions of the theory behind each technique.

A.3   Electrochemical methods

The purpose of this section is to provide the reader with basic fundamentals of battery science and electrochemistry in order to gain an operational knowledge of the work addressed in this dissertation and work that is performed in a battery research laboratory. For a more thorough

SS cap

Gasket

Spring

SS disk spacer

Li metal foil

Glass microfiber
separator

Si-based electrode

SS can
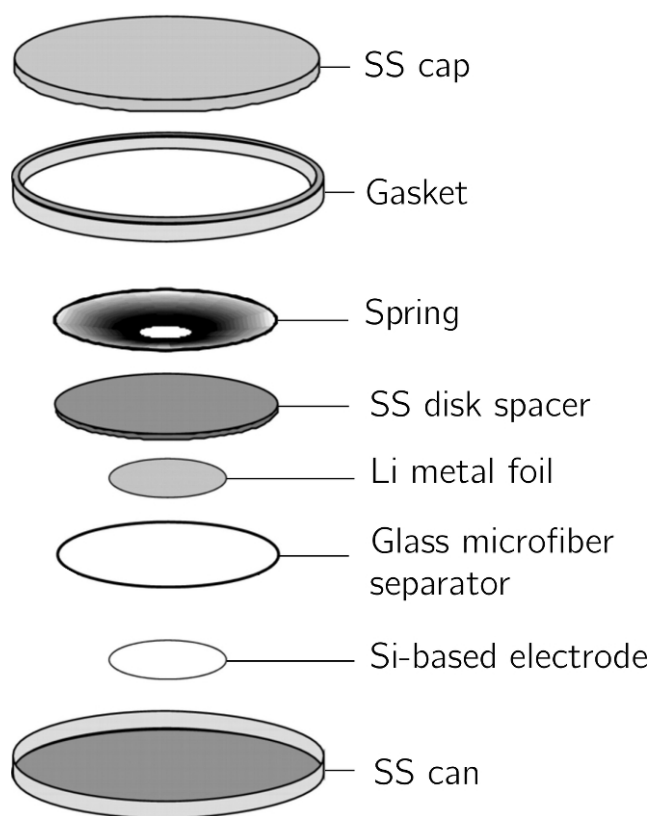
Figure A.2: Simple schematic of coin cell architecture.

treatment in electrochemical theory the reader is referred to a book on applied electrochemistry by Allen J. Bard and Larry R. Faulkner [18], the Handbook of batteries [132], a book on the thermodynamics of materials by David R. Gaskell [73], and an introductory text on basic chemistry by Steven S. Zumdahl [250].

A.3.1   Electrochemical terminology

This excellent section is excerpted from Leah Autumn Riley's dissertation [177] and amended in places.

There exists no standardized method for reporting electrochemical capacities. For example, storage capacity can be normalized to mass (mAh g^{-1}), electrode area (mAh cm^{-2}), or electrode volume (mAh cm^{-3}). Commercial, large scale results on the other hand tend to report the absolute capacity (Ah) while others will only publish x_{Li}, making values difficult for comparison. As an additional variable, batteries are also comprised of an array of inactive, supporting materials, such as binder, conductive agents, battery housing, etc. Reported capacities may include or exclude the non-active material. For uniformity, this dissertation will report specific capacity as a function of mass (mAh g^{-1}) normalized to the active material mass, unless otherwise stated. While the exclusion of supporting agents and other cell components yields an inaccurate measurement of the actual capacity of the battery, the purpose of this research is to focus on the fundamental science to analyze and improve materials for energy storage, not for the commercial production and sale of lithium batteries.

The fundamental electrochemical processes are oxidation and reduction which occur at opposing electrodes during cycling of a battery. However, since the oxidation at one electrode infers the reduction at the counter electrode, it becomes convenient to refer to the electrochemical reactions relative to a counter electrode. While the commonly used terms in the field of electrochemistry are *charge* and *discharge*, few consistencies within the literature can be found as to their proper use. Electrochemists may assign the labels anode and cathode to electrodes based on desired use, rather than the electrochemical reactions taking place there at a given time. This becomes particularly

confusing since a single electrode will, by definition, undergo both *cathodic* reaction when lithium is inserted and an *anodic* reaction when lithium is extracted. The two categories of test cells are separated into half-cells and full-cells. In a half-cell, the counter electrode is lithium metal and the electrode under study can either be a cathode or an anode. In a full-cell, a cathode is paired with a counter electrode that is an anode other than lithium metal.

In order to lessen any confusion, the following definitions will be used:

(1) **Lithiation** - Electrochemical intercalation (insertion) of lithium into a crystal structure or reaction of lithium with a chemical compound

(2) **Delithiation** - Electrochemical de-intercalation (extraction) of lithium from a crystal structure of reaction of a chemical compound to remove lithium

(3) **Anode** - Electrode at which oxidation occurs spontaneously in a full-cell

(4) **Cathode** - Electrode at which reduction occurs spontaneously in a full-cell

(5) **Discharge** - Spontaneous electrochemical processes ($\Delta G < 0$)

(6) **Charge** - Nonspontaneous electrochemical processes ($\Delta G > 0$)

A commercially popular, and regularly misused, electrochemical terminology is the current rate of *C-rate*. Broadly, *C-rate* is defined as the current necessary to charge (or discharge) an electrode to its theoretical capacity within a given time. For example, a *C-rate* of $C/10$ indicates that, theoretically, the complete electrochemical process will take 10 hours, while $10C$ indicates 6 minutes. *C-rate* is not a measure of the actual time for the cell to charge and discharge, though it can be. For a given material with a capacity, Q_{max}, determination of *C-rate* is based only upon the desired charge/discharge time. *C-rate* cannot account for the solid-state diffusion of lithium and other species, the charge-transfer resistance, or the possible alteration of the electrode surface. To clarify any confusion with the utilization of *C-rate* in this dissertation, we have provided a range of active material mass per electrode in each of the studies, which was used to calculate the

current applied in the system at a specific *C-rate* by multiplying active mass of Si by its theoretical capacity at room temperature and by the desired charge/discharge time. The slow initial charging rate ($C/20$ is used to allow the electrode to undergo surface structural changes, which normally occur during the first 3-5 cycles.

A.3.2   Electrochemical testing

Coin cells are electrochemically cycled using an Arbin BT2000. All cells undergo at least 6 hours of rest prior to testing in order to allow for the liquid electrolyte to fully permeate the porous electrodes. After resting, cells are cycled either with a constant current (CC) or constant current, constant voltage (CCCV) protocol as specified in each study.

The application of a constant current implies measuring the changing voltage, just like the application of a constant voltage implies the measuring of the changing current. Applying a constant current is also known as *galvanostatic*, while applying a constant voltage is also known as *potentiostatic*. The specific testing protocol for most cells in this dissertation is depicted in Figure A.3. In this figure voltage (left y-axis, blue) and current (right y-axis, red) are plotted with respect to time. The vertical dotted lines (grey) separate the regimes of *galvanostatic* and *potentiostatic* cycling. Initially, the cell is cycled with a constant current until it reaches a voltage cutoff at 0.05 V (*vs.* Li$^+$/Li), unless otherwise stated. After this voltage cutoff the cell is then cycled with a constant current until it reaches a voltage cutoff at 1 V (*vs.* Li$^+$/Li). Subsequently, after 1 V (*vs.* Li$^+$/Li) has been reached, the cycling protocol transitions to a regime of constant voltage operation for a period of 30 minutes. During this time, the current of the cell decays according to Fick's 2nd law as the ionic concentration gradients developed in the electrode during constant current operation are smoothed. Commonly, constant voltage operation of a cell is known as a voltage hold. The constant voltage regime is continued until either a fixed time is reached (as is the case for the work presented in this dissertation) or the current drops below a certain value. The completion of the voltage hold regime corresponds with the completion of one full cycle. Figure A.3 shows one and a half cycles with this testing protocol.
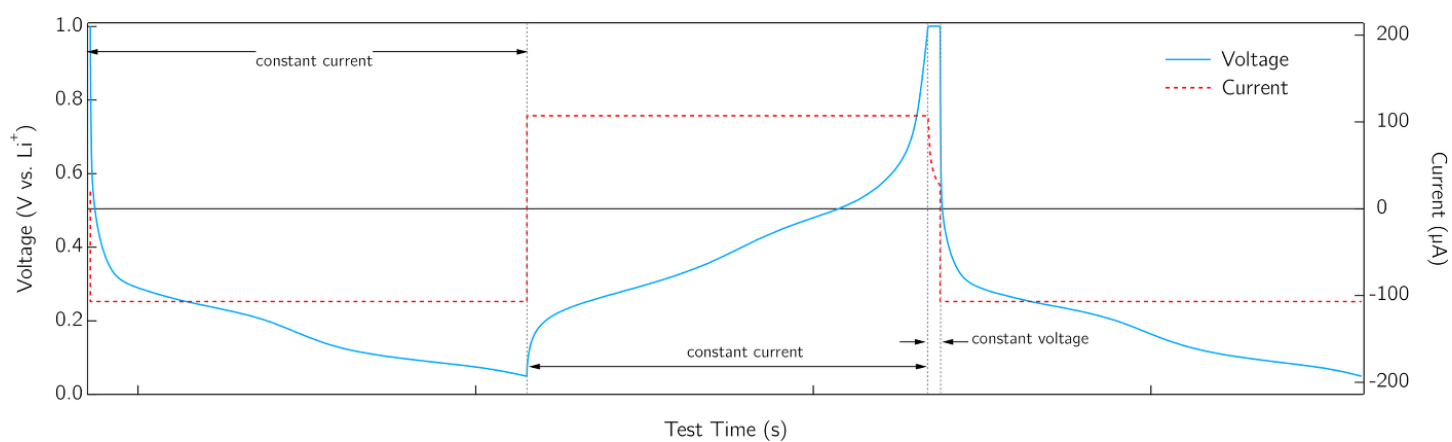
Figure A.3: Schematic of a typical constant current, constant voltage testing protocol utilized for most of this dissertation's work.

The sign of the applied current frequently causes much confusion. The convention used here is opposite of that used in the introductory text on electrochemical methods by Bard and Faulkner [18]. Here, positive current refers to the charging of a cell (synonymous with the progression of a non-spontaneous chemical reaction, *electrolytic cell*). A negative current refers to the discharging of a cell (synonymous with the progression of a spontaneous chemical reaction, *galvanic cell*).

A.3.3   Electrochemical impedance spectroscopy

Electrochemical impedance spectroscopy (EIS) is a powerful technique for understanding electrochemical systems. This technique involves a determination of cell impedance, in response to a small (5-10 mV amplitude) alternating current (AC) signal at any constant direct current (DC) potential (at the open circuit voltage of the cell or at different states of charge), over a span of frequencies ranging typically from 5 MHz to 10 mHz. From the measured cell impedance in the form of *real* (Re) and *imaginary* (Im) components and *phase angle*, it is possible to examine and qualitatively determine several processes such as the electronic/ionic conduction in the electrode and electrolytes, interfacial charging at the surface films or the double-layer, charge transfer processes and mass transfer effects (if any). With each of these processes having different time constants, features in the EIS spectra will show up at different frequencies, making it possible to analyze them independently. In other words, EIS is an *in situ* technique that further distinguishes the electron and ion transport properties of multi-layered structures.

Coin cells can be thought of in terms of a linear combination of layers: a current collector, a composite electrode film, a surface interfacial layer, a liquid electrolyte, and a lithium metal counter electrode. When subjected to a constant, direct current (DC), the multi-layered materials act as a single resistor and the measured resistance is the sum of the individual resistances of each component. However, when DC is replaced with AC, time constants from each cell component change according to frequency showing quite different effects, as discussed below [177].

The impedance of the entire cell is determined for different frequencies (ω) and is a function of the resistance (R) and the capacitance (C), $Z(\omega) = Z_{Re} - jZ_{Im}$, where [18],

$$Z_{Re} = R, \tag{A.1}$$

and

$$Z_{Im} = 1/\omega C \tag{A.2}$$

Equation A.1 and A.2 reveal that a purely resistive-like behavior will only yield a *real* impedance component while purely capacitor-like behavior will only produce an *imaginary* impedance.

A Nyquist plot (Z_{Im} *vs.* Z_{Re}) can then be used in order to determine the equivalent resistor and capacitor values based upon the *real* and *imaginary* impedance. Each material's frequency response is governed by a unique time constant, $\tau = RC$. The peak for each semicircle occurs when [19]

$$\omega\tau = 1 \tag{A.3}$$

which can also be written as,

$$Z_{Re} = Z_{Im} \tag{A.4}$$

Each layer, with unique values of R and C, will require a different frequency, ω, to satisfy Equation A.3. Therefore, each semicircle corresponds to the impedance of a single time constant (material/charge-transfer process) within the composite. The proper identification of each feature strongly depends on the conductive properties of the individual materials.

The final common Nyquist feature normally occurs at low frequencies and is called the Warburg impedance, Z_w. The Warburg impedance describes the impedance due to mass transfer derived from Fick's Law for a concentration gradient at low frequencies. At high frequencies, the value of Z_w is small. Only at low, near-DC frequencies, is the impedance of mass transfer measurable with EIS.

Figure A.4 illustrates an example of a Nyquist plot along with its respective equivalent circuit. As the frequency is increased, the materials begin to act as capacitors when the rate of change in the current becomes faster than the motion of charges. In this medium frequency region the finite impedance of the capacitance (C_d, the imaginary component of the impedance) manifests itself as a significant impedance, and is usually attributed to processes such as charge-transfer. At very high frequencies, the capacitance contribution usually falls to zero offering no impedance. All the current at high frequencies becomes charging current, and the only impedance seen is the ohmic resistance (R_Ω). At very low frequencies, C_d offers high impedance resulting in the passing of current flow mostly through charge-transfer resistance (R_{ct}) and R_Ω. Thus, at this very low frequency region the imaginary impedance component falls off again. In general, the departure of the Warburg impedance, Z_w, at this point is expected to become significant. Take note that the semicircle is a characteristic of a single time constant and real electrochemical systems show impedance plots often containing several time constants.

A.3.4 Differential capacity analysis

The differential capacity curve ($\mathrm{d}Q/\mathrm{d}V$) is obtained by differentiating the capacity (Q) versus the voltage (E), defined by

$$\frac{|dQ|}{dE} = \frac{|Q_t - Q_{t-1}|}{E_t - E_{t-1}}, \tag{A.5}$$

where Q_t and E_t are capacity and voltage values measured at a given time (t), respectively. And Q_{t-1} and E_{t-1} are capacity and voltage values measured at a previous time (t-1), respectively.

The $\mathrm{d}Q/\mathrm{d}V$ as a function of potential gives information about the structural transformations during charge/discharge process. The advantage of the $\mathrm{d}Q/\mathrm{d}V$ curve is that voltage transitions and/or plateaus observed in the voltage versus capacity plots appear as clear identifiable peaks in the $\mathrm{d}Q/\mathrm{d}V$ curve. These peaks are usually associated to phase transitions and/or chemical reactions taking place in the electrode material. Note that polarizations due to rate, temperature, or electrode composition can cause $\mathrm{d}Q/\mathrm{d}V$ peaks to 'float' so care must be taken to control experimental
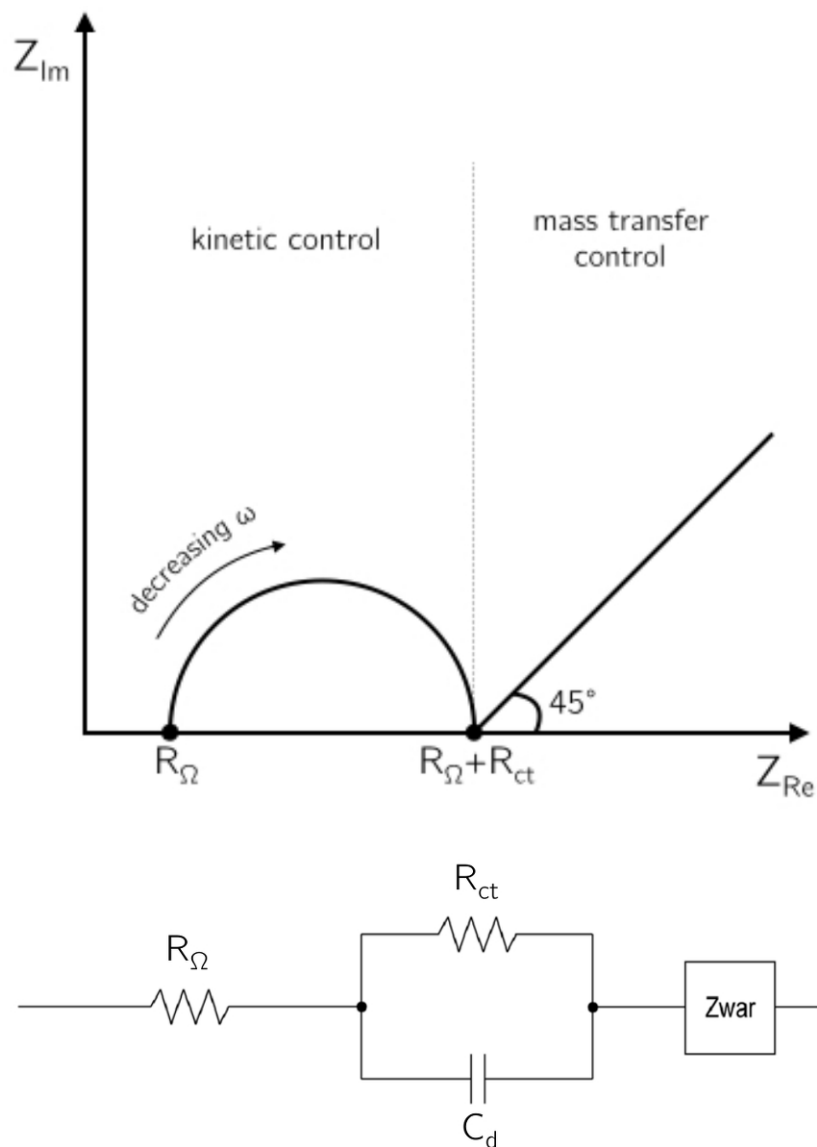
Figure A.4: Example of an impedance (Nyquist) plot for an electrochemical system with its respective equivalent circuit. Regions of mass-transfer and kinetic control are found at low and high frequencies, respectively.

parameters when comparing the $\mathrm{d}Q/\mathrm{d}V$ profiles of different samples.

In this discussion, we will use the silicon-lithium alloying redox to describe $\mathrm{d}Q/\mathrm{d}V$ electrochemical analysis. The first-cycle alloying curves exhibit a moderately sloping single plateau at around 0.1 V (*vs.* Li$^+$/Li), indicating a quasi-two-phase addition reaction instead of the multiphase reactions predicted by the equilibrium Li-Si phase diagram [130]. Moreover, the subsequent alloying curves are round-shaped with no potential plateaus in accordance with a solid-solution reaction.

For those sloping voltage curves, two broad peaks are often observed on the corresponding $\mathrm{d}Q/\mathrm{d}V$ plots in both the alloying and dealloying regimes. The peak potentials of most Si-alloys distribute at ~0.06 V and ~0.25 V (*vs.* Li$^+$/Li) for alloying, and ~0.3V and ~0.5V (*vs.* Li$^+$/Li) for dealloying. The structural changes responsible for these peaks are not clearly understood yet. It may be a result of short-range ordering in the amorphous Li$_x$Si-alloys [242]. Figure A.5 compares the charge and discharge profile of a conventional Si-based electrode versus lithium metal (Figure A.5a) with the corresponding dQ/dV profiles of the same charge and discharge (Figure A.5b). The $\mathrm{d}Q/\mathrm{d}V$ plot is rotated and reflected in order to make it clear that a $\mathrm{d}Q/\mathrm{d}V$ profile peak corresponds to a voltage plateau.

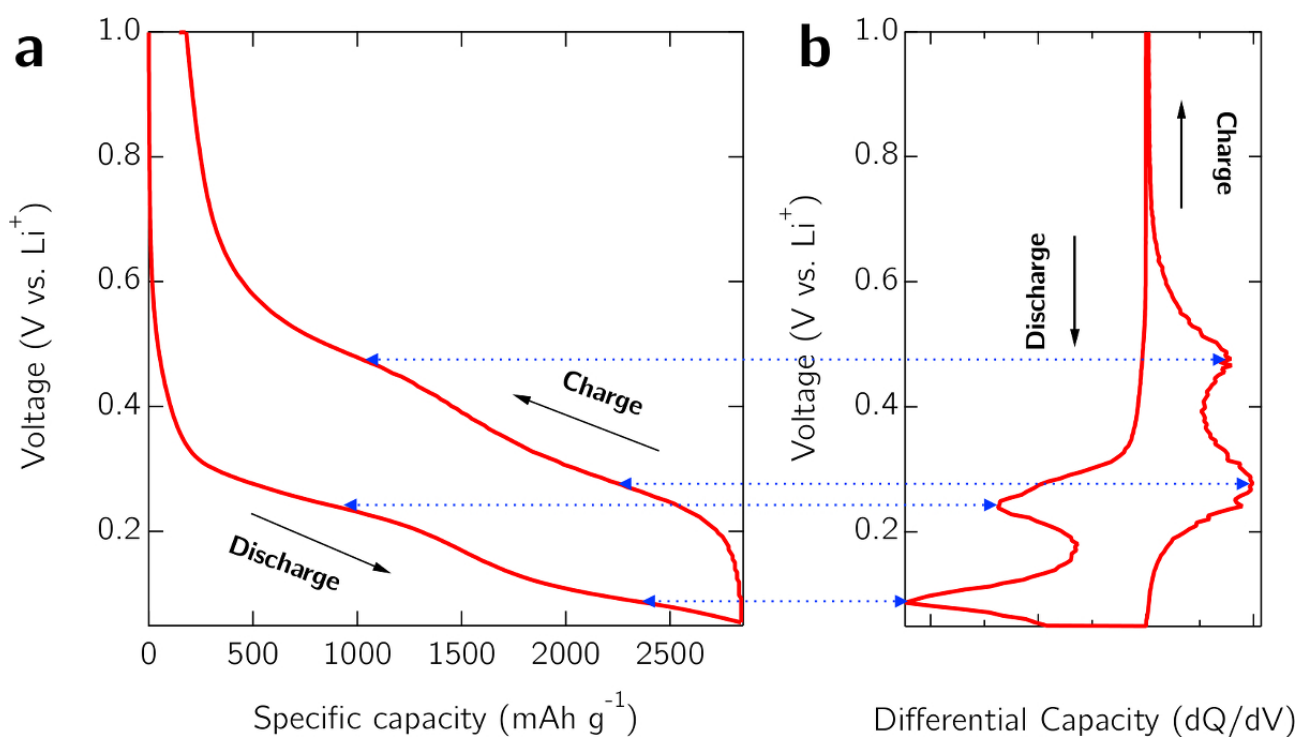Figure A.5: (a) Typical discharge and charge voltage traces for a conventional Si-based anode. (b) $\mathrm{d}Q/\mathrm{d}V$ plot of the same discharge and charge traces in (a), rotated and reflected in order to demonstrate that a $\mathrm{d}Q/\mathrm{d}V$ peak is associated with a specific voltage 'plateau' as depicted by blue dashed arrows.

A.4 Experimental - Corrosion of stainless steel battery components by bis(fluorosulfonyl)imide based ionic liquid electrolytes

$PYR_{13}FSI$ was the ionic liquid selected for this study. Ionic liquid solutions were provided by Boulder Ionics Corporation (U.S.A.) and contained less than 20 ppm (w/w) of moisture and less than 10 ppm (w/w) of halide and metal-ion impurities. A 1:2 weight ratio of ethylene carbonate and ethyl methyl carbonate (EC:EMC; BASF) was utilized as organic solvent and added to the $PYR_{13}FSI$ electrolytes in 10 vol.% EC:EMC and 50 vol.% EC:EMC mixtures. LiFSI ($1.2M$), provided by Boulder Ionics Corp., was added as the lithium salt subsequent to mixing the electrolyte solvents.

To evaluate the corrosion behavior, high-grade aluminum foil (ESPI Metals; $25\mu m$ thick; greater than 99.5% purity) and SS316 foil (MTI Corp.; 0.1 mm thick) were punched into 1.27 cm diameter disks, rinsed in dimethyl carbonate (DMC) and dried at 120 °C in a vacuum oven for 12 hours before testing. Corrosion cells contained an aluminum or SS316 disc working electrode and lithium foil counter electrode and were assembled in 2032 coin-type cells (Hohsen). Cyclic voltammetry (CV; Solartron 1280C), chronoamperometry (Arbin BT2000), and low vacuum scanning electron microscopy (LVSEM; JEOL SEM 6480LV) were utilized to characterize oxidative currents and morphological changes associated with the corrosion process. Cyclic voltammetry was performed on corrosion cells by cycling potential between 3.0 V and 4.6 V vs. Li/Li^+ at a scan rate of 1 mV s^{-1}. During chronoamperometry, the working electrode potential was ramped from open circuit voltage (OCV) to 4.2 V vs. Li/Li^+ at a sweep rate of 100 mV s^{-1} and held for 12 h; the potential was then ramped from 4.2 V to 4.6 V vs. Li/Li^+ at a sweep rate of 100 mV s^{-1} and held for 24 h. Infrared (IR) spectroscopy was used to characterize possible changes in solution chemistry induced by SS316 oxidation. Energy-dispersive X-ray spectroscopy (EDX; JEOL SEM 6480LV) was used to characterize changes in SS316 elemental composition after corrosion by $PYR_{13}FSI$-based electrolyte.

Composite electrodes were fabricated using $Li(Ni_{1/3}Mn_{1/3}Co_{1/3})O_2$ powder active material

(Johnson Controls), acetylene black (AB; Afla Aesar) as a conductive additive, and polyvinyldene fluoride (PVDF; Kynar) binder in a weight ratio of (85:7.5:7.5). The composite was mechanically cast onto a clean, high-grade aluminum foil current collector, dried, and calendared to 75% of its initial thickness to ensure adequate electrical contact. Potentio-galvanostatic cycling (Arbin BT2000) experiments utilized $Li(Ni_{1/3}Mn_{1/3}Co_{1/3})O_2$ positive electrodes and lithium foil negative electrodes assembled in 2032 coin-type cells (Hohsen). All cells used in this study contained glass microfibre filters (Whatman; grade GF/F) wetted with the IL-EC:EMC solutions as the electrolyte separator layer.

A.5   Experimental - Effect of organic solvent addition to $PYR_{13}FSI + LiFSI$ electrolytes on aluminum oxidation and rate performance of L333 cathodes

A.5.1   Electrolyte preparation

$PYR_{13}FSI$ was the ionic liquid selected for this study. Ionic liquid solutions were provided by Boulder Ionics Corporation (U.S.A.) and scanned for halide impurities. Impurities (F^-, Cl^-, Br^-, $SO4^-$) were quantified using a Dionex ICS-1100 ion chromatograph, calibrated for sensitivities as low as 1 ppm. All ionic liquids and lithium salts used in this study were subjected to ion chromatography, and the total impurity content of every solution prepared was calculated based off the mass percentage of electrolyte component in the total mass of the electrolyte. The solutions contained less than 20 ppm (w/w) of moisture and less than 10 ppm (w/w) of halide and metal-ion impurities. Ethylene carbonate (EC):ethyl methyl carbonate (EMC) (BASF) mixed in a 1:2 weight ratio was utilized as organic co-solvent and added to the $PYR_{13}FSI$ electrolytes in 10 vol.% and 50 vol.% mixtures. LiFSI or LiTFSI, provided by Boulder Ionics Corp., was added in a $1.2M$ concentration subsequent to mixing of the electrolyte solvents.

A.5.2   Electrode/ electrochemical cell fabrication

To evaluate the aluminum corrosion behavior, high-grade aluminum foil (ESPI Metals; $25\mu m$ thick; greater than 99.5% purity) was punched into 1.27 cm diameter disks, rinsed in dimethyl

carbonate (DMC) and dried at 120 °C in a vacuum oven for 12 hours before testing. Composite electrodes were fabricated using $Li(Ni_{1/3}Mn_{1/3}Co_{1/3})O_2$ powder material (Johnson Controls), acetylene black (Afla Aesar, AB) as a conductive additive, and polyvinyldene fluoride (Kynar, PVDF) binder in a weight ratio of (85:7.5:7.5). The composite was cast onto clean, high-grade aluminum foil current collector using a 5 mil doctor blade to achieve an active material mass loading of approximately 3 mg cm^{-2}. The electrodes were dried for 12 h at 80 °C. In order to ensure adequate electrical contact and to improve overall energy density, the electrodes were calendared to 75% of their initial thickness. Electrode disks of 1.27 cm diameter were punched and then dried at 120 °C in a vacuum oven for 12 hours before testing.

Corrosion cells contained a high-grade aluminum foil disk working electrode and lithium foil counter electrode. Electrochemical cycling tests utilized $Li(Ni_{1/3}Mn_{1/3}Co_{1/3})O_2$ positive electrodes and lithium foil negative electrodes. Both configurations were assembled in aluminum clad 2032 coin-type cells (Pred/Hohsen). Glass microfibre filters (Whatman; grade GF/F) were wetted with the IL-EC:EMC solutions and used as the electrolyte separator.

A.5.3 Electrochemical characterization

Cyclic voltammetry was performed on corrosion cells by cycling potential between 3.0 V and 4.6 V vs. Li/Li$^+$ at a scan rate of 1 mV s^{-1} (Solartron 1280C). Chronoamperometry was performed on aluminum corrosion cells containing each electrolyte solution. Assembled corrosion cells containing each electrolyte composition were allowed to rest for 5 min. The working electrode potential was ramped from open circuit voltage (OCV) to 4.2 V vs. Li/Li$^+$ at a sweep rate of 1 mV s^{-1} and held for 12 h; the potential was then ramped from 4.2 V to 4.6 V vs. Li/Li$^+$ at a sweep rate of 1 mV s^{-1} and held for 24 h (Arbin BT2000). The current was continuously monitored during voltage ramps and holds. Subsequent to chronoamperometry, corrosion cells were disassembled and the aluminum foil working electrode was washed in DMC. Low-vacuum scanning electron microscopy (JEOL SEM 6480LV) was performed on the surface of the Al electrode.

Lithium transference number, $t_{+,Li}$, was determined for electrolytes containing LiFSI salt

using the potentiostatic polarization (PP) method devised by Bruce and Vincent et al. [30, 29]and adapted for liquid electrolytes, including IL based electrolytes [249, 84, 236]. EIS and potentiostatic polarization (Solartron 1280C) were performed on cells containing lithium foil electrodes, which were scraped clean to ensure minimal charge transfer resistance, in coin-type cells. EIS was performed between a frequency range of 20 kHz - 10 mHz with an a.c. amplitude of 10 mV. σionic was determined for electrolytes containing LiFSI using the standard complex impedance method on a Solartron 1280C for a frequency range of 20 kHz - 10 mHz. Constant current-constant voltage (CC-CV) cycling of Li(Ni$_{1/3}$Mn$_{1/3}$Co$_{1/3}$)O$_2$ half-cells was carried out between 3.0 - 4.2 V vs. Li/Li$^+$ and 3.0 - 4.5 V vs. Li/Li$^+$ at room temperature in Al clad coin-type cells (Arbin BT2000). Rate studies were carried out with discharge/charge rates increasing to 8C before extended cycling at a rate of 1C, with the 1C rate corresponding to a current density of about 380 μA cm^{-2}.

A.6   Experimental - Electrospun polyacrylonitrile microfiber Separators for ionic liquid Electrolytes in Li-ion batteries

A.6.1   Fabrication of PAN microfiber separators

PAN microfiber-based nonwoven separators were prepared via electrospinning of a PAN/N,N-dimethylformamide (DMF) solution. A 10 wt.% solution was prepared by dissolving polyacrylonitrile (PAN, Sigma Aldrich) in DMF. This solution was ejected through a voltage applied (27 kV) nozzle to the grounded target plate with a feeding rate of 1.5 mL h^{-1}. The distance between the nozzle and the grounded target was 32 cm. Electrospinning for 2 h resulted in circular fiber mats with a thickness of approximately 200 μm and a diameter of approximately 13 cm.

A.6.2   Physical/ mechanical characterization of PAN microfiber separators

Morphological analysis of the as-made and post-test (100 charge-discharge cycles in a L333 half-cell) electrospun PAN fiber separators was carried out using low-vacuum scanning electron microscopy (JEOL SEM 6840LV). The wettabilities of the PAN separators, a conventional polyolefin microporous separator (PP, Celgard), and a glass fiber separator (GF/F, Whatman) by both ionic

liquid electrolytes and organic electrolyte were estimated by monitoring the variation of contact angle between the liquid electrolyte and the membranes at every 0.01 s using a high shutter speed camera. Porosity of the PAN fiber separators was determined using the Archimedes Technique, also known as the Immersion Technique. PAN microfiber mats were punched into the planar dog-bone configuration (20 mm length) for tensile testing (Shimadzu MMT-500 N, Japan) at a strain rate of 2.5×10^{-4} s^{-1}, with a 100% strain corresponding to 20 mm.

A.6.3 Electrochemical characterization PAN microfiber separators

RTIL electrolytes consisted of the N-methyl-N-propyl-pyrrolidinium (PYR$_{13}^+$) cation and either the FSI$^-$ or TFSI$^-$ anion. The RTIL electrolytes studied were PYR$_{13}$FSI ($1.2M$ LiFSI), PYR$_{13}$TFSI ($0.6M$ LiTFSI), and $1M$ LiPF$_6$ in ethylene carbonate, diethyl carbonate (50:50, Soulbrain) was used as a conventional organic electrolyte. Ionic liquid solutions were provided by Boulder Ionics Corporation (U.S.A.) and scanned for halide impurities. Impurities (F$^-$, Cl$^-$, Br$^-$, SO4$^-$) were quantified using a Dionex ICS-1100 ion chromatograph, calibrated for sensitivities as low as 1 ppm. All ionic liquids and lithium salts used in this study were subjected to ion chromatography, and the total impurity content of every solution prepared was calculated based off the mass percentage of electrolyte component in the total mass of the electrolyte. The solutions contained less than 20 ppm (w/w) of moisture and less than 10 ppm (w/w) of halide and metal-ion impurities. σionic was determined for the electrolytes using the standard complex impedance method on a Solartron 1280C for a frequency range of 20 kHz - 10 mHz.

A symmetric rate study (charge rate=discharge rate) was carried out using L333 positive electrodes and lithium foil negative electrodes with the cycling protocol outlined in a previous study, in which three cycles were performed at each rate (C/10, C/5, 1C, 2C, 4C, and 8C) to study cycling stability at higher rates and capacity recovery upon lowering rate [57].Composite electrodes were fabricated using slurry coating of Li(Ni$_{1/3}$Mn$_{1/3}$Co$_{1/3}$)O$_2$ powder material (Johnson Controls), acetylene black (Alfa Aesar, AB) as a conductive additive, and polyvinyldene fluoride (Kynar, PVDF) binder in a weight ratio of (85:7.5:7.5). The composite was cast onto clean, high-

grade aluminum foil current collector using a 5 mil doctor blade to achieve an active material mass loading of approximately 3 mg cm^{-2}. The electrodes were dried for 12 h at 80 °C. In order to ensure adequate electrical contact and to improve overall energy density, the electrodes were calendared to 75% of their initial thickness. Electrode disks of 1.27 cm diameter were punched and then dried at 120 °C in a vacuum oven for 12 hours before testing. PAN separators were soaked in RTIL electrolyte for 12 hours prior to fabrication of full-cells. Full-cells were built and tested according to the procedure outlined in our previous work, in which each electrode were electrochemically pre-conditioned prior to placing in the full-cell to allow precise control of the amount of lithium in the system [106]. Calculated from the active material mass, nSi-cPAN anodes were fabricated and matched with L333 cathodes such that the total anode capacity was 160% of that of the cathode capacity. Both electrodes were then pre-conditioned: the anodes were allowed to run for 10 charge-discharge cycles in a half-cell configuration and were stopped after full lithiation, while the cathodes were allowed to run for 3 charge-discharge cycles in a half-cell configuration and were stopped after full delithiation. The half-cells were then disassembled and the electrodes were used to fabricate 2032 coin-cell (Al-clad cathode cup) type full-cells. This method of pre-conditioning allows for full control of the amount of lithium in the system.

A.7 Experimental - Ionic liquid enabled FeS$_2$ for high energy-density Lithium-Ion batteries

Naturally occurring pyrite (FeS$_2$, Alfa Aesar) was mechanically milled at 400 rotations per minute (rpm) for 1 h using a planetary ball mill (MTI Corporation) in order to reduce the average particle size. For details on the ball-milling process, including post-milling material characterization, see Son et al. 2013 [198]. Composite electrodes were fabricated by mixing the ball milled FeS$_2$, acetylene black (AB, Alfa Aesar) as a conductive additive, and poly(vinylidene fluoride) (PVDF, Alfa Aesar) binder in a 60:20:20 weight ratio respectively, in a 1-methyl-2-pyrrolidinone (NMP, Alfa Aesar) solvent. The slurry was cast onto a clean, high-grade aluminum foil current collector using a 5 mil doctor blade to achieve an average FeS$_2$ active material mass loading of 1.2 mg cm^{-2}. The

electrodes were dried for 12 h at 80 °C and calendared to 75% of their initial thickness. Electrode disks of 1.27 cm diameter were punched and then dried at 120 °C in a vacuum oven for 12 h before testing.

Coin-type cells (2032, Pred Materials) were assembled using the prepared FeS_2 working electrode, a lithium metal foil counter electrode (Alfa Aesar), a glass fiber separator (GF/F, Whatman), and various electrolyte solutions. $1M$ $LiPF_6$ in ethylene carbonate, diethyl carbonate (50:50, Soulbrain) was used as a control electrolyte. IL solutions were provided by Boulder Ionics Corporation (U.S.A.) and scanned for halide impurities. Impurities (F^-, Cl^-, Br^-, $SO4^-$) were quantified using a Dionex ICS-1100 ion chromatograph, calibrated for sensitivities as low as 1 ppm. All ILs and lithium salts used in this study were subjected to ion chromatography, and the total impurity content of every solution prepared was calculated based off the mass percentage of electrolyte component in the total mass of the electrolyte. The solutions contained less than 20 ppm (w/w) of moisture and less than 10 ppm (w/w) of halide and metal-ion impurities.

Test cells were cycled using a constant current, constant voltage (CCCV) testing protocol between the voltage range of 1 V and 3 V vs. Li^+/Li at a constant rate of 0.1C, corresponding to a current density of about 100 μA cm^{-2} (Arbin BT2000). The voltage is held constant at 3 V for 30 min at the end of each charging cycle. EIS was performed on cells every 5th cycle at 2.25V during charge (Solartron 1280C) between a frequency range of 20 kHz - 10 mHz with an a.c. amplitude of 10 mV.

Microstructure of the FeS_2 composite cathode was investigated by analytical TEM (TECNAI F20 equipped with EDS) operating at 200 keV. As previously described, the TEM samples were prepared by sectioning electrodes, both cycled and uncycled, using a FIB's Ga^+ beam (FEI, NOVA200 dual beam system).

A.8   Experimental - Stable silicon-ionic liquid interface for next generation Lithium-ion batteries

A.8.1   Electrode and electrolyte preparation

nSi-cPAN and $Li(Ni_{1/3}Mn_{1/3}Co_{1/3})O_2$ electrodes were fabricated according to our procedures described in Ref. [173] and Ref. [58], respectively. Active material mass loading on both cathode and anode is at least double that of the referenced works. Ionic liquid electrolytes were provided by Boulder Ionics Corporation (U.S.A.) and scanned for halide impurities. Impurities (F^-, Cl^-, Br^-, $SO4^-$) were quantified using a Dionex ICS-1100 chromatograph, calibrated for sensitivities as low as 1 ppm. Ion chromatography was performed on all ionic liquids and lithium salts used in this work, and the total impurity content of every solution was calculated based off the mass percentage of electrolyte component in the total mass of electrolyte. The solutions contained less than 20 ppm (w/w) of moisture and less than 10 ppm (w/w) of halide and metal-ion impurities. $1M$ $LiPF_6$ in ethylene carbonate:diethyl carbonate (50:50, Soulbrain) was used as a conventional organic electrolyte.

A.8.2   Electrochemical characterization

Electrochemical measurements were carried out using an ArbinTM BT2000 battery test station. All half-cells were assembled using our prepared nSi-cPAN electrodes as the working electrode and lithium metal foil as the counter electrode. The separator was a glass micro-fiber disk (WhatmanTM GF/F) and the shell was a stainless steel CR2032 coin cell (Pred Materials). The electrolyte systems utilized were EC/DEC ($1M$ $LiPF_6$), $PYR_{13}FSI$ ($1.2M$ LiFSI), $PYR_{13}TFSI$ (0.6M LiTFSI), and EMIMFSI ($1.2M$ LiFSI). We used a constant current (CC) testing scheme to cycle our half-cells. No voltage holds were utilized during cycling (lithiation or delithiation), preventing the currents applied to relax and supply/remove extra Li^+, to highlight the true values of the cells' coulombic efficiencies for each respective current. The half-cells were discharged (lithiated) and charged (delithiated) with various cycling currents (where a C/10 rate is equivalent to 353.6 μA

cm^{-2}) between 0.05 and 1V (vs. Li/Li$^+$). Electrochemical measurements of half-cells were all normalized based on the mass of Si active material in each electrode (typically 1.1-1.3 mg). We used a constant current constant voltage (CCCV) testing scheme to cycle our full-cells. The full-cells were discharged and charged with various cycling currents (where a C/2 rate is equivalent to 502.9 μA cm^{-2} for the full-cells in Fig. 6a and 197.3 μA cm^{-2} for the full-cell in Chaper 8, Fig. 6b) between 2 and 4.15V (vs. Li/Li$^+$). Electrochemical measurements of full-cells were all normalized with respect to total mass of electro-active material in both cathode and anode electrodes (typically 7-9 mg).

A.8.3 Electronic structure calculations

Two types of calculations were conducted as mentioned in the main text. A detailed description of both the static cluster-based calculation and ab initio molecular dynamics (AIMD) simulations with a bare or cPAN-coated Li$_{13}$S$_4$ slab, and further discussions of the theoretical literature, can be found in the Supplementary Information. cPAN is modeled as graphene strips terminated with CN=C bonds, with a gap between the terminal sp2$^-$hybridized N atoms to allow for the intercalation of lithium, necessary for the Li$^+$ transport (Chapter 8, Fig. 2i).

Two types of calculations were conducted. Static cluster-based calculations, with a Li$^+$ and two FSI$^-$ or TFSI$^-$ anions, were performed using the Gaussian suite of programs, both the PBE and PBE0 functionals, a basis 6-31+G(d,p) for optimization, and the SMD dielectric continuum approximation with the dielectric constant, ε, set to 40. One excess electron is added in these calculations, so that the clusters exhibit a net charge of -2e and a net spin. Note that, if we had used a Li$^+$/FSI$^-$ or a Li$^+$/TFSI$^-$ pair only, adding an excess electron would have led to the unphysical reduction of Li$^+$ instead. The inclusion of two anions in the model was necessary to yield a physical solvation environment for Li$^+$.

Ab initio molecular dyamics (AIMD) simulations with a Li$_{13}$Si$_4$ slab and an anion were conducted using the VASP code version 4.6, PAW pseudopotentials, and are based on spin-polarized DFT/PBE calculations. The dimensions of the simulation cell are 15.84 x 34.00 x 13.32 with the

(010) surface exposed; 2 x 1 x 2 Monkhorst-Pack Brillouin sampling, 400 eV cutoff for wavefunctions, 1-fs time steps, and a 10^{-6} eV energy convergence criterion per time step. The protons are given tritium masses and a Nose thermostat maintains the simulation temperature at T=350 K. As such, the timescales reported are approximate and not directly comparable to measurements. Ion pairs of PYR_{13}^+/FSI^- and $PYR_{13}^+/TFSI^-$ are first optimized on the $Li_{13}Si_4$ (010) surface. While the potential (voltage) associated with such calculations are not transparently deduced, the decomposition mechanism is general invariant over large voltage windows.

A.8.4 Morphological characterization

FIB (FEI, NOVA200 dual beam system) equipped with a mobile air-lock chamber was used for TEM sample preparation. TEM and EELS analysis were performed with a FEI Tecnai F20 operated at 200 keV. A detailed description of our TEM and EELS characterization procedures can be found in Ref. [196].

A.8.5 X-ray photoelectron spectroscopy

XPS spectra were obtained on an AXIS His 165 and ULTRA spectrometer (Kratos) to determine the bonding configurations and chemical state of the elements present on the surface of the cycled nSi-cPAN particles. Argon milling was utilized for depth profiling (20 nm of depth).

A.8.6 Electrochemical quartz crystal microbalance

Similar to the electrode preparation for the coin-cell testing, nSi-cPAN films were coated on 1 in. diameter Pt 5MHz resonating quartz crystals (Stanford Research Systems; SRS). The electrochemically active area in the cell was determined to be 1.359 cm^2, based on the Pt pattern on the crystal. In order to mitigate error associated with frequency measurements using thick films on quartz crystals, all nSi-cPAN films were prepared with thicknesses under 10 μm. The crystals were placed in a SRS QCM200 crystal holder. The holder was modified with PEEK insulation so that a standalone cell, with a volume of 2.5 mL, could be enclosed with a lid. The ceiling of the cell

was lined with a Li foil counter electrode and connected to a copper wire. All current and potential parameters were consistent with the electrochemical characterizations of the coin-cells.

A.8.7   Full-cell fabrication

Full-cells were fabricated from pre-conditioned electrodes selected based on deliverable capacity. Calculated from the active material mass, nSi-cPAN anodes were fabricated and matched with L333 cathodes such that the total anode capacity was approximately 160% of that of the cathode capacity. Both electrodes were then pre-conditioned: the anodes were allowed to run for 10 charge-discharge cycles in a half-cell configuration and were stopped after full lithiation, while the cathodes were allowed to run for 3 charge-discharge cycles in a half-cell configuration and were stopped after full delithiation. The half-cells were then disassembled and the electrodes were used to fabricate 2032 coin-cell (Al-clad cathode cup) type full-cells. This method of pre-conditioning allows for full control of the amount of lithium in the system.

A.9   Experimental - Optimized silicon electrode-architecture, -interface, and -micro-geometry for next-generation Li-ion batteries

A.9.1   Material, electrode and electrolyte preparation

The SiNWs were fabricated using porous anodized alumina templates according to procedures described in Ref. [219]. The nSi-cPAN and $Li(Ni_{1/3}Mn_{1/3}Co_{1/3})O_2$ electrodes were fabricated according to our procedures described in Ref. [173] and Ref. [58], respectively. Ionic liquid electrolytes were purchased from Boulder Ionics Corporation (U.S.A.) and scanned for halide impurities. Impurities (F^-, Cl^-, Br^-, $SO4^-$) were quantified using a Dionex ICS-1100 chromatograph, calibrated for sensitivities as low as 1 ppm. Ion chromatography was performed on all ionic liquids and lithium salts used in this work, and the total impurity content of every solution was calculated based off the mass percentage of electrolyte component in the total mass of electrolyte. The solutions contained less than 20 ppm (w/w) of moisture and less than 10 ppm (w/w) of halide and metal-ion impurities. $1M$ $LiPF_6$ in ethylene carbonate:diethyl carbonate (50:50, Soulbrain) was used as a conventional

organic electrolyte.

A.9.2 Electrochemical characterization

Electrochemical measurements were carried out using an ArbinTM BT2000 battery test station. All half-cells were assembled using our prepared SiNW-cPAN electrodes as the working electrode and lithium metal foil as the counter electrode. The separator was a glass micro-fiber disk (WhatmanTM GF/F) and the shell was a stainless steel CR2032 coin cell (Pred Materials). The electrolyte systems utilized were EC/DEC ($1M$ LiPF$_6$), PYR$_{13}$FSI ($1.2M$ LiFSI). We used a constant current (CC) testing scheme to cycle our half-cells. No voltage holds were utilized during cycling (lithiation or delithiation), preventing the currents applied to relax and supply/remove extra Li$^+$, to highlight the true values of the cells' coulombic efficiencies for each respective current. The half-cells were discharged (lithiated) and charged (delithiated) with various cycling currents (where a C/10 rate is equivalent to 157.5 μA cm^{-2}) between 0.05 and 1V (vs. Li/Li$^+$). Electrochemical measurements of half-cells were all normalized based on the mass of Si active material in each electrode (typically 0.5-0.7 mg). We used a constant current constant voltage (CCCV) testing scheme to cycle our full-cells. The full-cells were discharged and charged with various cycling currents (where a C/2 rate is equivalent to 405.5 μA cm^{-2}) between 2 and 4.15 V (vs. Li/Li$^+$). Electrochemical measurements of full-cells were all normalized with respect to total mass of electro-active material in both cathode and anode electrodes (typically 6-8 mg). The conducted supercharging rate study (Chapter 9, Figure 3b) was carried out with discharging (lithiation) rates ranging from C/20 to 5C with all the rates after C/10 and including C/10 done at 60C. The charge (delithiation) rates were started at C/20, increased to C/10 and maintained at this rate for subsequent cycling and all done at room temperature. The conducted rate study (Chapter 9, Figure 3a) followed the same procedure described above, with the only difference being that all the charging and discharging rates were done at room temperature and ranged from C/20-1C.

A.9.3   Material characterization

FIB (FEI, NOVA200 dual beam system) equipped with a mobile air-lock chamber was used for TEM sample preparation [194]. TEM and EELS analysis were performed with a FEI Tecnai F20 operated at 200 keV. A detailed description of our TEM characterization procedures can be found in Ref. [196].

A.9.4   Full-cell fabrication

Full-cells were fabricated from pre-conditioned electrodes selected based on deliverable capacity. Calculated from the active material mass, SiNW-cPAN anodes were fabricated and matched with L333 cathodes such that the total anode capacity was approximately 130% of that of the cathode capacity. Both electrodes were then pre-conditioned: the anodes were allowed to run for 6 charge-discharge cycles in a half-cell configuration and were stopped after full lithiation, while the cathodes were allowed to run for 3 charge-discharge cycles in a half-cell configuration and were stopped after full delithiation. The half-cells were then disassembled and the electrodes were used to fabricate 2032 coin-cell (Al-clad cathode cup) type full-cells. This method of pre-conditioning allows for full control of the amount of lithium in the system.

Appendix B

Publications and Presentations

B.1   Peer Reviewed Publications

(1) Evans, T; Molina Piper, D.; Sun, H.; Porcelli, T.; Kim, S.C.; Han, S.S.; Kim, Y.S.; Ban, C.; Lin, F.; Cho, S.-J.; Leung, K.; Oh, K.H.; Lee, S.-H.* In Situ Engineering of the Electrode-Electrolyte Interface for Stabilized Over-lithiated Cathodes. Prepared for submission to Nature Materials (2015/16).

(2) Molina Piper, D.*; Evans, T.*; Xu, S.; Kim, S.C.; Han, S.S.; Liu, K.L.; Oh, K.H.; Yang, R.; Lee, S.-H. Optimized silicon electrode-architecture, -interface, and micro-geometry for next-generation lithium-ion batteries. Submitted to Advanced Materials (2015).

(3) Molina Piper, D.; Lee, Y.; Son, S-B.; Evans, T.; Lin, F.; George, S.M.; Lee, S.-H.; Ban, C. Robust and conductive trimethylaluminum-hydroquinone films for conventional high-capacity nano-Si anodes via molecular layer deposition. Submitted to Nano Letters (2015).

(4) Evans, T.; Lee, J.-H.; Bhat, V.; Lee, S.-H. Electrospun polyacrylonitrile microfiber separators for ionic liquid electrolytes in Li-ion batteries. Journal of Power Sources 2015, 292, 1-6.

(5) Molina Piper, D.*; Evans, T.*; Leung, K.; Watkins, T.; Olson, J.; Kim, S.C.; Han, S.S.; Bhat, V.; Oh, K.H.; Buttry, D.A.; Lee, S.-H. Stable silicon- ionic liquid interface for next generation lithium-ion batteries. Nature Communications 2015, 6, 6230.

(6) Evans, T.*; Molina Piper, D.*; Han, S.S.; Kim, S.C.; Oh, K.H.; Bhat, Vinay; Lee, S.-H., Ionic Liquid Enabled FeS$_2$ for High Energy Density Lithium-ion Batteries. Advanced Materials 2014, 26, 7386-7392.

(7) Evans, T.; Olson, J.; Bhat, V.; Lee, S.-H. Corrosion of stainless steel battery component by bis(fluorosulfonyl)imide based ionic liquid electrolytes. Journal of Power Sources 2014, 269, 616-620.

(8) Evans, T.; Olson, J.; Bhat, V.; Lee, S.-H. Effect of organic solvent addition to PYR$_{13}$FSI + LiFSI electrolytes on aluminum oxidation and rate performance of Li(Ni$_{1/3}$Mn$_{1/3}$Co$_{1/3}$)O$_2$ cathodes. Journal of Power Sources 2014, 265, 132-139.

(9) Yersak, T.A.; Evans, T.; Whiteley, J.; Son, S.-B.; Francisco, B.; Oh, K.H.; Lee, S.-H. Derivation of an iron pyrite all-solid-state composite electrode with ferrophosphorus, sulfur, and lithium sulfide as precursors. Journal of The Electrochemical Society 2014, 161, A663-A667.

B.2   Presentations

1. Stable silicon- ionic liquid interface for next generation lithium-ion batteries. Molina Piper, D.*; Evans, T.*; Leung, K.; Watkins, T.; Olson, J.; Kim, S.C.; Han, S.S.; Bhat, V.; Oh, K.H.; Buttry, D.A.; Lee, S.-H., 2015 Graduate Engineering Annual Research and Recruitment Symposium, 5 March 2015, University of Colorado, Boulder, Colorado.

2. Ionic Liquid Enabled FeS$_2$ for High Energy Density Lithium-ion Batteries, Evans, T.*; Molina Piper, D.*; Han, S.S.; Kim, S.C.; Oh, K.H.; Bhat, Vinay; Lee, S.-H., Proceedings of the Materials Research Society Symposium, Poster Session, 30 November 5 December 2014, Boston, Massachusetts.

3. Ionic Liquid Electrolytes for Advanced Lithium-ion Batteries. Evans, T.; Bhat, V.; Lee, S.-H., Spring 2013, Fall 2013, Spring 2014, Fall 2014, Posters and Presentations, Membrane Science, Engineering and Technology Center.